UNIVERSITY OF SOUTHAMPTON

SCHOOL OF ENGINEERING SCIENCES

MATERIALS RESEARCH GROUP

STRUCTURAL CHARACTERISATION OF SILICON-GERMANIUM VIRTUAL SUBSTRATE-BASED HETEROSTRUCTURES GROWN BY LOW PRESSURE CHEMICAL VAPOUR DEPOSITION

by Gabriela Delia Mihai-Dilliway

Thesis submitted for the degree of Doctor of Philosophy

March 2002

UNIVERSITY OF SOUTHAMPTON

ABSTRACT

SCHOOL OF ENGINEERING SCIENCES

MATERIALS RESEARCH GROUP

Doctor of Philosophy

STRUCTURAL CHARACTERISATION OF SILICON-GERMANIUM VIRTUAL SUBSTRATE-BASED HETEROSTRUCTURES GROWN BY LOW PRESSURE CHEMICAL VAPOUR DEPOSITION

by Gabriela Delia Mihai-Dilliway

Silicon-germanium heterostructures incorporating compositionally graded virtual substrates are important for the fabrication of a variety of advanced electronic devices. Their successful application depends critically on their surface morphology and defect content.

The aim of this research project is to characterise the way in which these structural properties are influenced by the growth parameters used in low pressure chemical vapour deposition (LPCVD) at the Southampton University Microelectronics Centre (SUMC). To this end, a comparative study of the surface quality and the distribution and density of misfit strain relaxation induced defects in SiGe virtual substrate-based heterostructures grown under varying conditions, was carried out. The growth parameters varied have been: growth temperature, initial and final Ge content, Ge concentration gradient, type of Ge grading profile (linear and stepwise) in the virtual substrate, and thickness and presence of a device structure in the capping layer of constant composition.

Characterisation was performed using Nomarski differential interference contrast microscopy, atomic force microscopy (AFM) and transmission electron microscopy (TEM).

Growth conditions combining a temperature of 800°C and a Ge concentration variation in the virtual substrate between 13% and 42% were found to activate an inefficient misfit strain relaxation mechanism in linear-graded heterostructures, whereby dislocation nucleation prevails over dislocation motion to relieve the misfit strain. Results showed rough surfaces with deep trenches and deep faceted pits, a high density of short misfit dislocation segments extending well into the capping layer of constant composition and a high density of threading dislocations reaching the surface. Additionally, threading dislocation pileups were observed at faceted pits.

At lower growth temperature (750°C) and for a Ge concentration variation in the virtual substrate between 12% and 42%, both surface morphology and defect configuration were improved. Furthermore, the step variation of the Ge composition in the virtual substrate was found to activate a misfit strain relaxation mechanism that resulted in superior surface quality than that obtained with linear grading. At the same temperature, the best surface properties were obtained for a Ge concentration variation in the virtual substrate between 0% and 32% and thicker capping layers for both step and linear grading of the Ge content. In these latter structures, the growth conditions used activate a relaxation mechanism that together with the increase in the capping layer thickness, which contributes to surface reshaping, result in smoother surfaces.

In conclusion, favourable conditions have been identified for the reproducible growth of device-grade SiGe virtual substrate-based heterostructures by low pressure chemical vapour deposition at the Southampton University Microelectronics Centre.

LIST OF CONTENTS

Page

LIST OF FIGURES AND TABLES

Figure/Table Page

Chapter 3

ACKNOWLEDGEMENTS

I would like to thank my two supervisors, Prof. Arthur Willoughby and Dr. Janet Bonar for their constant support and understanding for the whole duration of this work. Furthermore, I would like to express my gratitude to Dr. Patrick McNally, for his help with this work.

I would especially like to thank my parents, who have made everything possible for me and, in particular, my mother who has constantly encouraged me and patiently waited for me to complete this work.

Special thanks to my colleagues from the Materials Research Group for their companionship and interesting discussions and especially to Dr. Barry McGregor and Dr. Thomas Connolley, for their invaluable help with TEM analysis.

Also special thanks to Eric Bonner, Ted Meech, Sue Walker, Gwyneth Skiller and all the administrative and technical support staff in both the Materials and Microelectronics groups.

My gratitude also goes to Andrew, without whom I would not be in this country, to my sister and my friends, especially Tony, who have supported and encouraged me throughout.

Finally, I would like to express my gratitude to my fiancé, Nick, for his extreme patience and understanding and his invaluable support.

LIST OF PUBLICATIONS

G. D. M. Dilliway, A. F. W. Willoughby, J. M. Bonar, "Characterisation of Morphology and Defects in Silicon-Germanium Virtual Substrates" *Mat. Res. Soc. Symp. Proc.* **618** (2000) p. 265-270.

P. J. McNally, G. D. M. Dilliway, J. M. Bonar, A. F. W. Willoughby, T. Tuomi, R. Rantamäki, A. N. Danilewsky, D. Lowney, "Observation of Misfit Dislocation Strain-Induced Surface Features for a Si/Ge–Si Heterostructure Using Total Reflection X-Ray Topography" *phys. stat. sol.* (a) **180** (2000).

G. D. M. Dilliway, A. F. W. Willoughby, J. M. Bonar, "Characterisation of Morphology and Defects in Silicon-Germanium Virtual Substrates" *J. Mat. Sc.: Mat. El.* **11** (2000) p. 549-556.

P. J. McNally, G. Dilliway, J. M. Bonar, A. Willoughby, T. Tuomi, R. Rantamäki, A. N. Danilewski, D. Lowney, "On the use of total reflection x-ray topography for the observation of misfit dislocation strain at the surface of a Si/Ge-Si heterostructure" *Appl. Phys. Lett.* **77** (2000) p. 1644–1646.

W. E. Chen, G. D. M. Dilliway, P. J. McNally, T. Tuomi, A. F. W. Willoughby, J. Bonar, "Stress characterisation of device layers and the underlying $Si_{1-x}Ge_x$ virtual substrate with high resolution micro-Raman spectroscopy" accepted for presentation at the 4th International Conference on Materials for Microelectronics and Engineering (10-12 June 2002) Espoo, Finland.

J. M. Bonar, G. D. M. Dilliway, U. Straube, B. J. Ault, A. F. W. Willoughby, A.G. R. Evans, "SiGe virtual substrates grown by LPCVD for MOS device applications" accepted for presentation at the 4th International Conference on Materials for Microelectronics and Engineering (10-12 June 2002) Espoo, Finland.

1. INTRODUCTION

SILICON-GERMANIUM VIRTUAL SUBSTRATE-BASED HETEROSTRUCTURES

Epitaxially grown lattice mismatched heterostructures are increasingly used for both microelectronic and optoelectronic applications. Silicon-germanium (SiGe) heterostructures are usually encountered in two types of configurations:

1. In coherent structures, in which the SiGe layer is in perfect crystallographic registry (has the same in-plane lattice constant) with the underlying Si substrate, hence being subjected to misfit strain. In this case, the SiGe crystalline lattice is distorted from its equilibrium cubic symmetry, being under tetragonal distortion, i.e. biaxial compression in the growth plane and elongation along the growth direction. This type of configuration is only possible below a certain thickness of the SiGe layer, known as the critical thickness. Above the critical thickness, the SiGe epilayer starts to relax toward its bulk lattice constant and misfit dislocations (MDs) are introduced in the interface plane, some of the components of which thread to the free surface.
2. Structures incorporating a virtual substrate, which is a $Si_{1-x}Ge_x$ layer of variable composition, x ($0\%<x<100\%$), relaxed from misfit strain. $Si_{1-x}Ge_x$ virtual substrates can be used for:
   - 2.1. Strain engineering, as lattice mismatched templates for strained layer overgrowth. By engineering the lattice mismatch between the $Si_{1-x}Ge_x$ layer and the Si substrate, as well as the lattice mismatch between individual $Si_{1-x}Ge_x$ layers of different compositions, a multitude of new electronic properties and advanced devices based on bandgap and strain engineering have been enabled. Many of these devices call for a virtual substrate with an adjustable lattice constant in order to provide the appropriate strain required to achieve these properties. For example, the need to produce devices with an appreciable confining potential barrier for electrons has led to the creation of structures in which the Si layer is under biaxial tensile strain and the SiGe layer is under compressive or no strain, both layers being grown on an unstrained layer of intermediate composition (a virtual substrate). Virtual substrates can also be used to confine holes in Ge and SiGe layers under biaxial compression;
   - 2.2. Lattice constant engineering for unstrained layer overgrowth. Some devices require a virtual substrate with a defined lattice constant for unstrained layer overgrowth. For example, the integration of GaAs-based

epitaxial devices with Si technology can be possible via a $Si_{1-x}Ge_x$ virtual substrate graded to pure Ge (as the lattice constants of Ge and GaAs have very close values).

Materials scientists have been challenged to grow layers on Si substrates, which can act as virtual substrates with a designed lattice constant somewhere between that of Si and Ge, that would either create appropriate biaxial strain in the overlying layers or provide a certain lattice constant for further unstrained growth. The problem has always been that once the SiGe layer relaxes, defects form at the substrate–virtual substrate interface, some of which can thread to the surface where the active layers are grown. High threading dislocation (TD) densities severely degrade carrier transport and recombination processes leading to device failure. Nowadays silicon substrate wafers can be routinely grown with fewer than 10 dislocations per cm^2 and homoepitaxial growth of Si can compete with this level of quality, hence if SiGe epitaxy is to be compatible with existing processing technologies, it must be of sufficient structural perfection. The magnitudes of defect densities tolerable in device and circuit production have not yet been definitely established, but maximum permissible densities of the order 10^6 cm^{-2}, in majority carrier devices, 10^4 cm^{-2}, in minority carrier devices, and 10 cm^{-2}, for Si integrated circuit technology, constitute the values typically quoted [1].

Additionally, for the $SiGe/Si_{1-x}Ge_x/Si$ (001) system, the virtual substrate relaxation has been observed to generate undulations on the surface mainly along two perpendicular <110> directions (the same directions as the MDs present in the virtual substrate) creating what is known as a crosshatch pattern. The effects of the crosshatch pattern on the electronic properties of the structures are determined both by the lateral spacing of the surface features and by their height. Surface properties are usually quantified with the help of the Root Mean Square (RMS) of the surface roughness values. These values have a decisive influence on the further growth and processing of the active layer.

The main growth techniques used to obtain high quality SiGe virtual substrate-based heterostructures are molecular beam epitaxy (MBE) and chemical vapour deposition (CVD), the most widely reported of the CVD techniques being ultra high vacuum chemical vapour deposition (UHCVD). The effects of the growth technique and of the various growth parameters on the properties of the SiGe heterostructures grown by each

technique have been extensively analysed and different possible relaxation mechanisms have been reported.

The only reliable way to avoid dislocations in SiGe-based heterostructures is to grow the SiGe layers well below the equilibrium critical thickness. However this would limit the applicability of these heterostructures. Low defect levels can also be achieved by growing in the metastable regime. However, in this case, post-growth thermal exposure during device processing may cause further dislocation nucleation and propagation, thus restricting each time-temperature cycle during processing to less than that of the original growth cycle, which may prove to be an impractical limitation.

A variety of methods for minimising the TD density as well as improving the surface quality of relaxed SiGe heterostructures have been reported and some of them will be summarised herein.

One mechanism for reducing the TD density associated with the use of virtual substrates concerns allowing the misfit segments to grow sufficiently long so as to terminate at the edges of the wafer instead of the active structure at the top. In this situation, the ideal relaxed heterostructure configuration would display two orthogonal sets of parallel equally spaced <110> dislocations running across the entire (001) surface of the structure. This would result in no TDs propagating to the surface. In practice however, finite dislocation propagation velocities and blocking via dislocation interactions prevent this from happening. One of the parameters that enhances dislocation propagation, is temperature. However, high growth temperatures contribute to surface roughening. Furthermore even at high temperatures, the lateral dislocation motion to the edges of the wafer becomes improbable because as relaxation proceeds toward its equilibrium limit, the excess stress that promotes dislocation motion, decreases causing dislocation blocking to become increasingly prevalent and propagation velocities to become increasingly low.

A technique for minimising dislocation blocking processes in the virtual substrate is the continuous grading of the misfit strain to which it is subjected by grading the Ge concentration. Compositional grading of the virtual substrate in the SiGe heterostructures has contributed to the decrease in TD densities down to 10^2-10^4 cm^{-2}. The main benefit of compositional grading is that instead of the MDs being confined to a single $Si_{1-x}Ge_x$/Si interface, they will be distributed through the $Si_{1-x}Ge_x$ layer, which will compensate for

the continuous increase in the misfit strain with the Ge concentration. This offers an extra degree of freedom for MDs to propagate past each other (as they may be at different heights in the epilayer) and thus minimises the pinning events. For $Si_{1-x}Ge_x$/Si (001) heterostructures, during cool-down, the complete relaxation of the compressively strained $Si_{1-x}Ge_x$ lattice that occurred at the growth temperature, can result in tensile strain, due to the effects of the different thermal expansion coefficients between SiGe and Si (which are higher for SiGe than Si). Another advantage of compositional grading is that the vertical distribution of MDs can also vary during specimen cool-down, thus minimising the effects of the different thermal expansion coefficients [1]. Two types of Ge concentration grading have been reported: linear and stepwise. Due to its slightly easier control, linear grading is much more widely reported in literature, by comparison with step grading.

Furthermore, dislocation interactions can even be exploited to advantage by encouraging dislocation annihilation processes. TDs of opposite Burgers vectors can attract each other and annihilate, thus transforming two dislocation loops into one and removing two threading segments from the structure. Both high temperature and thicker virtual substrates enhance the total annihilation probability. However, the thermal budget required by growth at high temperatures for long durations (to obtain thick virtual substrates) is not easily achievable with all growth techniques and equipments.

High temperature growth ($\approx$ 900°C) of SiGe heterostructures incorporating virtual substrates initially by MBE and rapid thermal CVD (RTCVD), and more recently, by UHVCVD has been extensively studied by E. A. Fitzgerald et al. [2–7]. Growth at high temperatures was justified in two ways [3]: (i) to allow fast propagation of the existing dislocations, which in turn keeps the residual strain and thus the dislocation nucleation rate low; (ii) to anneal point defects present in the structure. Extensive studies of the role of Ge composition grading and of the thickness of the capping layer on the surface roughness were carried out. Fitzgerald et al. also characterised the effects of the strain fields created by the presence of MDs in the virtual substrate on the surface roughening of the capping layer [4, 5]. They showed that the crosshatch pattern at the surface of the capped highly relaxed layers correlates with the MD groups present in the $Si_{1-x}Ge$ layer and is the response of the epitaxial surface to the strain fields of these buried dislocations [4]. In graded layers, the distance between the buried MDs and the free surface is controlled by the grading rate, i.e. the amount of misfit introduced per unit thickness. Thus by keeping the total relaxation the same, a comparison between the effects of the

buried MD strain fields on the surface morphology of relaxed $Si_{1-x}Ge_x$ layers grown with different grading rates was carried out. This comparison is typically made through measurements of the root mean square (RMS) value of the surface roughness. Fitzgerald et al. observed that the RMS of the surface roughness increases for higher grading rates [4, 5]. Analyses of SiGe heterostructures incorporating relaxed graded layers grown at different grading rates showed that there is an increase in the TD density with increasing grading rate due to an increase in dislocation pileups within the graded layer. It is possible that groups of MDs block the glide of a perpendicular TD. In order for the threader to bypass the pinning dislocations, an excess stress is required, which according to Fitzgerald's calculations, can be provided by grading the Ge concentration with 10% per μm of thickness [3-5]. Furthermore, the increased formation of dislocation pileups with increased grading rate was found to be related to the inhomogeneous distribution of MDs in the relaxed $Si_{1-x}Ge_x$ layer [3]. The strain fields from groups of MDs create infrequent deep troughs in the crosshatch pattern, which block TDs, thus contributing to a further increase of the trough depth. One way of decreasing the formation of pileups consists in preventing the groups of MDs from creating large stress disturbances in the structure, thus avoiding long lengths of deep crosshatch. Fitzgerald et al. [6] accomplished this by growing on off-axis (miscut) (001) wafers (the angle of miscut was as high as 6° towards the <110> axis). Additionally, by introducing a chemical mechanical polishing (CMP) step at a certain stage of the Ge grading, Fitzgerald and et al. contributed to the planarisation of the surface and the release of blocked TD pileups, allowing them to relieve the strain introduced during subsequent growth and subsequently, eliminating the driving force for the nucleation of additional threaders [7]. Surfaces with reduced roughness and low TD densities for virtual substrates graded to pure Ge were obtained in this way. For UHVCVD growth to high Ge concentration (70-100%), Fitzgerald et al. reduced the growth duration by increasing the growth rate to 2 nm/s through rising the pressure from a few mTorr to 50-70 mTorr. As a consequence of their extensive research work, Fitzgerald and his co-workers obtained SiGe heterostructures incorporating virtual substrates grown at high temperatures, with TD densities as low as 10^4 cm^{-2}, which were successfully used for high mobility devices as well as for the integration of III–V devices on Si [4].

Low temperatures (≈ 500-560°C) growth of SiGe virtual substrate-based heterostructures especially by UHVCVD has been extensively studied by F. K. LeGoues, P. M. Mooney et al. [8-18]. Relaxation by a modified Frank Read (MFR) mechanism for dislocation

multiplication was identified and explained for these heterostructures [9, 10, 12, 13]. This mechanism only operates in heterostructures grown under 'very clean' conditions, as it requires the MD nucleation sources to be spaced by at least 1300 Å, hence it has not been widely reported. Mooney et al. also reported on the use of step grading in SiGe virtual substrates, which relaxed through the MFR mechanism [12]. They concluded that these heterostructures relax continuously during growth and after the onset of relaxation, the misfit strain at the start of growth of each step is essentially the same for steps of nearly equal change in Ge concentration and thickness. Furthermore, provided the required minimum value for thickness and Ge fraction of each layer of the step-graded region are exceeded, the residual strain is essentially independent of the thickness or growth temperature of the capping layer, but the surface roughness is strongly influenced by these parameters. LeGoues, Mooney and co-workers have also used different ways of reducing the TD density and the surface roughness in SiGe heterostructures incorporating virtual substrates grown at low temperatures, including:

- Grading of the Ge composition in the virtual substrate with rates of 50% / μm [12], thus much higher than those used by E. A. Fitzgerald et al. [3-5];
- Growth on miscut wafers [11] (with an angle of miscut lower than that used by Fitzgerald and co-workers, i.e. only 1–2° towards <110> axis).

F. K. LeGoues, P. M. Mooney et al. have also achieved heterostructures with TD densities as low as 10^4 cm^{-2}. Their SiGe heterostructures were successfully used for high electron and hole mobility devices [15-18].

Step-grading of the Ge concentration in the virtual substrate coupled with an in situ equilibration anneal after each step, in atmospheric pressure CVD (APCVD), has resulted in the lowest TD densities ever reported, as shown by G. Kissinger et al. (10^2-10^3 cm^{-2}) [19]. By annealing each Ge concentration step at temperatures of 1050-1095°C for ≈ 1h, G. Kissinger et al. ensured that total relaxation of each step occurred prior to the growth of the following step, thus resulting in heterostructures with low TD densities. Furthermore, due to the high temperature-long duration induced relaxation, the Ge concentration steps were much thinner than in usual compositional graded layers. However, the thermal budget required by this method is not suitable for all growth techniques, hence it cannot be widely used.

In the low range of growth temperatures, E. Kasper et al. used the injection of point defects in MBE-grown virtual substrates in order to reduce the kinetic barrier to MD nucleation and thus generate relaxation at reduced thicknesses and to aid dislocations climb, hence promoting TD annihilation [20]. Both low temperature MBE and Si^+ ion bombardment have been used as point defect sources during growth in the metastable regime and results obtained have been promising. Relaxed SiGe layers with thicknesses below 0.1 μm have thus been obtained.

The use of surfactants in solid source MBE (SS-MBE) growth, at 510°C has been shown to increase the critical thickness of the SiGe layer, thus pushing the surface further from the strain fields of the interfacial MDs and resulting in a smoothing process [21]. Very low RMS values (≈ 2 nm for 20x20 μm^2 surfaces) as well as low TD densities (≈10^4 cm^{-2}) have been obtained by J. L. Liu et al. in compositionally graded SiGe virtual substrates grown using antimony (Sb) as surfactant.

In the intermediate range of temperatures (560-800°C), systematic studies of the effects of the growth temperature and Ge gradient (4-50% / μm) on the structural properties of SiGe heterostructures incorporating virtual substrates graded to 29% Ge, grown by LPCVD, with growth rates of 0.1-0.4 nm/s and growth pressures ≈ 100 mTorr, have been carried out and reported by A. J. Pidduck et al [22]. The best surface quality and highest electron mobilities for SiGe heterostructures grown with this method were obtained in the high temperature-low Ge grading rate regime [22-24].

Additionally, in the intermediate range of temperatures (640-725°C), SiGe virtual substrates successfully used for Si-modulation doped field effect transistor (MODFET) structures grown by low energy plasma enhanced CVD (LEPECVD) with high growth rates, in the range 0.9-3.8 nm/s, have been reported by Rosenblad et al. [25, 26]. A strong temperature dependence of the TD density in the virtual substrates grown by this method has been observed.

Other techniques used for decreasing the TD density concerned the use of strained layer superlattices, which enhance the probability of TD annihilation by designing the thickness and strain of each individual layer in the superlattice to be insufficient to allow significant nucleation of additional dislocations, but sufficient to deflect TDs into being MDs at the

superlattice interfaces, process known as dislocation 'filtering'. Defect densities as low as $\approx 10^6$ cm^{-2} have been obtained with the help of this method [27].

The use of limited area growth is another promising approach to reducing TD densities. By growing on mesas or in windows, typically with dimensions in the range 10-100 μm, the number of heterogeneous dislocation nucleation sites is substantially reduced and furthermore, dislocations have to propagate more limited distances to reach the mesa edges, thus resulting in a reduction of the TD densities down to $\approx 10^6$ cm^{-2} [2]. The main disadvantage of this technique is the reduced dimensions for device processing that it imposes.

Many techniques have been developed in order to reduce the TD density and improve the surface roughness in the SiGe virtual substrate-based heterostructures. Most of them rely on removing TDs either by encouraging propagation over nucleation or by annihilation. Reduced TD densities and especially pileups also play an important part in improving the surface roughness. Additionally, reducing the occurrence of surface roughening (3D growth) contributes to low TD densities. Each of these techniques presents its advantages and its disadvantages, hence research continues in the efforts to obtain SiGe heterostructures incorporating virtual substrates with a minimal defect density and excellent electronic and optical properties.

The aim of our research, the results of which are presented herein, was to identify suitable growth conditions for obtaining high quality SiGe virtual substrate-based heterostructures in a LPCVD reactor designed and fabricated at the Southampton Universiy Microelectronics Centre (SUMC), which operates at growth pressures that have not previously been reported in the literature. To this aim, extensive systematic studies of the effects of growth parameters on the surface morphology and defect content of these heterostructures were carried out.

The SiGe heterostructures for this study were grown at temperatures in the intermediate-high range, both for this technique and by comparison with other techniques (i.e. 750 and 800°C). Thus, the growth temperatures have been high enough to thermally activate MD nucleation and elongation, but not too high, so as to cause thermal roughening. The growth pressure used (500 mTorr) resulted in growth rates (0.8-2 nm/s) similar for the two growth temperatures. The growth rate regime used in the SUMC-LPCVD has not been

explored previously. It covers growth rates lower than in APCVD and in the LEPECVD technique reported in [25, 26], and higher than in the LPCVD technique reported in [22-24] and in high vacuum growth techniques (UHVCVD and MBE).

In order to improve the effects of misfit strain relaxation on the structural properties of these heterostructures, two profiles of Ge concentration grading in the virtual substrate (linear and stepwise) were comparatively explored for different final Ge concentration values and different Ge concentration gradients. Emphasis was placed on the step grading of the Ge concentration, due to the superior structural properties displayed in an initial series of experiments. As already mentioned, step grading of the Ge concentration is less widely reported by comparison with linear grading. The Ge concentration value for the initial set of heterostructures studied has been chosen in the intermediate-high range, 42%, whilst in the second set, it has been in the intermediate range, 32%. Furthermore, for the second set of heterostructures, the last step of 2% Ge concentration has been kept compressively strained, thus contributing to turning the threaders into misfit segments, through a process similar to the dislocation 'filtering' obtained with the use of superlattices [27], thus keeping the dislocations well confined within the virtual substrate. The Ge concentration gradient values have been for most structures kept in the intermediate range, 16% and 22% / μm, higher than those used by E. A Fitzerald et al. (10%) and lower than those used by P. Mooney et al. (50%), but well below the limit for generating high TD densities, found by D. Dutartre et al. as being 137% / μm [28]. These grading rates coupled with the growth rates used, resulted in relatively thin virtual substrates (1.36-2.10 μm). Only one structure studied has been characterised by a low concentration gradient, 8%, resulting in a thick virtual substrate (3.9 μm).

From systematical studies of the effects of the growth parameters used by the SUMC-LPCVD technique on the structural properties of the SiGe virtual substrate-based heterostructures, suitable conditions for device-grade structures have been identified together with directions for further research.

2. THE AIM AND STRUCTURE OF THIS THESIS

The aim of our research, the results of which are presented herein, was to study the effects of some growth parameters on the morphology and defect content of SiGe virtual substrate-based heterostructures grown in a low pressure chemical vapour deposition reactor designed and fabricated at the Southampton University Microelectronics Centre (SUMC), in order to produce structures with high surface quality and low threading dislocation density, suitable for device fabrication.

Silicon and germanium, both crystallising in a diamond lattice, form a continuous series of solid solutions ($Si_{1-x}Ge_x$, with x ranging from 0% to 100%), the lattice constants of which are determined by their compositions [29-30]. **Chapter 3** of this thesis introduces the SiGe system, providing information on its crystalline structure and characteristic parameters and on the SiGe alloy phase diagram.

$Si_{1-x}Ge_x$ layers grown on Si substrates form SiGe heterostructures. Up to a certain thickness, known as the critical thickness, the SiGe layer grows in perfect crystallographic registry (has the same in-plane lattice constant) with the underlying Si substrate, hence being subjected to misfit strain. Above the critical thickness, the SiGe epilayer tends to relax toward its bulk lattice constant and MDs are introduced in the interface plane, some of the components of which thread to the free surface. A review of the work published on the subject of the critical thickness and relaxation sources and mechanisms in the $Si_{1-x}Ge_x$/Si (001) system, starting from the very early work of Frank and van der Merwe [31-34] and Matthews and Blakeslee [35-39] up to the most recent work concerning relaxation mechanisms, such as surface roughening [40-43] and MD sources like the 'diamond defect' [44], and the Hagen–Strunk [45-46] and the modified Frank Read (MFR) [9-12] dislocation multiplication mechanisms, is also included in this chapter.

In order to study the effects of different growth parameters on the surface morphology and the type and density of virtual substrate relaxation induced defects, two sets of SiGe heterostructures incorporating virtual substrates were grown, using different combinations of the growth parameters, and subsequently analysed. The growth parameters varied were:

- For the virtual substrate: growth temperature, initial and final Ge concentration, thickness, Ge concentration gradient, type of variation of the Ge concentration (linear and stepwise);
- For the capping layer: thickness and presence of a device structure.

The results obtained on the first test set of heterostructures served as guide for the choice of growth parameters for the second set of structures. Emphasis was placed on the step grading of the Ge concentration in the virtual substrate, as it exhibited superior structural properties. All heterostructures were grown in the Southampton University Microelectronics Centre (SUMC) by LPCVD. A description of the SUMC-LPCVD process as well as of the SiGe heterostructures grown and analysed for this study are contained in **Chapter 4**.

The complexity of the misfit strain relaxation activation process and of the defects induced by misfit strain relief as well as of the effects of these defects on the structural properties of SiGe heterostructures incorporating virtual substrates required extensive analyses to be carried out. The analysis methods employed for this study are presented in **Chapter 5** and the experimental results obtained are reported in **Chapter 6**.

Based on the experimental results presented in Chapter 6 and comparisons with the results already reported by other authors and summarised in Chapter 3, some conclusions could be drawn and are included in **Chapter 7** of this study. This chapter also presents further directions in which the research carried out could proceed.

3. LITERATURE REVIEW

This chapter describes the SiGe system, providing information on its crystalline structure and characteristic parameters of interest for this study, as well as on the SiGe alloy phase diagram. It also contains a review of the work published on SiGe virtual substrate-based heterostructures.

3.1. SILICON-GERMANIUM SYSTEM

This section contains crystallographic information concerning the SiGe system and an introduction to the SiGe alloy phase diagram.

Qualitatively, Si and Ge are very similar in their structural and electronic properties. They both crystallise in a diamond structure and form a continuous series of solid solutions, of the type $Si_{1-x}Ge_x$ where the Ge composition, x, ranges between 0% and 100% and the lattice constant varies significantly with composition [29, 30]. The diamond lattice consists of two interpenetrating face-centred cubic (fcc) sublattices, shifted by one fourth of the major diagonal (Figure 3.1). The unit cell contains **8 atoms**, which occupy the following positions:

0 0 0	**0 1/2 1/2**	**1/2 0 1/2**	**1/2 1/2 0**
1/4 1/4 1/4	**1/4 3/4 3/4**	**3/4 1/4 3/4**	**3/4 3/4 1/4**

The fractions indicate the height above the cube base in units of the cube edge (**a**). In this structure, the coordination number is 4, i.e. each atom is bonded to **4 nearest-neighbours** arranged in the corners of a tetrahedron and separated by distances of $(\sqrt{3}/4)\mathbf{a}$. The diamond structure is the result of covalent bonding between atoms (bonds are represented by rods in Figure 3.1).

The lattice constant of Si, confirmed by high resolution X-ray diffraction measurements on pure single crystal, is $\mathbf{a_{Si}} \approx \mathbf{5.431}$ **Å** [29]. The published room temperature data on undoped Ge single crystal give lattice constant values ranging from $\mathbf{a_{Ge}} \approx \mathbf{5.6573}$ **Å – 5.6579 Å** [29]. Hence, the Ge lattice is $\approx \mathbf{4.2\%}$ larger than the Si lattice. To date, the most precise and comprehensive determination of bulk lattice parameters and densities across the whole $Si_{1-x}Ge_x$ system has been carried out by Dismukes et al. [29]. The lattice

parameter was found to increase almost linearly with increasing Ge concentration in accordance with Vegard's rule:

$$a_{Si_{1-x}Ge_x} = a_{Si}(1-x) + a_{Ge}\,x \qquad (3.1)$$

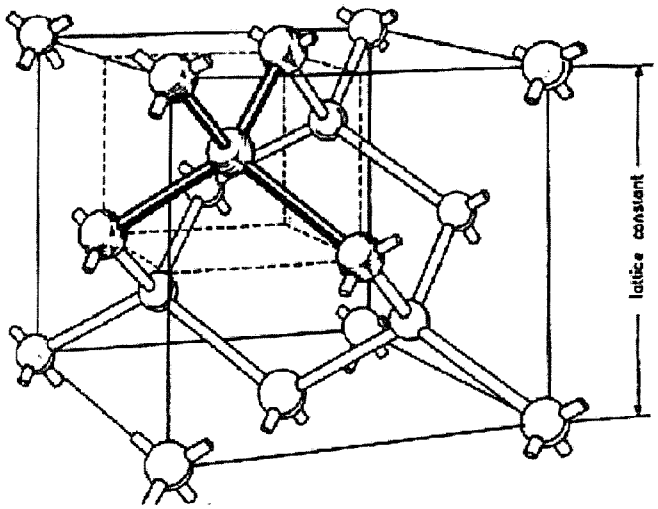

Figure 3.1. Schematic representation of the diamond lattice in the hard sphere model (atoms are represented by solid spheres with well-defined diameters), as reproduced from [29].

The SiGe phase diagram (Figure 3.2) has been determined by elaborate thermal and X-ray analyses [29]. It shows that Si and Ge are completely miscible in the liquid as well as in the solid state. The SiGe phase diagram has implications for both the production and the application of SiGe alloys. A positive aspect is that by simply choosing the alloy composition, an alloy with a well-determined lattice constant given by Vegard's rule (Equation 3.1) and the same crystalline structure as silicon and germanium (diamond cubic) will be obtained. The negative aspect is that it is difficult to produce a high quality, homogeneous solid solution from Si and Ge, using bulk crystal growth techniques, because during solidification from the molten phase the Si component strongly segregates. The combination of the difficulty in growing bulk SiGe and the desire to integrate SiGe with Si technology has led to the use of different epitaxy techniques for growing SiGe on Si substrates, one of which is chemical vapour deposition (CVD). One particular form of this technique i.e. low pressure CVD (LPCVD), presented in more detail in Chapter 4, was used to grow the virtual substrate-based heterostructures of interest for this study.

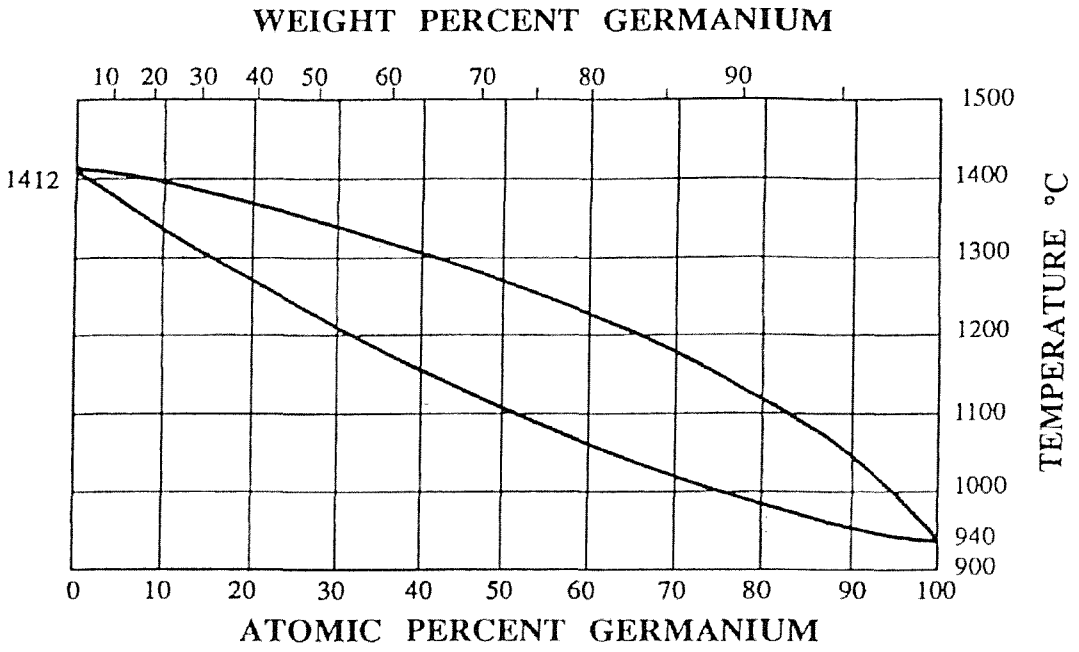

Figure 3.2. Phase diagram for the SiGe system reproduced from [29]; the melting point for Ge ($\mathbf{T_{mGe} \approx 938.3°C}$) is much lower than the melting point for Si ($\mathbf{T_{mSi} \approx 1414°C}$).

3.2. SILICON-GERMANIUM HETEROSTRUCTURES

This section introduces the notion of lattice-mismatched structures and provides information on SiGe heterostructures.

3.2.1. MISFIT STRAIN

The term *epitaxy* refers to the deposition of material onto a single crystal in such a way that the newly formed atomic layers maintain perfect registry with the underlying crystal.

The term *homoepitaxy* refers to the epitaxial deposition of more material to enlarge a single crystal (e.g. the growth of a Si layer on a Si substrate). Homoepitaxy is almost the only example of unstrained or lattice-matched thin film deposition (Figure 3.3 a).

The term *heteroepitaxy* refers to the epitaxial deposition of a layer made of a certain material on a substrate made of a different material (e.g. SiGe or Ge on a Si substrate). Heteroepitaxy always induces strain because of the differing lattice constants of the layers. For many years, this strain has been considered a major problem for the semiconductor industry, because it accounted for device failure through structural damage, adhesion issues between the epilayer and the substrate, and other similar problems [30]. Advances in crystal growth technology led to the growth of deliberately

strained as well as relaxed heterostructures for their electronic performances. Although it is the strain effects on the electronic properties (electronic band structure and carrier mobility) that are of interest, strain also has important consequences for the mechanical stability and structural properties of the semiconductors. In devices, even if grown homoepitaxially (i.e. silicon devices), strain may occur due to doping, bonding, coating, encapsulation, etc. In the early days of strained-layer work, it was felt that strain could not be incorporated into reliable devices [30]. At present, better control during growth and processing and a better understanding of the mechanical properties of heterostructures led to the fabrication of enhanced performance devices incorporating highly strained as well as totally relaxed epilayers.

Lattice misfit (mismatch) characterises heteroepitaxy. The *lattice mismatch* accommodation is commonly discussed in terms of three possible mechanisms:

1. Through *misfit strain* (ε_0). If the lattice constant of the substrate is smaller than that of the epilayer (e.g. epilayers of SiGe or Ge grown on a Si substrate), the *lattice mismatch* is accommodated through biaxial compression in the interface plane and elongation along the growth direction, creating a tetragonal distortion of the cubic crystal. This is known as *the pseudomorphic regime*, characterised by the growth of a thermodynamically stable layer strictly epitaxial (in perfect crystalline registry) on its substrate (Figure 3.3 b) and occurs only below a certain value of the epilayer thickness, known as the critical thickness ($\mathbf{h_c}$). *Misfit strain* (ε_0) is defined by:

$$\varepsilon_0 = \frac{a_l - a_s}{a_s} \tag{3.2}$$

where $\mathbf{a_l}$ is the lattice constant of the epilayer at equilibrium, in its natural state, and $\mathbf{a_s}$ is the lattice constant of the substrate in its natural state.

For alloys of variable composition, the mathematical expression for *misfit strain* can be obtained from Vegard's rule for the variation of the lattice constant with the alloy composition and in the case of $Si_{1-x}Ge_x$ grown on Si, is:

$$\varepsilon_o = \frac{a(x) - a_{Si}}{a_{Si}} \tag{3.3}$$

Where **a(x)** is the lattice parameter of $Si_{1-x}Ge_x$ and is given by Vegard's rule (Equation 3.1).

2. *Roughening of the epilayer surface*, which allows the atomic bonds near the surface to relax toward their equilibrium length and orientation (Figure 3.3 c). The basic energetic competition, in this case, is between the surface energy of the epilayer (representing an increase in the system energy, as surface roughening increases the total surface area and hence the surface energy) and the elastic energy (which is reduced by roughening, therefore representing a decrease in the system energy). Relaxation via roughening can occur for any epilayer thickness;
3. *Misfit dislocations* (MDs) and elastic strain (Figure 3.3 d). *Misfit dislocations* occur only in an elastically strained crystal, usually when it is grown beyond the critical thickness, and are meant to relax part or the whole of the misfit strain. The distinction between *dislocations* (generally) and *misfit dislocations* is very important. *Dislocations* in an unstrained crystal increase its energy and are not required by thermodynamic equilibrium, whilst *misfit dislocations* in an elastically strained crystal, allow the crystal to relax toward its bulk equilibrium lattice constant, thus decreasing its energy.

Both surface roughening and MDs are kinetically limited processes. Surface roughening is limited by surface diffusion lengths, whilst MDs are limited by nucleation/propagation barriers. These two processes can be competitive, such that the strain relaxed by surface roughening (which may occur before the critical thickness is reached and thus MDs nucleated) can reduce or eliminate the driving force for dislocation nucleation. Alternatively, they can be cooperative, as in the observed reduction of energetic barriers for dislocation nucleation associated with surface morphology [40, 41-43], and surface morphology induced by MDs [3-6]. However, the balance between relaxation through surface roughening and through MD generation is still the topic of active experimental research and theoretical simulations [1, 29].

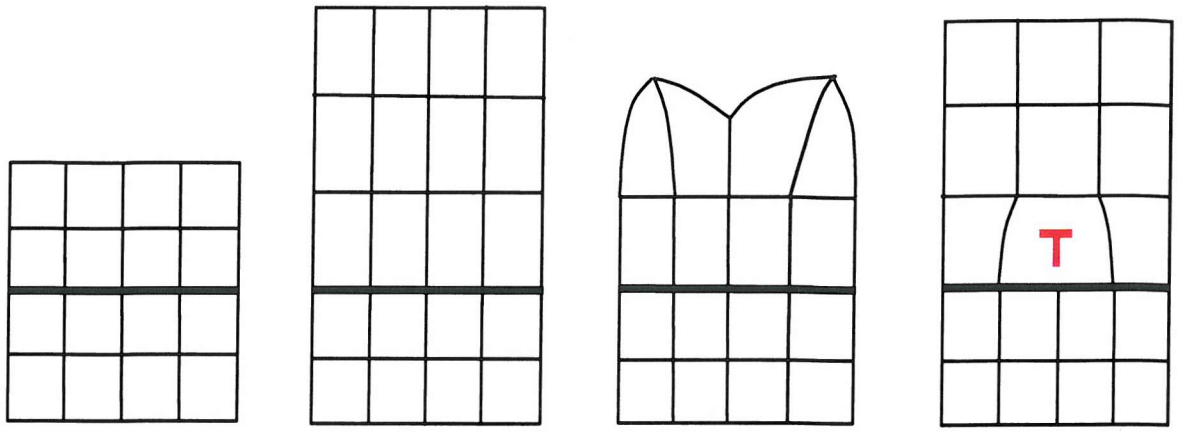

Figure 3.3. Different types of epitaxy in which the substrate is underneath the bold dark line and the epilayer above it: (a) homoepitaxy, in which more material is deposited in order to enlarge a single crystal; (b) heteroepitaxy below the critical thickness, in which the in-plane lattice of the epilayer matches that of the substrate, the epilayer being elastically strained (in the case of the SiGe/Si system, illustrated here, being under biaxial compression in the growth plane and elongated along the growth direction); (c) heteroepitaxy, in which the epilayer tends to relax toward its bulk lattice constant through surface roughening; (d) heteroepitaxy beyond the critical thickness, in which the epilayer tends to relax toward its bulk lattice constant with the introduction of MDs (represented in red).

3.2.2. MISFIT STRAIN ACCOMMODATION BY SURFACE ROUGHENING

Thin crystalline films grown near thermodynamic equilibrium exhibit one of three growth modes:

1. The Frank and van der Merwe (FM) growth or monolayer by monolayer (ML by ML) or two-dimensional (2D);
2. Volmer-Weber (VW) or cluster or three-dimensional (3D);
3. Stranski-Krastanov (SK) or layer-cluster, which starts off as 2D and ends as 3D growth.

The mode in which a particular combination of materials grows, depends on the relative bond strengths of the atoms in the deposited layer and between these atoms and the substrate atoms, and on the degree of lattice mismatch between the two materials. The way to predict the growth mode involves the relationship between the surface and interfacial free energies. Surface free energy is defined as the free energy to create an unit

area of surface on an infinite bulk solid [1]. If γ_s and γ_f are the surface energies of the substrate and deposited film respectively, and γ_{in} is the interfacial energy (where **n** is the number of monolayers deposited), ML by ML growth occurs only if:

$$\Delta\gamma_n = \gamma_{fn} + \gamma_{in} - \gamma_s \leq 0 \qquad (3.4)$$

for all values of **n** [1]. The term γ_{in} includes the excess free energy needed to create the initial interface between the two materials γ_{i0} and the additional free energy arising from strain due to lattice mismatch between the overlayer and the substrate.

Cluster or island growth is obtained when for all values of **n**:

$$\Delta\gamma_n = \gamma_{fn} + \gamma_{in} - \gamma_s > 0 \qquad (3.5)$$

In the intermediate case, SK growth, the overlayer initially grows in a ML by ML manner, but because of lattice mismatch, as **n** increases, strain energy contributes to γ_{in} to the point at which MDs are incorporated to relieve the strain and preferential growth will occur in the relaxed regions leading to the nucleation of 3D islands. Alternatively, the roughening of the growth front can relieve misfit strain at the expense of additional surface energy as already explained in § 3.2.1.

Equations 3.4 and 3.5 show thermodynamic equilibrium predictions in a very simplified way. Additional terms need to be incorporated into the interfacial energy γ_{in} , e.g. in the case where surface segregation of the more weakly bonded material (Ge in SiGe) occurs in order to reduce surface free energy [1]. Consequently, all the terms needed to fully describe the thermodynamics of the growth cannot always be known a priori.

ML by ML growth occurs only for a material deposited onto itself (i.e. in homoepitaxy), in which case $\gamma_{fn} = \gamma_s$ and $\gamma_i = 0$. For an overlayer deposited on a substrate made of a different material (in heteroepitaxy), ML by ML growth occurs only up to a certain thickness. The SiGe/Si system is considered a typical model for SK growth. As strain can be tuned by changing the alloy composition, it was expected that the growth of a $Si_{1-x}Ge_x$ alloy on a Si substrate could be used as a model system for understanding the influence of strain on growth [1]. However, this was not the case, as Ge is well known to segregate to

the surface of Si and $Si_{1-x}Ge_x$ alloys because dangling Ge bonds cost less energy than dangling Si bonds and the Ge-Ge bond **≈-1.92 eV** is weaker than the Si-Si bond **≈-2.31eV**, thus lowering the surface free energy [1]. In addition, in the presence of non-uniform strain, which can be caused by surface roughening (3D growth), it has been shown that there is a driving force for lateral concentration gradients in the SiGe alloy and Ge preferentially incorporates in regions in which strain has been relaxed, while Si preferentially incorporates in regions that are still lattice matched to the substrate. Alloy concentration gradients have been confirmed experimentally by Walther et al. [42]. The stress state of the heteroepitaxial $Si_{1-x}Ge_x/Si$ system depends on the growth conditions (temperature, growth rate, sample orientation, miscut, etc.). Under given growth conditions, the mode of stress relaxation depends critically on the misfit strain, which is given by the alloy composition during growth. Understanding the conditions under which strain is relieved by dislocation formation rather than roughening, is crucial in the growth of SiGe relaxed layers with low TD density, as island formation prior to dislocation formation, can severely alter the dislocation nucleation mechanisms, resulting in high dislocation densities [15, 40]. Tersoff and LeGoues [43] demonstrated that misfit strain relaxation through surface roughening is thermally activated, with an activation barrier that scales with misfit strain as ε^{-4} whilst relaxation through dislocation nucleation is characterised by an activation barrier that scales with misfit strain as ε^{-1}. Consequently, they concluded that relaxation via surface roughening is kinetically favoured at large misfit, while at smaller misfit, relaxation via MD nucleation dominates. However, in high temperature growth, surface roughening was observed to occur even for moderate misfit values [41].

The morphologies of $Si_{1-x}Ge_x$ alloy films grown on Si (001) substrates were found to be similar to those observed for Ge grown on Si (001) for a wide range of Ge concentrations ($x \geq 0.15$) [1]. These morphologies have been obtained with a variety of epitaxy techniques including MBE and CVD. While the general features of the observed morphologies are similar, there are differences that raise questions about the mechanisms that create these morphologies.

For example, the $Si_{1-x}Ge_x$ films deposited using LPCVD by Cullis et al. [41] were described as exhibiting ripples, which extended along [100] and [010] directions, with slopes ≈ 11°-12° from the (001) substrate. In cross-section transmission electron microscopy (XTEM) images, the waviness appeared somewhat rounded, but the values of

the sloping angle of the ripples were consistent with {105} facets previously observed in the growth of pure Ge "hut" clusters on Si (001). Ripple spacing values measurements carried out by Pidduck et al. over an alloy concentration range $0.15 \leq x \leq 0.27$ fitted well with the continuum elasticity models of strain relief, which predicted that strained films are unstable to roughening [1]. By comparison, the $Si_{1-x}Ge_x$ films with concentrations $x \leq 0.50$ MBE-deposited at room temperature by Jesson et al. and subsequently annealed in order to allow relaxation to occur, were described as exhibiting isolated pyramidal 3D islands with {105} facets and under certain conditions, pyramidal-shaped pits [1]. Jesson et al. concluded that their observation of isolated faceted islands and pits was an evidence that these surface features occur through a nucleation process, thus indicating that island formation is an activated process.

These two different explanations provided for similar-looking morphologies point to the difficulty in attempting to understand morphology evolution by looking at the final result. Understanding the mechanisms that govern surface roughening is additionally complicated by lateral as well as vertical concentration gradients [41]. While the formation of 3D islands indicates the possibility of an activation process, open questions, such as what is controlling their size and distribution, still remain and are the topics of on-going research [1].

3.2.3. MISFIT STRAIN ACCOMMODATION BY MISFIT DISLOCATIONS

3.2.3.1. Review of basic dislocation theory

Definition and geometry

A total dislocation is a linear, one-dimensional defect around which some of the atoms are misaligned. A circuit drawn round atoms enclosing this defect will exhibit a closure failure, which gives the *Burgers vector* of the dislocation, $\vec{\mathbf{b}}$. The *Burgers vector* of a dislocation characterises the magnitude and direction associated with the lattice distortion caused by the dislocation. For a total dislocation, the *Burgers vector* is a lattice translation vector. Although the *line direction* of a dislocation, characterised by $\vec{\mathbf{l}}$, may vary arbitrarily, its *Burgers vector* is constant at all points along the line. A total dislocation cannot end within the bulk of a crystal; it must terminate at the free surface of the crystal, its interface with a noncrystal, a node with another defect or upon itself to form a loop [1, 47].

The requirement concerning dislocation termination implies that an interfacial MD (already defined in § 3.2.1) cannot simply end within the interface. If the defect density is relatively low, making dislocation interactions unlikely, the most obvious place for MDs to terminate is at the nearest free surface, which in general is the epilayer surface. In order for this to happen, *threading dislocations* (TDs) which traverse the epilayer from its interface with the substrate to its free surface, are required (segment AB in Figure 3.4). In general, each MD is associated with a threading defect at each end, unless the length of the MD grows sufficiently thus enabling it to terminate at the wafer or mesa edge (C in Figure 3.4) or at a node with another defect.

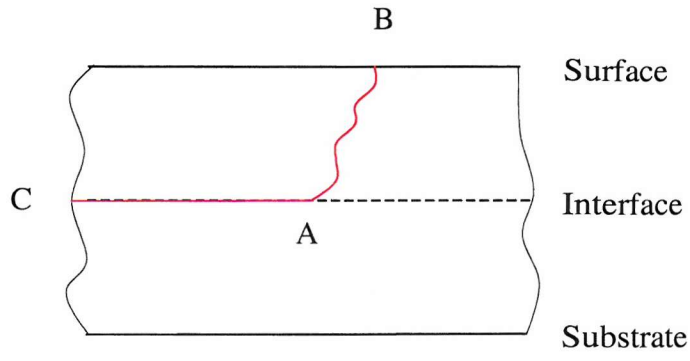

Figure 3.4. Schematic representation of an interfacial misfit dislocation, AC, with one end terminated at the edge of the wafer or mesa (C) and the other end terminated at the free surface through the threading segment AB.

Propagation of MDs occurs by lateral motion of their threading arms, which are extremely deleterious to the device application of heterostructures. For many device applications, a high interfacial MD density is tolerable if the epilayer surface is of sufficiently high quality, but even in this case, the presence of TDs compromises the device application.

The character of a dislocation is defined by the relationship between its Burger vector $\vec{\mathbf{b}}$ and its line, characterised by $\vec{\mathbf{l}}$. If $\vec{\mathbf{b}}$ is perpendicular to $\vec{\mathbf{l}}$, the dislocation is an edge dislocation, whilst if $\vec{\mathbf{b}}$ is parallel or antiparallel to $\vec{\mathbf{l}}$, the dislocation is a screw dislocation. In intermediate configurations, the dislocation is mixed character. As $\vec{\mathbf{l}}$ may vary along a dislocation, but $\vec{\mathbf{b}}$ may not, a nonstraight dislocation can vary in character along its length.

Dislocation energy

A dislocation has a self-energy arising from the distortions it produces in the surrounding medium [1, 47]. This energy is made of two contributions: those arising from inside and those arising from outside the dislocation core. The distortions of the atomic positions inside the dislocation core are so high that linear elastic theory can no longer be applied to model them, thus the dislocation core energy is not well known, but it is considered to depend upon both the material type (predominantly the nature of the interatomic bonds) and the dislocation character and Burgers vector [1]. The distortions of atomic positions outside the dislocation core may be modelled using linear elastic theory and expressions for the associated energy were derived. The self-energy per unit length of an infinitely long dislocation parallel to a free surface a distance **R** away is given by the expression [1]:

$$\mathbf{E_d} = [\mathbf{Gb^2}(1-\nu\cos^2\theta)/4\pi(1-\nu)]\ln(\alpha \mathbf{R}/\mathbf{b}) \qquad (3.6)$$

where **G** is the shear modulus and ν is the Poisson's ratio of the material, **b** is the magnitude of the Burgers vector of the dislocation, θ is the angle between the Burgers vector of dislocation ($\vec{b}$) and the dislocation line ($\vec{l}$) and α is a factor which accounts for the dislocation core energy and has values in the range 1 - 4 for semiconductors [1].

Thus, the dislocation self-energy varies as the square of the magnitude of its Burgers vector. This encourages the Burgers vector of a dislocation to be the minimum translation vector for a certain crystalline structure. For the diamond cubic structure of Si, Ge and SiGe, this minimum vector is **a/2<110>**, this being indeed the Burgers vector almost invariably observed for total dislocations in this type of crystalline structure [1, 29, 30]. The value of **R** from Equation 3.6 used in calculations of interfacial MD energies for uncapped strained layers, corresponds to the epilayer thickness, **h**. For interfaces with very high defect densities, a 'cut-off' value for **R**, corresponding to the average distance between defects (if this is less than the distance to the epilayer surface), is more appropriate.

Forces on dislocations

The self-energy of a dislocation produces a virtual force, which pulls the dislocation towards an 'image dislocation' on the opposite side of a free surface. Image effects also exist across internal interfaces between materials with different shear moduli [1].

The stress field around each dislocation produces interaction forces between separate dislocations. The magnitude of this forces is configuration dependent. In the simplest case of two parallel dislocation segments (**i** and **j**), the interaction force per unit length of dislocation is given by [1]:

$$\mathbf{F_{ij}} = \mathbf{Gk_{in}}(\vec{\mathbf{b}}_i \cdot \vec{\mathbf{b}}_j)/\mathbf{R'} \qquad (3.7)$$

Where: **R'** is the distance between the two dislocation segments and $\mathbf{k_{in}}$ is a constant of proportionality having different values for different types of dislocations [47]. The other terms in Equation 3.7 have been defined previously. The expressions for $\mathbf{F_{ij}}$ are much more complex and beyond the purpose of this study; they are explained in [47]. Equation 3.7 shows that the force with which two dislocations interact due to the stress fields around each of them is maximally attractive for antiparallel Burgers vectors, maximally repulsive for parallel Burgers vectors and zero for orthogonal Burgers vectors.

Dislocation motion

Dislocations move most easily within their *glide planes*, which are the planes containing both their Burgers vectors and their dislocation lines [47]. For an edge ($\vec{\mathbf{b}}$ perpendicular to $\vec{\mathbf{l}}$) or mixed ($\vec{\mathbf{b}}$ and $\vec{\mathbf{l}}$ at an angle) dislocation, there is only one unique glide plane, whose normal is given by $\vec{\mathbf{b}}\mathbf{x}\vec{\mathbf{l}}$, whilst for a screw dislocation ($\vec{\mathbf{b}}$ parallel to $\vec{\mathbf{l}}$) any plane can be a glide plane. Glide occurs more easily on the widest spaced planes in a given system, because the Peierls stress resisting dislocation motion decreases with increasing planar separation [1]. For diamond cubic, zincblende and fcc crystals, the widest spaced planes are the **{111}** set of planes, which are indeed the most observed glide planes in these crystalline structures [1, 29, 30]. Glide occurs by reconfiguration of bonds at the dislocation core in order to effectively move the core one atomic spacing. No mass transport of point defects is required during the glide process. Motion out of the glide plane, called climb, occurs by the extension or shrinkage of the half plane terminating at the dislocation core and hence requires mass transport of point defects. Such diffusion processes are generally much slower than glide processes in most temperature regimes.

Interfacial misfit dislocations arrays

The resolved lattice misfit stress (σ_a) acting on a MD with Burgers vector $\vec{b}$ is given by the Schmid factor **S** [1]:

$$\sigma_a = \sigma_0 S = \sigma_0 \cos\lambda \cos\Phi \qquad (3.8)$$

where λ is the angle between $\vec{b}$ and that direction in the epilayer/substrate interface perpendicular to the dislocation line direction, ϕ is the angle between the glide plane and the interface normal and σ_0 is the lattice misfit stress, which is given by standard isotropic elasticity theory as:

$$\sigma_0 = 2G\varepsilon(1+\nu)/(1-\nu) \qquad (3.9)$$

where all terms have been defined previously. In the $Si_{1-x}Ge_x/Si$ system, $\sigma_0 \approx$ **9.4 x GPa** [1].

The effective strain relieving component of the MD is characterised by:

$$b_{eff} = |\vec{b}|\cos\lambda \qquad (3.10)$$

Equation (3.8) shows that only dislocations gliding on planes inclined to the interface experience a resolved stress (for $\phi = 90°$, $\cos\phi = 0$; for $\phi = 0°$, $\lambda = 90°$ and $\cos\lambda = 0$).

For the SiGe/Si **(001)** system, the 4 possible **{111}** glide planes intersect the **(001)** interface plane along orthogonal in-plane **[110]** and **[1$\bar{1}$0]** directions, with a pair of glide planes intersecting along each direction. For the SiGe/Si **(001)** orientation, only dislocations with Burgers vectors lying within these **{111}** planes will be able to move by glide. For a given glide plane, three such Burgers vectors exist (e.g. for the **(111)** glide plane, $\vec{b}$ can be **a/2[101]**, **a/2[110]** or **a/2[01$\bar{1}$]**). Of these three Burgers vectors, the last one is a screw dislocation and does not experience any resolved lattice mismatch stress, as $\cos\lambda = 0$. The first two are of mixed edge and screw character and are known as 60° dislocations, corresponding to the angle between $\vec{b}$ and $\vec{l}$ (Figure 3.5). Equation 3.10 and the schematic representation in Figure 3.5 show that for the 60° dislocations, only 50% of

the magnitude of their Burgers vector projects onto the interfacial plane ($b_{eff} = |\vec{b}|\cos\lambda = |\vec{b}|\cos 30^\circ \cos 54.7^\circ = |\vec{b}|/2$), thus they are only 50% effective in relieving lattice misfit. However, because of their ability to propagate rapidly by glide, these are the total dislocations generally associated with strain relief in SiGe/Si **(001)** heterostructures [1, 29, 30]. The geometry of MDs is different on interfaces oriented differently than **(001)**.

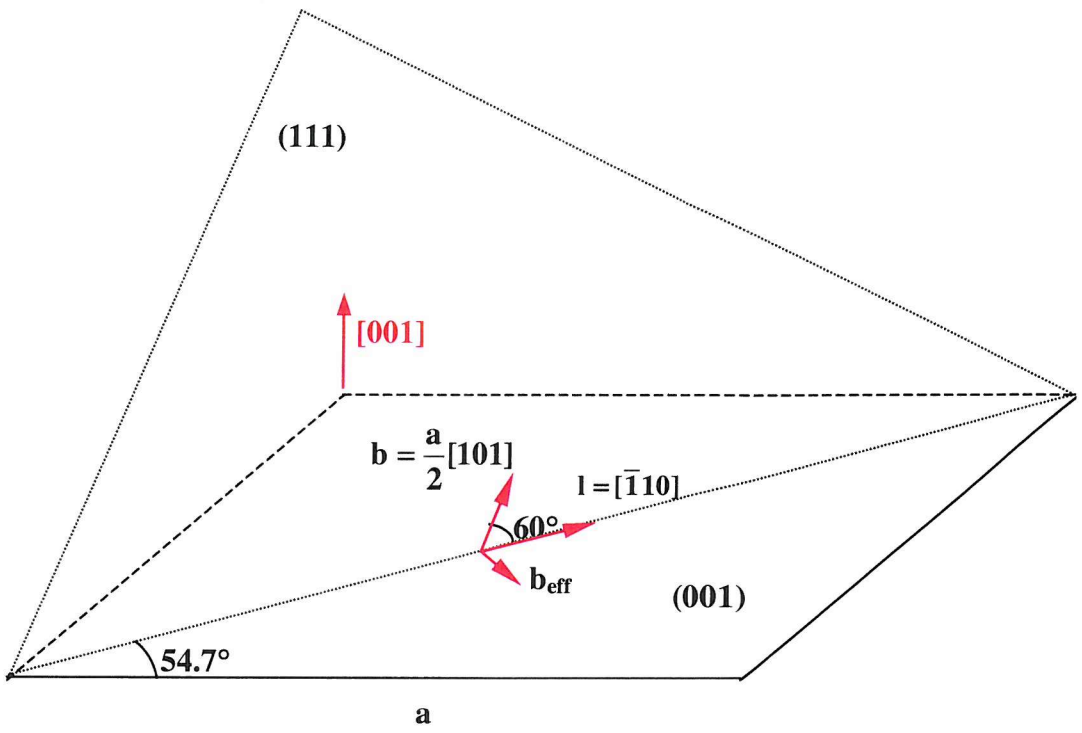

Figure 3.5. Schematic representation of a 60° dislocation in the diamond cubic system, the Burgers vector $\mathbf{b} = \frac{\mathbf{a}}{2}[101]$ lies in the glide plane **(111)** at **60°** orientation from the dislocation line $\mathbf{l} = [\bar{1}10]$, lying in the **(001)** interface plane.

The only other possibility to consider are the edge dislocations (e.g. for **(001)** plane $\mathbf{b} = \mathbf{a}/2[011]$). Such dislocations have their Burgers vectors lying within the interfacial plane and are 100% effective in removing lattice misfit. However, their Burgers vectors do not lie within any glide plane and thus these defects move by the far slower processes of climb. Nevertheless, such dislocations have been observed in systems characterised by high misfit strain [1]. At low and moderate strains, the 60° dislocations are prevalent [1, 29, 30].

3.2.3.2. Critical thickness

The theoretical approach for deriving the mathematical expression for the critical thickness, $\mathbf{h_c}$ is based on two well-known models: the Frank and van der Merwe also known as the energy minimisation model and the Matthews and Blakeslee also known as the force balance model. The Frank and van der Merwe theory [31-33] has been accepted as a qualitative and, to some extent, quantitative approach to the pseudomorphic growth of a deposit on a crystalline substrate of different lattice parameter below a 'critical misfit' [34]. Their models were mathematically complex and had analytical solutions only in the limits of very thin or very thick epilayers. Nevertheless, the energy minimisation approach set the foundations for subsequent developments. Conversely, the expression for the critical thickness derived by Matthews et al. [35-37] and known as the Matthews and Blakeslee critical thickness is used even at present. The Matthews and Blakeslee model adopted a force balance approach on propagating misfit/threading dislocations, which is equivalent to the energy minimisation concept. Matthews et al. showed that a dislocation already present in the substrate, which threads through the deposited layer (Figure 3.6 a), as it cannot end inside the crystal (§ 3.2.3.1), bows under the influence of stress (Figure 3.6 b). When the critical thickness is exceeded, the dislocation glides laterally producing a misfit segment at the interface (Figure 3.6 c). The kinetics of this process was determined from the forces on the bowed segment of the dislocation. The driving force was considered the misfit strain, which drives the threading arm motion so as to increase the interfacial MD and thus relax misfit in the epilayer, whilst the opposing force was what Matthews et al. called the 'line tension' in the MD.

By accurately expressing the stresses (rather than the forces) that act on the TD represented in Figure 3.6, Hull provided a more generally applicable theory for deducing the expression for $\mathbf{h_c}$ [1]. The primary stresses acting on the TD considered are: the resolved lattice misfit stress, σ_a, which drives the growth of the MD by lateral propagation of the TD, because up to an equilibrium density, the growth of MDs relaxes elastic strain by allowing the epilayer to relax toward its equilibrium lattice constant. The expression for σ_a is given by Equations 3.8 and 3.9. Furthermore, in § 3.2.3.1, the expression for the self-energies of MDs, arising from their strain fields in the surrounding crystal, is given, in Equation 3.6. This energy produces a restoring stress, σ_T (referred to by Matthews and Blakeslee, as the 'line tension' of the dislocation), which acts in order to inhibit the growth of the MD. The magnitude of this stress can be derived from the expression of the self-

energy (Equation 3.6) per unit length of dislocation. The net stress, σ_{ex}, is thus given by [1]:

$$\sigma_{ex} = \sigma_a - \sigma_T = 2GS\varepsilon(1+\upsilon)/(1-\upsilon) - [Gb\cos\phi(1-\nu\cos^2\theta)/4\pi h(1-\nu)]\ln(\alpha h/b) \quad (3.11)$$

where ε is the residual elastic strain in the system following partial plastic relaxation, through dislocation formation, and h is the film thickness. The other parameters have already been defined.

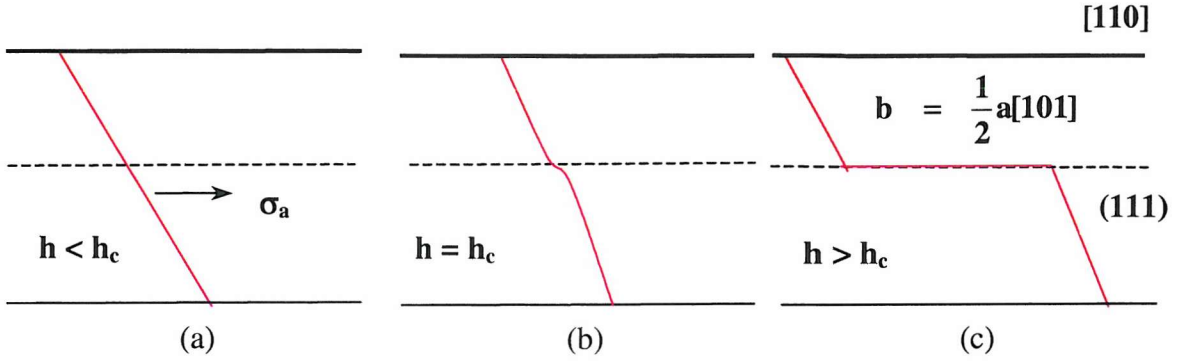

Figure 3.6. The generation of a MD in a diamond or zincblende system: (a) a dislocation line that initiates in the substrate and terminates at the surface of the sample threading through the heterostructure ($h < h_c$); (b) when the critical thickness is reached ($h = h_c$), the TD starts to bow; (c) when the critical thickness is exceeded ($h > h_c$), the threader produces a MD at the interface. The two continuous lines represent the intersection of the **(111)** slip plane with the upper (bold line) and lower surfaces of the heterostructure. The dashed line represents the intersection of the slip plane with the epilayer-substrate interface. The red line is the dislocation.

Equation 3.11 shows that for low values of h, σ_{ex} has large negative values, this corresponding to the regime in which the introduction of MDs would increase the energy of the system. With increasing h, σ_{ex} becomes less negative until at $h = h_c$, it becomes zero. This condition defines the critical thickness, h_c. With increasing $h > h_c$, σ_{ex} becomes increasingly positive, indicating that the MD array is increasingly favoured in the heterostructure. The equilibrium condition for any $h > h_c$, is given by $\sigma_{ex} = 0$. The magnitude of the critical thickness, h_c, is obtained by resolving Equation 3.11 for $\sigma_{ex} = 0$ and $h = h_c$:

$$h_c = b(1-\upsilon\cos^2\theta)\ln(\alpha h_c/b)[8\pi(1+\upsilon)\varepsilon\cos\lambda] \quad (3.12)$$

The equation for the critical thickness does not have analytical solutions, but is simple to resolve numerically. Because of its technical importance, the critical thickness has been studied extensively, both from the theoretical and experimental point of view and one of the most important conclusions drawn was that two definitions have to be considered for it [30]:

1. The equilibrium (theoretical) critical thickness, at which the pseudomorphic layer becomes unstable and starts to relax toward its bulk lattice constant;
2. The relaxation (observed) critical thickness, at which the introduction of MDs becomes significant.

Figure 3.7 shows plots of the predictions of the Matthews and Blakeslee theory for **60° a/2<110>** MDs in the SiGe/Si (001) system, using: **G = 64 GPa**, **ν = 0.28**, **cosλ = 0.5**, **cosθ = 0.5**, **b = 3.9 Å**, **ε = 0.041 x**, as well as plots of the experimental values obtained by various authors [1].

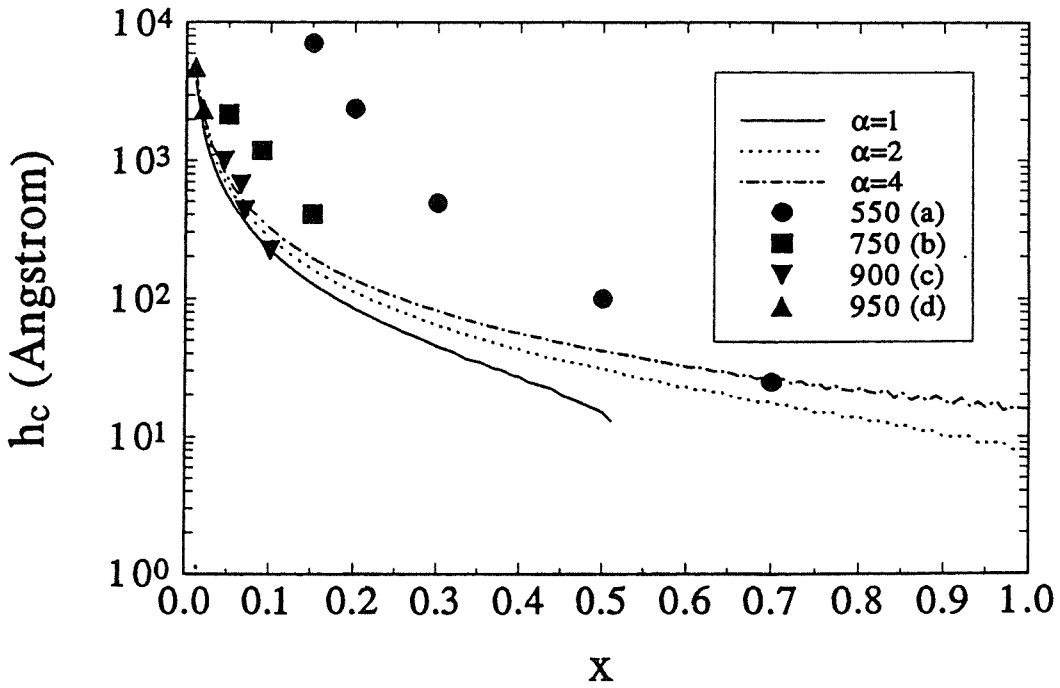

Figure 3.7. Predictions of the Matthews and Blakeslee theory for the critical thickness in the $Si_{1-x}Ge_x/Si$ (001) system for different values of the dislocation core energy parameter, α, reproduced after [1]. The experimental values obtained for $\mathbf{h_c}$ for different growth/annealing temperatures by (a) Bean et al. [48], (b) Kasper et al. [49], (c) Green et al. [50], (d) Houghton et al. [51] are also shown.

From the critical thickness curve (Figure 3.7), it can be observed that in the limit of high growth temperatures (relative to the melting points of the constituent materials,

$T_m \approx 1414°C$ for Si and $T_m \approx 938.3°C$ for Ge) the experimental and theoretical prediction for the critical thickness variation with the Ge concentration (x) agree well. At lower temperatures, experiment and theory are seen to diverge increasingly, in that larger critical thicknesses are measured experimentally as the temperature decreases, due to the thermally activated kinetics of the MD array generation. A brief explanation for this observation is as follows: as the equilibrium (or calculated) critical thickness is exceeded, plastic relaxation, by the generation of interfacial MDs is favoured, but barriers exist to the nucleation and propagation of MDs. With decreasing temperature, the nucleation and propagation rates decrease and plastic relaxation by MDs lags increasingly behind the equilibrium limit [1]. The equilibrium theory can predict when the first MDs are formed (which happens somewhere near the equilibrium critical thickness), but what happens after that is rather unpredictable in that the generation of fresh dislocations does not take place until much greater thicknesses (a few times the equilibrium critical thickness) [30]. In the metastable regime, some of the TDs may form MDs and some may not. The length of misfit that each threader can form is variable according to the other defects it encounters, to temperature, time and to other growth and/or post-growth annealing conditions. However, relaxation is negligible in this regime [30]. Relaxation is kinetically limited by the effects of the substantial energetic barriers associated with the MD nucleation and propagation, which have to be overcome by thermal activation and with the interactions between the different dislocations in the array. Kinetic effects are substantial in the SiGe heterostructures, as the covalent bonds in the Si and Ge lattices are relatively strong. The activation energies for dislocation motion in bulk Si and in bulk Ge are of the order **2.2 eV** and **1.6 eV**, respectively. These values are much greater than the thermal activation energy that can be reached at the temperatures used during crystal growth. Dislocation nucleation is also associated with significant activation barriers, thus the actual development of the MD array may lag well behind the equilibrium configuration generating large excess stresses (up to **1.0 GPa**) [30]. This can explain the growth of low MD densities far beyond the equilibrium critical thickness at lower growth temperatures, as can be seen in Figure 3.7.

Hence, the relaxation (measured) critical thickness depends on the dislocation kinetics. Furthermore, dislocation multiplication plays a very important part in misfit strain relaxation. Much work has been published on the dislocation movement and multiplication processes, some of which will be presented in the next section. When layers are grown thick enough to relax significantly, a great variety of behaviour has also been reported in

literature. The fact remains that relaxation occurs for values of the critical thickness several times higher than the calculated values.

In the case of confinement of the $Si_{1-x}Ge_x$ layers between a Si substrate and a Si and/or SiGe (of lower Ge concentration) cap, the MD configuration may involve interfacial segments at both the top and bottom interface, respectively [1, 37]. In this case, the segment of dislocation at the lower interface allows the lattice parameter of SiGe to be relaxed toward its equilibrium value by increasing the average lattice spacing of the material above the dislocation segment, whilst the upper dislocation segment adjusts the lattice constant of the capping material back to its unstrained value (Figure 3.8 b). In the absence of the MD segment at the upper interface, the capping layer would also have its lattice constant increased to match that of the relaxed underlying SiGe layer, thus generating a tensile-strained capping layer (Figure 3.8 a). It has been found that for capped SiGe layers, the critical thickness is increased approximately by a factor of two by comparison with uncapped layers [1].

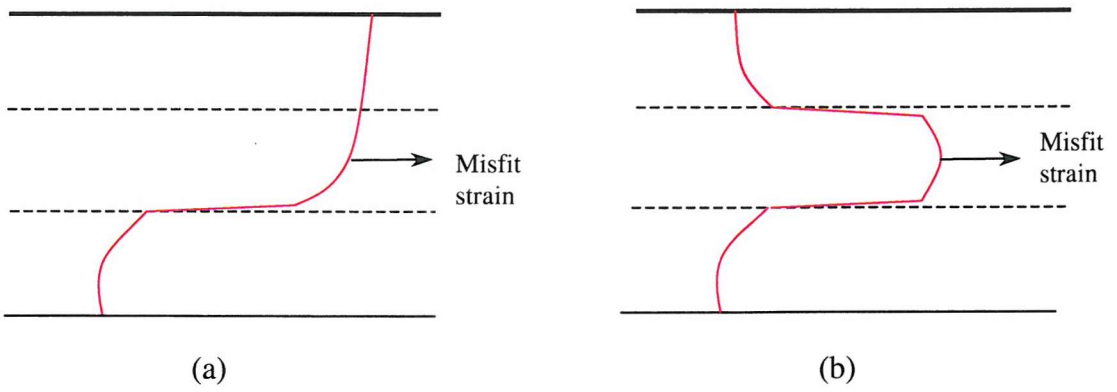

Figure 3.8. Schematic representation of MD configuration in a capped Si/SiGe/Si heterostructure: (a) single interfacial dislocation; (b) double interfacial dislocation (reproduced after [1]).

In the case of a multilayer structure, if each of the individual layers is thinner than the critical thickness of the layer grown directly onto the substrate, then most of the strain relaxation will occur via a MD array at the interface between the substrate and the first strained layer. If individual strained layers within the structure exceed the critical thickness, then substantial MD densities will generally be observed at the intermediate interfaces within the multilayer [1, 37].

A distinctively different situation is that of highly mismatched layers or layers grown on inadequately prepared substrates, conditions that can cause severe break-down in the ML by ML growth and lead to 3D growth or islanding. Equilibrium critical thickness is no longer applicable in this case and edge effects dominate i.e. islands relax through the injection of dislocations from the stress concentration at their edges. It has been found experimentally that in this case, relaxation can occur at thicknesses of a few monolayers, usually less than the equilibrium critical thickness, as there is no need for dislocation multiplication sources to be activated [30]. As growth continues, islands coalesce, but there is a remaining network of dislocations of very high density (threaders usually occur everywhere where the islands have coalesced) [30].

In general, low mismatch and/or high quality heterostructures exhibit similar behaviours and are characterised by low dislocation density. High mismatch and/or poor epitaxial quality heterostructures can differ in a multitude of ways, but are essentially characterised by a high dislocation density and/or inhomogeneities. Each type of heterostructures needs to be analysed extensively in order to be able to develop a theoretical model that characterises it. There is no model developed to date that seems to have generality.

3.2.3.3. Misfit dislocation nucleation

A variety of MD nucleation sources operating in the $Si_{1-x}Ge_x/Si$ (001) system have been identified to date and reported by different authors. Some of them are presented here.

Essentially, dislocation sources can be divided into three groups:

1. *Heterogeneous nucleation*, at specific local strain concentrations, due to growth artefacts or pre-existing surface defects;
2. *Homogeneous (spontaneous) loop or surface half-loop nucleation;*
3. *Multiplication processes* generated by dislocation interactions.

1. Heterogeneous nucleation sources

The process of dislocation nucleation from sources that are not inherent to the structure is known as *heterogeneous nucleation.*

One of these sources is represented by dislocations already present in the substrate and 'inherited' by the epilayer. Matthews et al. analysed their contribution to relaxation (§3.2.3.2, Figures 3.6 and 3.8). These dislocations act as nucleation sites for MDs, since their lateral glide in the epilayer can produces one MD segment, in the case of uncapped layers (Figure 3.6) or two MD segments, in the case of capped layers (Figure 3.8). These sources are characterised by low activation energy, as the MDs are the only new dislocation segments created. However, contemporary commercial Si substrates are characterised by dislocation densities < 10 cm^{-2}, which clearly provide a reduced density of defect sources.

Apart from substrate dislocations, other heterogeneous sources may develop prior to, or during, the epitaxial growth. Examples are: residual substrate surface oxide or carbide after cleaning, particulates on the substrate surface or included during growth from the deposition sources or the vacuum chamber, mechanical defects of the 'diamond' type [44] (which will be described in the following section), etc. An inhomogeneity results in stress concentrations, which can extend into the epilayer, thus lowering the activation energy for dislocation half-loop nucleation from the surface. In addition, a large inhomogeneity may have already created dislocations around it, in which case the activation energy is the energy required for the loop to break away from the surrounding structure of dislocations.

Although each of the features listed here can provide sufficient misfit nucleation densities if the growth quality is poor enough, in high-quality epitaxy they are usually controllable. While a single source may emit more than one MD (as will be seen in the next section), each source will only be able to relax strain in the heterostructure over dimensions comparable to its size [1].

Consequently, it is difficult to imagine that any of the heterogeneous nucleation mechanisms can generate the high density of dislocations consistent with the observed relaxation of moderately or high strained heterostructures [1].

2. *Homogeneous nucleation sources*

Dislocation nucleation from sources that are inherent to the structure is known as *homogeneous nucleation.*

The most obvious driving force for homogeneous nucleation in lattice-mismatched heteroepitaxy is the elastic strain, which if sufficiently high, can lead to spontaneous nucleation of dislocation loops or surface half-loops.

This source was studied by Matthews et al. [36] and is described here and presented schematically in Figure 3.9. A dislocation half-loop grows under the influence of misfit strain until it reaches the mismatched interface, where it deposits a misfit line. The difficulty of this mechanism consists in the nucleation of a half-loop large enough to grow under the influence of the misfit strain so as to generate the MD line.

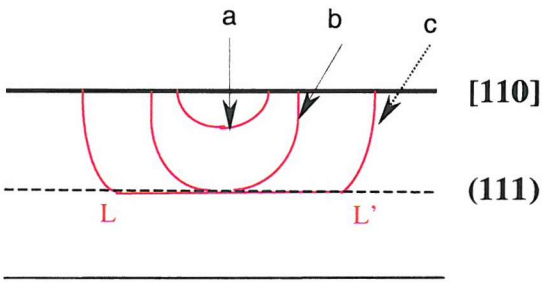

Figure 3.9. (a) A subcritical dislocation half-loop; (b) a half-loop, which is stable under the influence of misfit stress; (c) a loop which has grown to generate a length of MD line LL'.

Studies carried out by Nabarro showed that if no features causing the local stresses to rise are present in the epilayer, the nucleation of surface half-loops is improbable unless the misfit strain is large [47]. However, in the presence of localised high stresses, the nucleation of surface half-loops is possible even when the misfit strain is small. The activation energy required by this type of source is very high compared to the thermal energy available during growth therefore it is not an often encountered source. Nevertheless, quasi-homogeneous sources can provide substantial densities of sites at the epilayer surface, which significantly reduce the homogeneous nucleation barrier. Quasi-homogeneous sources are features in the crystal that although arising from inherent physical processes in the crystal growth, represent perturbation in the crystal structure. For example Hull and Bean in [52] demonstrated that statistical fluctuations in the Ge concentration in the $Si_{1-x}Ge_x$ alloy can produce significant densities of local volumes

where the Ge concentration is much higher than the average matrix concentration and Perovic and Houghton in [53] implicated Ge rich regions in dislocation nucleation. Another quasi-homogeneous process that can reduce the local activation barrier for dislocation nucleation is the roughening of the epilayer surface during growth. Jesson et al. have demonstrated the formation of surface cusps during the strained epilayer evolution [40]. These cusps are associated with large local stress concentrations, which reduce the dislocation nucleation barriers. Similar observations of dislocation injection associated with troughs in the surface roughness have been reported by Cullis et al. [41].

In general, the boundary between 'homogeneous' and 'heterogeneous' MD nucleation mechanisms can become indistinct. Few nucleation events can be described as truly homogeneous as nucleation will much more probably occur at a nonperiodic feature such as a surface step, cusp or locally enhanced Ge concentration.

3. Dislocation interaction and multiplication

Dislocation interaction and multiplication constitute a major factor in producing high MD and TD densities. At low mismatch, $Si_{1-x}Ge_x$/Si **(001)** structures relax by the introduction of **60°** dislocations (§ 3.2.3.1, § 3.2.3.2). At low temperatures, where diffusion is difficult and in the absence of point defects, the movement of 60° dislocations is restricted entirely to glide on **{111}** planes in the crystal (§ 3.2.3.1, §3.2.3.2). Glide plays an important role in strain relaxation independently whether dislocations existing in the substrate are grown into the layer or dislocations nucleate in the layer during growth. Glide of **60°** dislocations in $Si_{1-x}Ge_x$ layers grown on Si **(001)** substrates was studied extensively using two different methods [54-57]. Both methods involved growing metastable strained layers, thicker than the equilibrium critical thickness, in which relaxation was kinetically limited by the low growth temperatures and short growth times. In one method, the strained structures were annealed in the temperature range from 550 - 950°C and subsequently etched. Afterwards the length of the misfit segments was measured by the means of Nomarski differential interference contrast microscopy, DIC (method described in Chapter 5, § 5.1) [54, 55]. The length and density of the misfit segments were found to increase with increasing annealing temperature. The thermal glide velocity as given by [55] was:

$$\mathbf{v_g = B\varepsilon \exp(-E_g / kT)} \qquad (3.13)$$

where **B** is a constant, **ε** is the misfit strain, $\mathbf{E_g}$ is the thermal activation barrier for dislocation glide, **k** is the Boltzman constant and **T** the temperature. Since the annealing time was known, the glide velocity at each temperature was determined and from this, the thermal activation energy for glide was calculated. It was found to be $\mathbf{E_g = 2.5 \pm 0.2\ eV}$, with no systematic dependence on the alloy composition in one experiment [55]. In another experiment, the activation barrier was found to vary with the alloy composition as: $\mathbf{E_g = (2.16 - 0.7\ x)\ eV}$ [55]. The latter result is in good agreement with the values measured in bulk Si (**2.2 eV**) and bulk Ge (**1.6 eV**) [15, 30].

Glide has also been observed in real time using cross-sectional transmission electron microscopy, XTEM (method described in Chapter 5, § 5.3) [56]. Metastable strained layers were thinned to electron transparency and annealed in-situ in the transmission electron microscope. Measurements of the glide velocity were made during annealing using a video camera and additional images were also taken after annealing. In these XTEM experiments on dislocation glide, similar values for the glide activation energy $\mathbf{E_g=(2.2 - 0.6\ x)\ eV}$ were found [56].

With the increased use of low temperature epitaxial growth techniques, it has been realised that strain relaxation is kinetically limited and that dislocation nucleation in the epitaxial film may be the limiting step. It was shown that for the growth rates and temperatures typically used, and at low misfit (< 1%), homogeneous dislocation nucleation cannot occur during growth [15]. Dislocation nucleation can only occur at defects (such as the 'diamond defect', [44]) or by multiplication of pre-existing dislocations [9-15, 45, 46, 57, 58]. Alternatively, dislocation nucleation may also occur via surface roughening [40-43].

3.2.3.4. Dislocation interactions

Interaction between MDs is a critical process in the later stages of plastic relaxation. The interaction mechanism between two dislocations arises from the force between them, which results from the interaction of the strain fields around them (Equation 3.7). The exact calculation of the magnitude, components and spatial variation for this force is complex for general configurations (as already mentioned in § 3.2.3.1).

One of the most dramatic effects of MD interactions is that they can pin the motion of propagating dislocations. Hull and Bean considered the case of a total dislocation propagating along one of the **<110>** directions in the **(001)** interface and intersecting a pre-existing orthogonal interfacial dislocation as illustrated in Figure 3.10 [53]. According to Equation 3.7, if the Burgers vectors of the two dislocations are parallel, there will be a repulsive interdislocation stress between them, which will act against the excess stress that allows the dislocation motion. This repulsive stress magnitude depends on the longitudinal coordinate along the threading arm, in that it will be highest at the points approaching the interface and lowest near the epilayer surface. As the two dislocations come closer, this repulsive stress will exceed the excess stress along greater fractions of the propagating TD, pinning the motion of those segments of the threading arm. If enough of the threading arm is pinned, it will become unable to move past the orthogonal dislocation. Although the preceding discussion assumes a repulsive interaction (i.e. parallel components of Burgers vectors) the outcome is similar for attractive interactions (i.e. antiparallel components of the Burgers vectors) as in this case, the excess stress, which enables dislocation motion, is reduced as the propagating dislocation attempts to pull away from the intersecting event.

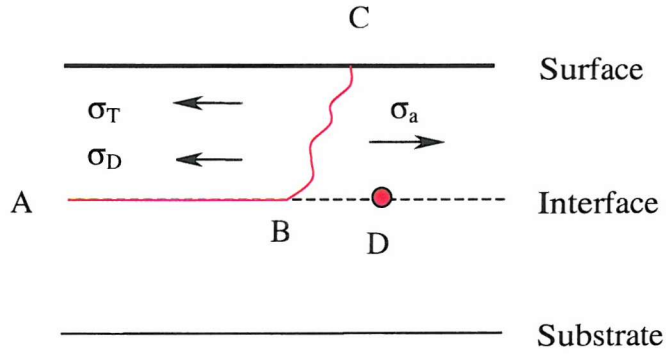

Figure 3.10. Schematic representation of the stresses acting on a propagating threading dislocation (BC) when it encounters a pre-existing orthogonal misfit dislocation, D; σ_a and σ_T are the Matthews and Blakeslee stresses, the mismatch stress and the 'line tension' respectively, whist σ_D is the horizontal component of the interdislocation stress between D and BC (reproduced after [1])

Dislocation interactions are very important also because they can inhibit complete strain relaxation in any thickness of strained epilayer, which is significant for the reduction of TD densities. This occurs because as the residual strain tends to zero, the blocking thickness tends to infinity and thus in the last stages of relaxation, dislocations will find it difficult to propagate past each other in any epilayer thickness, thus leaving a residual

density of TDs. One of the effects of dislocation interaction on TD density and surface morphology has been observed and subsequently explained by Fitzgerald et al. [4-6]. The presence on the surface of compositionally graded capped $Si_{1-x}Ge_x/Si$ heterostructures grown at high temperatures (≈ 900°C), of gradual undulations along two perpendicular <110> directions forming, what is usually referred to as, a crosshatch pattern, was explained as a response of the epitaxial surface to the strain fields associated with the MDs present in the graded layer, well under the capping layer. Fitzgerald et al. demonstrated that the strain fields associated with groups of MDs can create deep (sometimes faceted) trenches along the crosshatch lines, where under certain misfit conditions, a TD blocking phenomenon occurs. The explanation provided was that at the deep troughs generated by groups of MDs, a perpendicular TD is left with a reduced gliding channel, not only because of the additive effect of the strain fields of the MDs, but also because of the decreased thickness above this strained area. Under these combined effects, the TD is trapped at the side of the trough. Other gliding segments travelling on the same or on parallel **{111}** planes can also become trapped in a similar way and furthermore, the already blocked threaders will contribute to the trapping of other gliding segments, which eventually results in TD pileups along trenches in the crosshatch. This mechanism is represented schematically in Figure 3.11. The effects of this process on the surface morphology are that the growth rate above the dislocation pileup will be effectively decreased, hence increasing the depth of the trough with further growth [6]. In the case of chemical vapour deposition (CVD) another deleterious effect occurs. As the grown surface rotates from the **(001)** orientation, the growth rate slows down due to the effect of the surface orientation on the decomposition of gas species (it was shown by Csepregi et al. [60] that the growth rate on Si surfaces is highest for **(001)**, lowest for **(111)** and intermediate for **(110)**). Consequently, while the growth rate above the pileups is reduced, the nearby **(001)** oriented surfaces continue to increase in thickness, rotating the local plane near the pileup even more and thus decreasing the growth rate even further. This effect can result in facet formation, as reported by Fitzgerald et al. [6].

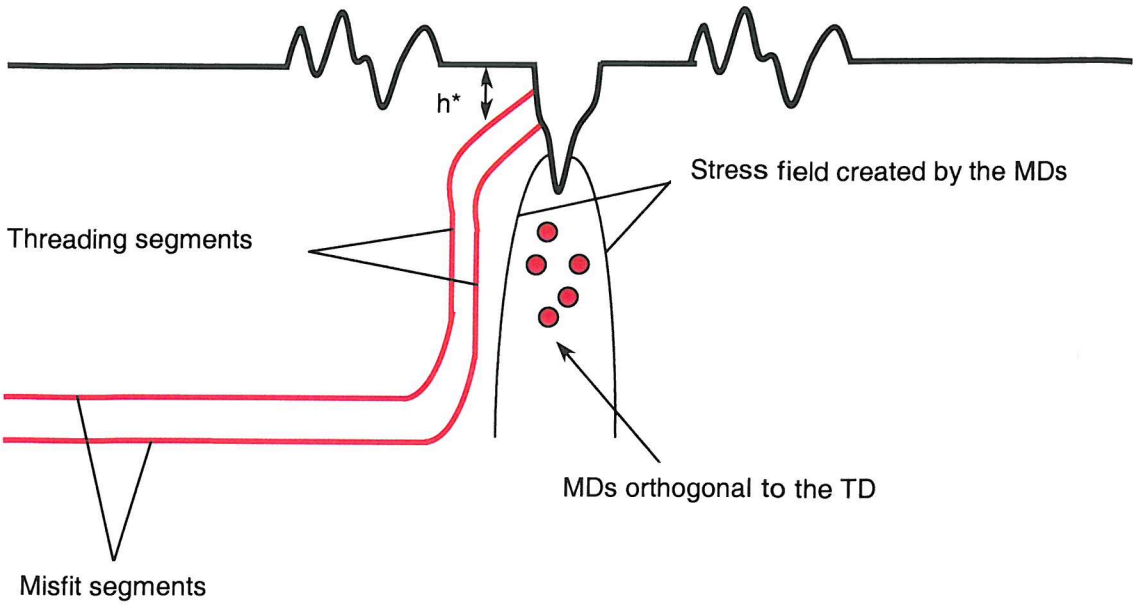

Figure 3.11. A schematic representation of the blocking mechanism of TDs caused by the stress fields of existing orthogonal groups of MDs (reproduced after [6]).

3.2.3.5. Dislocation multiplication mechanisms

The Hagen-Strunk mechanism

Hagen and Strunk reported on a type of MD multiplication source, which could explain the groups of MDs with identical Burgers vectors observed in systems with low misfit [45].

The reported mechanism represented schematically in Figure 3.12 is generated by two MDs (1 and 2 in Figure 3.12 b) with the same Burgers vectors (in this case, **b = a/2[101]**) that glide on two different **{111}** planes and cross each other at a right angle in the **(001)** plane (Figure 3.12 b). At the intersection point, an annihilation reaction leads to the formation of two angular dislocations in an asymmetric configuration (Figure 3.12 c). One dislocation line, 1-2, shows a 90° edge (the tip may be rounded due to local climb [45]). The other dislocation line 1A-2A shows two transition segments inclined to the growth plane (analysed through stereomicroscopy they proved to be always inclined towards the surface [45]). This asymmetric arrangement at the crossing point was assumed to be caused by the attractive image forces from the surface of the layer (§ 3.2.3.1). It was observed, especially in thin layers (≤ 0.5 μm), that the transition segments reach the surface of the layer and form two individual dislocation segments (1A and 2A in Figure 3.12 d). Dislocations 1A and 2A may further elongate by glide under the acting misfit stress, but their glide possibilities are restricted by the presence of the adjacent

dislocations (1 and 2). The most probable elongation mechanism hypothesised is shown in Figure 3.12 e-f, in which the segment attached to dislocation 1A cross-slips and glides on its second **{111}** glide plane. This process is illustrated in Figure 3.13 b. The tip of the newly formed angular dislocation 1A-1B can, once again, exhibit two inclined transition segments due to the image forces (Figure 3.14 e). The segment of dislocation 2A can pass between adjacent dislocations 1-2 and 1A-1B by double cross-slip leading to the formation of a new dislocation parallel to dislocation 2 (Figure 3.12 f). This mechanism can be repeated, if the new transition segments of dislocation 1A-1B reach the surface.

Hagen and Strunk observed that for a given misfit, this multiplication mechanism seemed to operate in a certain range of layer thicknesses. In the case of Ge grown on GaAs, (where $\varepsilon = 0.074\%$) this range was $\approx$ **1.0 - 0.5 μm**. Only within this thickness range could the inclined dislocation segments reach the layer surface during growth in order to form individual dislocations, which in turn can glide to produce further dislocations.

Strunk, Hagen and Bauser identified three other types of crossing of dislocations in their study of Ge on GaAs [46]:

1. Crossing without any reaction, which was originally attributed to crossing pure edge dislocations with perpendicular Burgers vectors, but was also observed for 60° dislocations by Strunk et al. [46];
2. Crossing of attractive 60° dislocations with identical Burgers vectors leading to local recombination;
3. Crossing of attractive 60° dislocations with identical Burgers vectors leading to the elimination of the crossing point.

The dislocation reactions 2 and 3 are expected to occur if the dislocations cross within what Strunk et al. identified as a 'critical distance' [46].

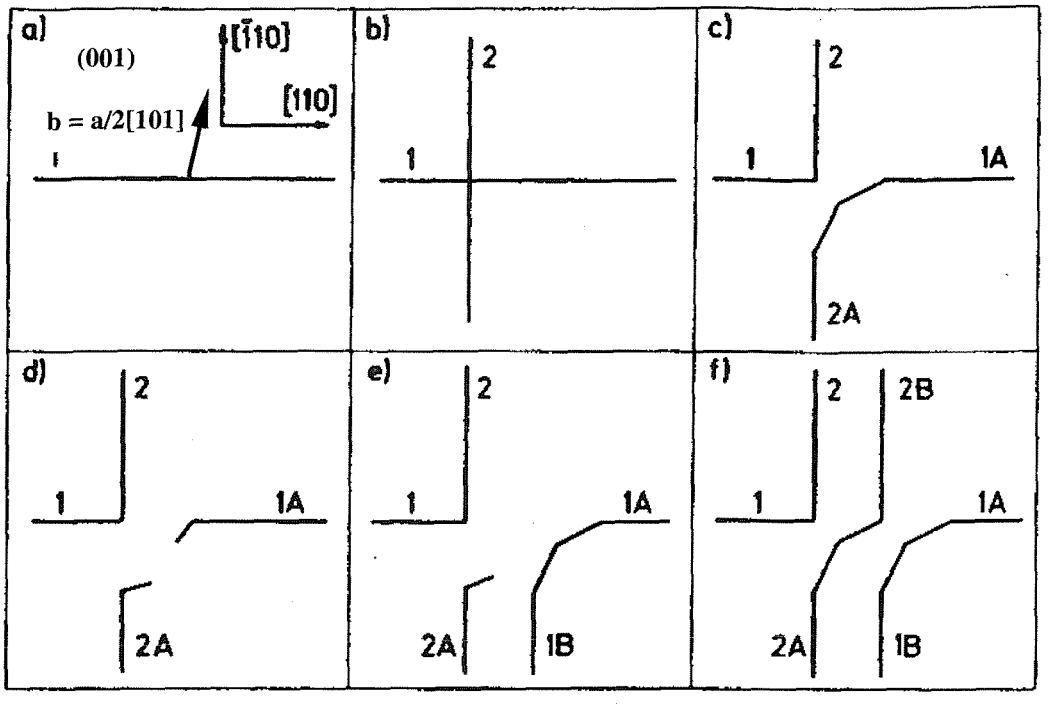

Figure 3.12 a–f. Schematic diagram of the Hagen-Strunk dislocation multiplication mechanism reproduced after [45]: (a) MDs 1 and 2 are both 60° dislocations with the same Burgers vectors; the arrangement in (b) is unstable, as described above; (c) - (f) intermediate stages as explained above.

Rajan and Denhoff reported the observation of the Hagen-Strunk dislocation multiplication mechanism in $Si_{75\%}Ge_{25\%}/Si$ (001) structures [58]. Independently, Eaglesham et al. showed that in the absence of evidence of the threading segments (1A and 2A in Figure 3.12 d, which are a mark of the intermediate stage of this multiplication mechanism), the morphology represented schematically in Figure 3.12 f can be characteristic of any intersection of clusters of 60° dislocations having the same Burgers vectors [44].

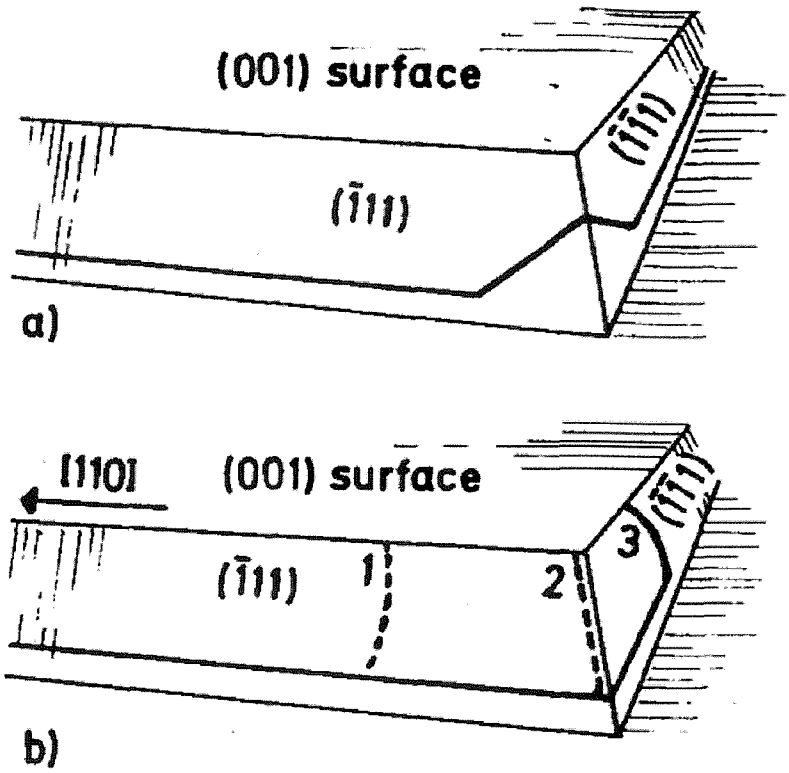

Figure 3.13. Intermediary stages in the Hagen-Strunk dislocation multiplication mechanism reproduced after [46]: (a) Inclined segments of an angular dislocation formed by glide; (b) Elongation of a MD involving cross-slip as represented in Figure 3.12 d-e; the numbers 1–3 show subsequent positions of the gliding segment. The final shape of the tip in the newly formed angular dislocation is shown in (a).

The 'diamond defect'

The 'diamond defect' was reported by Eaglesham et al. [44] as a new heterogeneous regenerative dislocation nucleation source operating in the first stages of coherency breakdown in $Si_{1-x}Ge_x$ / Si (001) epilayers, at low misfit.

Analyses carried out on $Si_{1-x}Ge_x$ grown by MBE on 200 nm Si buffer layers showed that at low misfit (10–20% Ge) the MDs were predominantly 60° in character and very long (**≈10 – 100 μm**) [44]. This observation contrasted with the short **≈ 0.1 – 1 μm** edge MDs observed at Ge concentrations of ≈ 50%. Also it was observed that the 60° dislocations were not evenly spaced, but closely grouped into bunches. One bunch observed in stereomicroscopy demonstrated that in three dimensions, the dislocations in a bunch were often arranged on the same **{111}** inclined plane and had identical Burgers vectors. The observed dislocation microstructure could be ascribed to a number of different processes in the growing film, one of which has previously been presented (the Hagen-Strunk mechanism) others will be described herein (the 'diamond defect') or in the next section.

In the studies carried out by Eaglesham et al., the examination of SiGe/Si (001) epilayers from several different wafers (different thicknesses and Ge compositions 10 – 60%) revealed the presence of heterogeneously distributed 1/6<114> 'diamond'-shaped faulted loops with dimensions of the order ≈ **20 - 200 nm**, lying on a **{111}** type plane and with inclined **<110>** edges (as shown in Figure 3.14). The importance of these 'diamond defects' consists mainly in their association with **60° a/2 <110>** MD sources. According to the observations of Eaglesham et al., a single 'diamond defect' was able to emit at least two or more, up to four distinct **a/2<110>** dislocations. They also observed that in the case of the operation of a 'diamond defect', in addition to the bunches of dislocations which are characteristic of any regenerative source, one should expect to see:

- Nearly coplanar bunches of MDs with different Burgers vectors;
- Perpendicular bunches generated by the same source.

The 'diamond defect' acting as a heterogeneous nucleation source, could provide an explanation for some distinctive features observed in $Si_{1-x}Ge_x/Si$ (001) low misfit layers (essentially dislocation introduction by the operation of a regenerative source, which can create closely spaced bunches of 60° MDs with different Burgers vectors from a single defect).

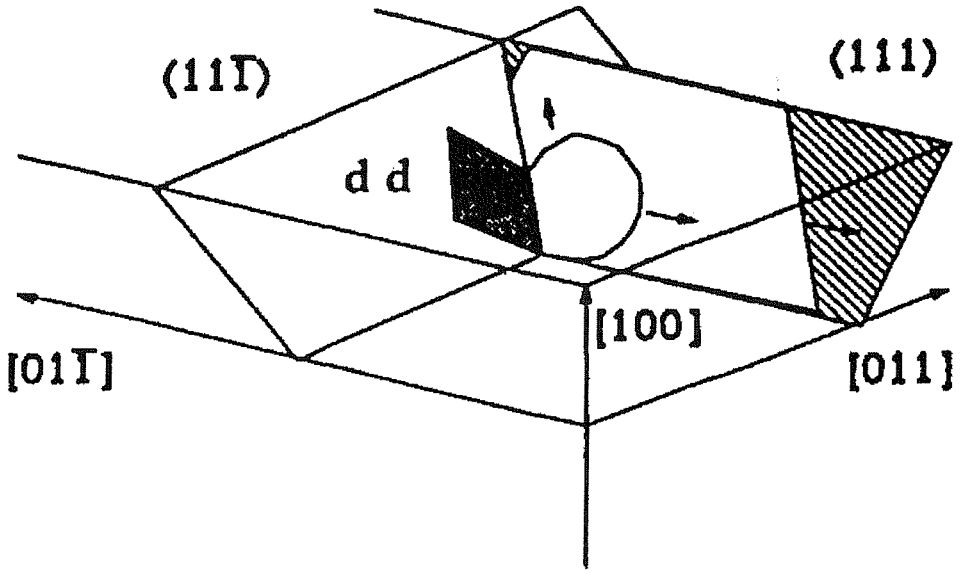

Figure 3.14. Schematic diagram of the process of emission of a glissile dislocation on one **{111}** type plane, **(111)**, by the diamond defect *dd*, lying on another **{111}** type plane, $(\bar{1}11)$, (reproduced after [44]).

The modified Frank-Read (MFR) mechanism

A further MD nucleation mechanism that can operate repetitively is the modified Frank-Read (MFR) mechanism, observed and reported for the first time by Meyerson, LeGoues, Mooney et al. [9-15]. They showed that significantly low TD densities (of the order of $10^4 cm^{-2}$) can be achieved in SiGe virtual substrate-based heterostructures grown at low temperatures ($\approx$ 500°C) with a steep grading of the Ge concentration (50% Ge per μm of thickness), in which the MFR mechanism for dislocation multiplication is operating.

Meyerson et al. grew a series of SiGe alloys by ultra high vacuum chemical vapour deposition (UHVCVD) at low temperatures (< 550°C) and subsequently analysed them, reporting, for the first time, a new type of dislocation nucleation and multiplication source, the MFR source [9]. This source was found to operate only in cases where no other low energy nucleation sites are provided and it accounts for the participation of the substrate to misfit strain relief, contrary to the basic assumption dating since Frank and van der Merwe [31-33] that this contribution was negligible.

LeGoues and Meyerson analysed samples grown by both UHVCVD and MBE for comparison. They also studied comparatively three different types of samples grown on 5 inch **(001)** Si wafers [9-10]:

- One 0.5 μm $Si_{75\%}Ge_{25\%}$ constant composition layer;
- One SiGe layer with a linear variation of the Ge concentration from 25% to 75%;
- One step-graded structure (Ge superlattice) made of compositionally graded SiGe layers separated by ≈ 130 Å thick Si layers.

All three structures had a 0.4 μm layer of constant Ge composition at the top. The structures were analysed using both cross-section and plan-view transmission electron microscopy (methods described in Chapter 5, § 5.3). Cross-sectional studies showed that the dislocations were located in the virtual substrate as well as in the Si substrate itself. Plan-view analysis quantified the density of TDs, found to be $< 10^4$ cm^{-2}. Several experiments were performed in order to identify the parameters that controlled the relaxation mechanism. The conclusions reached were:

- Results were independent of the growth technique;
- Results depended critically on the perfection of the growth interface;
- A good starting surface was not sufficient to avoid TDs (Ge concentration made the difference in relaxation kinetics for identically prepared surfaces);
- Similar dislocation structures resulted independently of how the Ge concentration was increased (linearly or in steps).

LeGoues et al. proposed a two-step mechanism [10]:

1. At a thickness significantly greater than the equilibrium critical thickness, a few dislocations are introduced, possibly as half-loops (as first described by Matthews et al. [37]) from the surface or as loops nucleated at defects in the film (such as the 'diamond defect' (described previously);
2. The network thus formed and, in particular, the nodes formed by intersecting dislocations begin to act as *Frank-Read sources*, which generate additional dislocations needed to relieve the increasing strain in the graded layer.

This mechanism could explain the presence of dislocations deep inside the substrate and their absence in the top layer. The operation of a Frank-Read source is schematically represented in Figure 3.15. A segment of interfacial dislocation pinned at two nodes by intersecting dislocations (Figure 3.15 a) starts operating as a Frank-Read source by

bowing out into the substrate (Figure 3.15 b). It loops into the film until it reaches the surface becoming in effect a half loop (Figure 3.15 c-d). The first loop formed in this manner is not expected to penetrate very deep into the substrate, because it is energetically rather costly to introduce dislocations into an unstrained material. Thus unlike the typical Frank-Read source (thus justifying the name of *modified* Frank-Read), this first loop is expected to be very elongated along the interface and into the thin film. Eventually, though, as more loops form, each new loop will push the preceding one further down, leading to the deep pileups observed (Figure 3.15 e-f). Careful calculations of the forces exerted on the pinned dislocation segment had to be carried out in order to explain its bowing into the Si substrate. Each threading part of a half-loop moves under the influence of misfit stress. The motion of these TDs leaves behind a MD (Figure 3.15 d-e). LeGoues et al. also showed how this type of mechanism actually leaves 'a trace' of each nucleation event directly observable by TEM even after growth had stopped and after TEM sample preparation [12].

LeGoues et al. also explained the way in which the interface grading helped reduce the density of TDs [12]:

- The initial dislocation nucleation is retarded because it is easier to grow a perfect interface when the difference in composition between the layer and its substrate is small. Hence, when the initial network of dislocations actually forms, there is a very high driving force for moving the TDs all the way to the edges of the wafer. As additional dislocations are formed though and the misfit stress is thus decreased, this driving force will also decrease, so that eventually the threading parts can become pinned.
- As each new dislocation loop is formed and as each new threader moves towards the edges of the wafer, the concentration grading provides 'fresh' interfaces, with almost no preexisting dislocations to pin the threader.

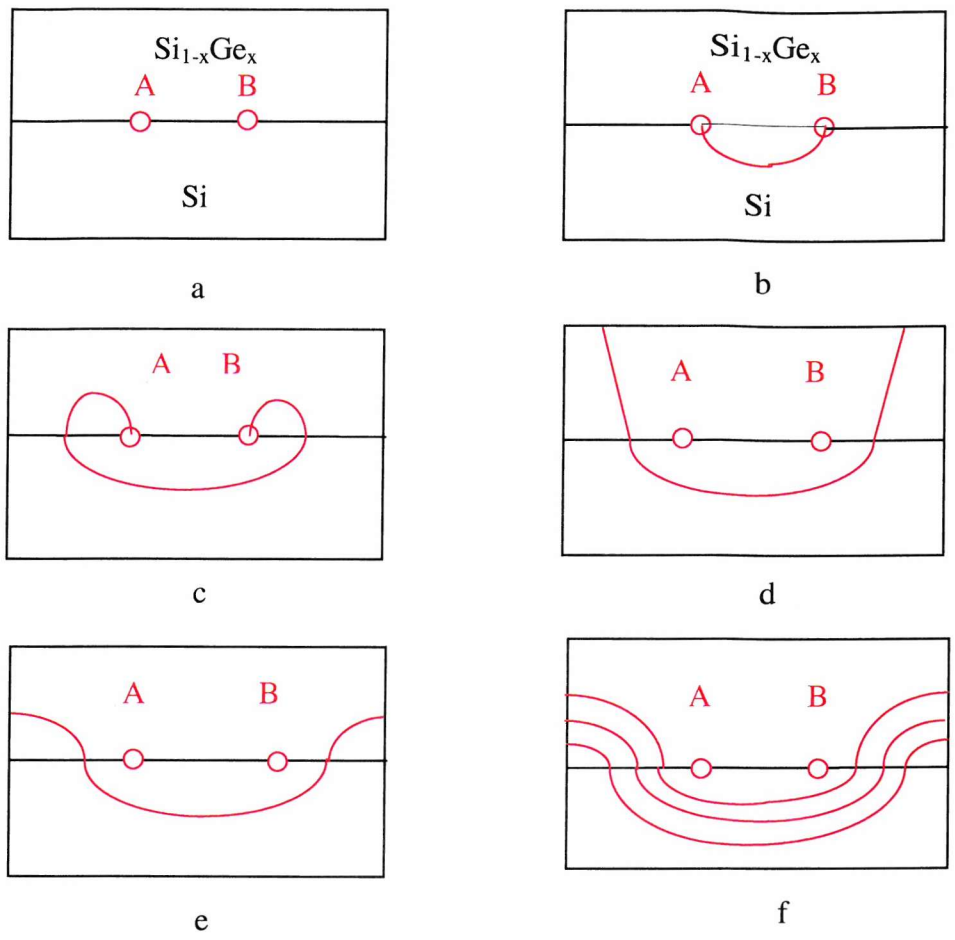

Figure 3.15 a-f. Schematic representation of the MFR dislocation multiplication mechanism operation described above (reproduced after [9]).

The interaction between intersecting dislocations provides the initial activation energy for the MFR mechanism and determines the direction of the bowing out, thus, initiating this process. At the beginning of the MFR process, there is no driving force that pushes dislocations into the substrate other than this interaction, since the shear stress exerted by the thin film goes to zero at the interface. But once the bowing out has been initiated by dislocation interaction, the loops can keep growing to relieve the misfit. Thus the nucleation barrier to initiate Frank-Read sources is dramatically lowered by dislocation interaction. The pinning points on each half dislocation are provided by other intersecting dislocations. The distance between pinning points may explain the difference between graded and ungraded epilayers. The shear stress necessary to activate a Frank-Read source is given by the expression [9]:

$$\tau = Gb/L \qquad (3.14)$$

where **L** is the distance between two pinning points and the other parameters have already been defined. In Equation 3.14, it is assumed that MFR sources act exactly like Frank-Read sources. In order to determine the minimum distance between pinning points at which the Frank-Read source becomes active ($\mathbf{L_{min}}$), it was necessary to determine τ_{min}. LeGoues et al. found the value of $\mathbf{L_{min}}$ to be **1300 Å**. Consequently only dislocations pinned at distances larger than **1300 Å** can operate as Frank-Read sources, while those that are pinned more closely cannot. This observation provided another explanation for the need for grading. If many dislocations are formed readily on one single plane, the pinning points (intersecting dislocations) are very close to each other; the stress necessary to bow the dislocation exceeds by far that provided by the compression in the film and the interaction between dislocations. The grading in Ge composition results, after relaxation, in a gradient in lattice parameter, which can only be achieved by grading the dislocation location, or in other words, by spreading the total number of dislocations required to go from the lattice parameter of the substrate to that of the overlayer over the thickness of the graded region. Consequently, each atomic plane will have fewer dislocations (i.e. pinning points will be further apart) and the process will keep repeating itself. The pileups have been noticed to go even deeper into the substrate as the Ge concentration increases, meaning that each MFR source has to produce more dislocations in order to relieve the extra strain. This repeated slip on a single **{111}** plane results in a surface step, which can be well visualised using Nomarski DIC microscopy (method described in Chapter 5, § 5.1).

To summarise, in order for the MFR mechanism to start operating, a few dislocations have to be initially available from the substrate or from another source. LeGoues et al. concluded that it was difficult to observe the nucleation of these precursor dislocations because they probably nucleated heterogeneously (as explained in § 3.2.3.3). However, if too many precursor defects are present, a dense network of dislocations forms with close pinning points, preventing the MFR mechanism from operating. These observations highlight the important role played by the substrate quality in the activation of the MFR mechanism. Other important parameters considered to influence the MFR mechanism are the growth temperature (i.e. the temperature has to be high enough for the initial precursor dislocations to be thermally activated) and the Ge concentration gradient [10].

4. ANALYSED STRUCTURES

This chapter contains information concerning the SiGe virtual substrate-based heterostructures grown and characterised for this study. It starts with a brief presentation of the technique used to produce the structures, low pressure chemical vapour deposition (LPCVD), and contains information on the two sets of heterostructures grown and subsequently studied.

4.1. LOW PRESSURE CHEMICAL VAPOUR DEPOSITION (LPCVD) AT THE SOUTHAMPTON UNIVERSITY MICROELECTRONICS CENTRE (SUMC)

All the analysed heterostructures were grown at SUMC using LPCVD. This section comprises a brief description of the performances that can be achieved with this technique. A comprehensive presentation of the SUMC-LPCVD technique and equipment can be found in [61].

The LPCVD system used is of the cold-wall type (using water for cooling), thus producing the least amount of chamber coating.

In the SUMC machine used, substrates are heated by a 300 mm diameter graphite meander mounted on the top flange of the chamber. In order to minimise possible carbon contamination during growth, every new heating element is coated with silicon at high temperature before any device layers are grown.

Substrates up to 200 mm diameter can be accommodated in the SUMC–LPCVD machine and different wafer sizes can easily be handled by changing the quartz platen upon which the wafers are supported. The structures of interest for this study were grown on 100 mm wafers. During growth, the substrates are continuously rotated in order to ensure uniformity. The machine is characterised by a thermal budget limited by to the lack of cooling of the base plate on which the platen with the wafer are seated, during growth. Epitaxial growth can be carried out in the temperature range from 1000°C down to less than 700°C, with a layer uniformity across a 100 mm wafer, of ±1% for layers grown at 960°C and of ± 4% for layers grown at 750°C [61].

The SUMC-LPCVD system uses gaseous sources, which can be replenished without needing to disturb the vacuum in the growth chamber. Up to eight independent gaseous sources can be used in the SUMC-LPCVD chamber and the gas supply design enables a minimal dead volume, which allows fast changes of the gas composition. The lowest base pressure in the SUMC-LPCVD machine is 10^{-3} Torr.

The LPCVD technique used allows control over both the growth pressure and the source gas flow, thus enabling additional control over the growth rates. Growth pressure values are between 0.03 - 1 Torr and the heterostructures for this study were grown at 0.5 Torr. Growth rates range from ≈ 200 Å/minute - 0.4 μm/minute, thus higher than in UHVCVD, MBE and in the LPCVD technique reported in [22-24] and lower than in APCVD [19] and LEPECVD [25, 26]. The slow growth rates possible in UHVCVD and MBE can allow for a two-dimensional Frank and van der Merwe (FM) growth (described in Chapter 3, § 3.2.2), but require very long growth times in order to grow the type of structures of interest to us [34]. Growth rate variation as a function of the Ge concentration at 750°C for SiGe grown by LPCVD at SUMC is represented in Figure 4.1. The growth rate at 800°C has been found to be lower than at 750°C by 7%. This value is similar to the uncertainty for this range of growth rates.

Because FM growth requires long times, the technological need for atomically smooth growth fronts (surfaces) has led to the use of (thermodynamically) non-equilibrium processes. These are extensively described in [1, 30, 34]. Essentially, at an appropriate supersaturation in the growth chamber, characterised by a relatively high deposition rate and/or a relatively low substrate temperature, the surface density of the forming nuclei will be of such magnitude that the average adatom migration range depending on the temperature, activation barriers and available time interval, will allow them sufficient time to join the edge of the neighbouring 2D cluster, but leave them too little time for shape equilibration. The clusters ultimately grow together as in FM growth by the process referred to as pseudo-2D growth [34]. Three-dimensional Volmer-Weber (VW) growth or Stranski-Krastanov (SK) growth, which starts as 2D, but ends-up as VW, can also occur for all epitaxy techniques for a variety of reasons, as described in Chapter 3, § 3.2.2.

In the case of the SUMC–LPCVD machine, the transfer of water or oxygen contaminants to the growth chamber is minimised by using a load lock through which the wafers are introduced in the chamber. The load lock is pumped down by a turbomolecular pump

backed by a rotary pump and its pressure is kept at smaller values than the chamber pressure. The use of the turbomolecular pump minimises the contamination of the load lock chamber with hydrocarbons from the pump oil backstreaming. Oxygen levels in the epitaxial layers grown by LPCVD at SUMC as measured by secondary ion mass spectrometry (SIMS) have been found to be similar to the ones reported for layers grown by other techniques [61].

The growth sequence used at SUMC for SiGe virtual substrate-based heterostructures is as follows:

- Ex-situ chemical clean (standard RCA), which leaves the wafers oxide terminated;
- Very brief dip in dilute HF:H_2O (1:100), which thins the 'RCA' oxide, thus allowing its reliable desorption at lower temperatures;
- Load wafer into the growth chamber through the load lock;
- Purge the chamber with hydrogen, at 900 °C, to thermally desorb the 'RCA' oxide that covers the wafer surface;
- LPCVD of the SiGe heterostructures using as gaseous sources: silane (SiH_4) and germane (GeH_4), for the dopants: diborane (B_2H_6) for p-type, and phosphine (PH_3) for n-type, and as carrier gas, hydrogen;
- Purge the growth chamber with hydrogen again at the end of the process, before transferring the wafer to the load lock;
- Unload the wafer ready to be analysed and further processed.

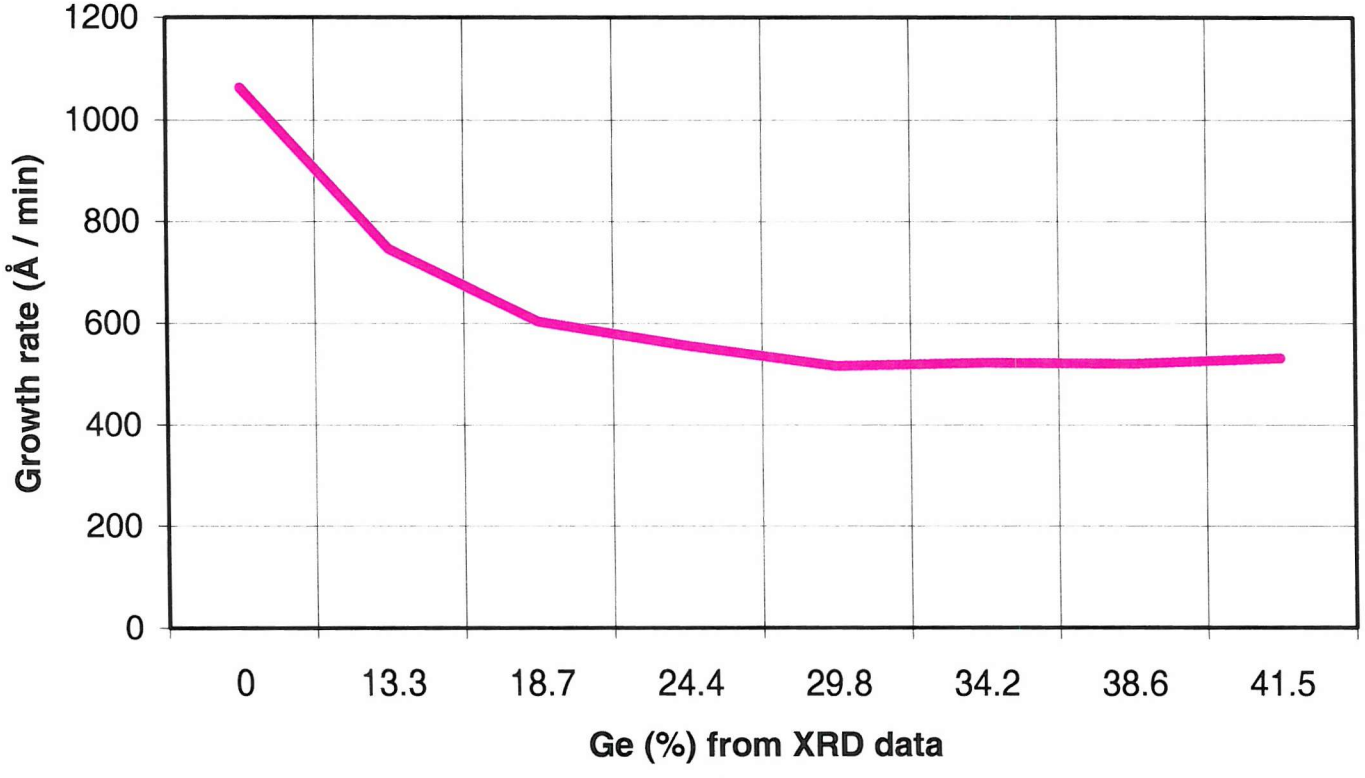

Figure 4.1. The variation of the growth rate as a function of the Ge concentration for SiGe grown at 750°C by LPCVD at SUMC.

4.2. SILICON-GERMANIUM VIRTUAL SUBSTRATE-BASED HETEROSTRUCTURES GROWN BY LPCVD AT SUMC

4.2.1. GENERAL PRESENTATION

In order to study the effects of growth parameters on the surface morphology and type and density of misfit strain relaxation induced defects, two sets of SiGe heterostructures incorporating virtual substrates were grown, using different combinations of the growth parameters, and subsequently studied using the analysis methods described in Chapter 5. Two types of Ge concentration grading in the virtual substrate (linear and stepwise) were used as techniques to decrease the TD density and improve the surface morphology. The growth parameters varied were:

- For the virtual substrate: growth temperature, thickness, initial and final Ge composition, Ge concentration gradient, type of variation of the Ge content (linear and stepwise);
- For the capping layer: thickness and presence of a device structure.

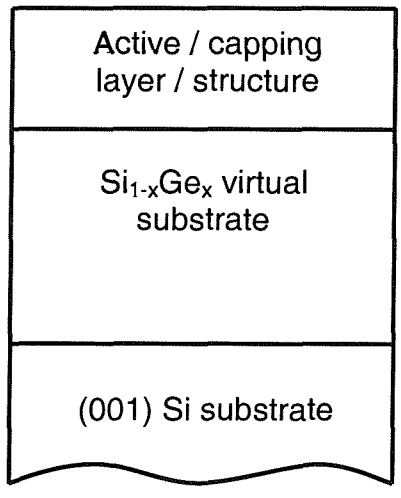

Figure 4.2. Schematic diagram of a SUMC-LPCVD grown SiGe heterostructure incorporating a virtual substrate. On a (001) Si substrate, a $Si_{1-x}Ge_x$ virtual substrate of variable Ge concentration (x) is grown beyond the critical thickness and relaxed from misfit strain during growth. A capping layer of constant Ge concentration, which may or may not incorporate a microelectronic structure and hence an active layer, is grown at the top.

Growth temperatures were chosen from the intermediate range for this method and by comparison with structures grown with other methods (Chapter 1) i.e. 750°C and 800°C.

In order to make an accurate selection of the growth parameters values to use, calibration structures were first grown and analysed. Thickness values for the different layers incorporated in the heterostructures to be studied were obtained by interpolating from SIMS results obtained on the calibration structures, whilst germanium concentrations

were estimated by interpolating from high resolution x-ray diffraction (HRXRD) results obtained on the same structures.

Using the SUMC-LPCVD technique previously described, two different sets of SiGe heterostructures were grown and characterised. Both sets incorporate the two different types of Ge concentration variation in the virtual substrate: linear and stepwise. All heterostructures were deposited on an LPCVD-grown Si buffer meant to bury the possible heterogeneous sources for dislocation nucleation existent at the interface with the Si substrate (i.e. impurities at the surface of the Si wafer, substrate dislocations, etc.), which are characterised by low activation energies, as described in Chapter 3, § 3.2.3.3.

The first test set was represented by two linear-graded heterostructures grown at different temperatures, with different initial Ge contents and the same final Ge content in the virtual substrates, with different Ge concentration gradients in the virtual substrates and different thicknesses of the capping layers. A step-graded heterostructure was also grown as part of the first set for comparison with one of the linear-graded heterostructures. The effects of the two different types of Ge concentration grading in the virtual substrate (linear versus stepwise), as well as the influence of the different growth temperatures, initial Ge contents, Ge concentration gradients in the virtual substrate and capping layer thicknesses, on the surface morphology and relaxation induced defects of these heterostructures were subsequently studied.

Based on the results obtained from the analysis of the first set of heterostructures, a second set was grown. It incorporated six different structures. Five of them were characterised by the same growth temperature and initial and final Ge concentrations in the virtual substrate, but different growth parameters were varied. The growth conditions varied were: the presence/absence of a device structure at the top of the capping layer, the thickness of the capping layer, the thickness of the virtual substrate and the Ge concentration gradient in the virtual substrate, and the type of grading of the Ge composition in the virtual substrate (i.e. linear, stepwise and in twice the number of half-sized Ge concentration steps, as an intermediate option between linear and step grading). Additionally, a sixth heterostructure was grown as part of the second set, using identical conditions as for the step-graded heterostructure of the first set, in order to check the reproducibility of the SUMC-LPCVD growth process for these types of SiGe heterostructures.

4.2.2. FIRST SET OF HETEROSTRUCTURES

4.2.2.1. Linear-graded heterostructures

Two SiGe heterostructures incorporating linear-graded virtual substrates (represented schematically in Figure 4.3) were grown as part of the test set. The heterostructure denominated *720* (Figure 4.3 a) was grown at **800°C** on a ≈ **525 μm** thick, half-masked (half-covered with silicon oxide) **100 mm p-type** Czochralski (CZ)-grown silicon wafer. It consisted of an LPCVD-grown Si buffer on top of which a virtual substrate characterised by a linear variation of the germanium concentration ≈ **13 - 42%** over **≈1.7μm** (resulting in a gradient of ≈ **16% / μm**) was grown. On top of the virtual substrate, a capping layer of constant germanium composition ≈ **42%** and thickness **≈0.3μm** was deposited. In this heterostructure, the initial Ge concentration in the virtual substrate is high and the Ge concentration gradient is intermediate by comparison with other structures reported [19-28].

The second linear-graded heterostructure of the first set denominated *775* (Figure 4.3 b) was grown at the lower temperature of **750°C** on a ≈ **525 μm** thick, unmasked **100 mm n-type** CZ–grown silicon wafer. It consisted of an LPCVD-grown Si buffer on top of which a virtual substrate characterised by a smaller initial Ge concentration ≈ **12%** and the same final Ge concentration ≈ **42%** as *720*, was grown. The Ge variation in the virtual substrate occurs over ≈ **1.36 μm**, thus resulting in a steeper gradient (≈ **22% / μm**). On top of the virtual substrate, a thinner capping layer ≈ **0.24 μm** of constant germanium composition, the same as for *720* (≈ **42%**) was deposited.

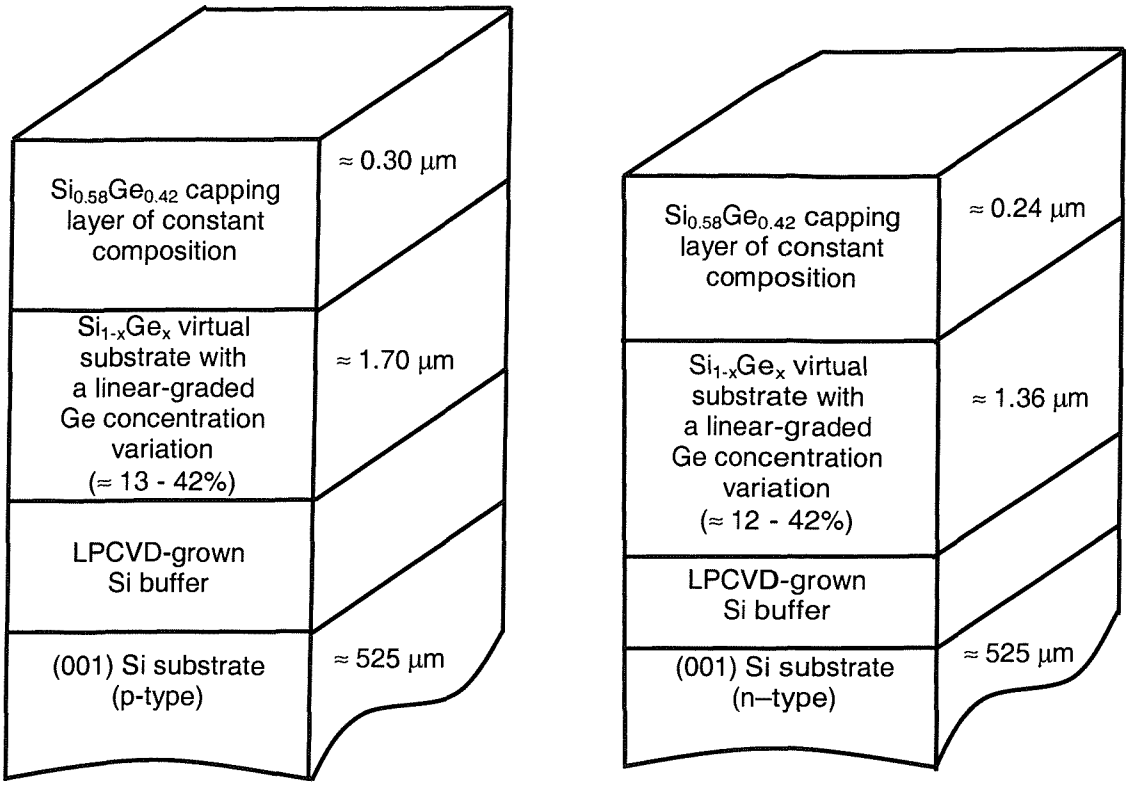

(a) (b)

Figure 4.3. Schematic diagram of the linear-graded heterostructures of the first set: (a) *720*, grown at the higher temperature, with the higher initial Ge composition in the virtual substrate, the lower Ge concentration gradient in the virtual substrate and the thicker capping layer; (b) *775*, grown at the lower temperature, with the lower initial Ge composition in the virtual substrate, the higher Ge concentration gradient in the virtual substrate and the thinner capping layer.

4.2.2.2. Step-graded heterostructure

Only one SiGe heterostructure incorporating a step-graded virtual substrate was grown as part of the first set of structures. In order to enable a comparison between the effects of the two types of Ge concentration grading in the virtual substrate (linear versus stepwise) the step-graded heterostructure was grown under identical conditions with the linear-graded heterostructure denominated *775*.

The step-graded heterostructure of the first set denominated *774* (represented schematically in Figure 4.4) was grown at the same temperature (**750°C**) and with the same variation of the germanium concentration in the virtual substrate as the linear-graded heterostructure of the first set, *775* (≈ **12 - 42%**, over ≈ **1.36 μm**), but with a different profile of the variation (in **5** steps of ≈ **6%**). This structure was grown on a Si buffer

LPCVD–grown on top of a **525 μm** thick, unmasked **100 mm n-type** CZ–grown silicon wafer and had a capping layer of constant Ge concentration (≈ **42%**) and ≈ **0.24 μm** thick.

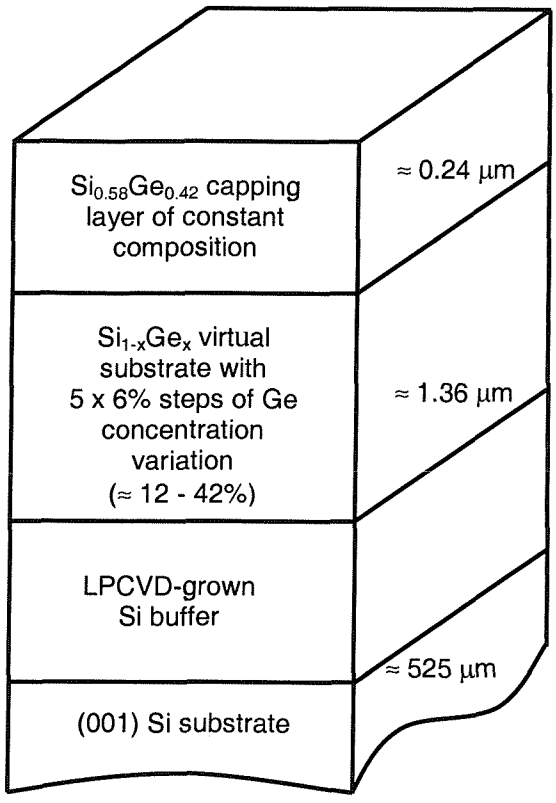

Figure 4.4. Schematic diagram of the step-graded heterostructure of the first set, *774*, grown under identical conditions with the linear-graded heterostructure of the first set, which was grown at the lower temperature, with the lower initial Ge composition in the virtual substrate, the higher Ge concentration gradient in the virtual substrate and the thinner capping layer, *775*.

The characteristic parameters of the first set of SiGe heterostructures are also shown in Table 1.

4.2.3. SECOND SET OF HETEROSTRUCTURES

Based on the results obtained from the analysis of the test set grown at the SUMC, a second set of six heterostructures was grown and the effects of the variation of different growth parameters on their structural properties were subsequently studied. The combinations of growth parameters used for the second set of heterostructures were carefully chosen, with the aim of improving their surface morphology and defect content.

All the heterostructures of the second set were grown at the same temperature as the samples *775* and *774* of the first set (**750°C**), which exhibited superior structural properties by comparison with the sample *720* of the first set, grown at a higher temperature (**800°C**).

Emphasis was placed on the step grading of the Ge concentration in the virtual substrate, due to its superior structural properties as resulted from the analysis of the first set of structures. Consequently, five different step-graded and only one linear-graded virtual substrates were incorporated in the heterostructures grown as part of the second set.

One heterostructure of the second set, *VSC6*, was grown under identical conditions with the structure of the first set, which exhibited the best structural properties, *774*, in order to test the reproducibility of the SUMC-LPCVD process for these types of heterostructures.

The other five structures of the second set (*VSC1-5*) have virtual substrates characterised by the same initial (**0%**) and final (**32%**) Ge compositions, respectively. By starting the Ge concentration grading at 0%, the virtual substrates of the second set, differently from those of the first set, are characterised by a very 'gentle' introduction of misfit strain, with the aim of resulting in a lower TD density and in superior surface morphology. It is most common to start the Ge concentration grading at zero [19-28]. However, in this case, in order to obtain the higher final Ge concentrations used in the first set of heterostructures, higher concentration gradients or thicker virtual substrates would have been required.

In the second set of heterostructures, the growth of the final step of the virtual substrate with a low Ge concentration gradient of only **≈ 6% / μm** (**≈ 2% Ge** over **≈ 300 nm**) was meant to improve the results of misfit strain relaxation on the TD density by acting as a 'filter' for dislocations, as explained in Chapter 3, § 3.2.3.2 and § 3.2.4. From the representation of the critical thickness variation with the Ge content shown in Chapter 3, Figure 3.7, for a Ge concentration of **2%**, a critical thickness of **≈ 1 μm** would be required. Hence, the last step of Ge concentration in these heterostructures by being still compressively strained contributes to turning the threading segments into misfit segments, thus keeping the dislocations well confined within the virtual substrate underneath. Moreover, should this last step relax, the growth of a tensile strained capping layer (of **≈ 30%** Ge concentration) would improve the surface morphology, as tensile strain does not encourage surface roughening [1].

The final Ge concentration value in the virtual substrates of the second set was chosen in order enable their use as templates for further strained overgrowth (as described in Chapter 1).

In order to carry out Hall mobility measurements on the heterostructures of the second set, to assess their suitability for device fabrication, **p-n junctions** were incorporated in each of their capping layers.

4.2.3.1. Step-graded heterostructures

Five different heterostructures incorporating step-graded virtual substrates (represented schematically in Figure 4.5) were grown at the same temperature of **750°C** and subsequently studied.

The structure denominated *VSC1* was grown on a ≈ **500 μm** thick, **100 mm p^+-type** silicon wafer. It consisted of a ≈ **300 nm** thick LPCVD-grown Si buffer on top of which a SiGe virtual substrate characterised by **6 steps** of **5%** Ge concentration variation ≈ **0 - 30%**, each step being ≈ **300 nm** thick, and **1 step** of **2%** Ge variation ≈ **30 - 32%** over ≈**300 nm** was grown. On top of the virtual substrate, a SiGe layer of constant composition (**$Si_{0.70}Ge_{0.30}$**) and ≈ **1 μm** thick was deposited. Finally, at the top of the capping layer a device structure consisting of: ≈ **70 Å** Si channel, ≈ **60 Å** SiGe layer and ≈ **70 Å** Si cap was incorporated.

The heterostructure denominated *VSC2* is the equivalent of *VSC1*, but without the device structure at the top. A comparison between the effects of the presence versus absence of a device structure on the structural properties of these heterostructures could thus be carried out.

The structure denominated *VSC3* is the equivalent of *VSC2*, but with a thicker capping layer (≈ **2 μm**) thus enabling the study of the effects of capping layer thickness variation on the structural properties.

The structure denominated *VSC5* is equivalent to *VSC2*, but has a different type of variation of the Ge composition in the virtual substrate, i.e. in **12 steps** of **2.5%** Ge (≈ **0 - 30%**), and half the Ge concentration gradient in the virtual substrate, as each step is ≈**300nm** thick. By using double the number of half Ge concentration steps in the virtual substrate, this structure was meant to act as an intermediary between the two types of Ge concentration grading i.e. step and linear grading, respectively. Furthermore, the effects of

a reduced Ge concentration gradient in the virtual substrate on the structural properties of this heterostructure could be analysed.

The structure denominated *VSC6* was grown under identical conditions with *774* from the first set of heterostructures (i.e. at **750°C**, with a Ge variation in the virtual substrate in **5 steps** of **6%** between ≈ **12 - 42%** over ≈ **1.36 μm** and a capping layer of constant Ge concentration ≈ **42%** and ≈ **0.24 μm** thick). This structure was used to verify the reproducibility of the SUMC–LPCVD growth technique for these types of heterostructures.

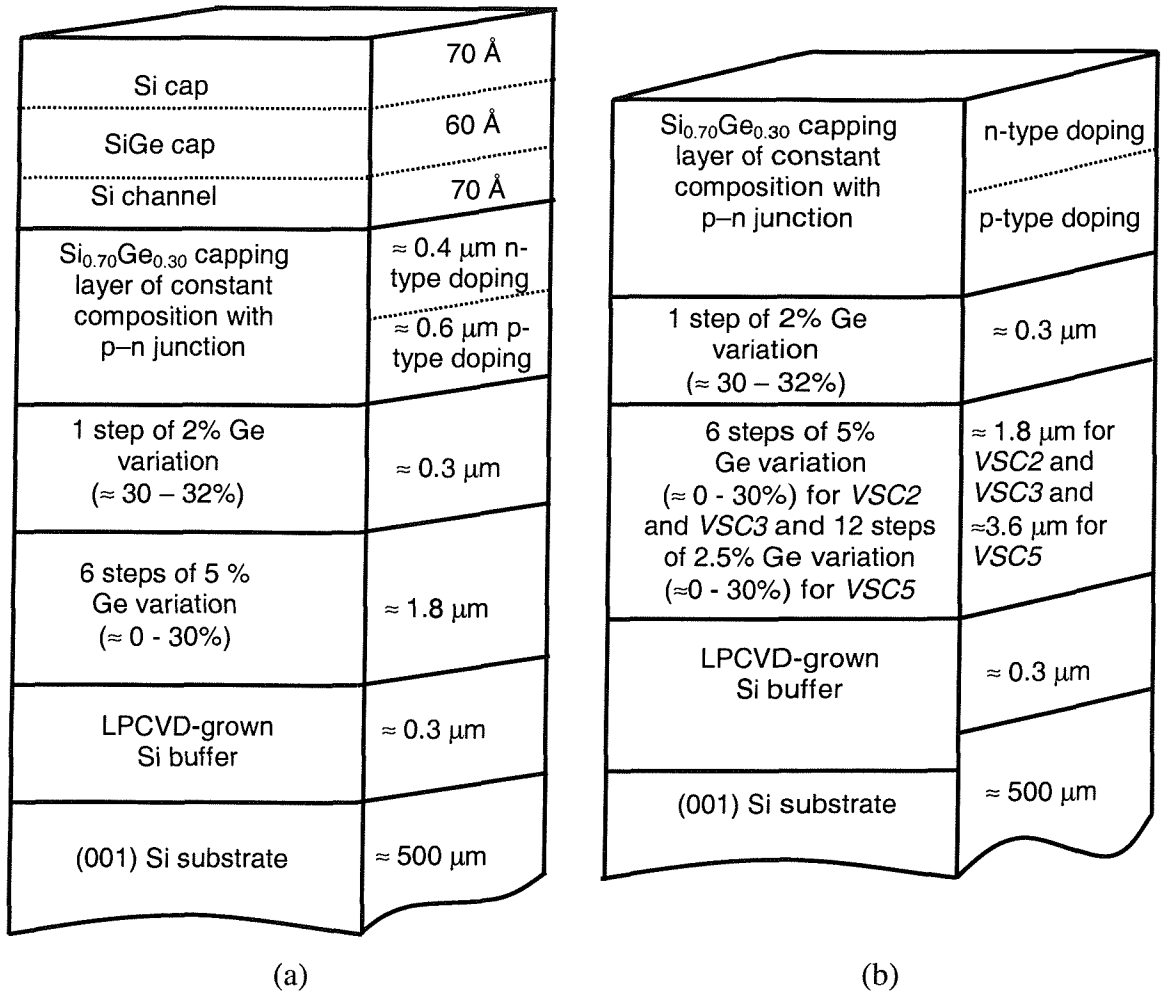

Figure 4.5. Schematic diagram of the step-graded heterostructures of the second set: (a) the heterostructure denominated *VSC1*, which contains a device structure at the top and (b) heterostructures *VSC2*, *VSC3* and *VSC5*, without the device structure at the top, but with different growth parameters varied as described previously.

4.2.3.2. Linear-graded heterostructure

Only one SiGe heterostructure incorporating a linear-graded virtual substrate (*VSC4*) was grown as part of the second set of structures. In order to enable a comparison between the two profiles of Ge concentration grading in the virtual substrate (linear versus stepwise), the linear-graded heterostructure of the second set was grown under identical conditions with the step-graded structure of the second set, *VSC2*.

VSC4 (represented schematically in Figure 4.6) was grown at the same temperature (**750°C**) and with the same germanium variation in the virtual substrate as *VSC2* (between **≈ 0% - 30%**, over **≈ 1.8 μm**, thus having a gradient of **≈ 16% / μm** and one step of **2%** between **≈ 30% - 32%** over **≈ 300 nm**), but with a different profile of the variation (linear-graded). This structure was grown on a **≈ 300 μm** LPCVD Si buffer deposited on a **≈ 500 μm** thick **100 mm p^+-type** silicon wafer and had a capping layer of constant Ge concentration (**≈ 30%**) and **≈ 1.0 μm** thick (the same as *VSC2*).

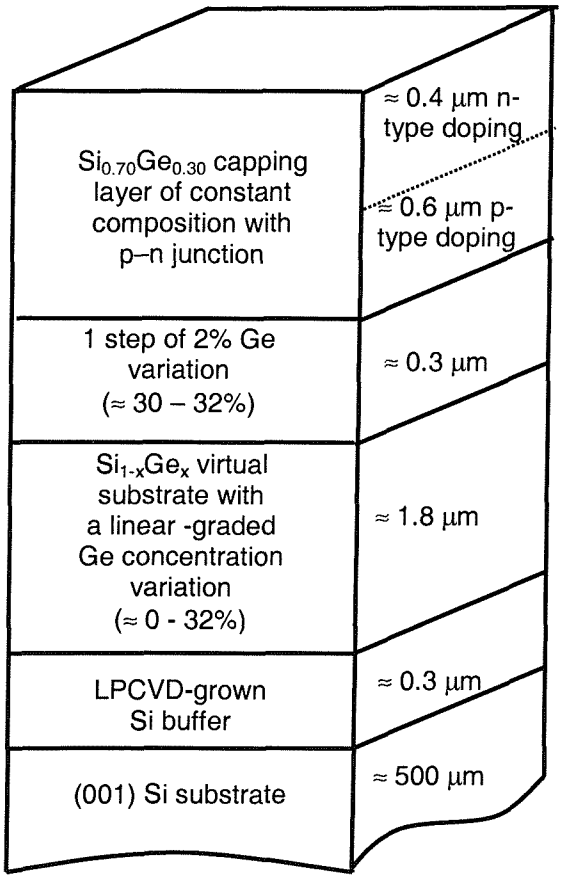

Figure 4.6. Schematic diagram of the linear-graded heterostructure of the second set, *VSC4*, grown under identical conditions with the step-graded heterostructure of the second set, *VSC2*.

The characteristic parameters of the second set of SiGe heterostructures grown for this study are also shown in Table 2.

It is important to mention that the second set of heterostructures was grown after a long period of contamination problems with the LPCVD equipment. The growth time sequence for the heterostructures of the second set is reflected in their denomination: from *VSC1*, grown first to *VSC6*, grown last. This sequence is important for understanding some of the surface morphology features displayed by these heterostructures, which will be presented in Chapter 6.

Sample denomi-nation	Si substrate		Growth temperature (ºC)	$Si_{1-x}Ge_x$ virtual substrate			SiGe capping layer of constant composition	
	Type	Approx. thickness (μm)		Approx. Ge concentration variation (%)	Type of grading	Approx. thickness (μm)	Composition	Approx. thickness (μm)
720	p half-masked	525	800	13 - 42	linear	1.70	$Si_{0.58}Ge_{0.42}$	0.30
775	n	525	750	12 - 42	linear	1.36	$Si_{0.58}Ge_{0.42}$	0.24
774	n	525	750	12 - 42	5 x 6% steps	1.36	$Si_{0.58}Ge_{0.42}$	0.24

Table 1. Characteristic parameters for the first set of SiGe virtual substrate-based heterostructures: sample denomination, growth temperatures and specifications for the three constituent layers: Si substrate, $Si_{1-x}Ge_x$ virtual substrate and SiGe capping layer.

Sample denomi-nation	Si substrate		Growth temperature (ºC)	$Si_{1-x}Ge_x$ virtual substrate			SiGe capping layer of constant composition	
	Type	Approx. thickness (μm)		Approx. Ge concentration variation (%)	Type of grading	Approx. thickness (μm)	Composition	Approx. thickness (μm)
VSC1	p^+	500	750	5 - 32	6 x 5% + 1 x 2% steps	2.10	$Si_{0.70}Ge_{0.30}$	1.00
VSC2	p^+	500	750	5 - 32	6 x 5% + 1 x 2% steps	2.10	$Si_{0.70}Ge_{0.30}$	1.00
VSC3	p^+	500	750	5 - 32	6 x 5% + 1 x 2% steps	2.10	$Si_{0.70}Ge_{0.30}$	2.00
VSC4	p^+	500	750	0 - 32	linear	2.10	$Si_{0.70}Ge_{0.30}$	1.00
VSC5	p^+	500	750	5 - 32	12 x 2.5% + 1 x 2% steps	3.90	$Si_{0.70}Ge_{0.30}$	1.00
VSC6	n	500	750	12 - 42	5 x 6% steps	1.36	$Si_{0.58}Ge_{0.42}$	0.24

Table 2. Characteristic parameters for the second set of SiGe virtual substrate-based heterostructures: sample denomination, growth temperatures and specifications for the three constituent layers: Si substrate, $Si_{1-x}Ge_x$ virtual substrate and SiGe capping layer.

5. ANALYSIS METHODS

Different methods were used to structurally analyse the heterostructures described in Chapter 4. An extensive characterisation of these structures as well as an assessment of the most suitable analysis techniques available were thus achieved.

Both qualitative and quantitative surface characterisations were carried out using optical microscopy techniques, especially Nomarski differential interference contrast (DIC) microscopy, in conjunction with scanning force microscopy (SFM), more specifically, atomic force microscopy (AFM). The internal structure, including relaxation-induced defects, was studied using bright-field transmission electron microscopy (TEM) both on plan-view (PV) and cross-sectional (X) samples.

The different analysis techniques used starting with optical microscopy, through scanning force microscopy and concluding with electron microscopy are described in this chapter.

5.1. OPTICAL MICROSCOPY: NOMARSKI DIFFERENTIAL INTERFERENCE CONTRAST (DIC) MICROSCOPY

5.1.1. INTRODUCTION

Optical microscopy, especially in the Nomarski DIC configuration, constitutes an analysis technique very sensitive to surface morphology; consequently, it was used for the initial topographic analysis of the samples. Although it has the known limitations of optical microscopy (a minimum resolvable feature size of $\approx$ 1 μm), this method is very easy to use, does not require preliminary sample preparation and offers the possibility of examining large areas, hence its use for the initial assessment of the surface quality of the samples. By using an eyepiece with calibrated area, measurements of the spatial size of surface features as well as a quantification of their density can be carried out.

5.1.2. PRINCIPLES AND EQUIPMENT

Analyses were carried out using an Olympus BHSM-313L microscope with Nomarski DIC attachments for the incident light. The available magnification options were: x25, 50, 100, 200, 500, 1000.

Light emitted by a 12 V, 50 W halogen bulb, linearly polarised after passing through the collector and polariser and divided into two linearly polarised rays (one ordinary and one extraordinary ray, respectively) by a modified Wollaston prism, impinges on the sample. On reflection from the sample, the two rays are recombined by the prism and visualised through the analyser (Figure 5.1). Any phase difference between them gives rise to an interference colour. The phase differences arise if the sample slopes, hence the sensitivity of this technique to surface topography [62].

A modified Wollaston prism is made of two wedge-like uni-axial crystals cemented together, the optical axes of which are perpendicular to each other, so that when a ray of linearly polarised light enters the prism, it will be divided into two rays (two polarisation states, in phase, but at slightly different positions). Upon emerging from the prism, the two rays intersect each other at a fixed point, in the vicinity of which, interference fringes form. The plane that includes the interference fringes and the point of intersection of the two rays is known as the plane of fringe localisation and the distance between the prism and this plane is a function of the properties of the crystal wedges. In order to equalise the intensities of the two emerging rays and therefore maximise the contrast of the interference fringes, the Wollaston prism must be placed with its principal axis at 45° with respect to the direction of the linearly polarised light incident on it. The plane of fringe localisation is made to coincide with the rear focal plane of the microscope objective. After passing through the objective, the rays become parallel to each other and impinge on the sample surface. The two rays reflected by the sample travel back on the same optical path, are focused on the plane of fringe localisation and then are recombined by the Wollaston prism. In order to observe the interference fringes, an analyser is introduced behind the half mirror. If the path difference between the two interfering rays changes (i.e. if they find differences in the planarity of the surface they impinge on), the fringe colour changes, this actually giving the 'interference contrast'. Interference colours can be seen in proportion with the gradient of path differences in the sample, hence the sensitivity of this method to topographic analysis [62].

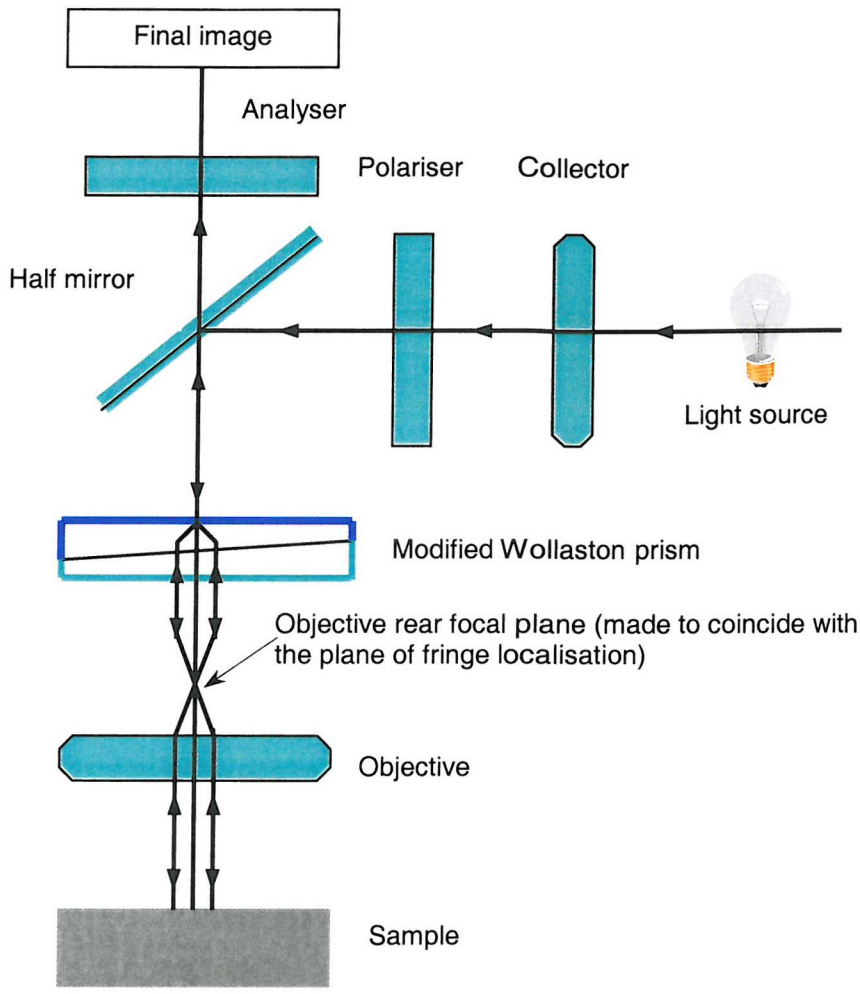

Figure 5.1. Schematic diagram of the Nomarski DIC microscopy equipment: light emitted by the halogen bulb is linearly polarised after passing through the collector and polariser. The modified Wollaston prism divides it into two linearly polarised rays (one ordinary and one extraordinary ray, respectively), which impinge on the sample. On reflection from the sample, the two rays are recombined by the prism and visualised through the analyser. Any phase difference between them, caused by the surface morphology, gives rise to an interference colour.

5.1.3 SAMPLE PREPARATION

There are no special requirements for the sample preparation for Nomarski DIC analysis, apart from the usual recommendations for the analysed surfaces and the optical equipment to be preliminarily cleaned in order not to introduce artefacts in the images obtained.

Chemical etching for revealing crystal defects

A variety of chemical etchants for revealing the emergence of dislocations on Si surfaces through etch pit formation have been developed and are reported in literature. In this study, attempts to quantify the TD density by using disclosure chemical etch combined

with optical microscopy were carried out. For this purpose, a few of the etchants commonly used for Si were applied:

- SECCO (1 HF (49%) : 1 $K_2Cr_2O_7$) is a very common Si etchant, meant to provide an isotropic etch, but not very well defined pits of circular and/or elliptical shape [63].
- DASH (1 HF (49%) : 3 HNO_3 (70%) : 10 CH_3COO_4 (glacial)) is also a very commonly used Si etchant, characterised by an isotropic etch with not well defined pits and longer etching times [64].
- YANG (1 HF (49%) : 1 CrO_3 solution (1.5M)) is also meant to ensure an isotropic etch, but with well defined etch pits [64].

5.2. SCANNING PROBE MICROSCOPY (SPM): ATOMIC FORCE MICROSCOPY (AFM)

5.2.1. INTRODUCTION

There are two methods used in SPM: atomic force microscopy (AFM) and scanning tunnelling microscopy (STM), both very useful for topographic analysis. They can be complementary to the Nomarski DIC technique, especially as they have the advantage of a minimum resolvable feature size of the order of 0.1 Å. Unfortunately, artefacts can easily be introduced due to the complexity of the image acquisition and analysis procedures. For the analysis of the heterostructures of interest to us, only the AFM technique was used.

5.2.2. PRINCIPLES AND EQUIPMENT

Atomic force microscopy (AFM) was used as a complementary method to Nomarski DIC for the study of surface morphology. A TopoMetrix Accurex II^{TM} scanning probe microscope was used for the SiGe heterostructures characterisation.

A scanning probe microscope is made of a sensitive probe, piezoelectric ceramics, a feedback electronic circuit and a computer for generating and presenting the results (Figure 5.2). One of the most important components of the scanning probe microscope is the high spatial resolution sensor, which can commonly measure distances with an accuracy of 0.1 Å. This sensor measures the deflection of a cantilever. A tip is mounted on the cantilever so that when the cantilever moves, the beam of light generated by a small laser and deflected by the tip of the cantilever moves across the face of a four-section detector. The amount of motion of the cantilever can then be calculated from the difference in the intensity of light on the four sectors of the detector. The control of the sensor over extremely small distances is made possible by the use of piezoelectric ceramics. By changing their physical dimensions upon the application of an electrical potential, these ceramics allow the accurate positioning of the probe tip. In order to create the positioning mechanism, a feedback electronic circuit is combined with the sensor and the piezoelectric ceramic. A PID (proportional, integral and derivative) feedback control system is used. The feedback response is based on an equation, which combines terms proportional to the error signal, the integral of the error signal and the derivative of the error signal to set the z position of the probe so as to maintain a constant sensor signal. The error signal is the difference between the sensor signal and a user-defined set point. When the interaction between the tip and sample increases (i.e. when the tip gets closer to the sample in non-contact mode or the interaction force between the tip and the sample increases in the case of contact mode), the output of the electronic circuit of the sensor increases; the differential amplifier compares this increased value with a reference value (V_s) and outputs a correction voltage, which excites the piezoelectric ceramic so that the sensor is pulled back from the surface, restoring it to its original output level. This feedback circuit operates continuously to maintain a constant *tip–sample separation*, for the *non-contact mode*, or a constant *force*, for the *contact mode* [65].

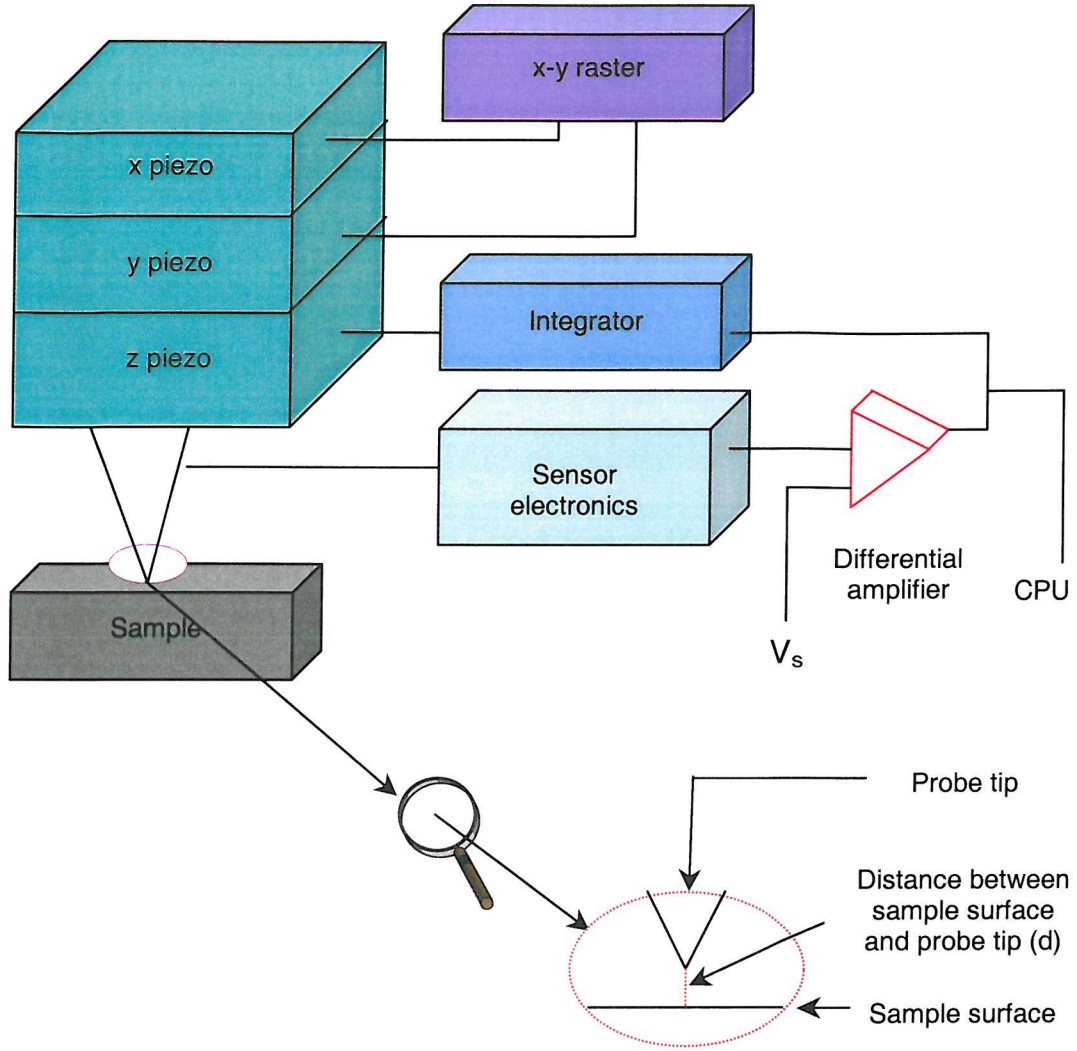

Figure 5.2. Schematic diagram of the scanning probe microscope.

5.2.3. AFM VARIABLES

5.2.3.1. The force-distance dependence

As the probe is brought close to the sample, it is first attracted to the sample surface as a result of long-range attractive forces (Van der Waals type). When the probe gets very close to the sample surface, the electron orbitals of the atoms on the surface probe and sample start to repel each other. As the gap between the probe and sample surface decreases, the repulsive forces neutralise the attractive ones and then become dominant as in Figure 5.3 below [65].

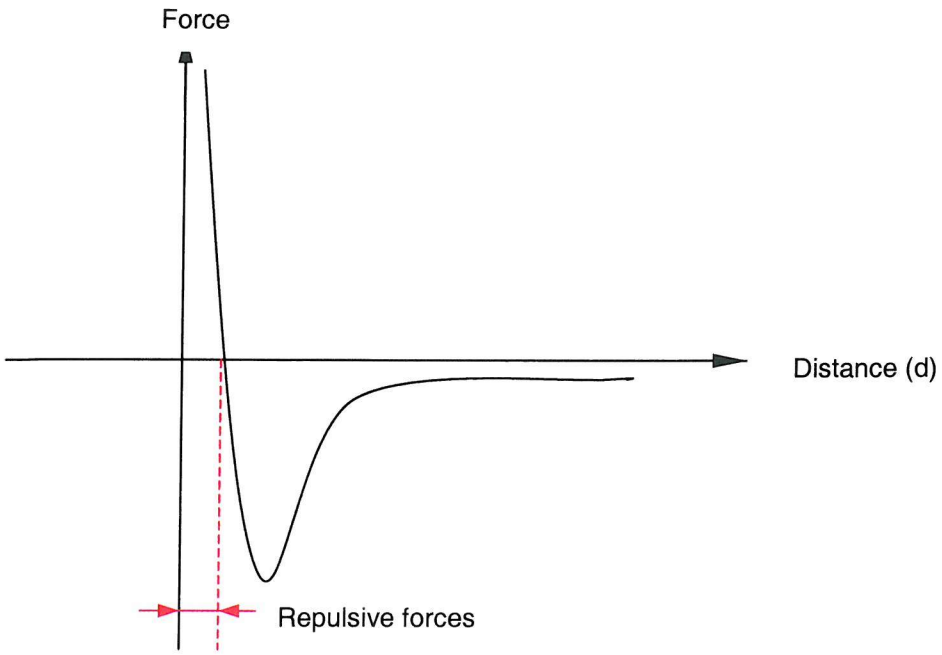

Figure 5.3. The force-distance dependence between the AFM probe tip and the sample surface (as reproduced after [65]).

5.2.3.2. Sample surface contamination

As the probe tip is moved toward a surface that has a contamination layer, at some point, it will be strongly pulled toward the surface by the capillary attraction of the contamination layer. Thus, clean and/or dry sample surfaces are always required in order to get an accurate image of the topography.

5.2.3.3. Probe tip geometry

The shape of the probe tip is very important for AFM imaging as the image is the result of both sample and probe shape. The geometry of the probe tip is also important for the different AFM imaging modes. A sharp, small radius probe tip has a much smaller area to interact with the contamination layer (in case that exists), thus having a lower capillary attraction toward the sample than a large radius tip. Small tips are also more versatile at moving toward and away from the sample surface. Integrated tip and cantilever assemblies can be fabricated from silicon or silicon nitride using photolithographic techniques. More than 1,000 tip and cantilever assemblies can be produced on a single silicon wafer. V-shaped cantilevers are the most popular, providing low mechanical resistance to vertical deflection, and high resistance to lateral torsion (Figure 5.4).

ThermoMicroscopes cantilevers typically range from 100 - 200 μm in length, 10 - 40 μm in width, and 0.3 - 2 μm in thickness. V-shaped high-resonance frequency probes were used for the analyses carried out for this study [65].

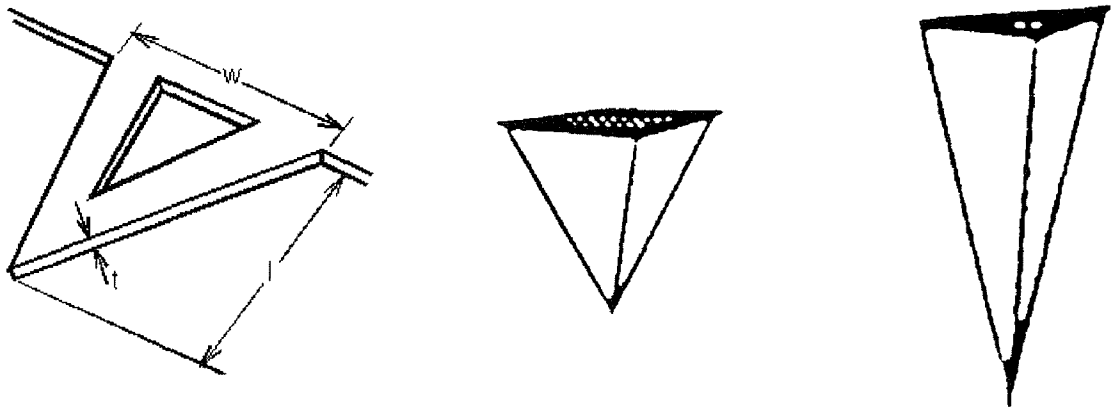

(a) (b) (c)

Figure 5.4. (a) V-shaped cantilever (reproduced from ThermoMicroscopes web page) showing length (l), width (w), and thickness (t); (b) ThermoMicroscopes 1520-00 silicon nitride pyramidal 1:1 contact probe (4 μm base and 4 μm high, < 50 nm tip radius); (c) ThermoMicroscopes 1660-00 silicon triangular pyramid 3:1 non-contact probe (3 - 6 μm base, 10 - 20 μm high, < 20 nm tip radius).

5.2.3.4. Nature of the sample

The nature of the sample affects the probe tip-sample forces. Also the force-distance dependence can be affected by the compliance of the sample surface.

5.2.4. AFM OPERATING MODES

AFM encompasses a number of acquisition methods each designed to obtain specific types of information from different types of samples.

5.2.4.1. Contact mode

In this mode, the probe tip comes into direct physical contact with the sample, being in the repulsive region of the force-distance dependence (Figure 5.3) and the cantilever is curved away from the sample surface. Feedback is given by the displacement of the probe, which through the feedback loop adjusts the z of the piezoelectric ceramic so that the force between the probe and sample stays constant. The voltage required to achieve this is used as z data for imaging. Contact AFM is the simplest method (involving the fewest

instrument variables) for collecting topographic information, even down to atomic level resolution.

SiGe is a hard material, suitable for analysis in contact-mode. Its surface does not deform easily under the force of the probe tip, hence offering the possibility of repeatedly scanning the same area.

5.2.4.2. Non-contact mode

In this mode, the cantilever is oscillated at its resonant frequency and the parameter detected is the change in force between the tip and sample, *even though they are not in contact* (these force changes are also referred to as *the force gradient*). As the probe gets closer to the sample surface, the force gradient changes, thus altering both the oscillation amplitude and phase of the vibrating cantilever. Either the change in amplitude or the change in phase can be detected and used to control the feedback loop. *Amplitude detection* is the non-contact method usually used for high-amplitude cantilever vibration, while *phase detection* is used when the cantilever vibration amplitude is relatively small and/or higher sensitivity is needed for stable feedback.

Non-contact AFM can produce high resolution images of hard materials such as SiGe, which may sometimes blunt the probe tip in the contact mode thus resulting in poor lateral resolution and damage to the probe.

5.2.5. DATA ACQUISITION

For data acquisition, adjusting the feedback parameters has proven to be crucial, but also rather difficult.

Several methods for obtaining surface topographic data/images can be used, each of them presenting particular advantages and disadvantages. The method used for this study was topography forward. In this mode, the probe tip is in the repulsive region of the force-distance dependence (Figure 5.3) and the cantilever is curved away from the sample surface.

Topography forward provides the greatest level of accuracy in measuring and imaging larger-scale features and topographic changes. This method involves optimising the PID

settings and taking the voltage reading directly from the z-piezo feedback signal during the scan.

Two scanners are available for the Accurex II™ microscope: a maximum scanning range of 100 μm in x and y and 10 μm in z scanner, and a high resolution tube scanner configuration with a scan range of 2 μm in x and y and 0.8 μm in z. In general, the larger the scan range, the lower the achievable resolution. The largest surface that can be rastered in the Accurex II™ is 100 x 100 μm^2. Images can be collected with a resolution up to 500 x 500 pixels.

5.2.6. IMAGE ANALYSIS

An SPM magnifies in three dimensions x, y and z. The maximum resolution in each of these directions is determined by different factors. Resolution in the z direction is limited by the level of mechanical noise between the probe and surface, by the electronic noise and the sensitivity of the sensor. The maximum achievable resolution in the x and y directions is established by the geometry of the probe itself (Figure 5.4): tip diameter and aspect ratio (l/w) are critical in determining the image accuracy when imaging larger surface features.

The image analysis software allows 3D projection from any viewpoint. Levelling the images by subtracting a plane of best fit or a second order surface of positive or negative curvature can be performed. In addition, each scan line can be levelled by the subtraction of a low order 1-6 polynomial approximation. Line measurement can be carried out along a horizontal, vertical or variable line. Area analysis allows the estimation of the Root Mean Square (RMS) of the surface roughness on the whole of the rastered surface or on any selected portions of it.

5.3. ELECTRON MICROSCOPY: TRANSMISSION ELECTRON MICROSCOPY (TEM)

5.3.1. INTRODUCTION

Transmission electron microscopy represents the main technique used to analyse the nature and quantify the density of the misfit strain relaxation induced defects encountered in the SiGe virtual substrate-based heterostructures of interest to this study.

5.3.2. PRINCIPLES AND EQUIPMENT

A J.E.O.L. JEM 2000FX transmission electron microscope was used. This machine is equipped with a double-tilt sample holder allowing a rotation of up to ± 30° about its long axis, y, and a tilt of up to ± 25° about the x axis (Figure 5.5).

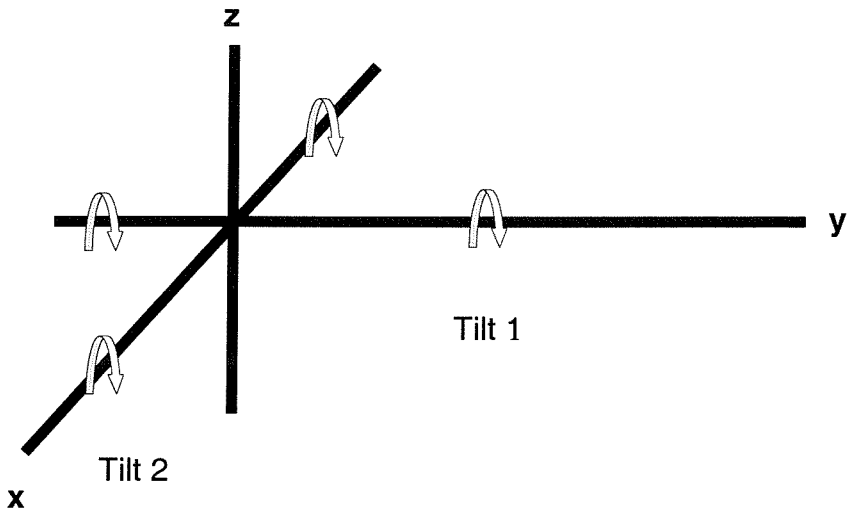

Figure 5.5. Schematic representation of the double-tilt holder: tilting is possible about the long axis, y (tilt 1) and about an axis perpendicular to it, x (tilt 2).

The information available in TEM can be generated using either a fixed electron beam, as in a conventional TEM or a scanning beam, as in a scanning TEM (STEM). In the conventional TEM, the whole area of interest is illuminated simultaneously, whilst in STEM, a probe is scanned across the area of interest and, in this case, a high electron density in a small probe is required. For the analysis of our heterostructures only conventional TEM was used.

An electron source (Figure 5.6) generates electrons and accelerates them through a range of selected potential differences, from 60-200 kV for the most common types of TEM microscopes, 300–400 kV, for the medium voltage range and up to 600–3000 kV, for the

high voltage range microscopes. These latter are not standard laboratory instruments, but can be found in a limited number of specialised laboratories. Accordingly, there are three different types of electron sources available:

- The conventional tungsten hairpin filament;
- The lanthanum hexaboride (LaB_6) crystal;
- The field emission source.

The J.E.O.L. JEM 2000FX TEM was used at 200 kV, both with the tungsten filament and with the LaB_6 crystal.

Underneath the electron source, the TEM has two or more condenser (electromagnetic) lenses whose main function is to demagnify the beam emitted and to control its diameter and convergence angle as it hits the sample. The most common condenser system has a two-lens configuration. The first condenser lens usually sets the demagnification of the gun crossover (labelled 'spot size'). The second condenser lens (often labelled 'intensity') provides control of the spot size at the sample surface and the beam convergence angle. At their simplest, the condenser controls can be thought of as brightness controls, which also allow control over the region to be 'sampled' and over the type of diffraction pattern.

Below the condenser lenses lies the specimen chamber, which is one of the most crucial parts of the microscope. A very small specimen must be held in precisely the correct position, but should also allow for rotation and tilt. The sample is usually located between the pole pieces of the objective lens. The role of the objective is to form the first intermediate image and diffraction pattern, one of which is enlarged by the subsequent projector lenses and displayed on the viewing screen.

The first projector lens can usually be switched between two settings (Figure 5.7). In the image mode, it is focused on the image plane of the objective (the magnification is then controlled by the strength of the remaining projector lenses). In the diffraction mode, the intermediate lens is focused on the back focal plane of the objective and the diffraction pattern is projected on the viewing screen.

An essential feature of the objective system is the aperture holder, which enables any one of three or four small apertures to be inserted into the column in the back focal plane. The objective aperture clearly defines the angular range of the scattered electrons, which can

travel further down the column and contribute to the image. Its diameter therefore controls the ultimate resolution. However, the highest resolution is not always required and the objective aperture serves more the function of controlling the contrast seen in the image [66].

The first image produced by the objective usually has a magnification of 50-100 times. This is further magnified by a series of intermediate and projector lenses and finally projected on the fluorescent screen. By using three or four lenses, each providing a magnification of up to 20 times, a total magnification of up to 10^6 can easily be achieved, but it is not always necessary to use all the lenses, therefore, one or more of them can be switched off at any time.

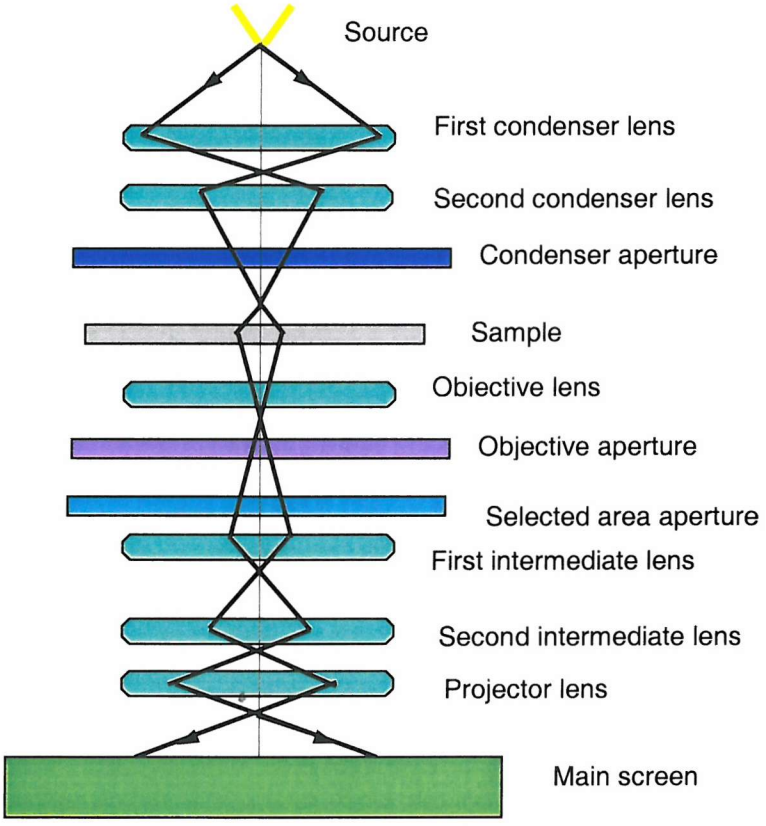

Figure 5.6. Schematic representation of a TEM column. The electron beam generated by the source and demagnified by the condenser lenses impinges on the sample, which is situated between the pole pieces of the objective lens. The objective lens forms the intermediate image or diffraction pattern, either of which is further enlarged by the projector lenses and projected on the fluorescent screen.

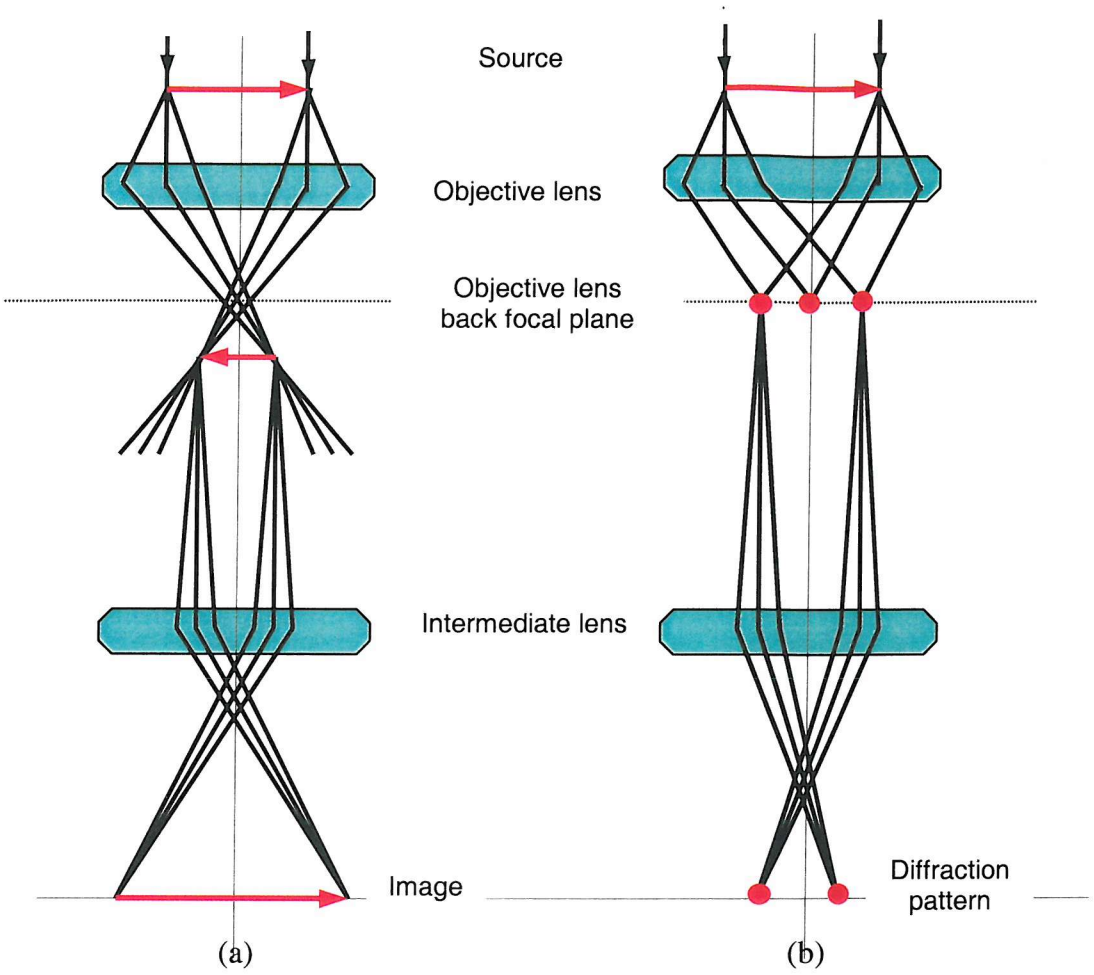

Figure 5.7. The objective and first intermediate lenses. The objective lens is focused on the sample and forms an intermediate image. (a) In the imaging mode, the intermediate lens magnifies the image further and passes it through the projector lenses to the viewing screen; (b) In the diffraction mode, the intermediate lens is focused on the back focal plane of the objective lens, where the diffraction pattern forms and passes it to the projector lens to be viewed.

5.3.3. IMAGING AND DIFFRACTION INFORMATION

The information obtained using electron microscopy derives from the scattering processes which take place when the electron beam travels through the sample. There are two types of scattering: elastic, which involves no energy loss and can be coherent or incoherent, hence is characterised by poor phase relationship, and inelastic, which involves energy loss and absorption. It is the elastic scattering that produces the diffraction pattern. If the scattering centres in the sample are arrayed in an orderly regular manner, as in crystals, the scattering is coherent and results in spot patterns. When an image is formed of the scattered beams, two contrast mechanisms can arise:

1. If the transmitted and scattered beams can be made to recombine, thus preserving their amplitudes and phases, a lattice image of the diffracting planes or even a structural

image of the individual diffracting atoms may be resolved directly with the help of the diffraction pattern (phase contrast).

2. Alternatively, amplitude contrast is obtained by deliberately excluding the diffracted beams and hence the phase relationship from the imaging sequences by introducing the objective aperture in the back focal plane of the objective lens (diffraction contrast). A *bright-field image* is thus obtained. By excluding all other beams apart from the particular diffracted ones of interest, a *dark-field image* is obtained.

A diffraction pattern is formed in the back focal plane of the objective lens of the TEM (Figure 5.7). Hence, if the diffraction lens is focused on the back focal plane of the objective lens (Figure 5.7 b) rather than on the first image plane (Figure 5.7 a) and the objective aperture is removed, the diffraction pattern is visible on the viewing screen. Figure 5.7 shows clearly the nature of an electron diffraction pattern. Beams leaving the sample in a specific direction are brought to focus at the same point, in the back focal plane of the objective lens, irrespective of where they originate from within the sample. By contrast, the formation of an image requires all the electrons originating from a specific area on the sample to meet at the unique point in the first image plane, irrespective of the direction in which they left the sample. To summarise very briefly: a diffraction pattern contains directional information and no positional information, whilst an image contains only positional information and no directional information. When using the TEM in the conventional imaging mode, *a bright-field image* can be formed if the directly transmitted beam is selected by the objective aperture (Figure 5.8). *A dark-field image* is formed if a diffracted beam is selected. In order to analyse the heterostructures of interest for this study, conventional bright-field imaging in different two-beam conditions was used.

The diffraction patterns characteristic of the heterostructures analysed in this study are presented in Figure 5.9 a–b for both cross-sectional and plan-view analyses.

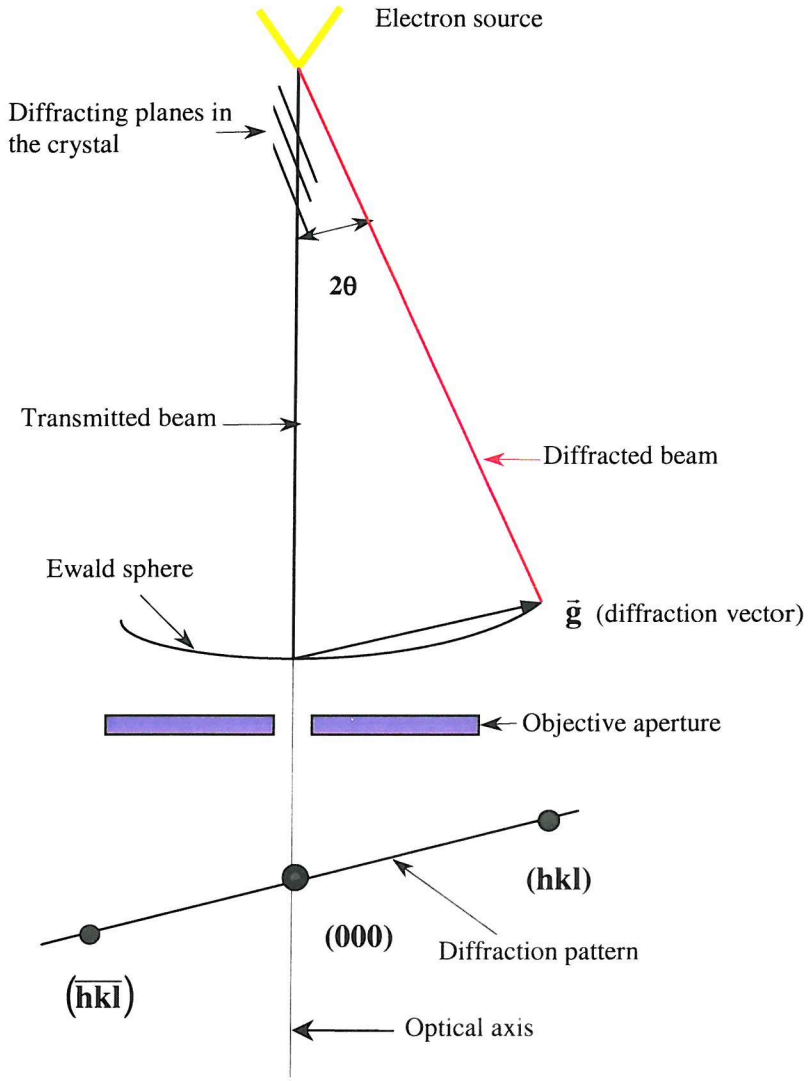

Figure 5.8. Electron beam diagram and Ewald sphere construction for conventional two-beam bright-field imaging. The main beam and the beams diffracted by the crystalline planes (hkl) form a diffraction pattern in the back focal plane of the objective lens.

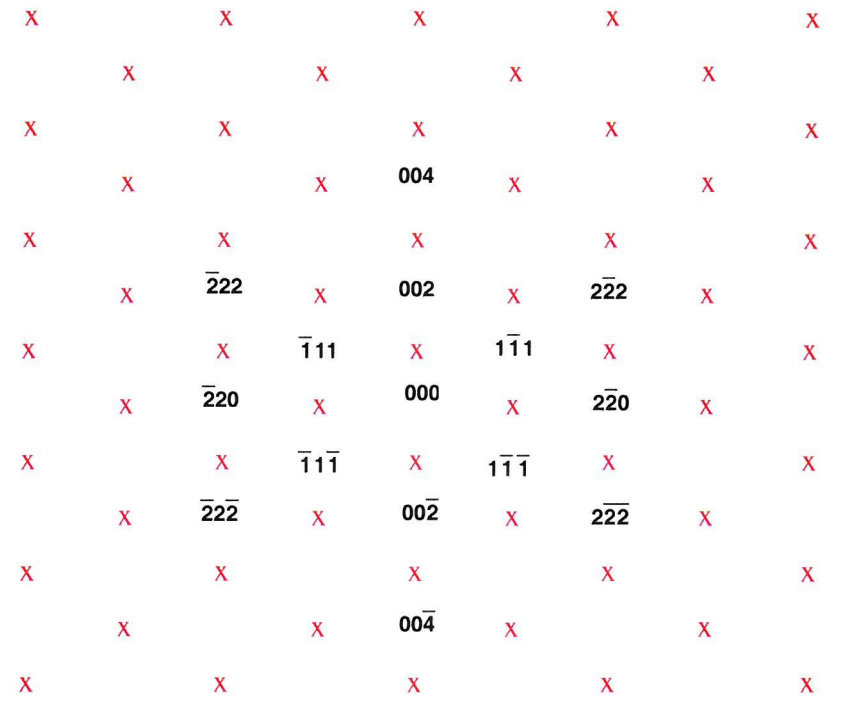

(a)

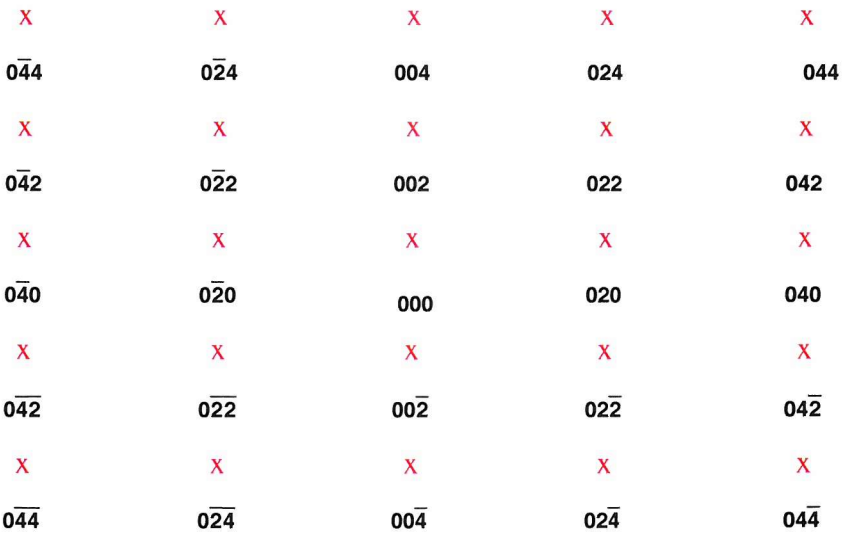

(b)

Figure 5.9. The diffraction patterns for an fcc (SiGe–type) crystal: (a) along the **[110]** direction (as used for XTEM analyses); (b) along the **[001]** direction (as used for PVTEM analyses).

5.3.4. DEFECT ANALYSIS

Bragg's law defines constructive interference as occuring when the path difference between waves scattered by successive parallel planes of atoms of interplanar distance **d** is equal to an integral number (**n**) of wavelengths (λ):

$$2d \sin\theta = n\lambda \qquad (5.1)$$

where θ is the angle between the incident beam and the diffracting plane.

The formation of images of lattice planes in crystals depends upon whether or not the recombination of diffracted and transmitted beams can occur.

Diffraction contrast is the dominant mechanism delineating object details ≥ 15 Å in the crystalline samples and is the most widely used contrast mechanism for defect analysis as opposed to phase contrast, which is the dominant mechanism for object details ≤ 10 Å and is used for lattice resolution studies.

Crystalline defects can be described in terms of translational vectors, which represent the displacements of atoms from their regular positions in the lattice ($\vec{\mathbf{R}}$). The visibility of these defects in TEM can be understood in terms of the simple $\vec{\mathbf{g}} \cdot \vec{\mathbf{R}}$ criterion (where $\vec{\mathbf{g}}$ is the diffraction vector as shown in Figure 5.8). The magnitude of $\vec{\mathbf{g}} \cdot \vec{\mathbf{R}}$ must be sufficient to change the intensity from background, so that contrast is detectable.

The magnitude and direction of the lattice distortion associated with a dislocation is expressed in terms of the Burgers vector $\vec{\mathbf{b}}$ and the dislocation line $\vec{\mathbf{l}}$ (as already described in Chapter 3, § 3.2.3.1). In the case of *a screw dislocation* of Burgers vector $\vec{\mathbf{b}}$, the only possible displacements within the crystalline lattice lie along the direction of $\vec{\mathbf{b}}$ and it is only the magnitude of the displacement that varies within the crystal. For this type of dislocation, the condition that would make the dislocation invisible in TEM (i.e. it would show no contrast) is given by [66]:

$$\vec{\mathbf{g}} \cdot \vec{\mathbf{b}} = 0 \qquad (5.2)$$

For all the other values of $\vec{g}\cdot\vec{b}$, the intensities of the diffracted beams will be changed near the dislocation, where the term $\vec{g}\cdot\vec{b}$ actually leads to significant changes in the intensity of the transmitted (diffracted) beams.

For *an edge dislocation*, with a line direction given by the vector $\vec{l}$, displacements from the Bragg conditions are more complex (because the line vector, $\vec{l}$, and the Burgers vector, $\vec{b}$, are perpendicular to each other). In this case the invisibility criteria, needed to be simultaneously satisfied are given by [66]:

$$\vec{g}\cdot\vec{b} = 0$$
and
$$\vec{g}\cdot(\vec{b}\times\vec{l}) = 0 \qquad (5.3)$$

The physical significance of this is that only if the particular set of planes defined by the above relations remains flat in the presence of the dislocation, the dislocation will show no contrast. For any other two-beam imaging conditions, contrast will be observed. This emphasises the power of two-beam imaging of defects; the electrons sample the perfection of selected planes and from this information, deduce the nature of the defect. The above presented invisibility criteria form the basis for the most common method to determine the Burgers vector of dislocations by using TEM imaging. If two sets of planes (characterised by the diffraction vectors $\vec{g}_1$ and $\vec{g}_2$, respectively) for which a dislocation is invisible are found, then the Burgers vector of the dislocation can be determined [66]:

$$\vec{b}=\vec{g}_1\times\vec{g}_2 \qquad (5.4)$$

For *mixed dislocations*, all planes are distorted to some extent and hence these types of dislocations never go completely out of contrast. The contrast for a mixed dislocation is controlled by the values of $\vec{g}\cdot\vec{b}$, $\vec{g}\cdot\vec{b}_e$ and $\vec{g}\cdot(\vec{b}\times\vec{l})$, for which $\vec{g}$, $\vec{b}$, $\vec{l}$ have their already described meaning, and $\vec{b}_e$ is the edge component of the Burgers vector [66].

5.3.5. SAMPLE PREPARATION

TEM samples must be thinned to electron transparency (a few hundred nm) and made into discs of 3 mm diameter (to fit into the TEM holder), without damaging them but at the same time making it possible to handle them repeatedly. These requirements make accurate TEM sample preparation a crucial stage.

5.3.5.1. Cross-section samples

XTEM analysis was possible, by making the samples into 'sandwiches' in which the epitaxially grown faces are glued together.

The wafer was cleaved along its natural cleaving direction, **<110>**, into slices of ≈5mmx10 mm, which were glued together using an epoxy resin (Araldite type). The cleaving process initiated with the help of a diamond scriber. Attention was paid to ensuring that the glue layer was as thin as possible, due to the fact that in subsequent processing (ion beam thinning), the glue line is preferentially milled away [67].

Two supports were glued to each side of the main layers as part of the 'sandwich' in order to secure the necessary edge thickness of the TEM samples, making it possible to handle them repeatedly.

The 'sandwiches' were left overnight for the Araldite to cure (typically, Araldite reaches its full strength at room temperature after 8 hours, whilst at 40°C – 60°C, after only 2 – 3 hours). After the Araldite had cured, the upper surface of the 'sandwich' was mechanically thinned by using emery paper with progressively finer grades of grit (600, 800 and 1200) and subsequently polished with the use of progressively finer types of alumina suspension (1, 0.5, 0.1 μm). Once the upper face was ready, the sandwiches were turned with the opposite face up and ground and polished, as described above, down to less than 50 μm (ideally, ≈ 35 μm) thickness. After which, supports (≈ 3 for a 10 mm long sample), in the form of copper-beryllium alloy grids (discs of 3 mm diameter with a 2 mm x 1 mm slot in the centre) were attached with Araldite (again a very thin layer, to ensure planarity), in order to provide mechanical support for the thin samples. Once the Araldite had cured, pre-thinned TEM samples were cut out (all around the grid) with the use of a fine scalpel.

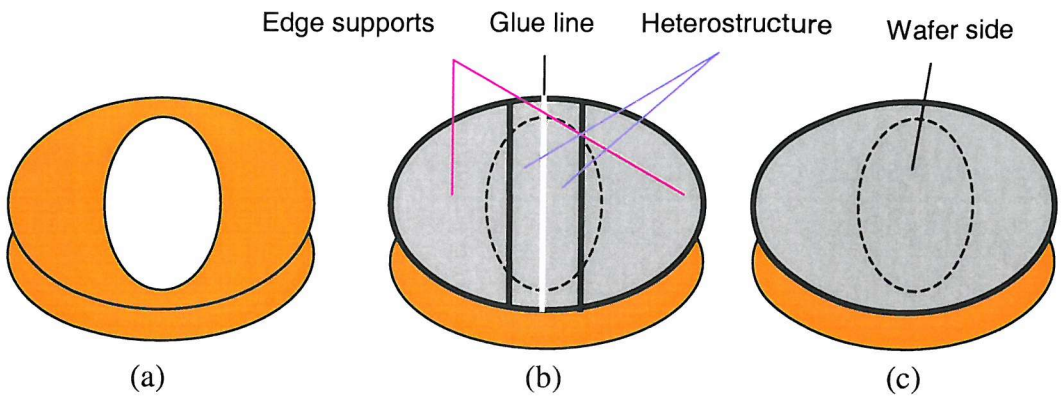

Figure 5.10. TEM support grid: (a) without sample, (b) with cross-sectional sample; (c) with plan-view sample.

5.3.5.2. Plan-view samples

The wafer was cleaved into slices of ≈ 5 mm x 10 mm, then mechanically ground and polished down to approximately 35 μm thickness, using the same procedure as for cross-section samples. The mechanical thinning had to be performed only on one side (the substrate side). As soon as the mechanical thinning was finished, grids (≈ 3 for a 5 mm x 10 mm slice) were attached in order to provide mechanical support (exactly as for cross-sectional samples). Pre-thinned TEM plan-view samples were cut out in the same way as the cross-section ones.

At this point, samples were ready to be ion beam thinned in the Gatan precision ion polishing system (PIPS) Model 691. The polishing is done by two miniature Penning ion guns aimed at glancing angles of incidence to the specimen. Low sputtering angles have the advantage of minimising radiation damage and beam heating while at the same time, producing specimens with large, clean electron transparent areas. Sample milling times in the case of the studied samples varied from 30 minutes to 2 hours depending on the initial thickness. Additionally, depending on the thickness of the pre-thinned samples (indicated by whether they are light transparent or not when examined with the PIPS microscope in transmission), they were milled at angles ranging from 7° down to 5° (the thinner the sample, the smaller the angle) and with a gun energy of 5 keV. Sample preparation was concluded with a polishing at 4 keV and 4° for a few minutes.

Cross-sectional samples were ion beam thinned in the Gatan DuoPost holder (either the glue type or clamp type), which allows a double-sided milling (top and bottom). Attention

had to be paid to aligning the sample glue line in the holder. Plan-view samples were ion beam thinned only from the top (the sample being positioned face down), in the Gatan molybdenum post.

Wax used for mounting during mechanical thinning was melted on a hot plate and the remaining traces dissolved by Iso-Propyl Alcohol (IPA). The low melting-point wax used to mount samples in the PIPS holders was dissolved by acetone.

6. EXPERIMENTAL RESULTS AND DISCUSSIONS

This chapter contains a detailed presentation of the results obtained from the structural characterisation of the two sets of virtual substrate-based SiGe heterostructures described in Chapter 4 by using the analysis methods presented in Chapter 5. Firstly, the experimental results obtained on the first set of test structures dived into two categories according to the Ge grading profile in the virtual substrate, i.e. linear-graded and step-graded, are presented comparatively. The results obtained are then summarised and discussed and conclusions are drawn. Secondly, the experimental results obtained on the second set of heterostructures are presented in the same manner and subsequently summarised and discussed and further conclusions are drawn. The results obtained from the comparison between the first and second set of heterostructures are also outlined. The discussion of the results obtained is carried out with references to the literature reviewed in Chapter 3, in order to enable general conclusions to be drawn and to outline possible directions for future work.

6.1. EXPERIMENTAL STRATEGY AND OBJECTIVES

In order to study the effects of growth parameters on the surface morphology and type and density of misfit strain relaxation induced defects, two sets of SiGe heterostructures incorporating virtual substrates were grown using different combinations of the growth parameters (as described in Chapter 4) and subsequently studied using the analysis methods presented in Chapter 5. Two types of Ge concentration grading in the virtual substrate (linear and stepwise) were used as techniques to decrease the TD density and improve the surface morphology. The growth parameters varied were:

- For the virtual substrate: growth temperature, thickness, initial and final Ge content, Ge concentration gradient, type of Ge variation (linear and stepwise);
- For the capping layer: thickness and presence of a device structure.

In order to make an accurate selection of the growth parameters values to use, calibration structures were first grown and analysed. Thickness values for the different layers incorporated in the heterostructures to be studied were obtained by interpolating from SIMS results obtained on the calibration structures, whilst Ge concentrations were estimated by interpolating from high resolution X-ray diffraction (HRXRD) results obtained on the calibration structures.

The first set of heterostructures grown was a test set and hence was extensively characterised after growth. Subsequently, some conclusions concerning the effects of the chosen growth parameters on the structural properties of the heterostructures of the first set were drawn. Furthermore, conclusions were drawn on the suitability of some of the characterisation techniques used. Based on the conclusions from the first set, the combinations of growth parameters used for the second set of heterostructures were carefully chosen, with the aim of improving their surface morphology and defect content. Nevertheless, a long period of contamination problems with the LPCVD equipment, prior to the growth of the second set of heterostructures, introduced some growth artefacts, which upon been analysed, were found as not influencing the effects of the incorporation of the virtual substrates on the structural properties of the samples. Overall, as expected, despite the contamination problems experienced, the SiGe virtual substrate-based heterostructures of the second set exhibited superior structural properties by comparison with the test structures of the first set.

All the heterostructures grown for this study had a preliminary assessment of their surface morphologies using Nomarski DIC microscopy. Analysed in Nomarski contrast, all the SiGe heterostructures studied exhibit lines on their surfaces running along two perpendicular <110> directions and creating a crosshatch pattern. These crosshatch lines have different aspects for each of the two sets of heterostructures analysed, but for both sets, they run along the two perpendicular <110> directions. For the first set of heterostructures, some of the crosshatch lines appear much more accentuated than others, the latter ones forming a fine uniform pattern. The fine pattern seems to be characterised by periodicity (similar spacing values), whilst the accentuated lines seem randomly distributed by comparison. The relative surface distribution of the accentuated lines and the fine pattern appears to be different for each type of heterostructure of the first set. For the second set of heterostructures, the accentuated lines are completely absent, thus leaving surfaces characterised by a fine, uniform crosshatch pattern.

AFM analyses were used in conjunction with Nomarski contrast for both a qualitative three-dimensional characterisation of the surface morphology, and for quantitative surface roughness measurements (e.g. Root Mean Square, RMS, of the surface roughness) and depth variation measurements along the crosshatch lines. Analysed in AFM, all the SiGe heterostructures studied exhibit to varying degrees undulations on their surfaces aligned along the crosshatch lines (i.e. along two perpendicular <110> directions). AFM analyses

revealed that the accentuated crosshatch lines, exhibited by the heterostructures of the first set, correspond to trenches (i.e. lines of somewhat increased depth) along the surfaces of these structures. Additionally, these analyses showed the presence of pits (i.e. undulations of somewhat increased depth) along the trenches. For the second set of heterostructures, AFM analyses showed both qualitatively (through the 3D images) and quantitatively (through the values of the RMS of the surface roughness) their superior surface morphology, by comparison with the first set. Furthermore, AFM analyses of the heterotructures of the second set enabled extensive characterisation of the contamination-induced growth artefacts, by allowing size (in-plane) and depth measurements. Based on the AFM results obtained from the characterisation of these growth defects, we could conclude that they were not affecting the structural properties of the heterostructures directly related to the incorporation of virtual substrates.

The effects of the crosshatch topography on the electronic properties of the heterostructure devices are determined both by the dimension of the surface features in the growth plane and by their height in the growth direction. The crosshatch size is decisive for the further use of the SiGe virtual substrate-based heterostructures for device fabrication, hence the need to extensively characterise it.

In order to reveal the underlying structure that generated the surface morphologies observed in both Nomarski contrast and AFM, TEM analyses were carried out. PVTEM analyses showed the presence of a network of MDs running along two perpendicular <110> directions in the (001) plane. The directions of the MDs correspond to those of the crosshatch lines, thus indicating the possibility of a correlation between them. XTEM analyses showed different MD distributions for the two types of Ge composition grading. Linear grading results in a 'continuous' distribution of the MDs through the depth of the virtual substrate, whilst step grading results in the grouping of the MDs at the different steps of Ge concentration variation. For the same type of grading, the lengths of the MD segments and the MDs densities are different for heterostructures grown under different conditions. Furthermore, the depth (from the free surface) at which the MD segments are encountered varies with the growth parameters. Additionally, XTEM analyses showed that dislocation segments threading through the structures to the free surface (TDs) are present in all the heterostructures studied, being characterised by higher densities in the first set. For the linear-graded heterostructures of the first set, XTEM analyses showed a correspondence between the terminations of TDs and the surface troughs, thus indicating

a possible correlation between the two structural features. Through introducing defect states into the bandgap, which can act as carrier trapping sites or recombination centres, TDs affect device performance and can even contribute to device failure, consequently their density needs to be minimised. The maximum tolerable TD density depends on the various applications (as discussed in Chapter 3, § 3.2.4). The TD density in virtual substrate-based heterostructures is usually expected to determine which device structures are possible and the ultimate level of integration that can be achieved. An estimation of the TD density in the studied heterostructures was obtained from XTEM analyses. However, this type of analysis can only offer a qualitative estimation, because of the reduced area probed, which may also not be the most representative. Attempts to quantify the TD density through disclosure chemical etching coupled with Nomarski DIC microscopy, for better statistical accuracy, have failed despite using various types of etchants for different etching times and different degrees of dilution for each of the etchants. In all cases, the crosshatch pattern was preferentially etched and consequently, the TD terminations could no longer be resolved from the crosshatch. PVTEM was also used to quantify the TD density, but it did not prove very successful either. XTEM analyses were carried out on all the heterostructures, whilst PVTEM were carried out only on the structures of the first set. Bright-field imaging in different two-beam conditions was used to study the defects present. XTEM also allowed measurements of thicknesses of the different layers incorporated in the analysed structures. The thickness values obtained for the test set from XTEM results were compared with the values estimated through interpolation from the SIMS results obtained on the calibration structures, which are presented in Table 1 and subsequently used for further growth calibration. XTEM results on surface feature height for the test set were also compared with AFM line analysis results for confirmation, because AFM results can be strongly dependent on the area scanned and the acquisition conditions used (as shown in Chapter 5, § 5.2).

The experimental results obtained on the first set (test set) of heterostructures enabled us to draw conclusions regarding the effects of the growth temperature, the initial and final Ge content, the Ge concentration gradient and grading profile (i.e. linear and stepwise) in the virtual substrate and of the capping layer thickness, on the surface morphology and defects of these structures. Additionally, they prove very useful for further growth calibration. These results also showed that neither Nomarski contrast coupled with disclosure chemical etch, or PVTEM can be successfully used for TD density quantification. Based on these results, all the heterostructures of the second set were

grown at the same temperature and emphasis was placed on the step grading of the Ge concentration in the virtual substrate. Consequently, five different step-graded and only one linear-graded virtual substrates were incorporated in the heterostructures grown as part of the second set. The effects of the presence of a microelectronic structure within the capping layer, of the thickness of the capping layer and of the Ge concentration gradient in the virtual substrate, on the structural properties of the SiGe heterostructures incorporating step-graded virtual substrates grown by SUMC-LPCVD were mainly studied for the second set of heterostructures. Further comparisons between the effects of step and linear grading of the Ge composition in the virtual substrate were carried out. Additionally, a check of the growth reproducibility for these types of SiGe heterostructures was carried out, by repeating the step-graded heterostructure grown as part of the first set, in the second set. Furthermore, only Nomarski DIC microscopy, AFM and XTEM analyses were used for the characterisation of the second set of heterostructures.

The surface morphologies of both sets of heterostructures were additionally studied, at the author's request, by Dr. Patrick McNally and co-workers from Dublin City University, using total reflection X-ray topography (TRXT). Results obtained are not presented herein. Some of them (obtained on the first set of heterostructures) have already been published (List of Publications, page xxiv). Other results (obtained on the second set of heterostructures) are still being analysed. Furthermore, the degree of relaxation that characterises the heterostructures of the second set was studied, at the author's request, by Dr. Patrick McNally and co-workers from Dublin City University, and Dr. Tatiana Perova and co-workers from Trinity College Dublin, using high resolution micro-Raman spectroscopy. The final results obtained will be presented at the 4th International Conference on Materials for Microelectronics and Engineering (10-12 June 2002) Espoo, Finland. Preliminary results show a total relaxation of the virtual substrate in the heterostructures analysed.

6.2. FIRST SET OF HETEROSTRUCTURES

6.2.1. OBJECTIVES

The first set of heterostructures was used as a test set. It consists of two structures *720* and *775*, characterised by a linear variation of the Ge concentration in the virtual substrate, and one structure denominated *774*, grown under identical conditions with *775* and characterised by a step variation of the Ge concentration in the virtual substrate. The growth parameters varied for the first set of heterostructures are:

- For the virtual substrate: the growth temperature (**800°C** for *720* and lower, **750°C** for *775* and *774*), the initial Ge concentration value (**13%** for *720* and lower, **12%** for *775* and *774*), which resulted in an initial lattice misfit (≈ **0.0056** for *720* and ≈ **0.0050** for *775* and *774*), the Ge concentration gradient (≈ **16% / μm** for *720* and steeper, ≈ **22%/μm** for *775*) and the type of grading of the Ge concentration (linear in *720* and *775* and in **5 steps** of **6%** Ge concentration in *774*);
- For the capping layer: thickness (≈ **0.30 μm** for *720* and thinner, ≈ **0.24 μm** for *775* and *774*).

All structures of the first set are characterised by the same final value of the Ge concentration in the virtual substrate, i.e. ≈ **42%** and were grown using the same gas sources (no change of gas bottles occurred between the three growth processes).

The effects of the growth parameters described above and of the two different types of Ge concentration grading in the virtual substrate (linear versus stepwise) on the surface morphology and defect content of the heterostructures of the first set were analysed using the methods described in Chapter 5. Firstly, the results obtained on the linear-graded structures of the first set are presented comparatively. Secondly, the results obtained on the step-graded heterostructure of the first set are shown and compared to the results obtained on the linear-graded heterostructure grown under identical conditions.

Finally, the results are summarised and discussed and conclusions are drawn.

6.2.2. FIRST SET: LINEAR-GRADED HETEROSTRUCTURES

6.2.2.1. Optical microscopy: Nomarski DIC analysis

Nomarski DIC microscopy studies were carried out on an Olympus BHSM-313L microscope with Nomarski DIC attachments for the incident light, the principle of which is described in Chapter 5, § 5.1.2 and represented schematically in Figure 5.1.

Low magnification (x50) Nomarski contrast analyses (Figure 6.1 a) showed that the linear-graded heterostructure of the first set grown at 800°C with an initial Ge content in the virtual substrate of ≈ 13%, a Ge concentration gradient in the virtual substrate of ≈16% / μm and a capping layer of ≈ 0.30 μm, *720*, exhibits large areas of accentuated crosshatch lines (indicated by the red arrows) and only reduced areas of fine, small-scale crosshatch pattern (indicated by the yellow arrows). Analysed under the same conditions, the linear-graded heterostructure of the first set grown at a lower temperature (750°C), with a lower initial Ge content in the virtual substrate (≈ 12%), a higher Ge concentration gradient in the virtual substrate (≈ 22% / μm) and a thinner capping layer (≈ 0.24 μm), *775*, shows by comparison, more extended regions of fine crosshatch pattern (indicated by the yellow arrows in Figure 6.1 b). In both heterostructures, the areas of accentuated crosshatch lines appear randomly distributed.

Higher magnification (x500) Nomarski studies (Figure 6.2) allowed the measurement of the lateral spacing of the crosshatch pattern. Values obtained are similar for the two linear-graded heterostructures of the first set and range from **≤ 1 μm** to **≈ 2 μm** for the fine, small-scale pattern (indicated by the yellow arrows in Figure 6.2 a-b). The accentuated lines (indicated by the red arrows in Figure 6.2 a-b) appear randomly distributed and are spaced by distances ranging from **≤ 5 μm** to **≥ 20 μm**. Additionally, at this magnification, crosshatch lines with a topography similar to that of intersections of clusters of 60° dislocations having the same Burgers vectors (as shown in Chapter 3, Figure 3.12 f) can be observed (blue arrow arrows in Figure 6.2 a-b).

At even higher magnification (x1000) in Nomarski DIC, the accentuated crosshatch lines appear similar for both linear-graded heterostructures of the first set, possibly indicating similar formation mechanisms (Figure 6.3 a-b). Some of the accentuated crosshatch lines run all the way to the edges of the Nomarski micrographs shown in Figures 6.1 - 6.3 a-b, others seem to end at other perpendicular accentuated lines, and others appear to end at

'round' and 'square' shaped features (indicated by the red arrows in Figures 6.3 – 6.4 a-b). These surface features appear to have random distributions in both linear-graded heterostructures of the first set.

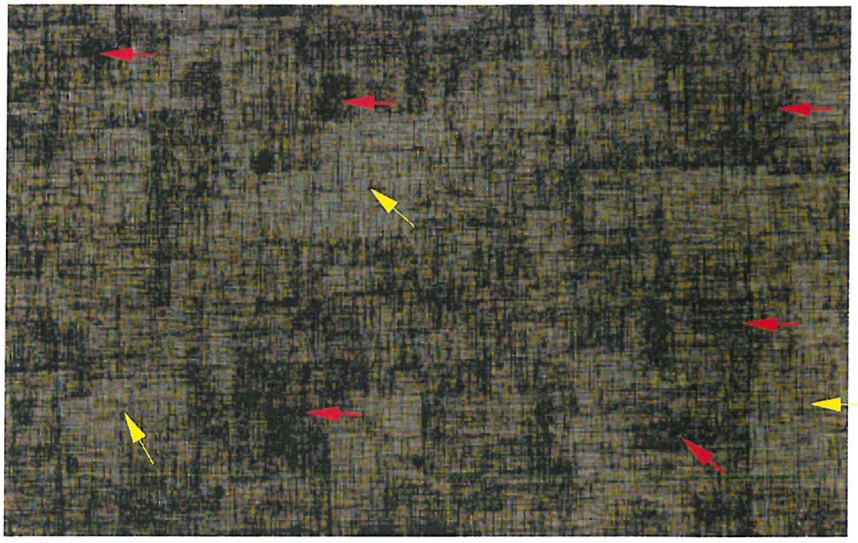

(a)

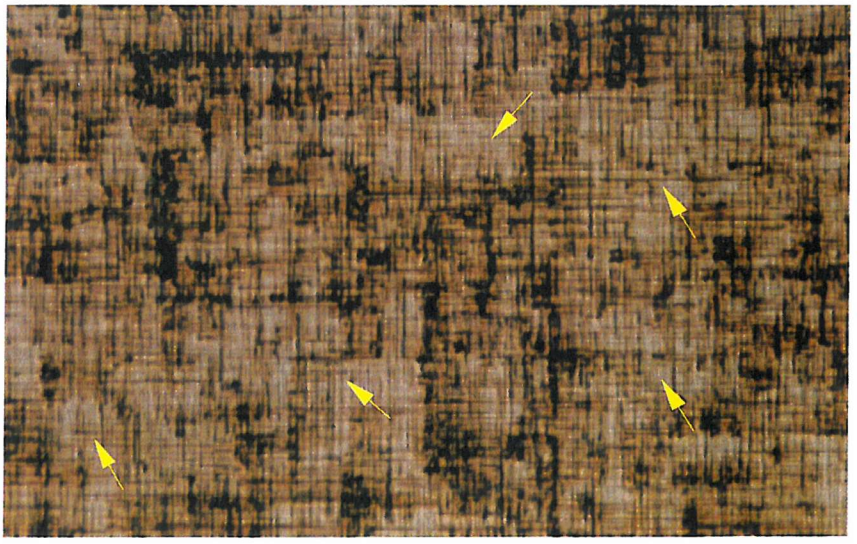

(b)

Figure 6.1. Nomarski micrographs (obtained at x50 magnification) of the two linear-graded heterostructures of the first set: (a) *720*, grown at the higher temperature, with the higher initial Ge content in the virtual substrate, the lower Ge concentration gradient in the virtual substrate and the thicker capping layer, showing a higher density accentuated crosshatch lines (indicated by the red arrows) and reduced areas of fine crosshatch pattern (indicated by the yellow arrows); (b) *775*, grown at the lower temperature, with the lower initial Ge content in the virtual substrate, the higher Ge concentration gradient in the virtual substrate and the thinner capping layer, showing larger areas of fine, regular crosshatch pattern (indicated by the yellow arrows).

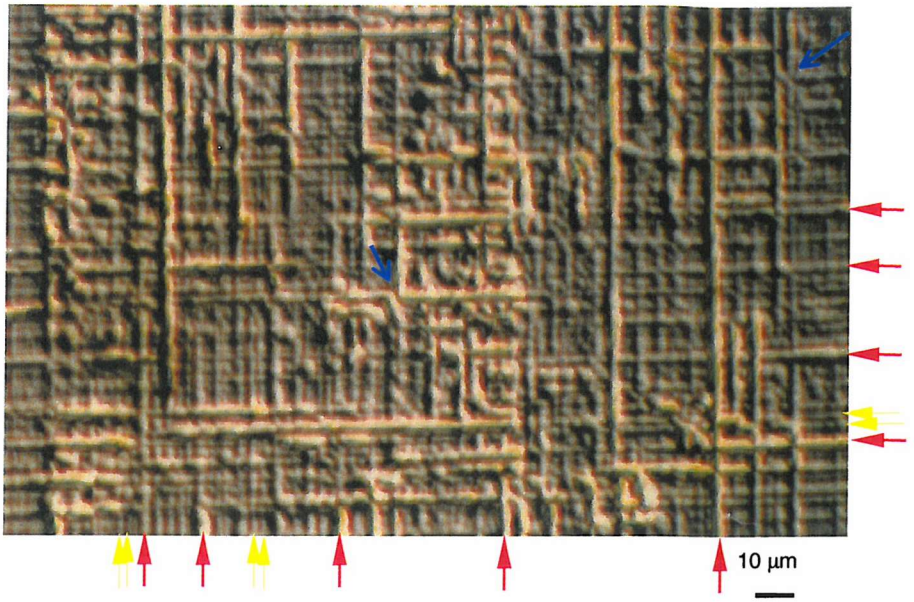

(a)

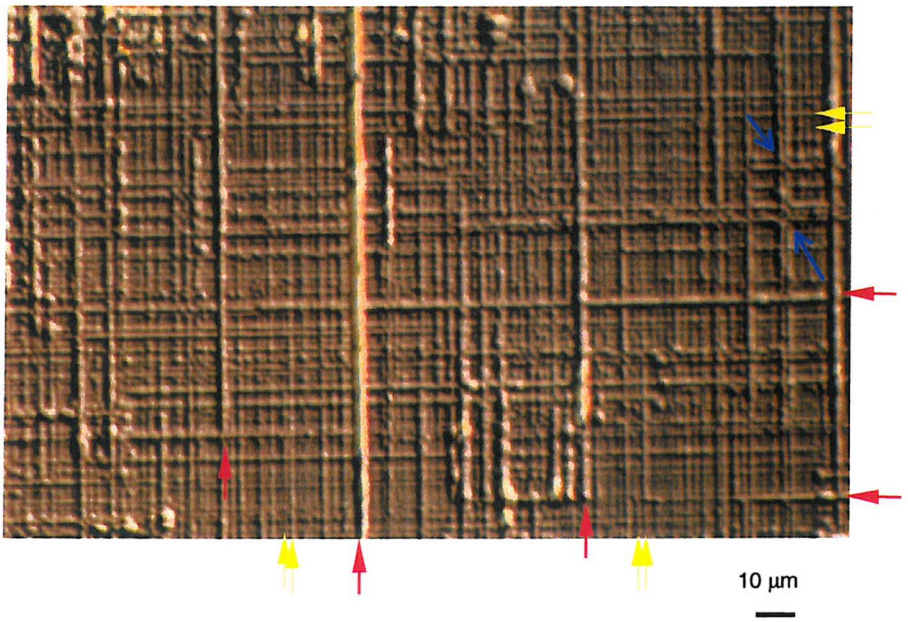

(b)

Figure 6.2. Nomarski micrographs (obtained at x500 magnification) of the two linear-graded heterostructures of the first set: (a) *720* and (b) *775*. Accentuated crosshatch lines are indicated with red arrows, while fine crosshatch lines are indicated with yellow arrows. Blue arrows point to crosshatch lines with a topography similar to that of intersections of clusters of 60° dislocations having the same Burgers vectors shown in Chapter 3, Figure 3.12 f.

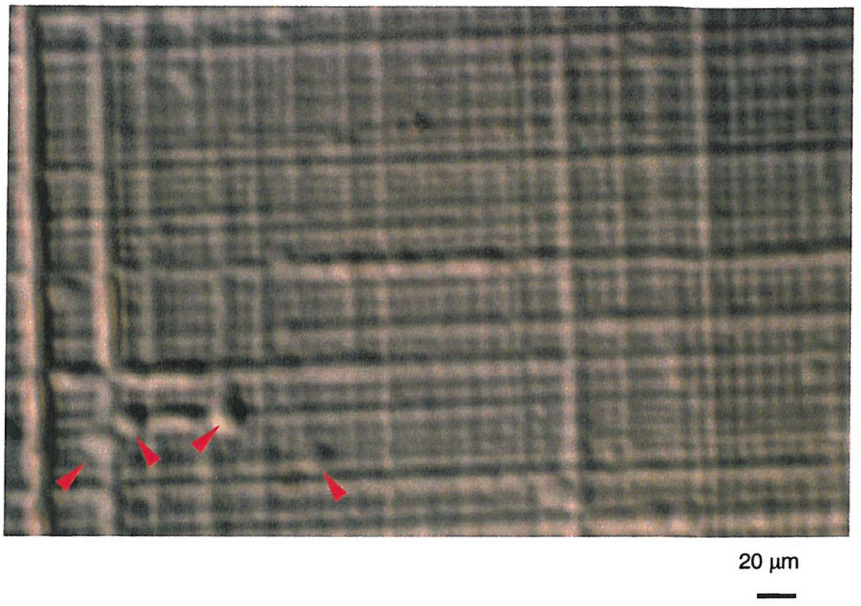

(a)

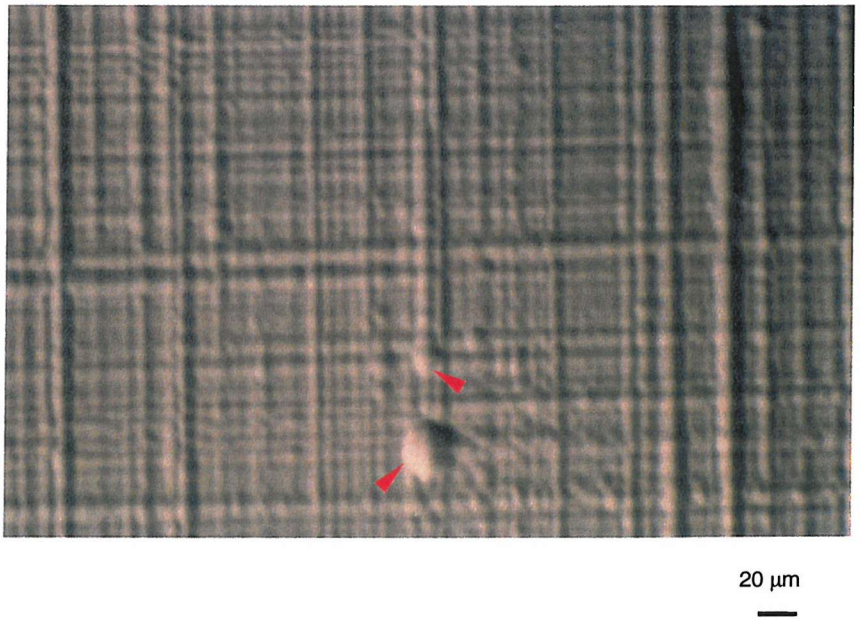

(b)

Figure 6.3. Nomarski micrographs (obtained at x1000 magnification) of the two linear-graded heterostructures of the first set: (a) *720* and (b) *775*. At this magnification, the accentuated crosshatch lines appear similar in the two linear-graded heterostructures. Some of the accentuated crosshatch lines run all the way to the edges of the micrographs, others seem to end at other perpendicular accentuated lines, and others appear to end at 'round'-shaped features (indicated by the arrows).

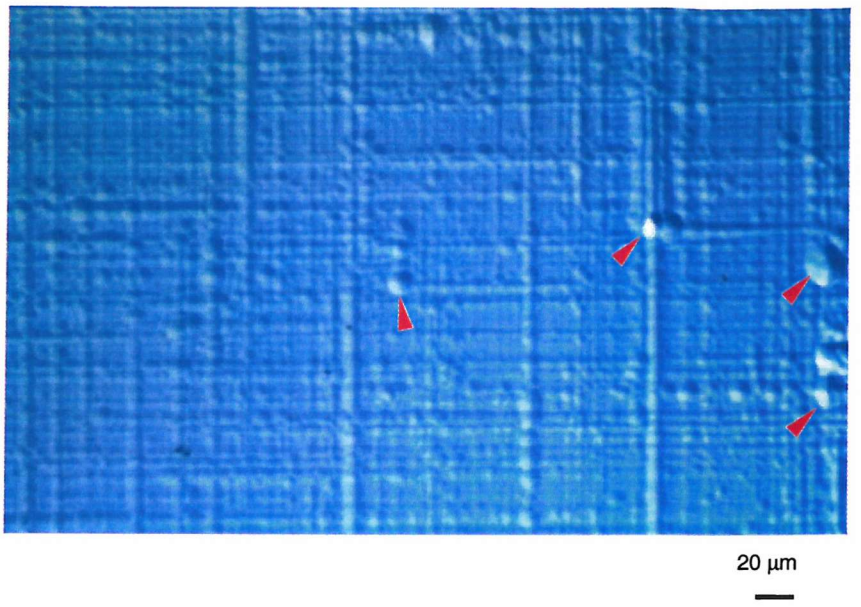

(a)

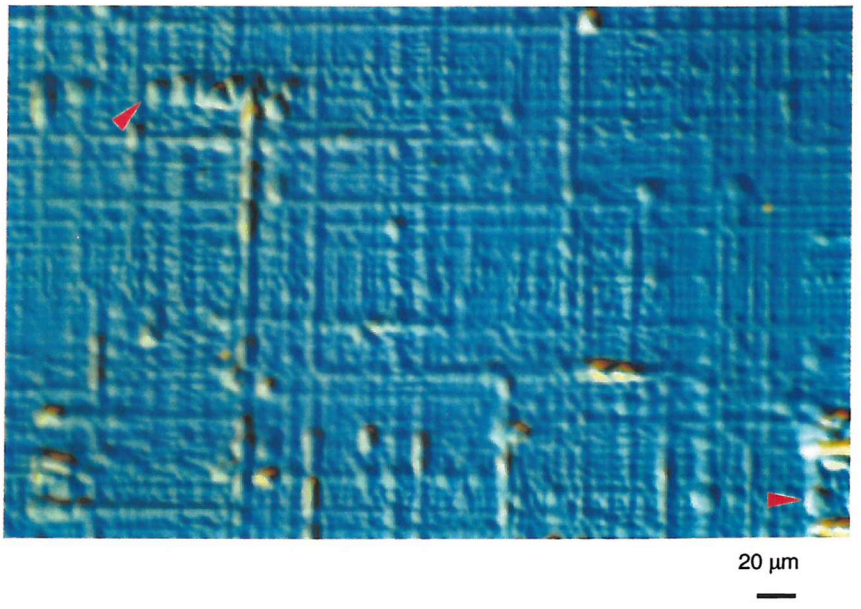

(b)

Figure 6.4. Nomarski micrographs (obtained at x1000 magnification) of the linear-graded heterostructure of the first set, *775*, showing the presence of surface features: (a) 'round-shaped'; (b) 'square-shaped'.

Disclosure chemical etch

Attempts to quantify the TD density by using disclosure chemical etch combined with optical microscopy were made for this study. The types of etchants used, Secco, Dash and Yang are described in Chapter 5, § 5.1.3.

Results obtained showed that all three etchants, independently of their degree of dilution or the etching duration, preferentially etch the crosshatch pattern, thus not allowing us to resolve the emergence of the TDs within the etched crosshatch lines. However, we could decide that the best results were obtained with the Dash etchant (Figure 6.5 a-e), which seemed to be very efficient in disclosing the emergence of dislocations at the edges of the SiGe wafers, where the crosshatch pattern is finer (as indicated by arrows in Figure 6.6 a-b).

(a)

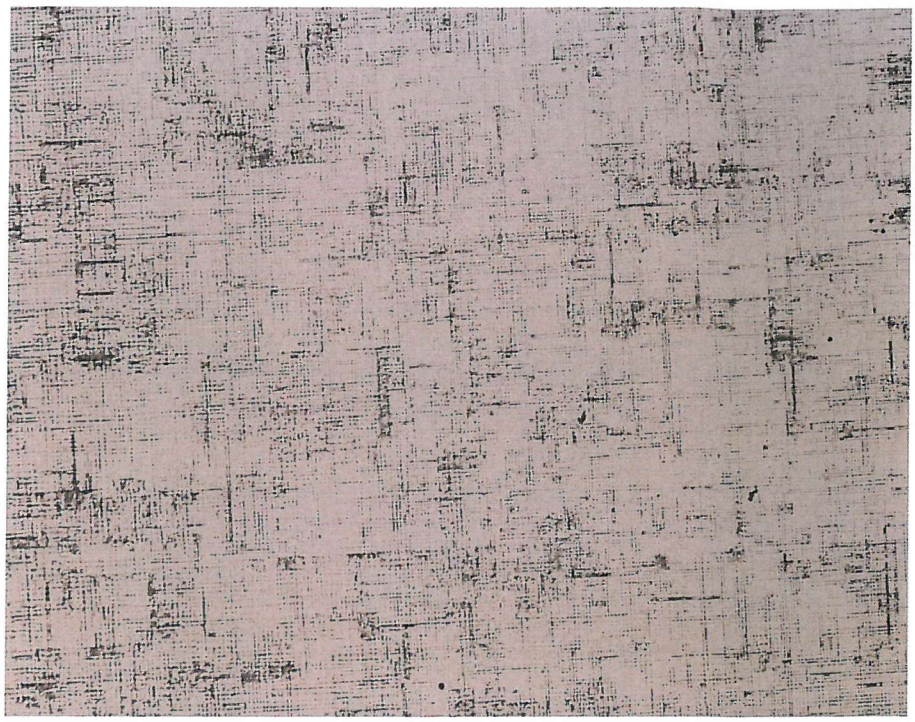

(b)

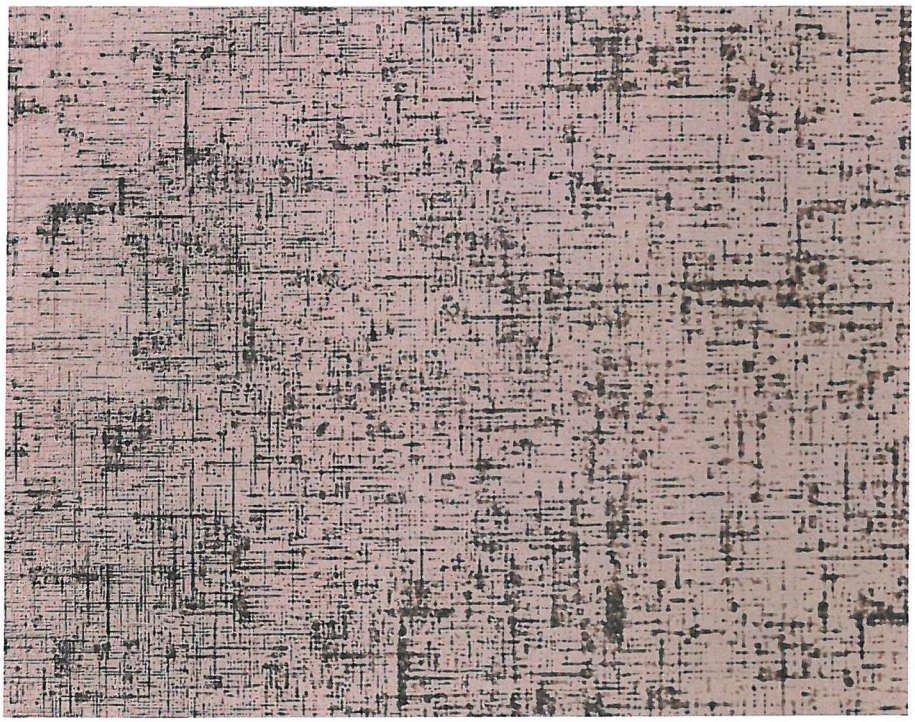

(c)

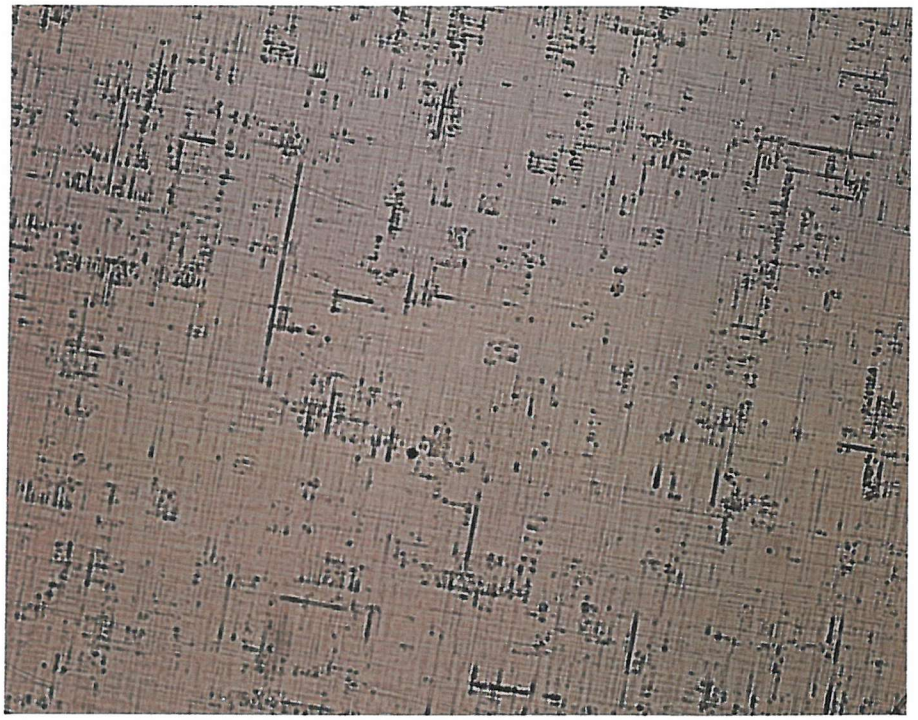

(d)

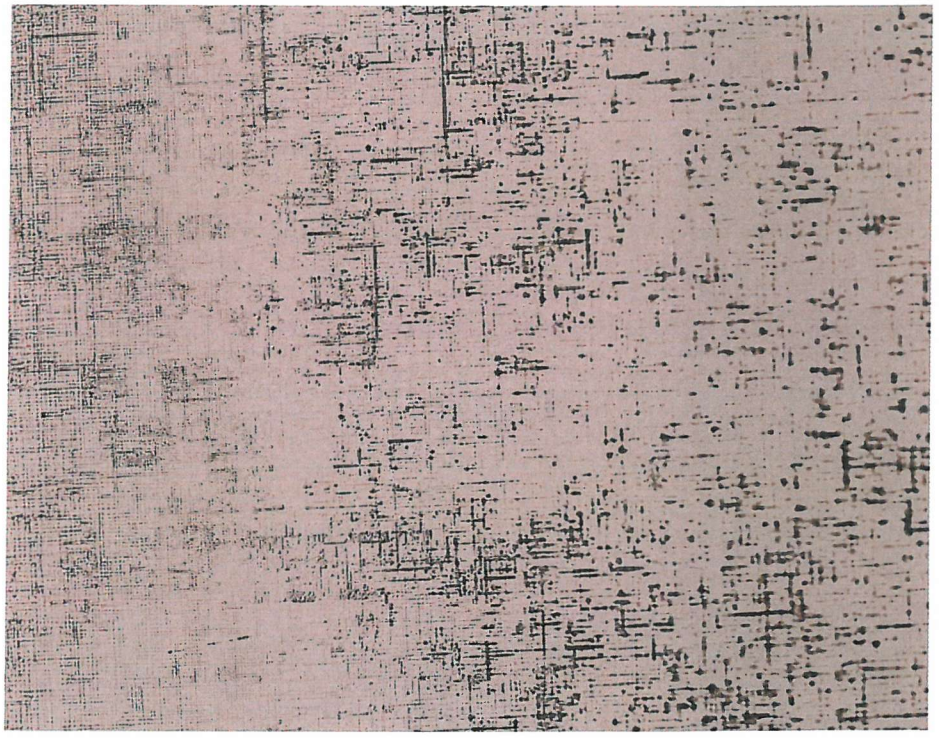

(e)

Figure 6.5. Optical micrographs (obtained at x100 magnification) of the linear-graded heterostructure of the first set, *775*, grown at the lower temperature, with the lower initial Ge content in the virtual substrate, the higher Ge concentration gradient in the virtual substrate and the thinner capping layer: (a) as-grown; Dash-etched for: (b) 50 s, (c) 55 s, (d) 60 s and (e) 65 s. The last four micrographs show the preferential etching of the crosshatch pattern and the inability to resolve the TD terminations within the crosshatch lines.

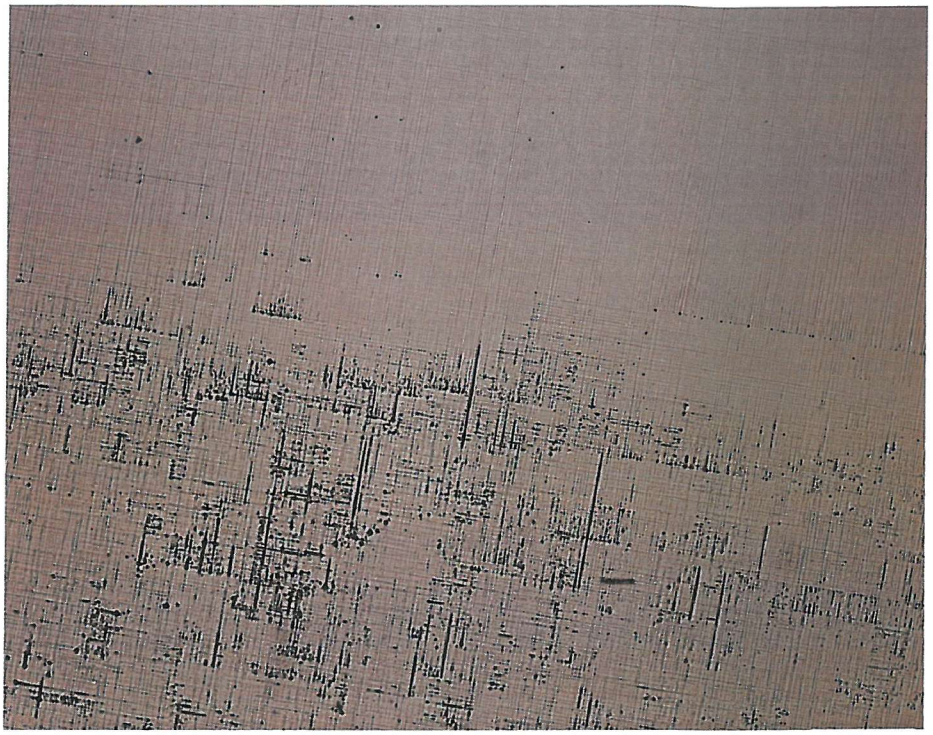

(a)

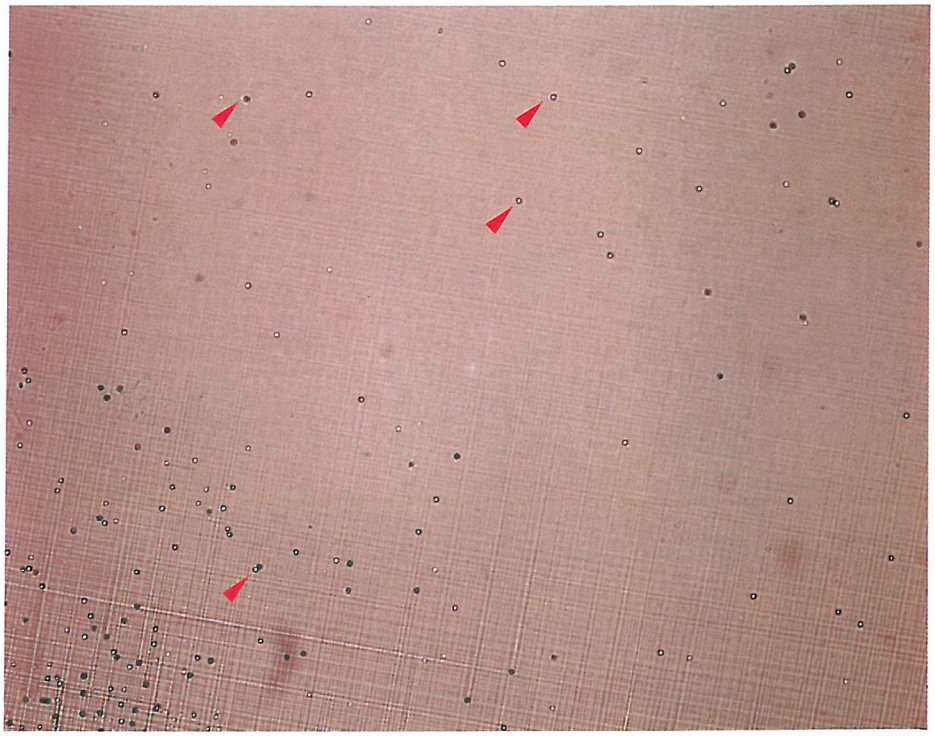

(b)

Figure 6.6. Optical micrographs (obtained at x100 magnification) of the linear-graded heterostructure of the first set, *775*, Dash-etched for 60 s: (a) shows the change in the crosshatch pattern, which occurs towards the edges of the wafer, where the pattern becomes finer; (b) shows the edge of the wafer, with clearly defined etch pits (indicated by the red arrows) caused by the defects present.

6.2.2.2. First set: linear-graded heterostructures Scanning probe microscopy: AFM analysis

AFM analyses were carried out on a TopoMetrix Accurex II^{TM} scanning probe microscope, the principle of which is described in Chapter 5, § 5.2.2. A 100 μm scanner and the ThermoMicroscopes 1520-00 pyramidal silicon nitride probes characterised by a 4μm base, a 4 μm height and a < 50 nm tip radius (Figure 5.4 b) were used. Images were acquired using the contact mode and the 'Topography Forward' method described in Chapter 5, § 5.2.4.1 and § 5.2.5. Image analyses were performed using the 'Area Analysis', 'Line Analysis' and 'Graphic' routines of the TopoMetrix SPMLab V4.0 software package [65].

The AFM results confirmed some of the surface morphology information already obtained using Nomarski DIC microscopy. Additionally, AFM provided quantitative information related to the surface topography (e.g. values for the RMS of the surface roughness and for depth variation along the crosshatch lines).

The 3D AFM results (Figure 6.7 a-b) showed that both linear-graded heterostructures of the first set exhibit to varying degrees, undulations on their surfaces along two perpendicular <110> directions (i.e. along the crosshatch lines observed in Nomarski contrast). AFM analyses revealed that the accentuated crosshatch lines observed in Nomarski correspond to trenches (i.e. lines of somewhat increased depth) in both linear-graded heterostructures of the first set. Furthermore, 3D AFM images outlined the regularity (periodicity) of the fine (shallow) crosshatch lines compared to the random distribution of the trenches. The density of trenches appears to be higher in the linear-graded heterostructure of the first set grown at the higher temperature, with the higher initial Ge composition in the virtual substrate, the lower Ge concentration gradient in the virtual substrate and the thicker capping layer, *720* (red arrows in Figure 6.7 a), by comparison with the same size of scanned area of the other linear-graded heterostructure of the first set, *775* (red arrows in Figure 6.7 b). This observation is consistent with the Nomarski results obtained (§ 6.2.2.1). Lateral spacing for the crosshatch lines obtained from AFM analysis are also consistent with the ones obtained from Nomarski microscopy, showing values of ≈ **a few microns** for the fine pattern, whilst the trenches are spaced by larger distances ≥ **15 μm**. Additionally, the 3D AFM results (Figure 6.7 a-b) show that the crosshatch lines of the sample *720* are characterised by a high density of small (in-plane

size) crests and troughs compared to the crosshatch lines of sample *775*, which appear as longer running ridges.

The RMS of the surface roughness values are dependent on the acquisition conditions used and the area scanned, as can be seen in Figure 6.8 a-b for the linear-graded heterostructure of the first set, *720*, and in Figure 6.9 a-b for the other linear-graded heterostructure of the first set, *775*. The acquisition conditions used for the 2D AFM images presented are also shown in these figures. The AFM images shown in Figures 6.8 - 6.9 were obtained using the same image analysis routine from the software package (2^{nd} order 2D levelling [65]) and the RMS values given are for the whole area of the acquired image. Results obtained show that for a 100 μm x 100 μm scanned area, the RMS of the surface roughness value for the sample *720* (**≈ 91.8 nm**, as shown in Figure 6.8 a) is almost three times higher than for the sample *775* (**≈ 35.6 nm**, as shown in Figure 6.9 a). The 2D image of the heterostructure *775* (shown in Figure 3.9 b) reveals the presence of a large square (rectangular)-shaped feature along one of the crosshatch trenches (indicated by the arrow).

Results of the height variation measurements carried out along the crosshatch lines for the two linear-graded heterostructures of the first set are shown in Figure 6.10 a-b. Height variation analysis along the crosshatch trenches revealed the presence of pits (i.e. undulations of somewhat increased depth) and enabled the measurement of their size (in the growth plane) and their depths (Figure 6.11 a-b). Results presented in Figures 6.10 - 6.11 show that the pit depths are similar for the two linear-graded heterostructures studied ranging from **≈ 6 nm** to **≈ 250 nm**. Figure 6.11 b indicates that the largest pits (in-plane dimension of **≈ 3 μm**) are also the deepest (up to **≈ 250 nm**) thus running all through the capping layer of the heterostructure *775*. The black arrows on the 3D images also point to pits along the trenches (Figure 6.7 a-b). Both 2D and 3D AFM images of the linear-graded heterostructures of the first set show that some of the large pits are pyramidal shaped. For the same size of scanned area, a higher density of trenches and pits can be observed in *720* compared to *775*. This observation together with the one indicating that *720* is also characterised by a higher density of smaller crests and troughs aligned along the crosshatch lines by comparison with *775*, which shows long running ridges (Figure 6.7 a-b) justify the higher RMS of the surface roughness value obtained for *720* compared with *775*.

Overall, AFM results showed that the linear-graded heterostructure of the first set, *775*, grown at the lower temperature and with the lower initial Ge composition in the virtual substrate, independently of its higher Ge concentration gradient in the virtual substrate and its thinner capping layer, is characterised by superior surface quality (flatter, more uniform surface, with a lower RMS of the surface roughness) compared to the heterostructure grown at the higher temperature, with the higher initial Ge content in the virtual substrate and despite its lower Ge concentration gradient in the virtual substrate and its thicker capping layer, *720*.

Some of the AFM results obtained for the first set of heterostructures are also presented in Table 3.

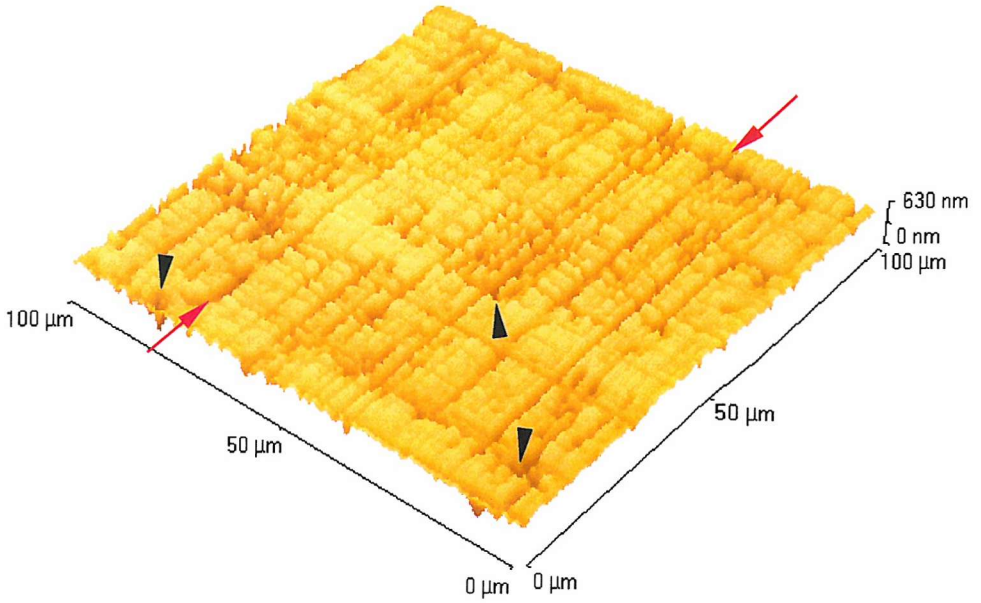

(a)

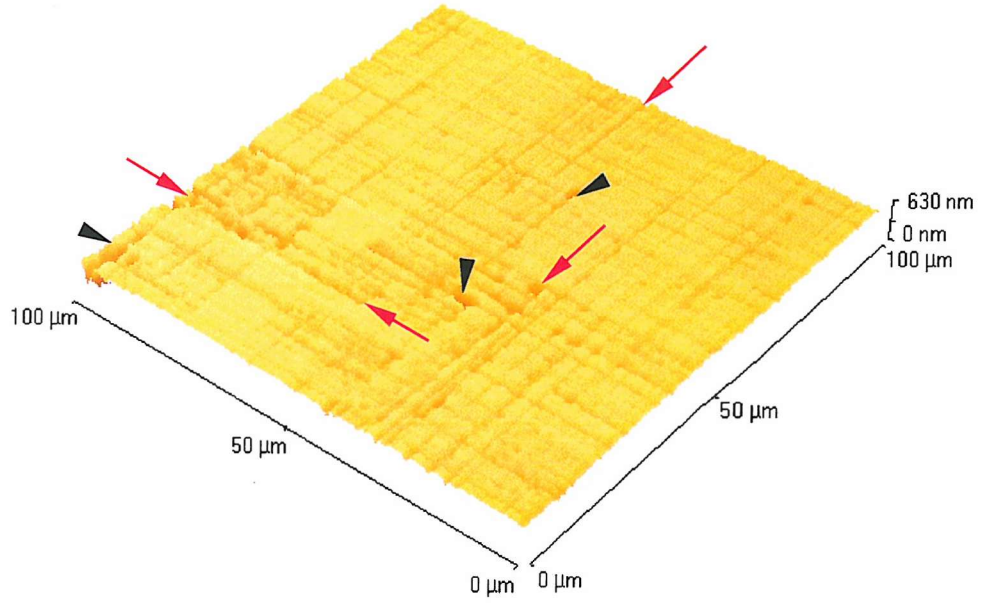

(b)

Figure 6.7. 3D AFM images of 100 µm x 100 µm scanned areas of the two linear-graded heterostructures of the first set: (a) *720*, grown at the higher temperature, with the higher initial Ge content in the virtual substrate, the lower Ge concentration gradient in the virtual substrate and the thicker capping layer, showing short-range crests and troughs aligned along the two perpendicular <110> directions, which create a rough surface; (b) *775*, grown at the lower temperature, with the lower initial Ge content in the virtual substrate, the higher Ge concentration gradient in the virtual substrate and the thinner capping layer, showing longer ridges aligned along the two perpendicular <110> directions, which create a smoother surface. The red arrows indicate the presence of trenches, with a higher density in *720* compared to *775*. The black arrows point to pits along the trenches, which also have a higher density in *720* compared to *775*.

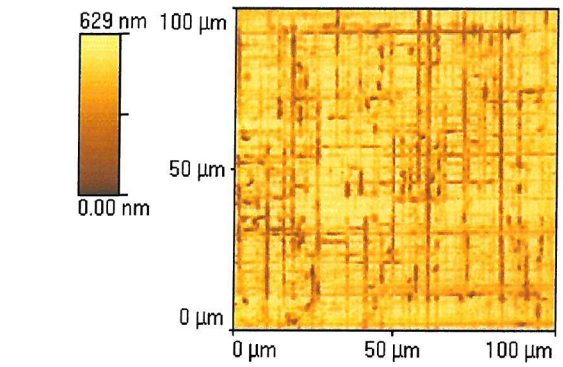

Version	v4.00
Date/Time	11/07/0 12:59:29
Description	720c 100x 50/s 200 +1
Data Offset	2112
Stage Type	Accurex II Analytical
Probe Type	AFM
Scanner SerialNum	X509603
Experiment Type	Plane Image
Data Type	Height
Calibration Type	System Calibration
Z Gain	High
Image Size	100 µm x 100 µm
Image Resolution	200 x 200 pixels
Data Range	0, 3346
Scan Rate	50 µm/s
Scan Direction	Forward
Rotation	1.17 degrees
PID Settings	1.175 0.770 0.020
Relative Set Point	1 nA
Sample Bias	0.00 mV

Whole Image

Area Ra:	69.3346 nm
Area RMS:	91.7659 nm
Avg. Height:	437.9544 nm
Max. Range:	629.0088 nm

(a)

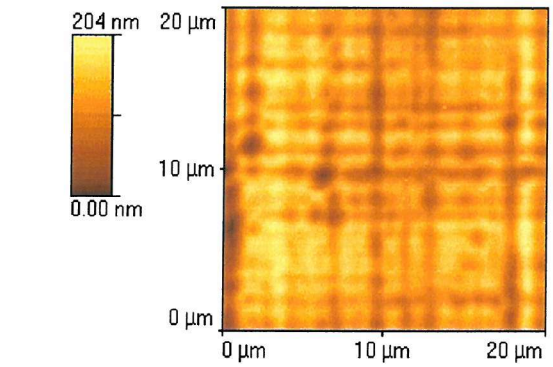

Version	v4.00
Date/Time	11/07/0 17:58:41
Description	720c 20x 10/s 200 +1levelled
Data Offset	2112
Stage Type	Accurex II Analytical
Probe Type	AFM
Scanner SerialNum	X509603
Experiment Type	Plane Image
Data Type	Height
Calibration Type	System Calibration
Z Gain	High
Image Size	20 µm x 20 µm
Image Resolution	200 x 200 pixels
Data Range	0, 1086
Scan Rate	10 µm/s
Scan Direction	Forward
Rotation	0.58 degrees
PID Settings	1.250 0.765 0.030
Relative Set Point	1 nA
Sample Bias	0.00 mV

Whole Image

Area Ra:	21.3384 nm
Area RMS:	27.3414 nm
Avg. Height:	124.8575 nm
Max. Range:	204.1553 nm

(b)

Figure 6.8. 2D AFM images, scan parameters and the RMS of the surface roughness values for the linear-graded heterostructure of the first set, *720*, for a: (a) 100µm x 100µm scanned area, with a scan rate of 50 µm/s; (b) 20 µm x 20 µm scanned area, with a scan rate of 10 µm/s.

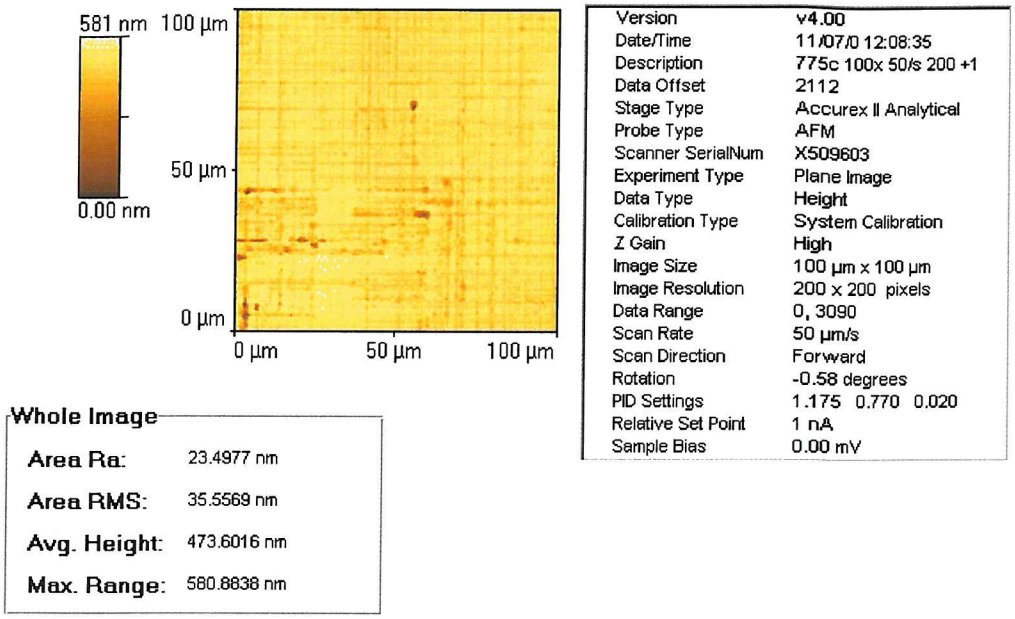

(a)

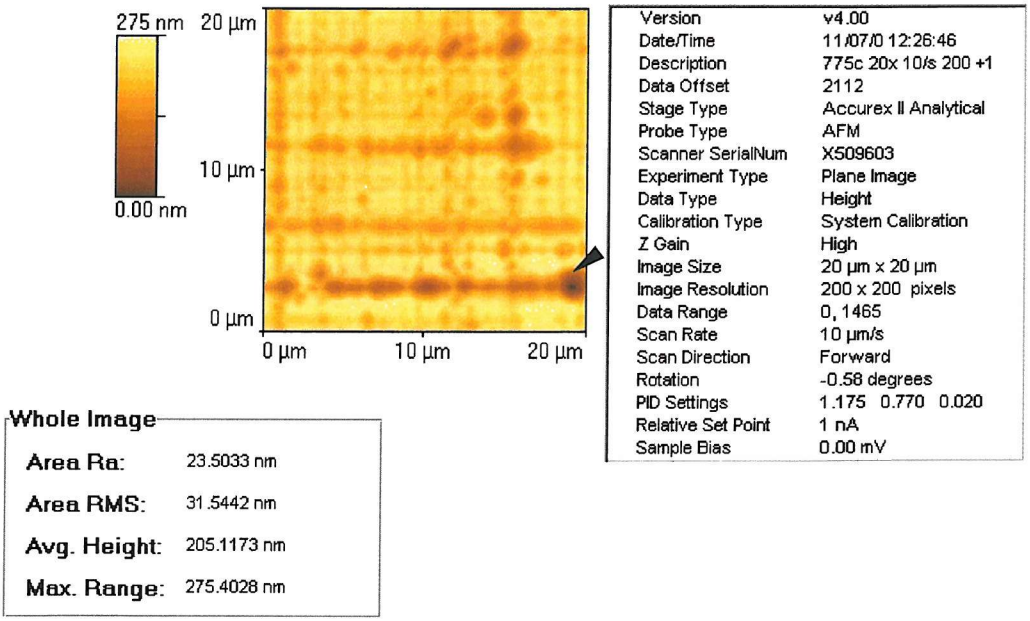

(b)

Figure 6.9. 2D AFM images, scan parameters and the RMS of the surface roughness values for the linear-graded heterostructure of the first set, *775*, for a: (a) 100µm x 100µm scanned area, with a scan rate of 50 µm/s; (b) 20 µm x 20 µm scanned area, with a scan rate of 10 µm/s. The arrow points to a pyramidal-shaped pit.

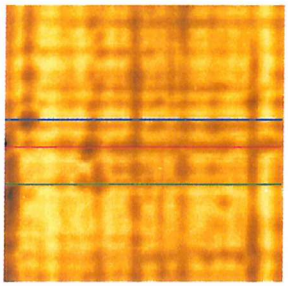

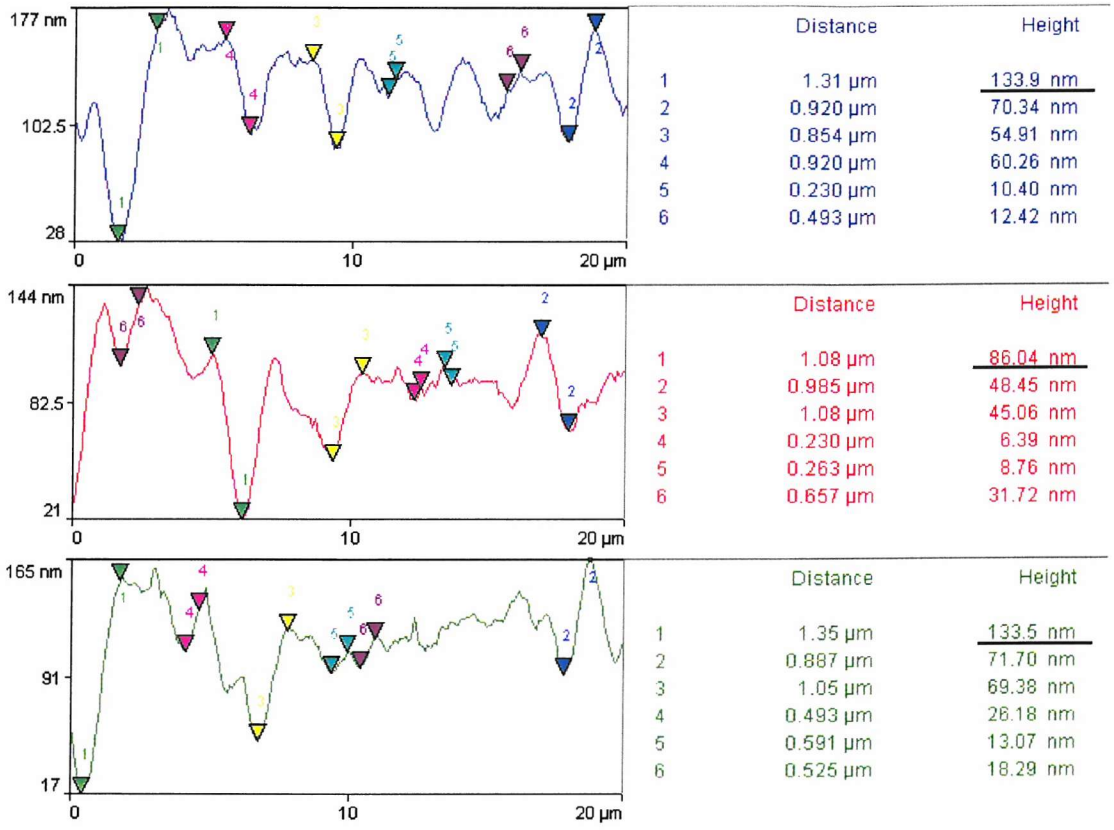
177 nm
102.5
28
0
10
20 µm
Distance
Height
1 1.31 µm 133.9 nm
2 0.920 µm 70.34 nm
3 0.854 µm 54.91 nm
4 0.920 µm 60.26 nm
5 0.230 µm 10.40 nm
6 0.493 µm 12.42 nm
144 nm
82.5
21
0
10
20 µm
Distance
Height
1 1.08 µm 86.04 nm
2 0.985 µm 48.45 nm
3 1.08 µm 45.06 nm
4 0.230 µm 6.39 nm
5 0.263 µm 8.76 nm
6 0.657 µm 31.72 nm
165 nm
91
17
0
10
20 µm
Distance
Height
1 1.35 µm 133.5 nm
2 0.887 µm 71.70 nm
3 1.05 µm 69.38 nm
4 0.493 µm 26.18 nm
5 0.591 µm 13.07 nm
6 0.525 µm 18.29 nm

(a)

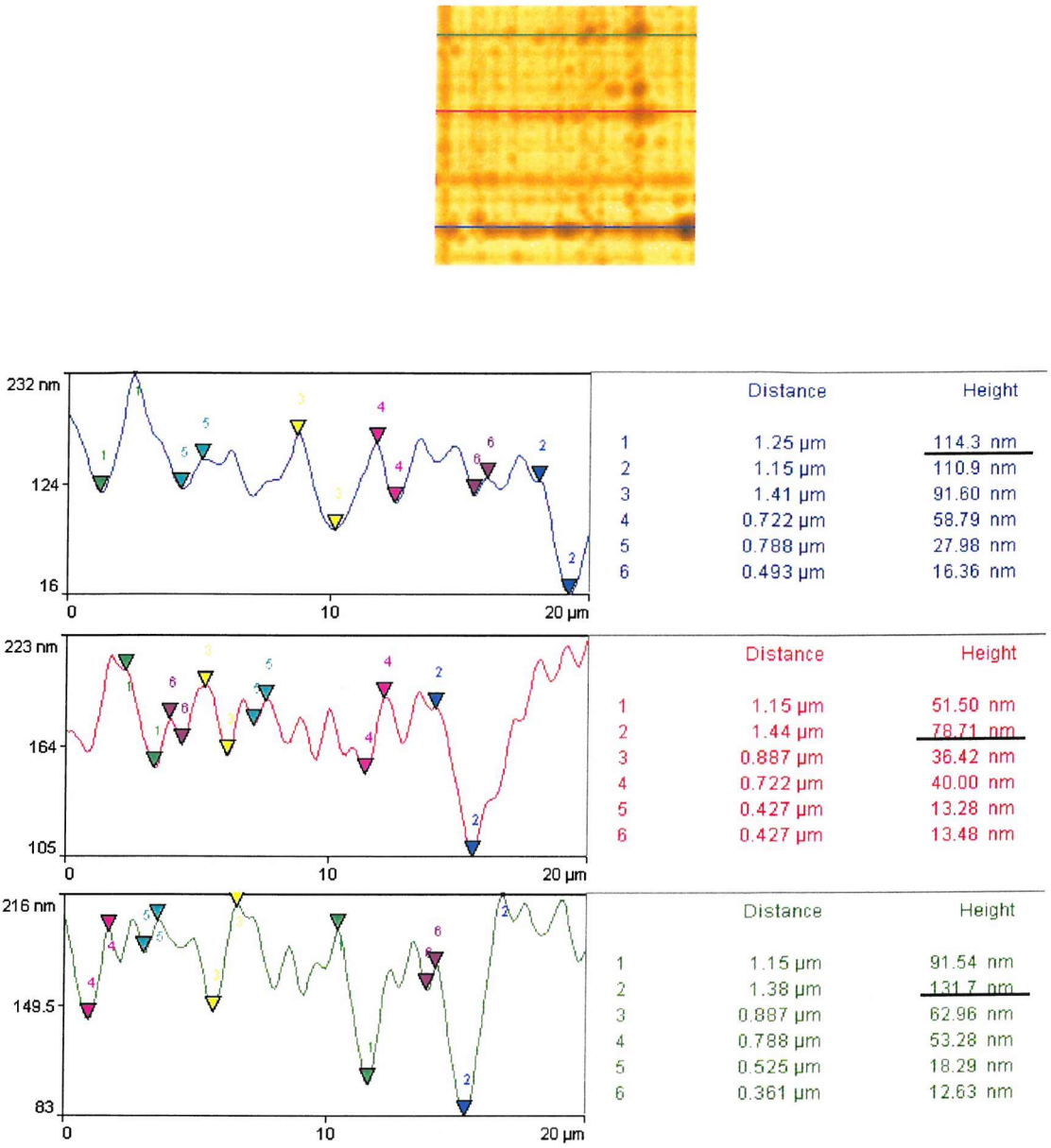

(b)

Figure 6.10. 2D AFM images of 20 µm x 20 µm scanned areas and line analysis results for: (a) the linear-graded heterostructure of the first set, *720*; (b) the linear-graded heterostructure of the first set, *775*. The underlined values correspond to the deepest pits.

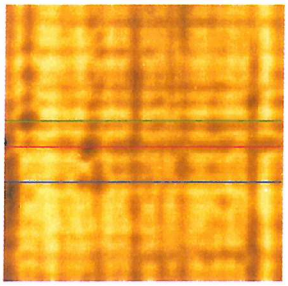

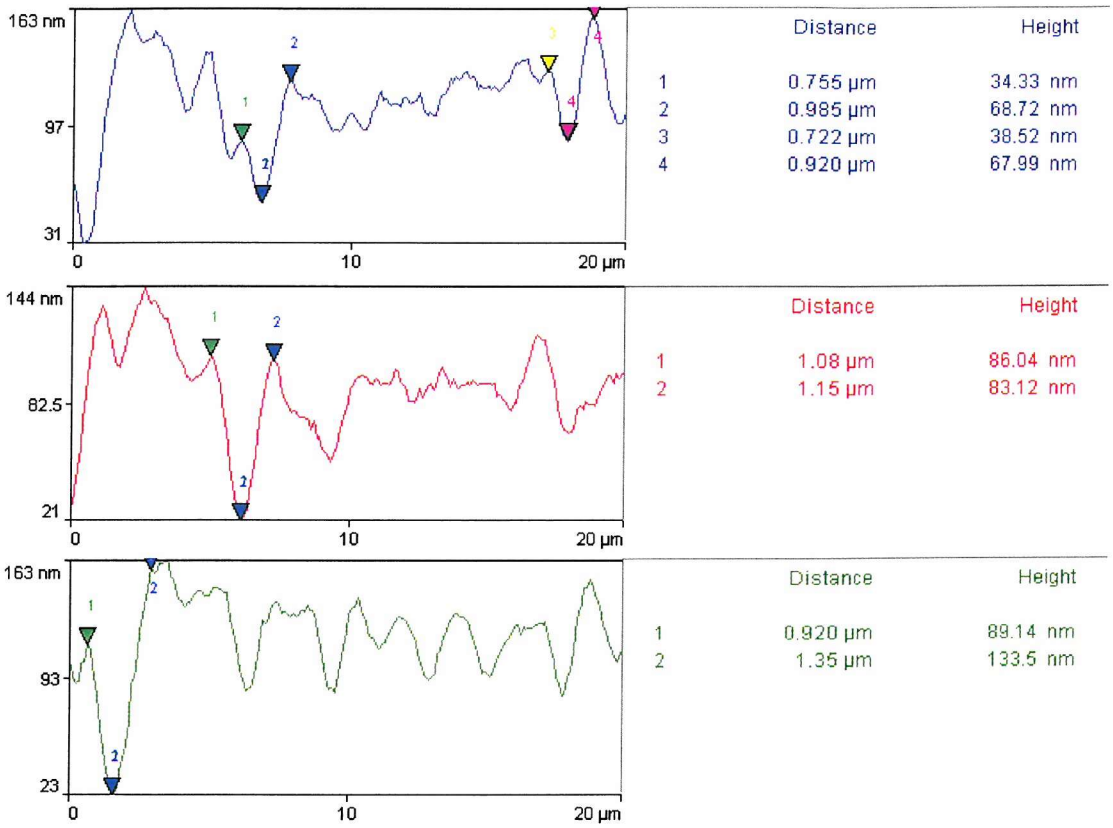
163 nm
97
31
0
10
20 µm
Distance
Height
1 0.755 µm 34.33 nm
2 0.985 µm 68.72 nm
3 0.722 µm 38.52 nm
4 0.920 µm 67.99 nm
144 nm
82.5
21
0
10
20 µm
Distance
Height
1 1.08 µm 86.04 nm
2 1.15 µm 83.12 nm
163 nm
93
23
0
10
20 µm
Distance
Height
1 0.920 µm 89.14 nm
2 1.35 µm 133.5 nm

(a)

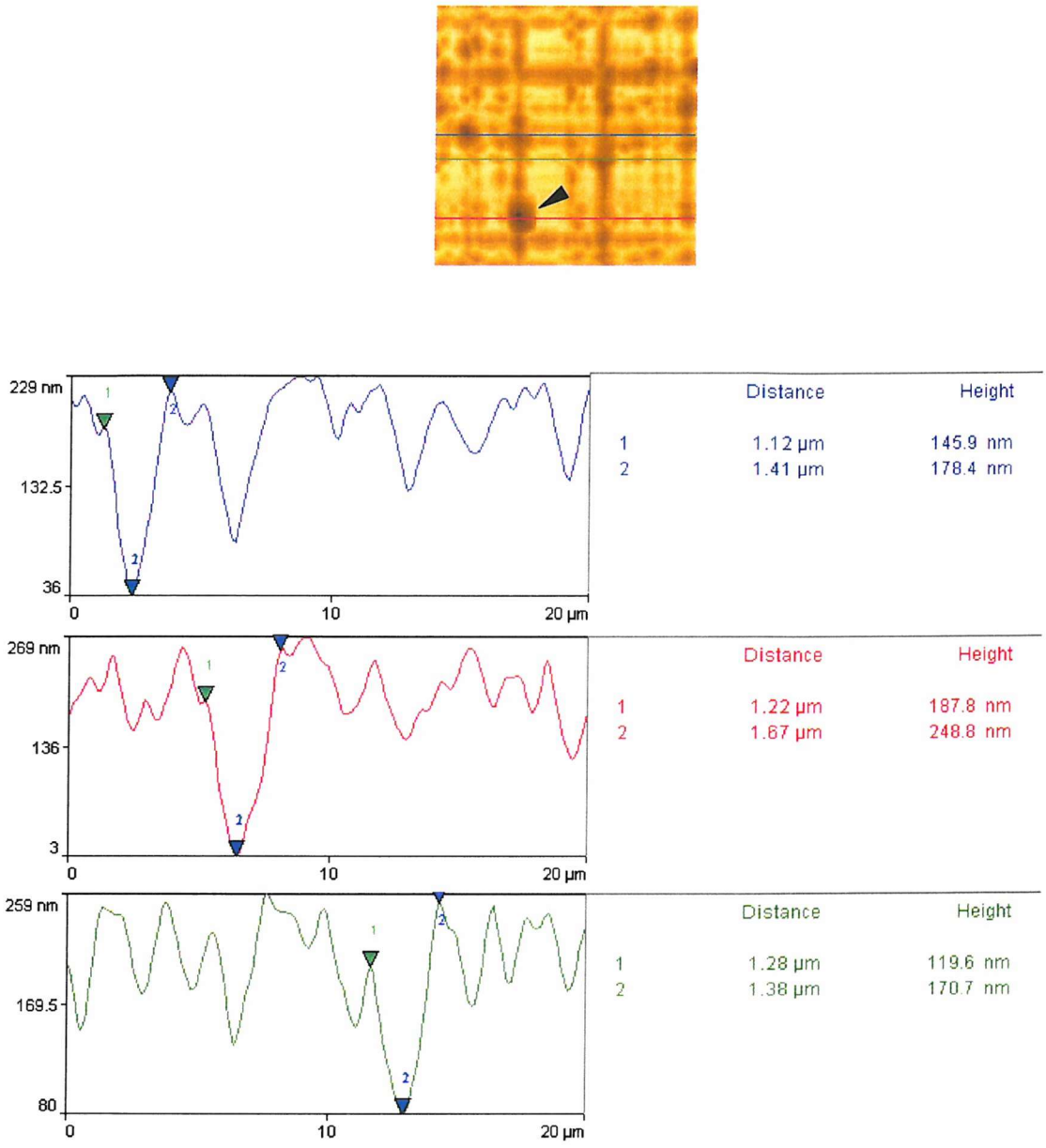

(b)

Figure 6.11. 2D AFM images of 20 µm x 20 µm scanned areas and line analysis results obtained from measuring the in-plane size and the depth of the deepest pits present along the crosshatch trenches in the two linear-graded heterostructures of the first set: (a) *720* and (b) *775*. The arrow points to a pyramidal-shaped pit.

6.2.2.3. First set: linear-graded heterostructures Electron microscopy: TEM analysis

TEM analyses were carried out on a J.E.O.L. JEM 2000FX transmission electron microscope (Figure 5.6) using the double-tilt sample holder (Figure 5.5). A tungsten filament with an applied beam acceleration voltage of 200 kV and the largest spot size (for the highest brightness) was used to analyse the two linear-graded heterostructures of the first set. The information on the defect content of the analysed heterostructures provided by TEM analyses was not obtainable using any of the other techniques, the results of which are presented in the previous two sections (§ 6.2.2.1 – 6.2.2.2). Thus TEM complemented the Nomarski DIC microscopy and AFM techniques, at the same time as confirming some of their results.

Cross-sectional samples were analysed in bright-field using different two-beam conditions, in order to select the best analysis settings and carry out dislocation analyses, as explained in Chapter 5, § 5.3.3 – 5.3.4. The XTEM micrographs presented in Figure 6.12 for the linear-graded heterostructure of the first set grown at the higher temperature, with the higher initial Ge concentration in the virtual substrate, the lower Ge concentration gradient in the virtual substrate and the thicker capping layer, *720* and in Figure 6.13 for the linear-graded heterostructure of the first set grown at the lower temperature, with the lower initial Ge concentration in the virtual substrate, the higher Ge concentration gradient in the virtual substrate and the thinner capping layer, *775*, were obtained using the main beam condition.

The XTEM micrographs shown in Figures 6.12 – 6.13 reveal the presence of a dark layer at the Si substrate-SiGe heterostructure interface (indicated by the pink arrows), which from comparisons with the SIMS results obtained on the calibration layers and other SUMC-LPCVD layers, was identified as being a carbon layer, with typical concentrations in the range $\approx$ **$5x10^{18}$ - $5x10^{19}$ atoms/cm^3**. The micrographs presented in Figures 6.12 – 6.15, show that most defects do not appear to form at the carbon layer, some defects do not even reach the layer, whilst others extend beyond it, into the Si substrate. By growing the Si layer, which precedes the growth of the SiGe heterostructure the carbon layer was buried and consequently prevented from acting as a heterogeneous source for dislocation nucleation. No obvious contribution of the carbon layer to misfit strain relaxation can be observed.

The interfacial defects in both linear-graded heterostructures of the first set (Figures 6.12 – 6.15) appear similar. Some loops run deeply into the Si substrate (≥ **1 μm**) on **{111}** type planes like in the MFR dislocation multiplication process (described in Chapter 3, §3.2.3.5). The XTEM micrographs of *720*, presented in Figure 6.12, show a random distribution of these deep loops, whilst the top micrograph of *775*, presented in Figure 6.13, shows a more regular distribution of these loops (indicated by the green arrows) that are spaced by distances ranging between ≈ **1 – 3.5 μm**. However, the high density of dislocation nucleation sites [12] does not support the hypothesis on the operation of such a multiplication mechanism in any of these heterostructures. Other interfacial defects common to both linear-graded heterostructures of the first set, consist of loops or loop segments, which intersect, forming V-shaped defects (as can be seen in Figures 6.12 – 6.15).

The two linear-graded heterostructures of the first set show different internal morphologies, as can be seen in the XTEM micrographs presented in Figures 6.12 – 6.13.

The virtual substrate of the heterostructure *720* is characterised by short segments of MDs, which extend well into the capping layer. The virtual substrate of the heterostructure *775* shows long MD segments, well contained within the virtual substrate and thus, leaving the capping layer MD-free.

All XTEM micrographs shown in Figures 6.12-6.13, show a surface rippling effect, which is a structural feature and not an artefact introduced by sample preparation or analysis settings, as justified by the following:

- During ion beam thinning, the glue involved in the XTEM sample preparation is preferentially milled away as already explained in Chapter 5 § 5.3.5. In Figures 6.12 – 6.13, regardless of having thinned the samples enough to provide a good quality TEM image, the glue can still be seen as adhering to the sample surface;
- The sample surface is 'in contrast' over the whole image.

Ripple spacings, measured on the XTEM micrographs of both samples (Figures 6.12 – 6.13), range between ≈ **0.93 - 2.59 μm**, thus in good agreement with the values for the lateral spacing of the fine crosshatch pattern obtained with the other analysis methods (§6.2.2.1 – 6.2.2.2).

The surface rippling of the linear-graded heterostructure *720* (as shown in both XTEM micrographs presented in Figure 6.12) appears much more accentuated than the surface rippling of the other linear-graded structure of the first set, *775* (as shown in both micrographs presented in Figure 6.13). This observation is in good agreement with the surface morphology results obtained using the other characterisation techniques (§ 6.2.2.1 – 6.2.2.2). Figures 6.12 and 6.13 show both the fine surface undulations (indicated by the yellow arrows) and the deep, faceted pits (indicated by the red arrows). Both lower images presented in Figures 6.12 and 6.13, show an almost periodic distribution of the fine surface ripples in both linear-graded heterostructures of the first set (as already observed in AFM). Furthermore, Figures 6.12 and 6.13 show that the fine ripples on the surface of *720* are characterised by steeper sides (with inclinations ranging between **≈ 5° - 12°**) by comparison with the fine surface ripples of the structure *775*, which are characterised by smaller inclination angles (**≈ 2° - 5°**). The deepest pits found in XTEM for the heterostructure *720* (indicated by the red arrows in Figures 6.12, 6.16 a-b) are characterised by in-plane sizes of **≈ 3 μm** (thus in agreement with the AFM results) and depth values ranging between **≈ 300 – 600 nm** (the lower limit being in agreement with the AFM results) and have side facets inclined at **≈ 24° - 30°**, thus possibly corresponding to **{203}** planes. Similar faceted pits (with sides inclined at **≈ 34°**) have been observed by Cullis et al. [41] in the SiGe heterostructures that relax by a surface roughening mechanism. The deepest pits found in XTEM for the heterostructure *775* (indicated by the red arrows in Figures 6.13, 6.17) are characterised by in-plane sizes of **≈ 3 μm** (hence again in agreement with the AFM results) and depth values of **≈ 150 nm** (thus lower than the AFM ones) and have side facets inclined at **≈ 10° - 12°**, thus possibly corresponding to **{105}** planes. Similar facets have been previously observed in the growth of pure Ge 'huts' on Si substrates (described in [1]). All these observations are consistent with those made in AFM, which show that the structure *720* is characterised by a more irregular and rougher surface compared with *775* (§ 6.2.2.2).

RMS of the surface roughness measurements were carried out on the XTEM images for comparison with the AFM results. For the area of sample shown at the bottom of Figure 6.12, a value of **≈ 30 nm** for the RMS of the surface roughness of *720* was obtained. This value is consistent with the AFM value obtained for a similar size area (20 μm x 20 μm), which was **≈ 27 nm** (Figure 6.8 b, Table 3).

For the area of sample shown at the bottom of Figure 6.13, the value obtained for the RMS of the surface roughness of *775* was ≈ **17 nm**, which is also similar with the value obtained by AFM for a similar size area (20 μm x 20 μm), which was ≈ **14 nm** (Table 3).

The RMS of the surface roughness measurements carried out on the XTEM images are influenced by the positioning of the cross-section on the sample, whilst the AFM results are dependant on the area selected to be scanned and the acquisition conditions used. Nevertheless, for the linear-graded heterostructures of the first set, the RMS of the surface roughness values obtained by AFM and XTEM appear consistent and they are higher for the structure *720* compared to *775*.

The presence of TDs can be observed in all XTEM micrographs of the two linear-graded heterostructures of the first set (brown and lavender arrows in Figures 6.12 – 6.13, 6.16 – 6.19). When analysed in different two-beam conditions (Figure 6.18 a–f), the TDs present in the two linear-graded heterostructures of the first set do not satisfy the invisibility criteria (Chapter 5, Equations 5.2 - 5.3) therefore we conclude that they are of the mixed type (Chapter 5, § 5.3.4) in good agreement with results reported in literature for the $Si_{1-x}Ge_x/Si$ (001) system (Chapter 3). The TD pileup shown in Figure 6.18 a-f appears to run through the whole heterostructure. Similar pileups have been observed in $Si_{1-x}Ge_x/Si$ (001) structures by other groups, who studied their formation and concluded that they are typically caused by an interfacial inhomogeneity, of the particulate type, that continuously 'punches out' dislocations under the influence of the misfit strain introduced continuously through Ge concentration grading [4]. The angle between this dislocation pileup and the MDs directions is ≈ **54°**, indicating that the pileup is made of **60°** dislocations (described in Chapter 3, § 3.2.3) lying on a **{111}** plane. Figure 6.19 a-d shows other TDs, most of which are 60° type lying on **{111}** planes.

Most TDs appear to end at troughs rather than crests on the surface, especially in *720*. A particular case is that presented in Figure 6.16 a-b for the structure *720* and in Figure 6.17 for *775*, which show groups of TDs terminated at faceted pits.

A rough estimation of the TD density was made based on XTEM results. Values obtained were higher for the structure *720* (≈ **$5x10^8$ - 10^9 cm^{-2}**) by comparison with *775* (≈ **$2x10^7$ - $4x10^7$ cm^{-2}**).

PVTEM, similarly to disclosure etch coupled with Nomarski contrast, appears to image mainly the MDs running along the two perpendicular <110> directions (Figures 6.20 – 6.21), hence regardless of the fact that it offers larger areas for analysis and consequently a better statistical accuracy than XTEM, this technique did not prove very successful for estimating the TDs densities. The brown arrows on the PVTEM images shown in Figure 6.20 c, d and f and Figure 6.21 a indicate dislocation terminations, which may correspond to TDs, or may just show MD segments interrupted by sample preparation (the samples have been thinned from the substrate side, as described in Chapter 5, § 5.3.5.2). The PVTEM micrographs shown in Figure 6.20 c and d reveal that under the diffraction conditions used, some dislocation terminations appear as 'round' features (indicated by the brown arrows). The same features can be seen in the micrograph shown in Figure 6.20 a (indicated by the brown arrows) possibly corresponding to the pits observed in AFM.

PVTEM micrographs of the two linear-graded heterostructures of the first set are very similar (Figure 6.20 – 6.21). This observation is in accordance with the ones made in high magnification Nomarski contrast and in the 20 μm x 20 μm AFM scans. During PVTEM sample preparation, most MD pileups were milled away (the samples being thinned from the substrate side as described in Chapter 5, § 5.3.5.2). Nevertheless, some remaining MD pileups can still be seen and they are delineated by yellow lines in Figures 6.20 a, 6.21 a-b. Additionally, the yellow arrows on the PVTEM micrographs in Figure 6.20 e and f and Figure 6.21 a show dislocations with a topography identical to that of intersections of clusters of 60° dislocations having the same Burgers vectors, of the type described in Chapter 3 and represented schematically in Figure 3.12 f, which have already been observed in Nomarski contrast (Figure 6.2 a-b) and can be responsible for a Hagen-Strunk type dislocation multiplication mechanism (Chapter 3, § 3.2.3.5). Cross-slip often occurs for perpendicular dislocations that glide on **{111}** planes (as described in Chapter 3, § 3.2.3.5) and groups of intersecting cross-slipping MDs are observed in the PVTEM micrographs of the linear-graded heterostructures of the first set (delineated by red lines in Figure 6.20 b).

Thickness values for the two linear-graded heterostructures of the first set were also obtained from measurements on the XTEM images (Figures 6.12 – 6.13), using the clearly delineated carbon layer as reference for the heterostructure origin.

The average thickness value for the whole of the linear-graded heterostructure of the first set, *720*, obtained by interpolation from SIMS results obtained on the calibration structures was ≈ **2 μm** (Table 1). The average value obtained from XTEM measurements was found to be ≈ **1.8 μm**, thus slightly smaller than the SIMS value. The extension of MDs well into the layer of constant Ge concentration of this structure made it difficult to delineate the different layers incorporated in it (Figure 6.12).

The average thickness value for the whole of the other linear-graded heterostructure of the first set, *775*, obtained by interpolation from SIMS results obtained on the calibration structures was ≈ **1.6 μm** (Table 1). The value obtained from XTEM measurements was found to be ≈ **2.14 μm**, thus higher than the SIMS value. For this structure, there is a distinct separation between the virtual substrate and the layer of constant Ge concentration on the XTEM images (Figure 6.13), thus allowing the measurement of their respective thicknesses. The virtual substrate thickness for this structure obtained from XTEM measurements (Figure 6.13) was ≈ **1.30 μm**, in good agreement with the interpolated SIMS value of ≈ **1.36 μm** (Table 1). The capping layer thickness obtained from XTEM measurements (Figure 6.13) was ≈ **0.82 μm**, thus higher than the interpolated SIMS value of ≈ **0.24 μm** (Table 1). The discrepancies between the interpolated SIMS values and the XTEM measured values observed for the linear-graded heterostructure of the first set, *775*, seem to be consistent. The higher values for the thickness of the whole structure obtained by XTEM compared to SIMS is caused by a higher value for the thickness of the capping layer than estimated from SIMS for this structure.

Comparisons between the thickness values obtained from XTEM measurements and interpolated from SIMS results obtained on the calibration structures, prove very important for subsequent growth calibration.

XTEM results showed that the linear-graded heterostructure of the first set grown at the higher temperature, with the higher initial Ge content in the virtual substrate, the lower Ge concentration gradient and the thicker capping layer, *720*, has a virtual substrate characterised by an inefficient misfit strain relaxation mechanism, which results in a high density of short MD segments piling up well into the capping layer. Its surface exhibits accentuated undulations and deep faceted pits, where groups of TDs terminate. By comparison, the linear-graded heterostructure of the first set grown at the lower temperature, with the lower initial Ge content in the virtual substrate, the higher Ge

concentration gradient and the thinner capping layer, *775*, has a virtual substrate characterised by an efficient misfit strain relaxation mechanism, which results in long MD segments, well contained within the virtual substrate, leaving the capping layer MD-free. For this latter structure, surface undulations are finer and shallower faceted pits characterise the termination of groups of TDs. Moreover, the structure *720* is characterised by a higher density of TDs by comparison with *775*.

TEM results show that the virtual substrate of the linear-graded heterostructure of the first set grown at the lower temperature, with the lower initial Ge composition and the higher Ge concentration gradient, *775*, is characterised by a more efficient misfit strain relaxation mechanism, which results in superior structural properties (i.e. better surface morphology and reduced TD density) compared to the other linear-graded heterostructure of the first set, *720*.

Overall, the growth conditions used for *775* result in a heterostructure with superior surface morphology and lower TD density. By using the same growth conditions used for *775*, but a lower initial misfit strain (Ge concentration), a lower Ge gradient and/or a thicker capping layer, we expect to improve both the surface morphology and the defect content. These assumptions guided the choice of growth parameters for the linear-graded heterostructure of the second set, *VSC4*.

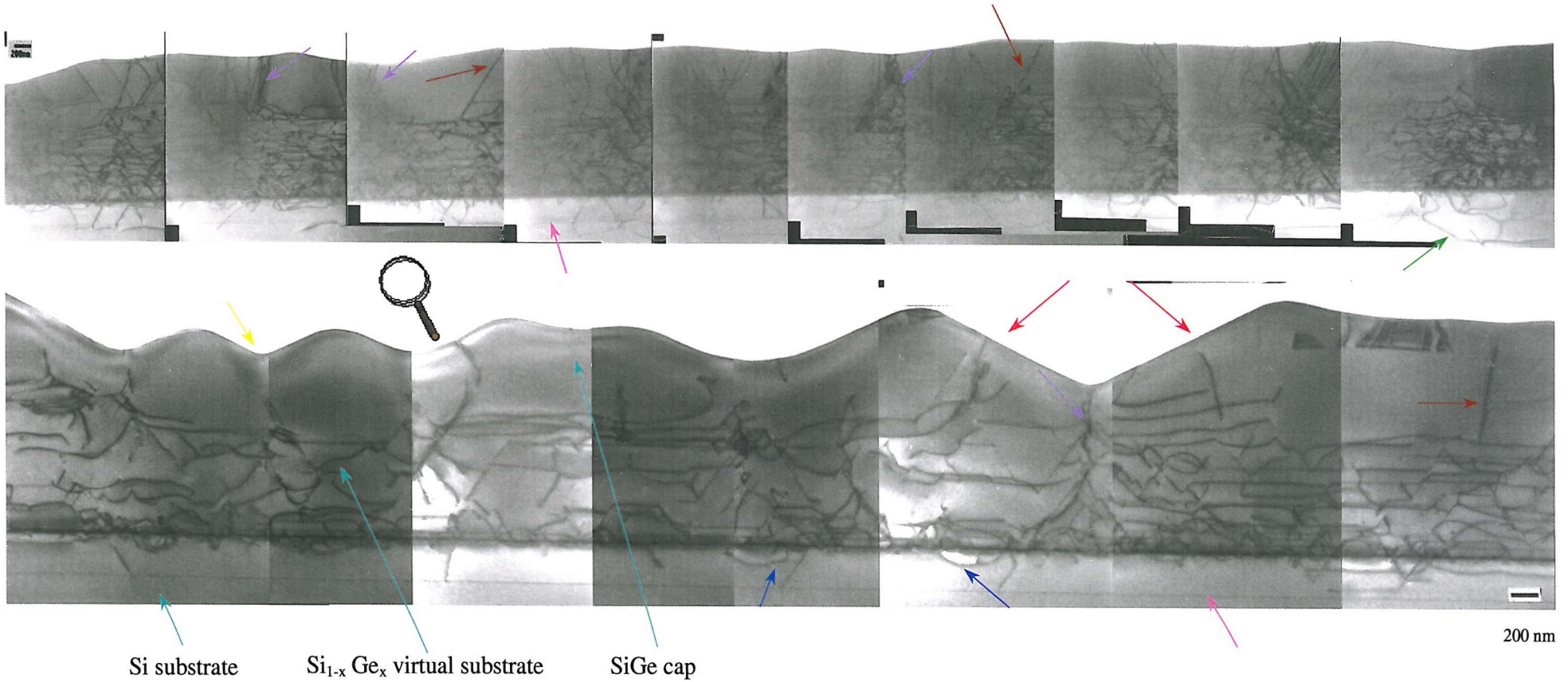

Figure 6.12. XTEM bright-field micrographs (obtained using the main beam condition) of the linear-graded heterostructure of the first set grown at the higher temperature, with the higher initial Ge concentration in the virtual substrate, the lower Ge concentration gradient in the virtual substrate and the thicker capping layer, *720*. The top image shows a larger area than the bottom image. Both images show the undulated surface morphology, with small ripples (indicated by the yellow arrow) and deep faceted pits (indicated by the red arrows). The presence of a carbon layer at the Si substrate-SiGe heterostructure interface is indicated by the pink arrows. Some defects extend into the Si substrate, well below the carbon layer (the green arrow on the top image); other defects stop well before the carbon layer (the blue arrows on the bottom image). The brown arrows indicate dislocation segments threading to the surface. The lavender arrows point to groups of TDs terminated at the surface where faceting occurs (indicated by the red arrows).

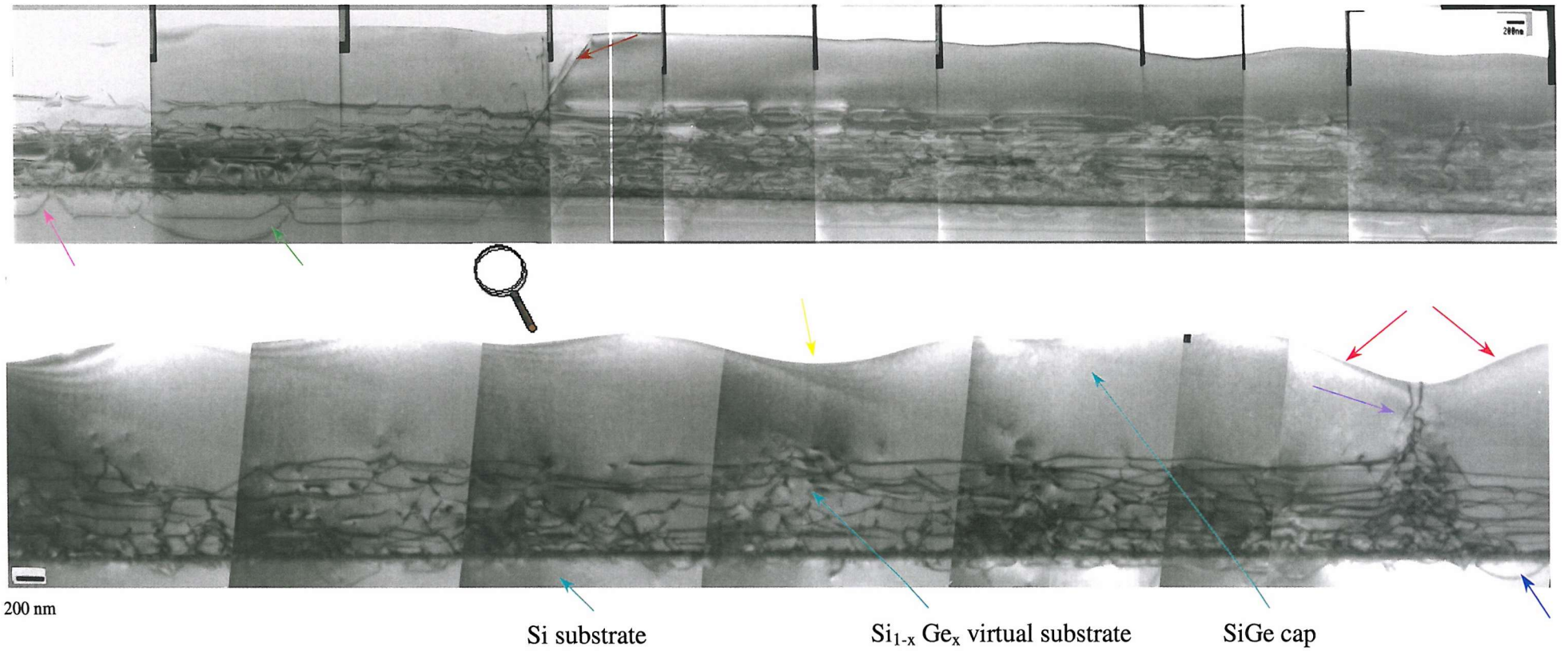

Figure 6.13. XTEM bright-field micrographs (obtained using the main beam condition) of the linear-graded heterostructure of the first set grown at the lower temperature, with the lower initial Ge concentration in the virtual substrate, the higher Ge concentration gradient in the virtual substrate and the thinner capping layer, *775*. The top image shows a larger electron transparent area than the bottom image. Both images show the undulated surface morphology, with fine ripples (indicated by the yellow arrow) and faceted pits (indicated by the red arrows). The presence of a carbon layer at the Si substrate-SiGe heterostructure interface is indicated by the pink arrow. Some defects extend into the Si substrate, well below the carbon layer (the green arrow on the top image); other defects stop well before the carbon layer (the blue arrow on the bottom image). The brown and lavender arrows, respectively, indicate two different types of TD groups; the one shown by the lavender arrow terminates at a faceting pit (indicated by the red arrows).

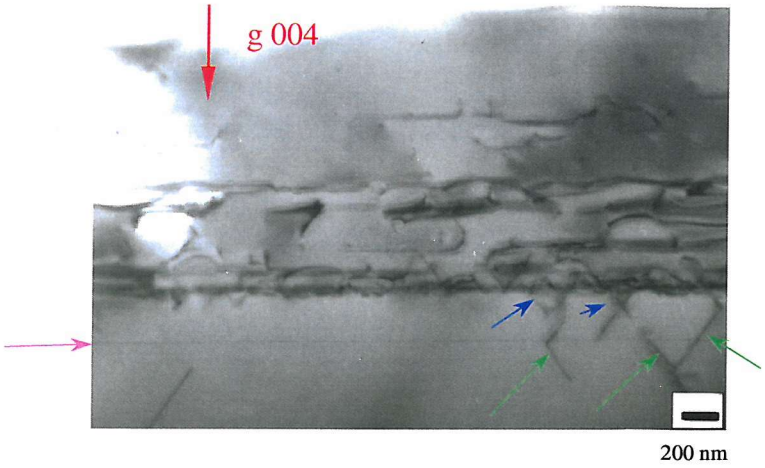

(a)

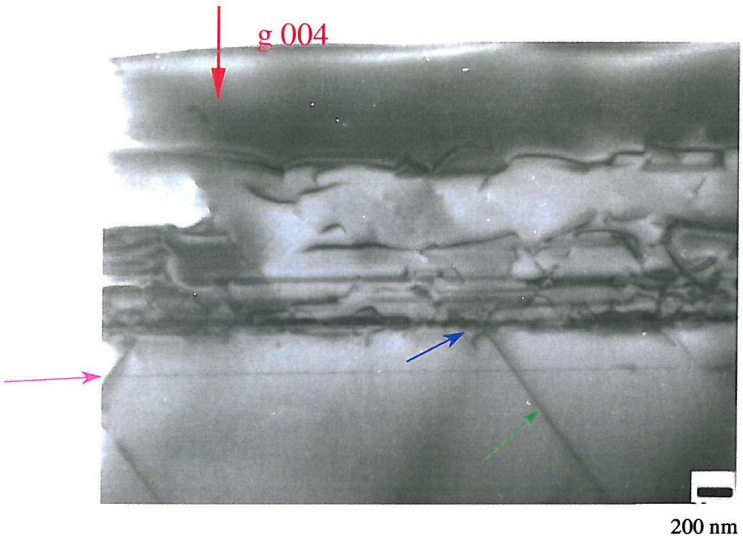

(b)

Figure 6.14 a-b. Bright-field XTEM micrographs of the linear-graded heterostructure of the first set, *720*, showing the carbon layer present at the Si substrate-SiGe heterostructure interface (pink arrows). Some defects seem to stop at or before the carbon layer (blue arrows). Others extend into the Si substrate, well beyond the carbon layer (green arrows), as deep as, or even deeper than 1 μm.

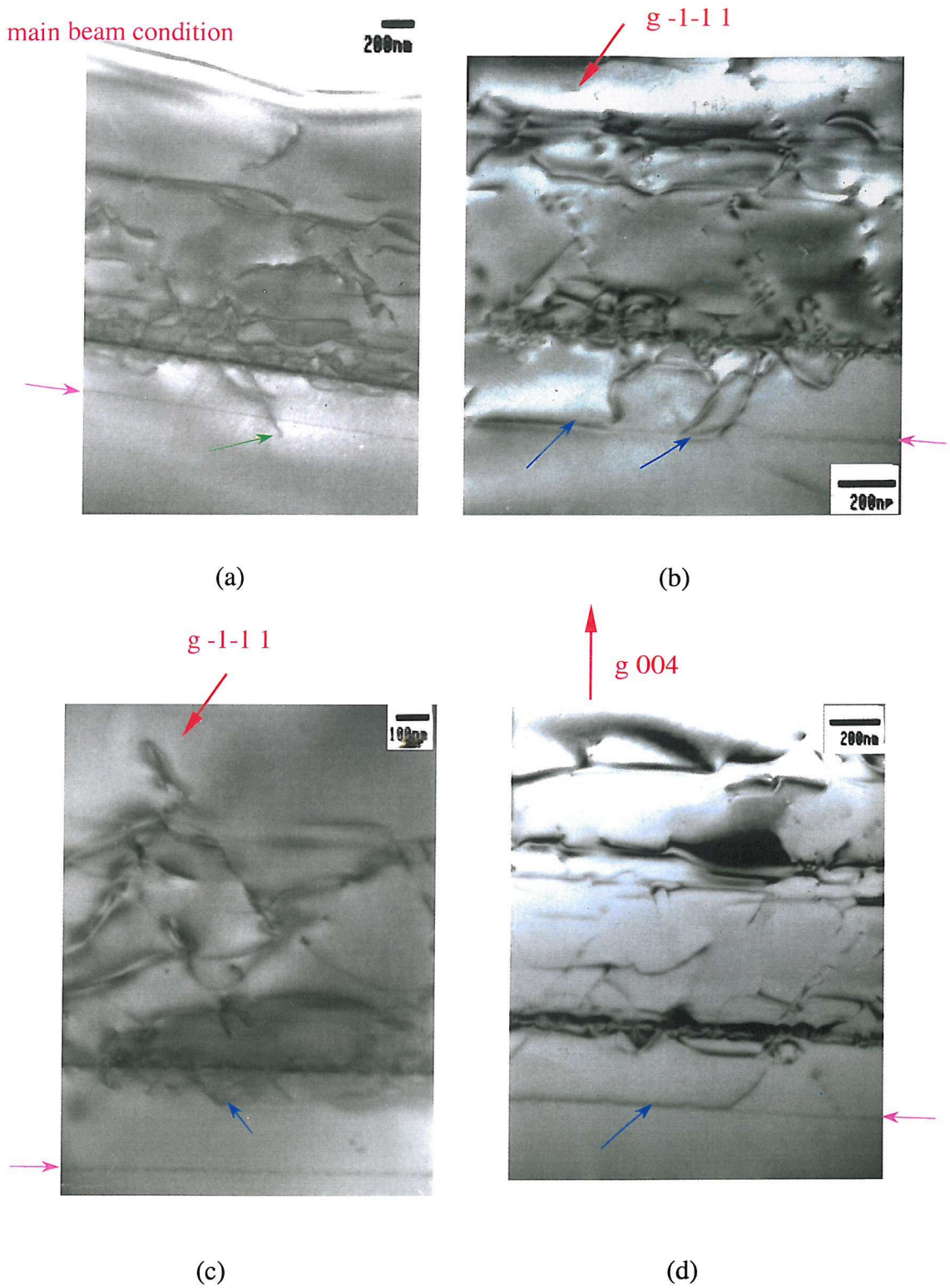

Figure 6.15. Bright-field XTEM micrographs of the linear-graded heterostructure of the first set, *775*, showing the carbon layer present at the Si substrate-SiGe heterostructure interface (pink arrows). Some defects extend into the Si substrate, well beyond the carbon layer (green arrow in a). Others seem to stop at the carbon layer (blue arrows in b and d). A large number of defects do not even reach the carbon layer (blue arrow in c).

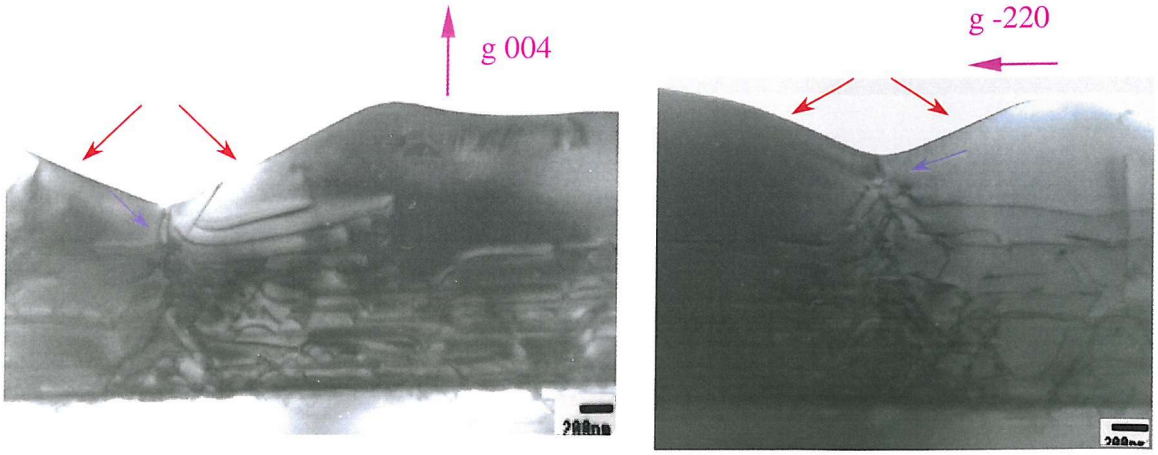

(a) (b)

Figure 6.16 a–b. XTEM bright-field images showing faceted pits (red arrows) where pileups of TDs (lavender arrows) terminate on the surface of the linear-graded heterostructure of the first set, *720*.

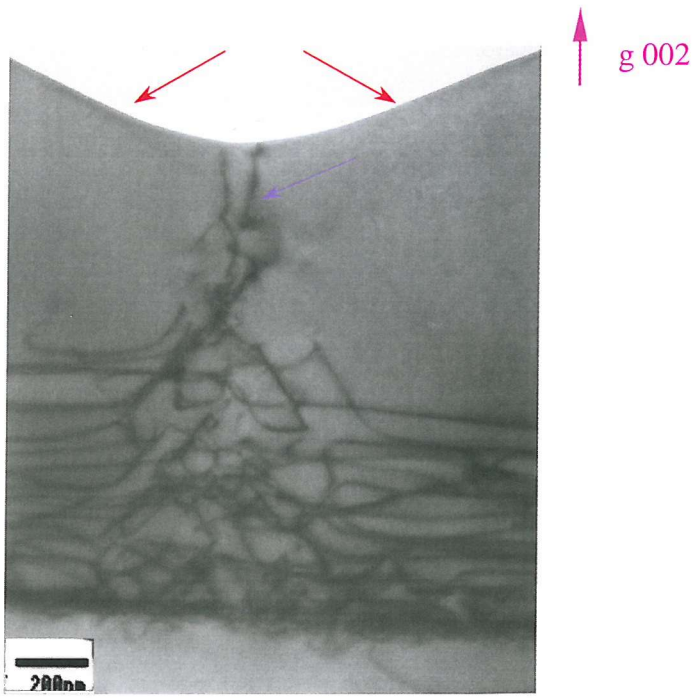

Figure 6.17. XTEM bright-field images showing faceted pits (red arrows) at the termination of pileups of TDs (lavender arrows) on the surface of the linear-graded heterostructure of the first set, *775*.

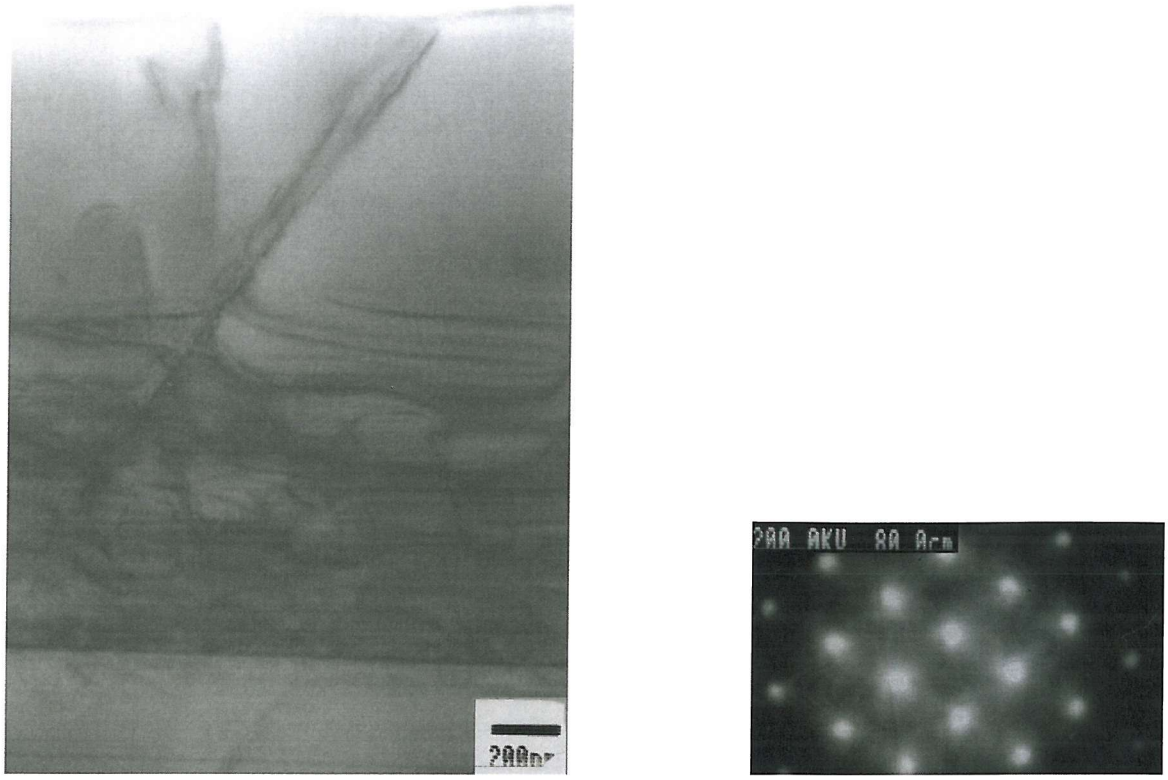

(a)

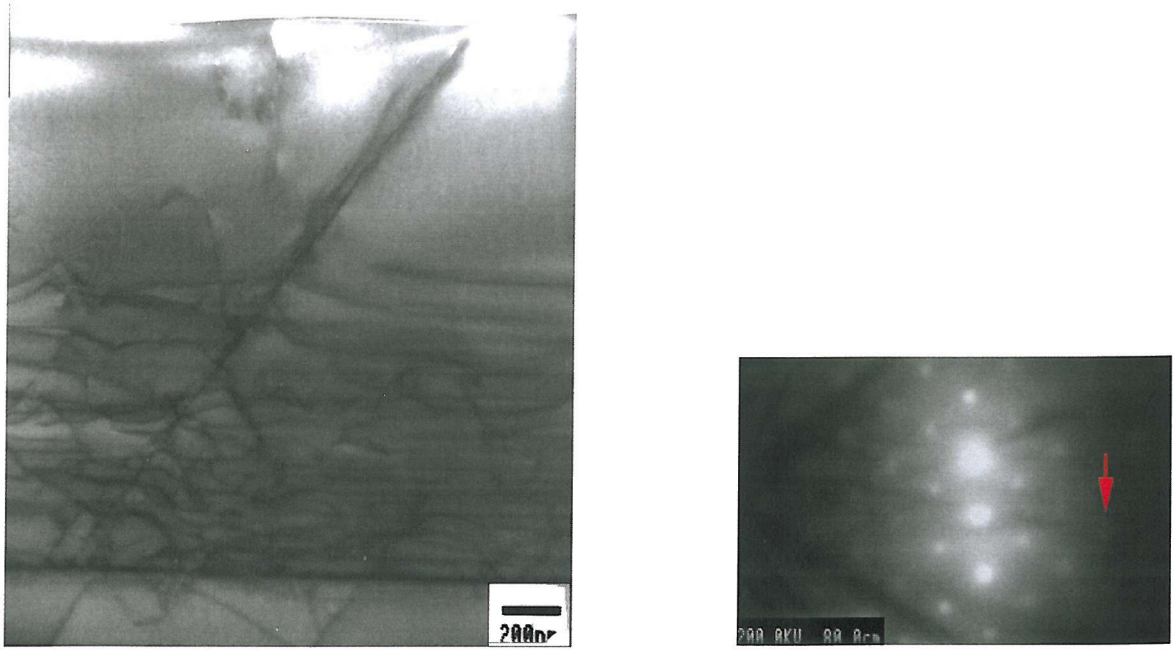

(b)

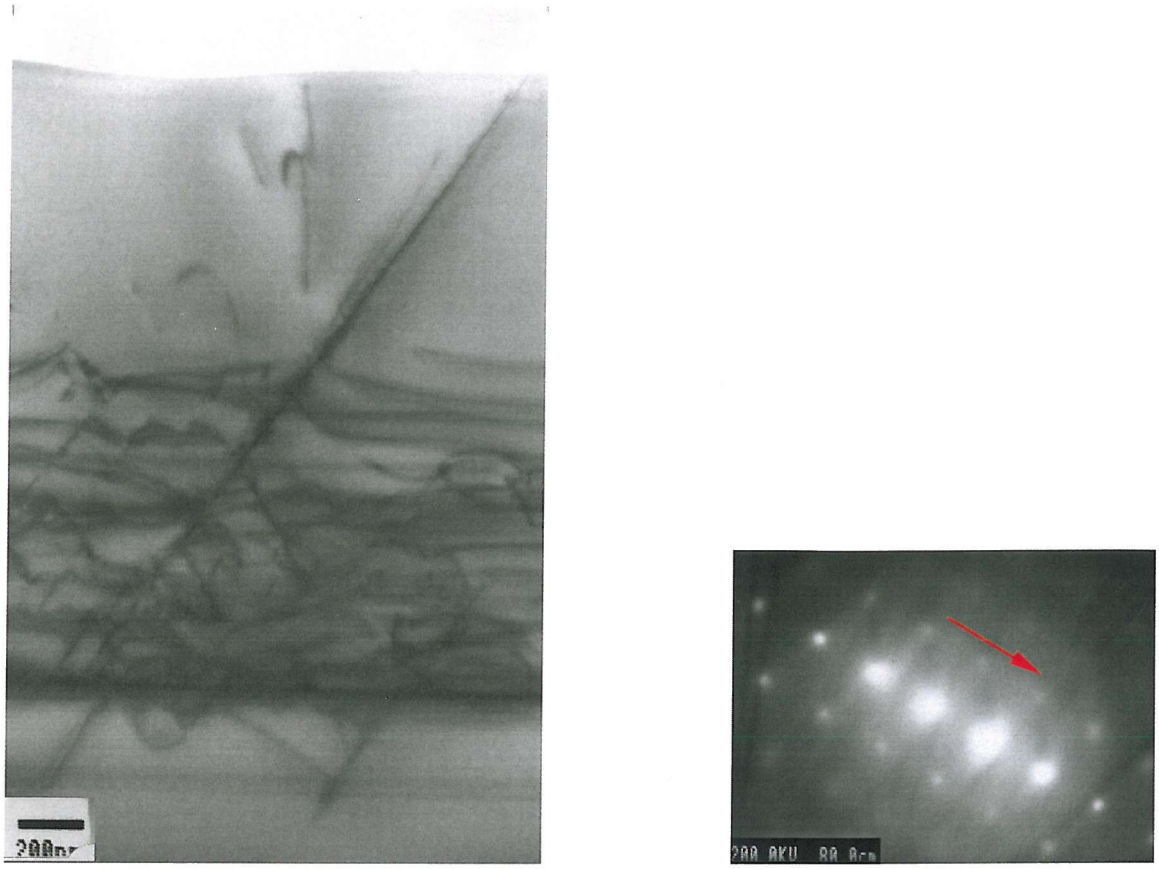

(c)

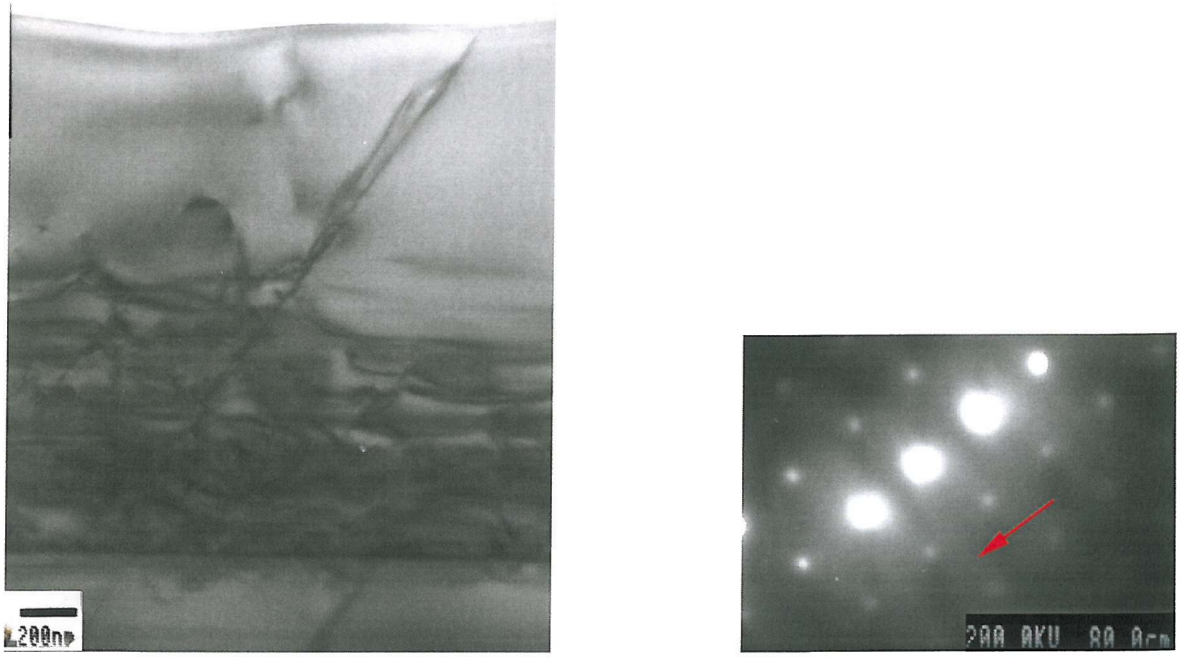

(d)

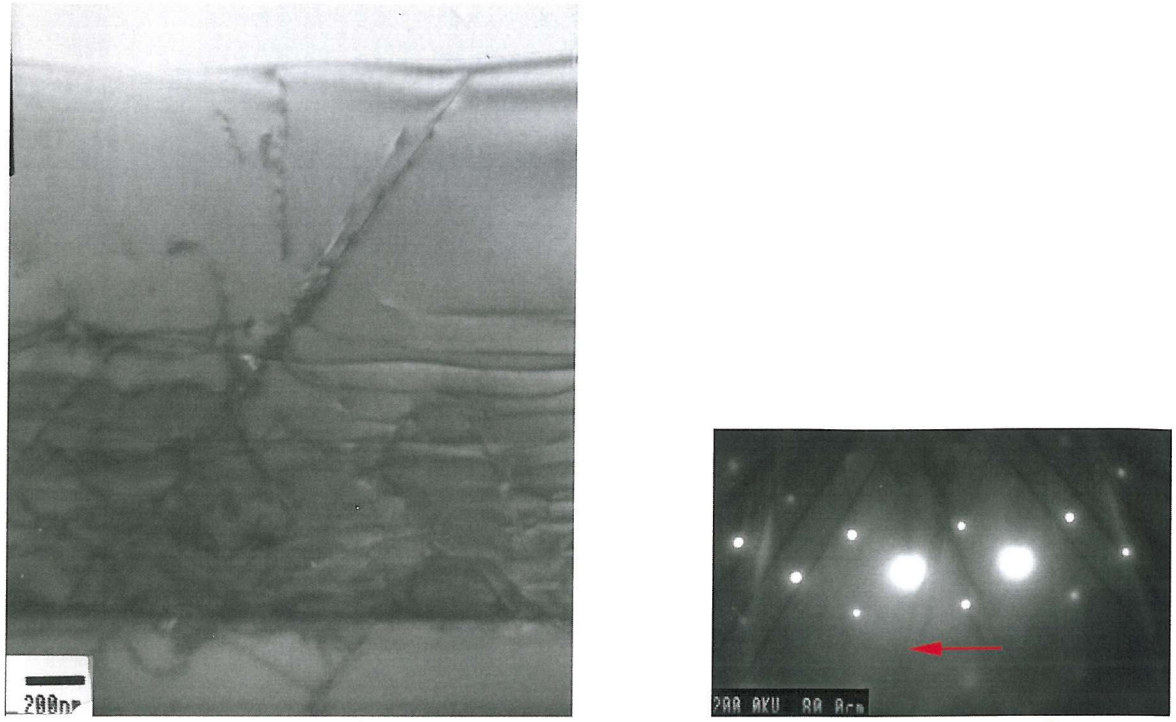

(e)

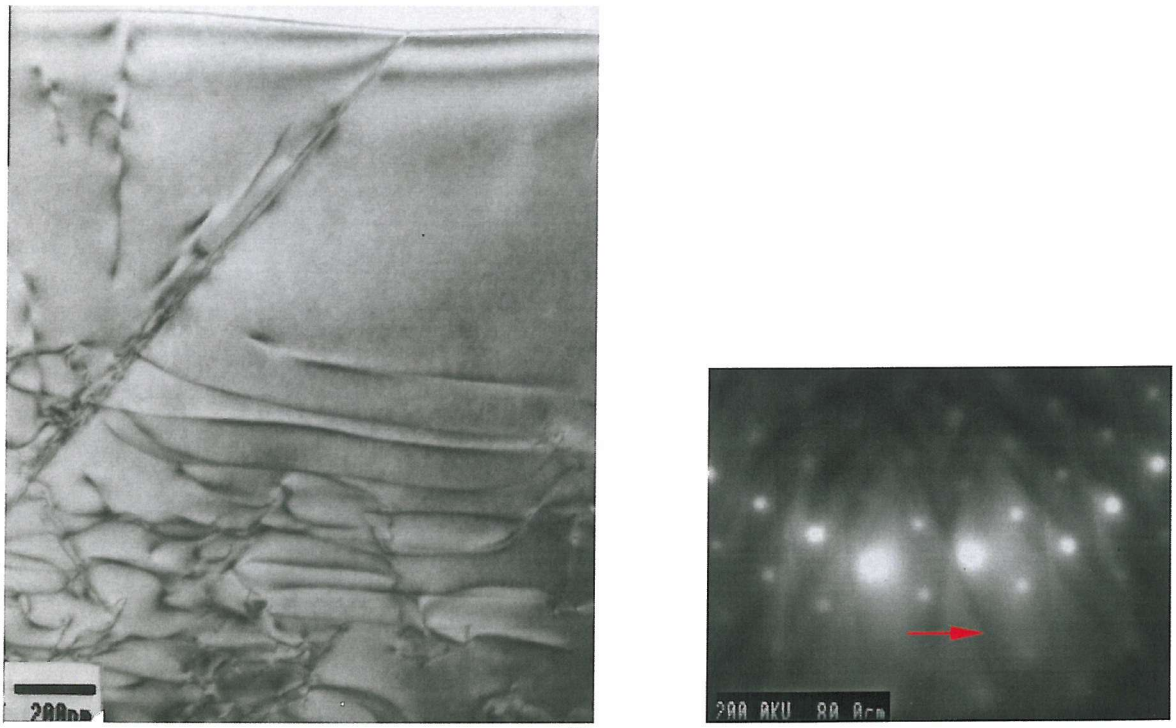

(f)

Figure 6.18. Bright-field XTEM micrographs of the linear-graded heterostructure of the first set, *775*, showing the same pileup of TDs imaged in different two-beam conditions and the corresponding diffraction patterns: (a) the main beam condition; (b) $\mathbf{00\bar{2}}$; (c) $\mathbf{1\bar{1}\bar{1}}$; (d) $\mathbf{\bar{1}11}$; (e) $\mathbf{\bar{2}20}$; (f) $\mathbf{2\bar{2}0}$. The fact that the TDs are visible in all two-beam conditions indicates their mixed type.

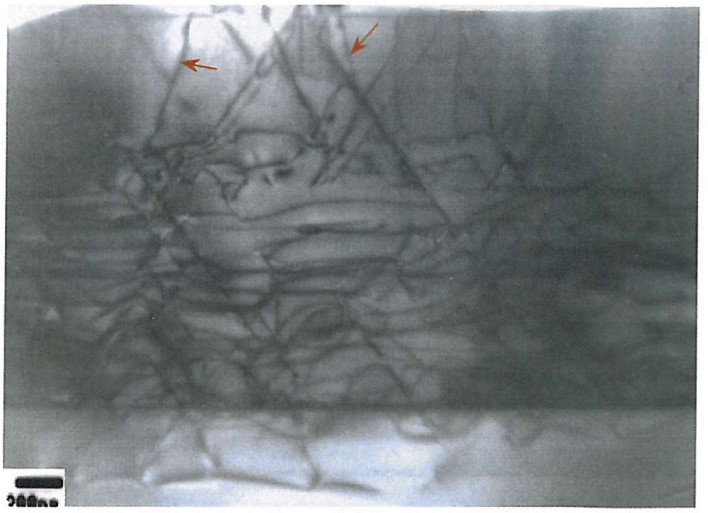

(a)

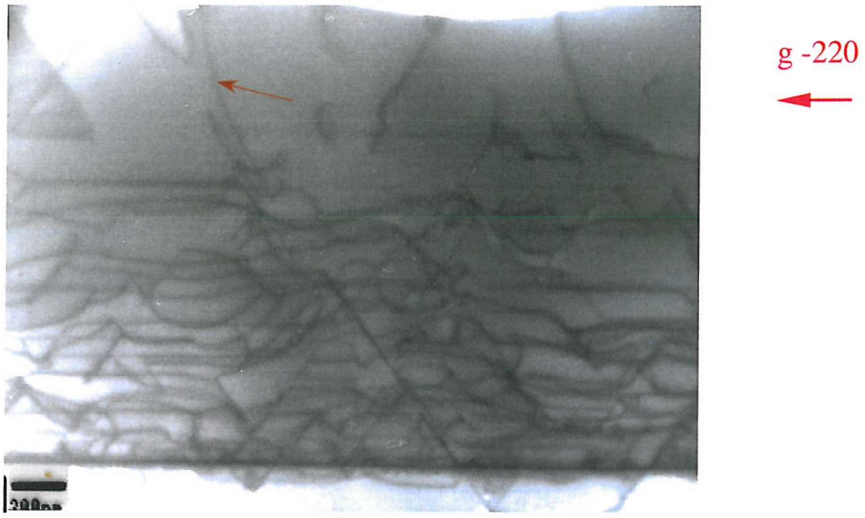

(b)

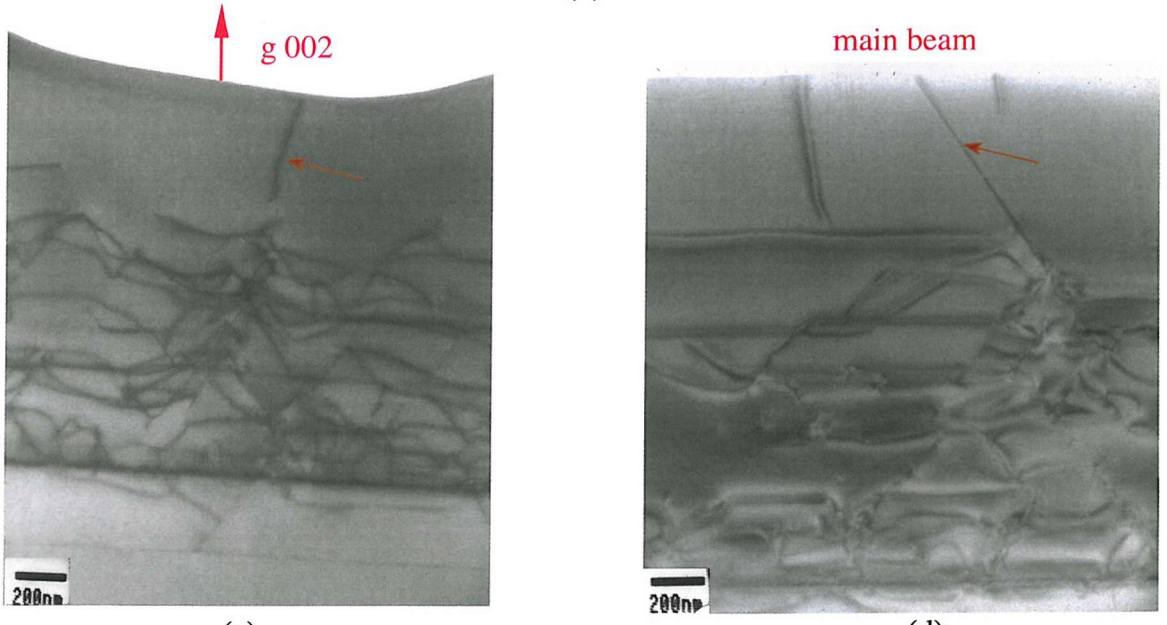

(c) (d)

Figure 6.19. Bright-field XTEM images taken in different two-beam conditions showing the presence of threaders (brown arrows) in both linear-graded heterostructures of the first set: (a–b) *720*, reveals a higher density of TDs; (c–d) *775*, shows a lower density of TDs.

(a)

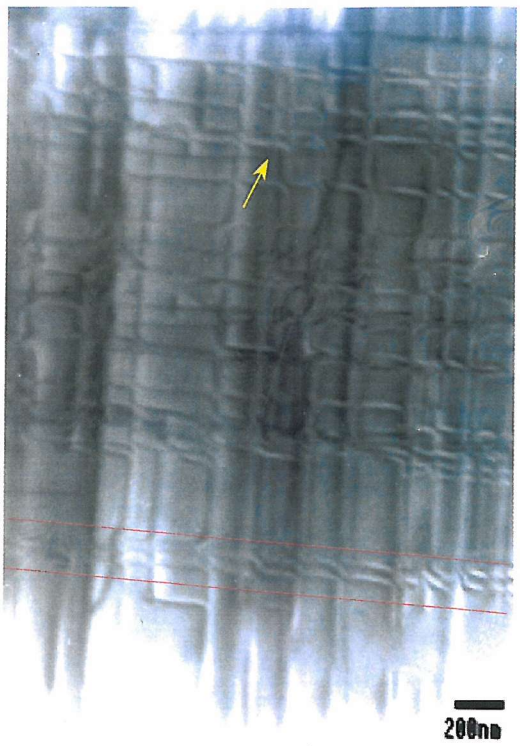

(b)

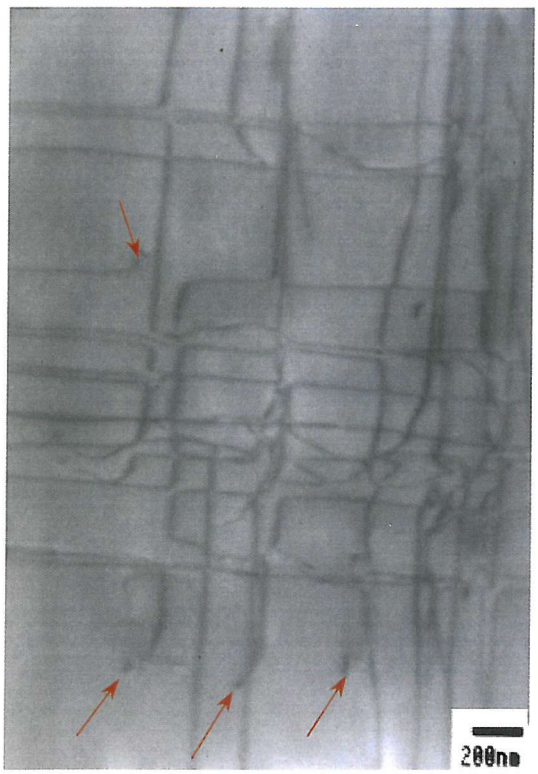

(c)

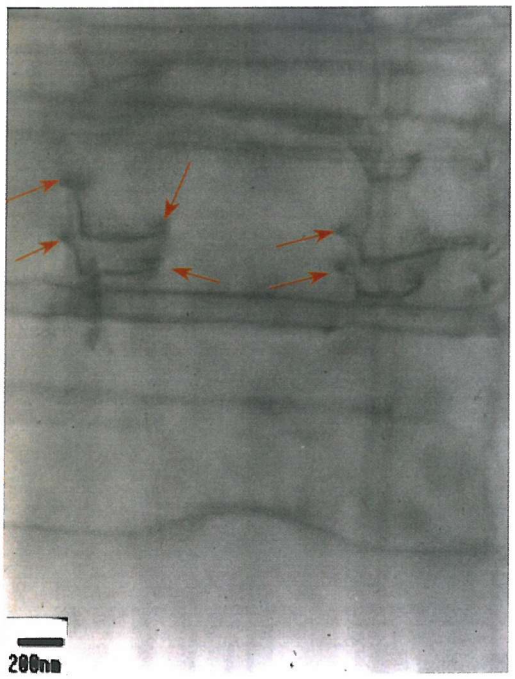

(d)

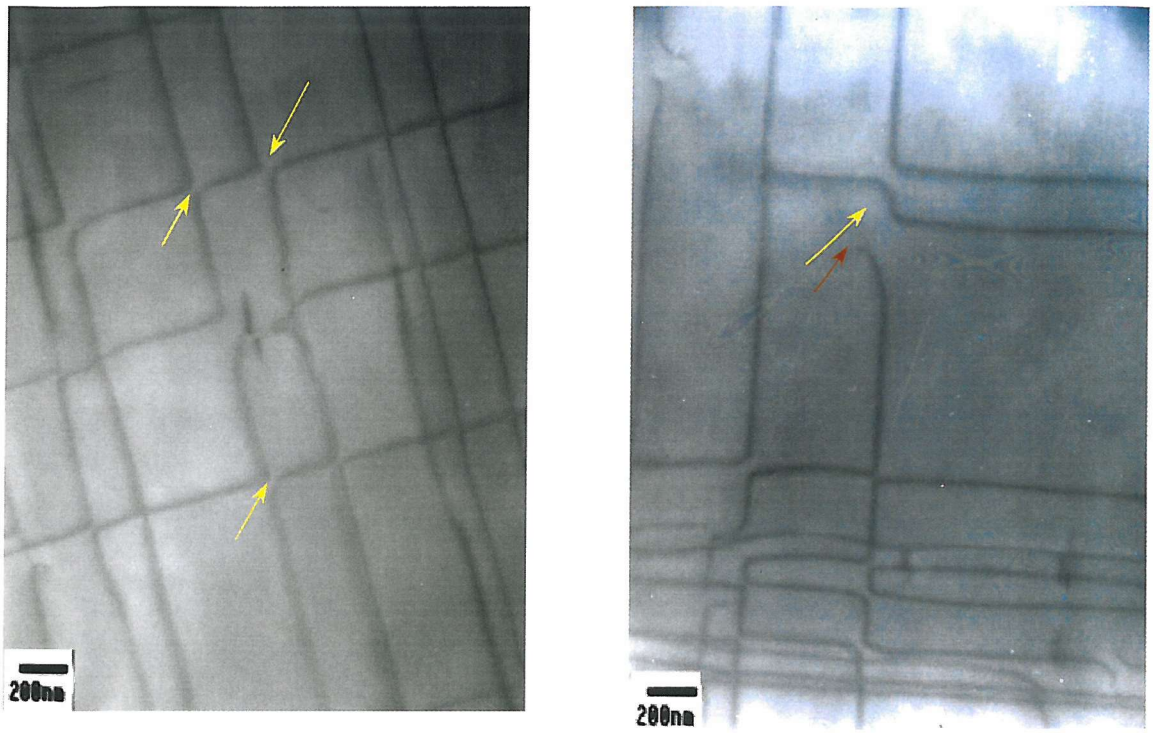

(e) (f)

Figure 6.20. Bright-field PVTEM micrographs (obtained using the main beam condition) of the linear-graded heterostructure of the first set, *720*, showing MDs lying in the (001) growth plane and running along the two perpendicular <110> directions: (a) thick sample, showing both pileups of MDs (delineated by the yellow lines) and singular MD lines. The brown arrows point to 'round'-shaped features; (b) a slightly thinner sample, which shows regions of groups of cross-slipping MDs (delineated by the red lines) as well as single perpendicular interacting MDs (indicated by the yellow arrow); (c) and (d) even thinner samples, from which most of the pileups have been milled away during sample preparation. The brown arrows point to dislocations terminations, which may be TD or MD segments interrupted by sample preparation. Some dislocation terminate in 'round'-shaped features (c); (e) and (f) yellow arrows point to a MD interaction configuration similar to that illustrated in Chapter 3, Figure 3.12 f.

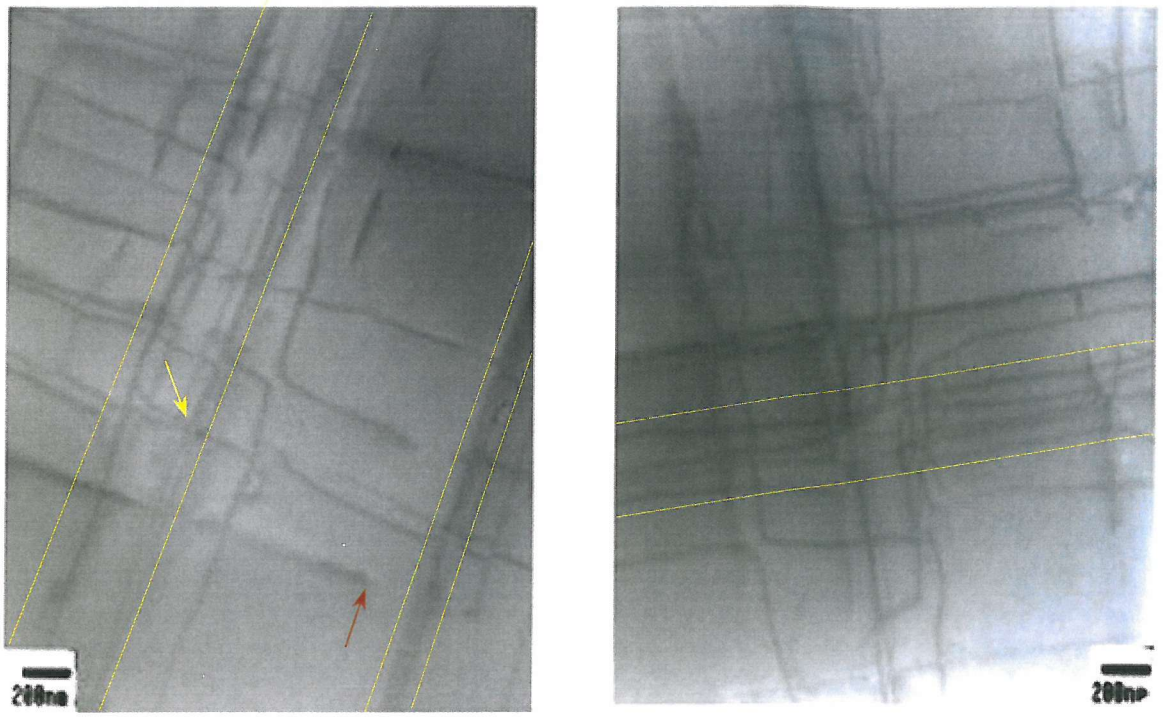

(a) (b)

Figure 6.21 a–b. Bright-field PVTEM micrographs (obtained using the main beam condition) of the linear-graded heterostructure, *775*, showing MDs lying in the (001) growth plane and running along the two perpendicular <110> directions. MDs pileups are delineated by the yellow lines, the brown arrow points to a dislocation termination and the yellow arrow indicates a MD interaction configuration similar to that illustrated in Chapter 3, Figure 3.12 f.

6.2.3. FIRST SET: STEP-GRADED HETEROSTRUCTURE

6.2.3.1. Optical microscopy: Nomarski DIC analysis

Nomarski DIC microscopy studies were performed for an initial assessment of the surface morphology of the step-graded heterostructure of the first set, *774*. Analyses were carried out on the same equipment and under the same conditions as those used to characterise the linear-graded heterostructures of the first set (§ 6.2.2.1).

When analysed at low magnification (x50) in Nomarski contrast, the step-graded heterostructure of the first set, *774*, shows very few small areas of accentuated crosshatch lines (indicated by the red arrows in Figure 6.22) and extended regions of fine, regular pattern (indicated by the yellow arrows in Figure 6.22 a). Similarly to the linear-graded heterostructures of the first set, the areas of accentuated crosshatch pattern are randomly distributed The low magnification Nomarski micrograph of the step-graded heterostructure (Figure 6.22 a) thus reveals a different surface morphology compared with the same magnification Nomarski micrographs of the two linear-graded heterostructures of the first set (Figure 6.1 a–b).

Higher magnification (x500) Nomarski analysis enabled the measurement of the lateral spacing of the crosshatch pattern of the step-graded heterostructure of the first set (Figure 6.22 b) and the results obtained coincide with those for the linear-graded heterostructures of this first set (i.e. values of $\approx$ **1 μm**, for the small-scale pattern and $\geq$ **15μm**, for the accentuated crosshatch lines). Additionally, at this magnification, crosshatch lines with a topography identical to that of intersections of clusters of 60° dislocations having the same Burgers vectors (as shown in Chapter 3, Figure 3.12 f) can be observed (blue arrow arrows in Figure 6.2 a-b). These surface features have also been previously observed in the linear-graded heterostructures of the first set, *720* and *775*, in Nomarski contrast (blue arrows in Figure 6.2 a) and in PVTEM (yellow arrows in Figures 6.20 e and f and 6.21 a).

At even higher magnifications (x1000) in Nomarski contrast, the accentuated crosshatch lines appear similar in all three heterostructures of the first set (Figures 6.3 a-b and 6.22 c), possibly indicating similar formation mechanisms. Similarly to the linear-graded heterotructures of the first set (Figures 6.3 – 6.4 a-b), some of the accentuated crosshatch lines in the step-graded heterostructure run all the way to the edges of the Nomarski micrographs shown in Figure 6.22, others seem to end at other perpendicular accentuated

lines, and others appear to end at 'round' or 'square' shaped features (indicated by the red arrows in 6.22 c). Additionally, these surface features appear to have random distributions in the step-graded heterostructure of the first set, similarly to the linear-graded heterostructures of the first set.

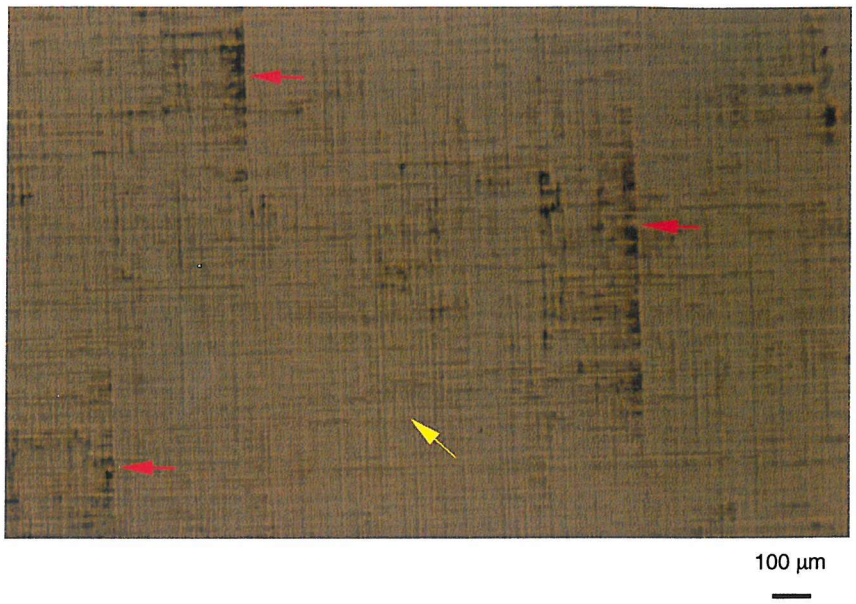

(a)

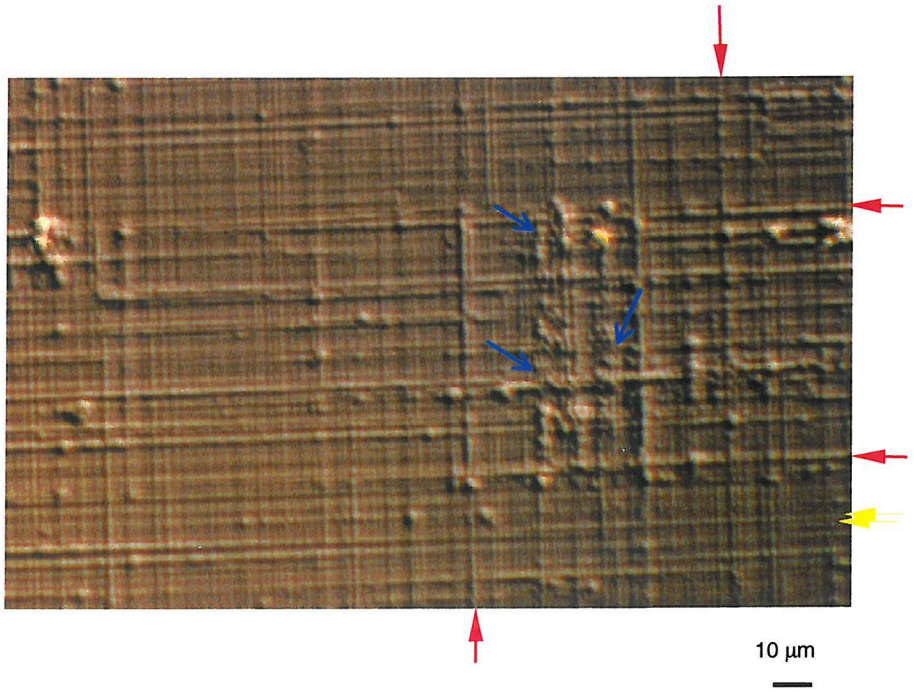

(b)

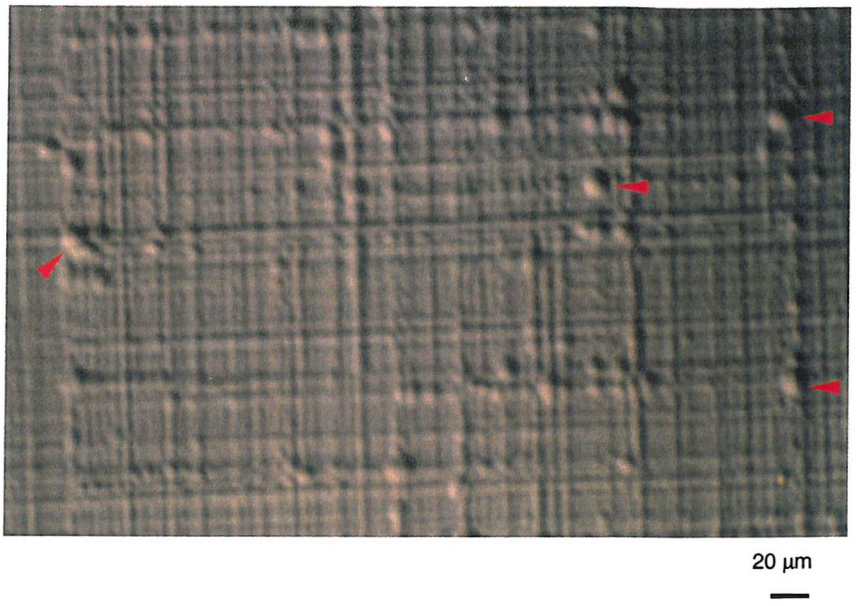

(c)

Figure 6.22. Nomarski DIC micrographs of the step-graded heterostructure of the first set, *774*, obtained at: (a) x50 magnification, showing large areas of fine, small-scale crosshatch pattern (indicated by the yellow arrows) and a reduced density of areas of accentuated crosshatch lines (indicated by the red arrows); (b) x500 magnification wherein the blue arrows point to crosshatch lines with a topography identical to that of intersections of clusters of 60° dislocations having the same Burgers vectors (as shown in Chapter 3, Figure 3.12 f); (c) x1000 magnification, showing accentuated crosshatch lines with a similar aspect with those encountered in the two linear-graded heterostructures of the first set (Figure 6.3 a-b) and the presence of randomly distributed pits (indicated by the arrows) of various sizes and 'round' and 'square' shapes along the accentuated crosshatch lines.

The effects of the different types of grading of the Ge composition in the virtual substrate on the surface morphology of the SiGe heterostructures were studied by comparing the results obtained on the linear-graded heterostructure of the first set, *775* and the step-graded heterostructure of the first set, *774*, grown under identical conditions. Comparative studies of the Nomarski contrast results obtained on these two heterostructures show that the essential difference between them is represented by larger areas of accentuated crosshatch lines in the linear-graded heterostructure (Figure 6.23 a) compared with the step-graded one, which shows larger areas of fine crosshatch (Figure 6.23 b).

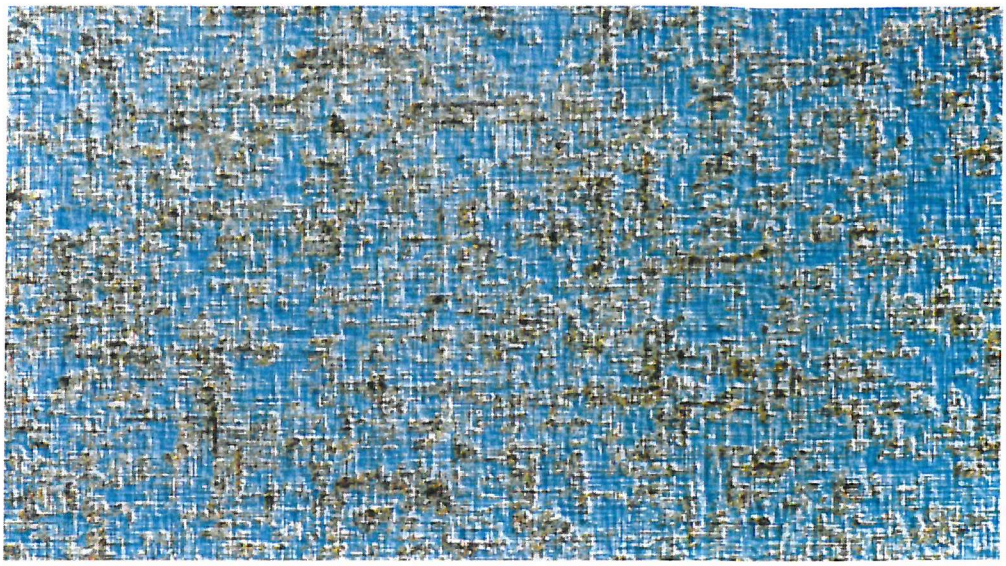

(a)

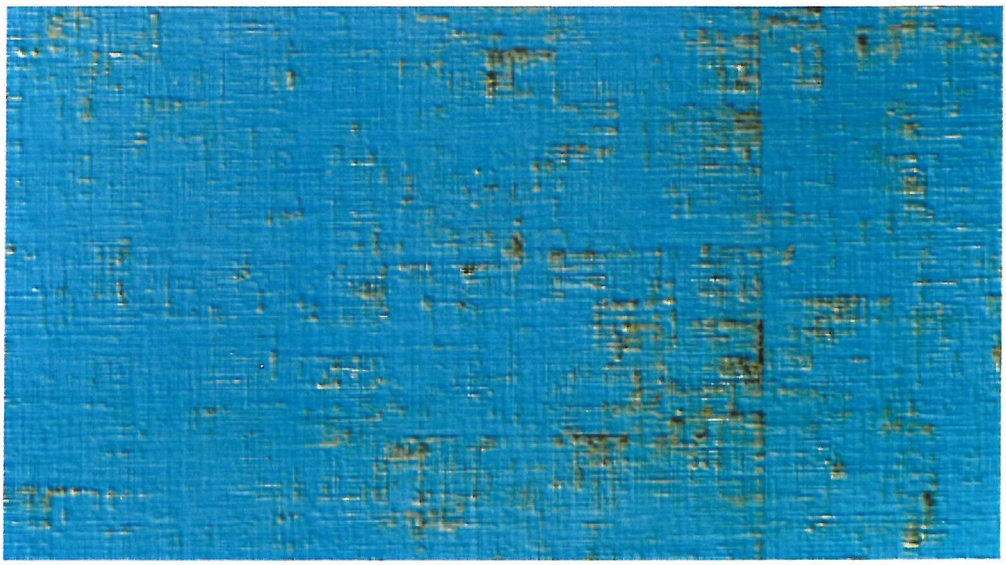

(b)

Figure 6.23. Nomarski DIC micrographs (obtained at x50 magnification) for a comparison between: (a) the linear-graded heterostructure of the first set, *775* and (b) the step-graded heterostructure of the first set, *774*, grown under identical conditions. Larger areas of accentuated crosshatch pattern are exhibited by the linear-graded heterostructure, whilst the step-graded one is characterised by larger areas of fine crosshatch.

Disclosure chemical etch

Attempts to quantify the TD density by using disclosure chemical etch combined with optical microscopy were also made in the case of the step-graded heterostructure of the first set.

Based on the conclusions drawn from analysing the efficiency of the different etchants used for the two linear-graded heterostructures of the first set, we only used the Dash etchant for the step-graded heterostructure.

Results obtained showed, once again, that regardless of the fact that the step-graded heterostructure of the first set is characterised by larger areas of fine crosshatch pattern, etching still preferentially discloses the crosshatch lines, thus not allowing us to resolve the emergence of the TDs (Figure 6.24 b-c), similarly to the results obtained for the linear-graded heterostructures. Even in this case, the Dash etchant prove to be very efficient in disclosing the emergence of dislocations at the edges of the wafers, where the crosshatch lines are much finer, (Figure 6.25).

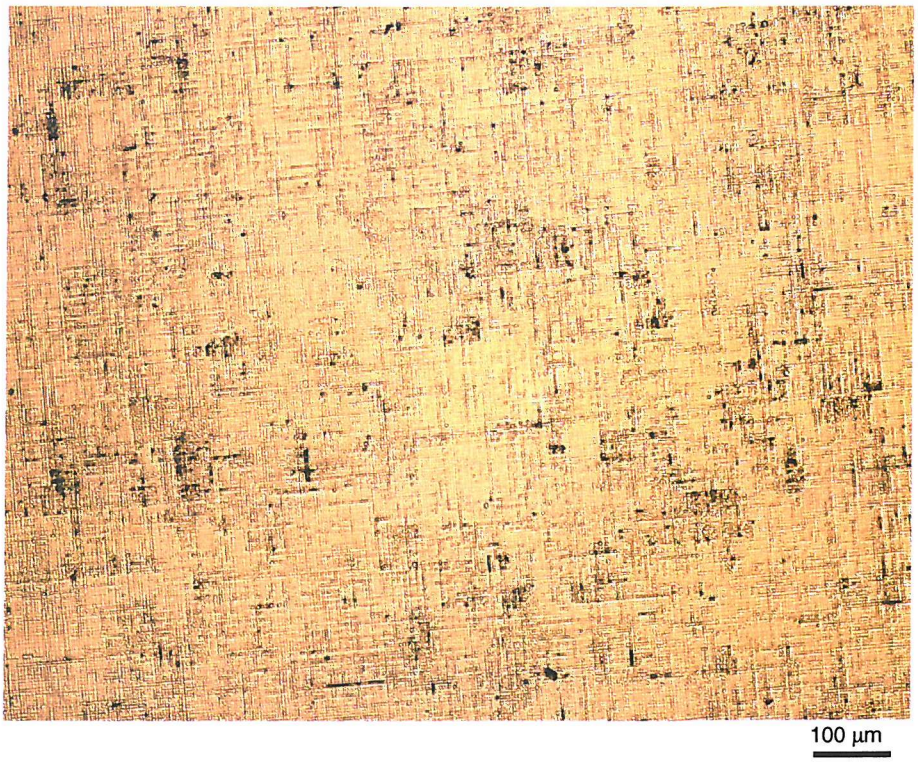

(a)

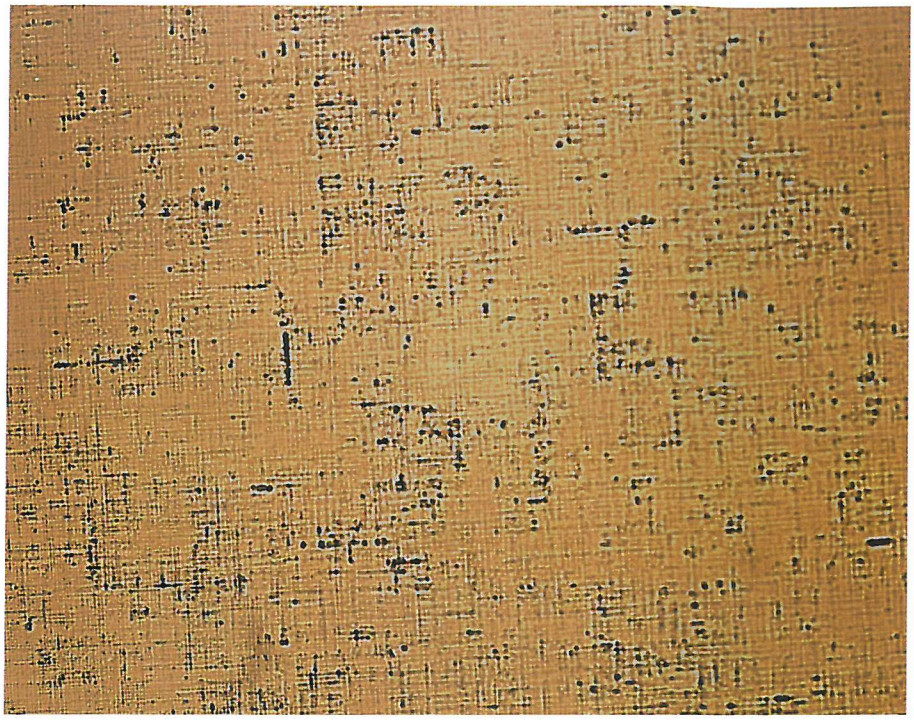

(b)

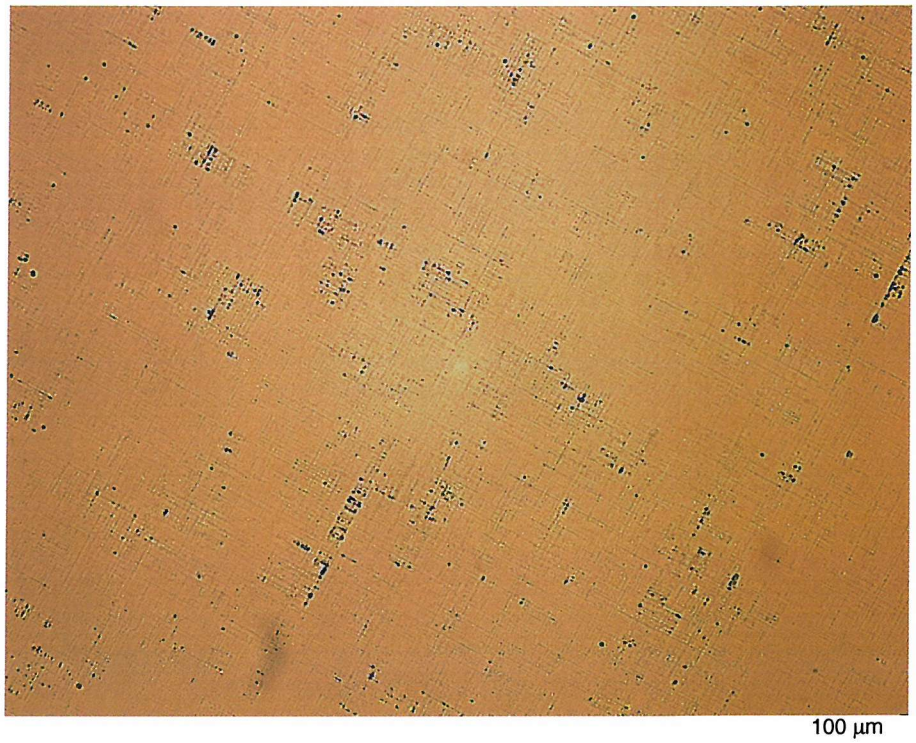

(c)

Figure 6.24. Optical micrographs (obtained at x100 magnification) of the step-graded heterostructure of the first set, *774*: (a) as-grown and Dash-etched for: (b) 50 s, (c) 60 s. The last two micrographs reveal the preferential etching of the crosshatch pattern and the inability to resolve the TD terminations within the crosshatch lines.

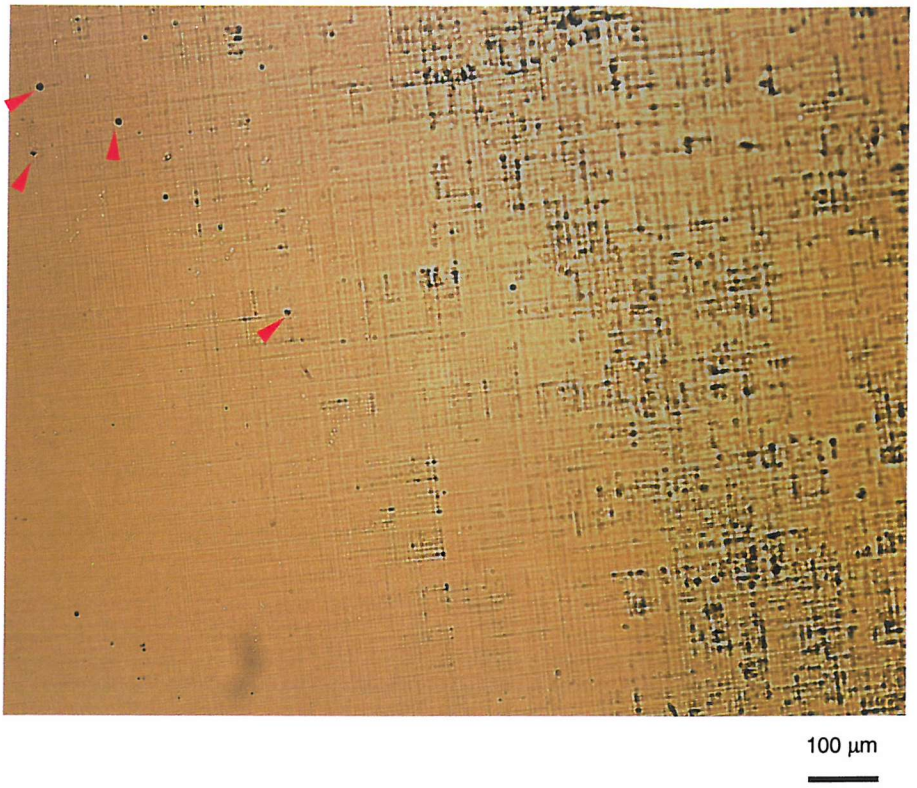

Figure 6.25. Optical micrographs (obtained at x100 magnification) of the step-graded heterostructure of the first set, *774*, Dash-etched for 40 s showing the change in the crosshatch pattern, which occurs towards the edges of the wafer, where the pattern becomes much finer, allowing the defects to be preferentially etched and thus disclosed (arrows).

6.2.3.2. First set: step-graded heterostructure Scanning probe microscopy: AFM

AFM analyses were carried out on the same scanning probe microscope (TopoMetrix Accurex II) using the 100 μm scanner and the ThermoMicroscopes 1520-00 pyramidal silicon nitride probes and under the same conditions (contact mode and 'Topography Forward') used for the linear-graded heterostructures of the first set.

The AFM results confirmed some of the surface morphology information already obtained using Nomarski DIC microscopy. Additionally, AFM provided quantitative information related to the surface topography (e.g. values for the RMS of the surface roughness and for the depth variation along the crosshatch lines).

The 2D AFM images of the step-graded heterostructure of the first set, *774* presented in Figure 6.26 show lateral spacing values ranging from **a few μm** for the fine pattern to **≥20μm** for the accentuated lines. These values are consistent with the Nomarski results for this structure and are similar to the ones obtained for the linear-graded heterostructure of the first set grown under identical conditions, *775*. Additionally, the 2D AFM image presented in Figure 6.26 b shows crosshatch lines (indicated by the blue arrows) with a topography similar to that of intersections of clusters of 60° dislocations having the same Burgers vectors, as described in Chapter 3 and represented schematically in Figure 3.12 f. Similar topographies have already observed in Nomarski contrast for this structure (as indicated by the blue arrows in Figure 6.22 b), and in Nomarski contrast (blue arrows in Figure 6.2 a) and PVTEM (yellow arrows in Figures 6.20 e and f and 6.21 a) for the linear-graded heterostructures of the first set.

The reduced density of trenches running along the surface of the step-graded heterostructure of the first set, *774*, by comparison with the linear-graded structure grown under identical conditions, *775*, results in a smoother surface morphology. This is reflected both qualitatively, in the 3D AFM images presented in Figure 6.27 a and b, and quantitatively in the RMS of the surface roughness values (i. e. ≈ **22.4 nm** for *774*, as shown in Figure 6.26 a compared to ≈ **35.6 nm** for *775*, as shown in Figure 6.9 a for a 100 μm x 100 μm scanned area, and ≈ **9.9 nm** for *774*, as shown in Figure 6.26 b compared to ≈ **13.8 nm** for *775*, as shown in Table 3, for a 20 μm x 20 μm scanned area). Additionally, the 3D AFM images show similar morphologies of the crosshatch lines for the two

heterostructures grown under the same conditions, i.e. long running ridges compared to small crests and troughs as observed in the linear-graded heterostructure of the first set grown at the higher temperature, with the higher initial Ge concentration in the virtual substrate, the lower Ge concentration gradient and the thicker capping layer, *720*.

Both the 3D AFM images (black arrows in Figure 6.27 a) and the height variation measurements along the crosshatch lines for the step-graded heterostructure of the first set, revealed even in this case, the presence of pits along the trenches and enabled the measurement of their in-plane dimension and their depth (Figures 6.28 - 6.29). The results obtained indicate a lower density of smaller and shallower pits present along the crosshatch trenches of the step-graded heterostructure of the first set, *774*, by comparison with the linear-graded one grown under the same conditions, *775*. The values obtained for in-plane dimension and depth of the pits (presented in Figures 6.28-6.29) show that the largest pits (size of $\approx$ **2 μm**) even in this case, are the deepest (up to $\approx$ **56 nm**). Nevertheless, the deepest pits in the step-graded heterostructure, *774*, are much shallower than the pits observed in the linear-graded heterostructure grown under identical conditions, *775* (Figures 6.10 b and 6.11 b). This explains even further the lower values of the RMS of the surface roughness obtained for *774* compared to *775*.

The AFM results showed that the step-graded heterostructure of the first set is characterised by superior surface morphology compared to the linear-graded heterostructures of the first set, grown under identical conditions (i.e. a smoother, flatter surface, with a lower density of trenches and pits).

Some of the AFM results obtained for the first set of heterostructures are also presented in Table 3.

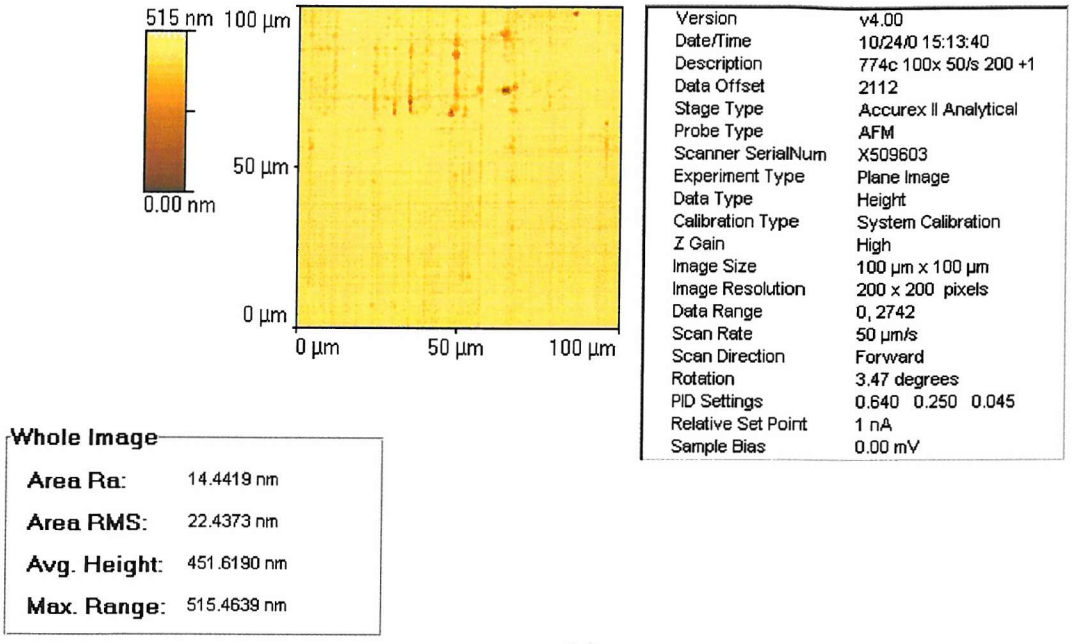

(a)

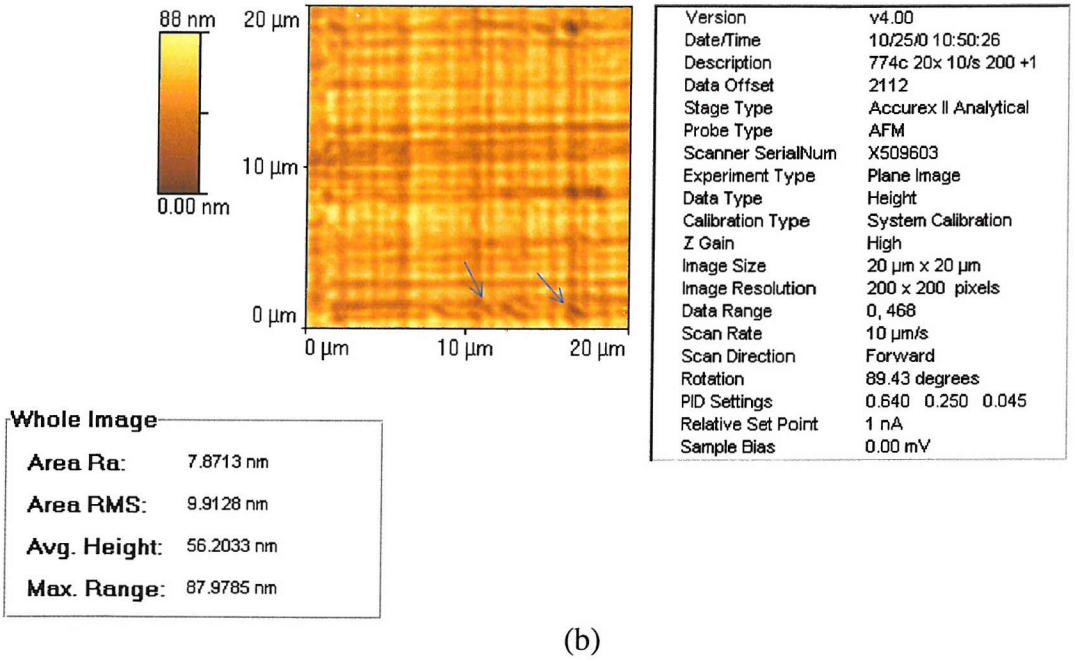

(b)

Figure 6.26. 2D AFM images, scan parameters and the RMS of the surface roughness values for the step-graded heterostructure of the first set, *774* for a: (a) 100 µm x 100 µm scanned area, with a scan rate of 50 µm/s; (b) 20 µm x 20 µm scanned area, with a scan rate of 10 µm/s. The arrows point to crosshatch lines with a topography similar to that of intersections of clusters of 60° dislocations having the same Burgers vectors (as shown in Chapter 3, Figure 3.12 f).

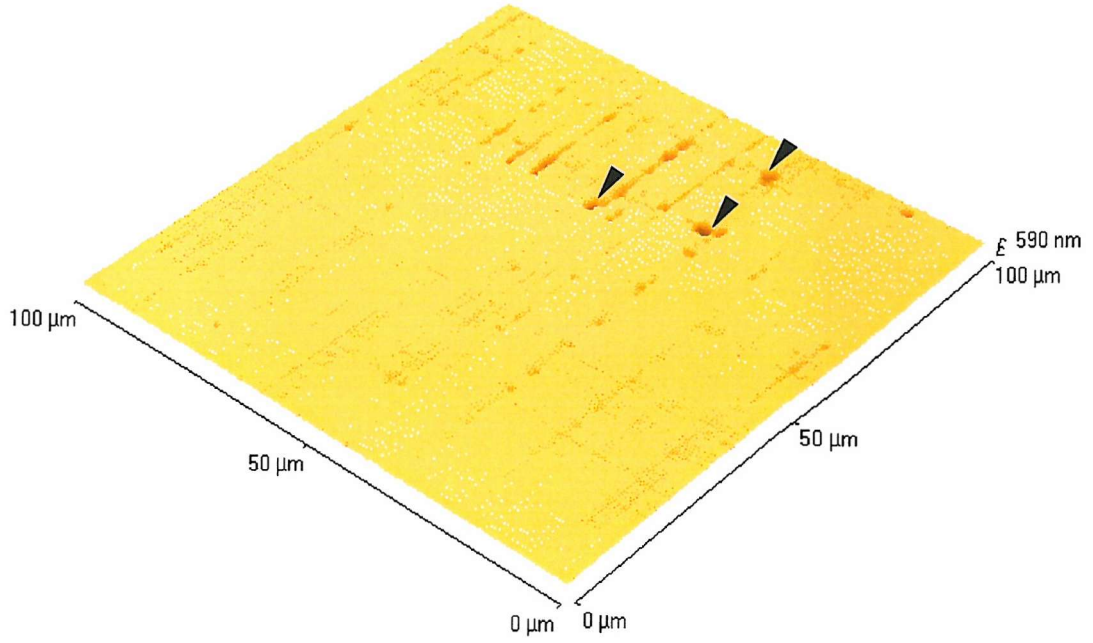

(a)

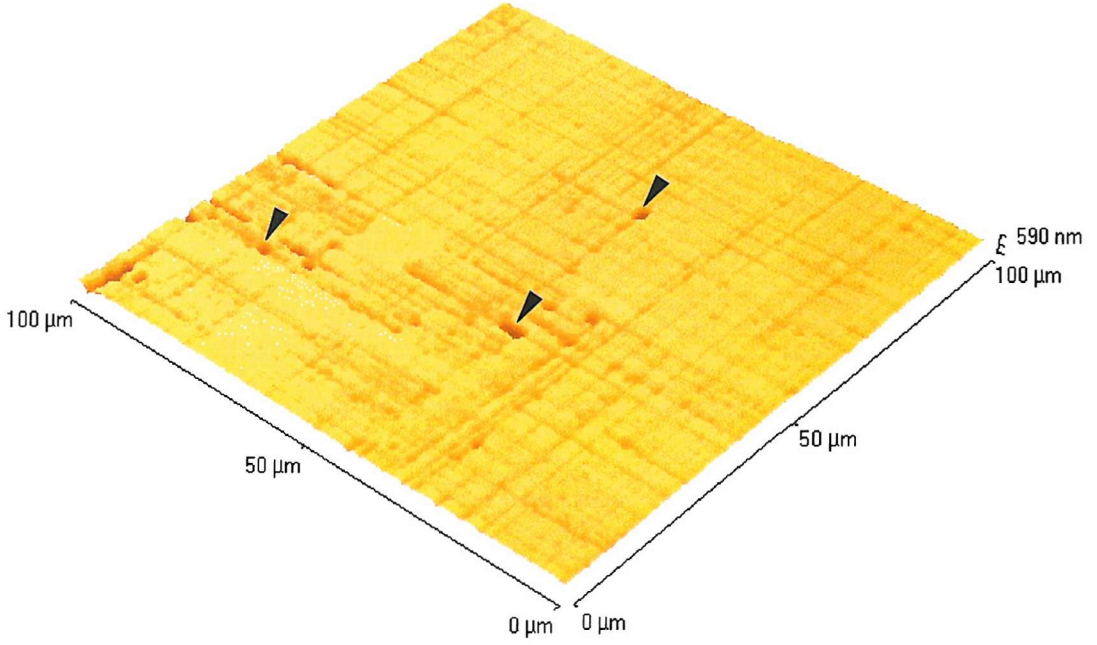

(b)

Figure 6.27. 3D AFM images of 100 µm x 100 µm areas scanned of the two heterostructures of the first set grown under the same conditions, but with different types of variation of the Ge concentration in the virtual substrate: (a) step-graded, *774*, showing a smoother surface characterised by a finer crosshatch pattern; (b) linear-graded, *775*, showing a rougher surface with a higher density of trenches and pits. The arrows indicate the presence of pits along the trenches.

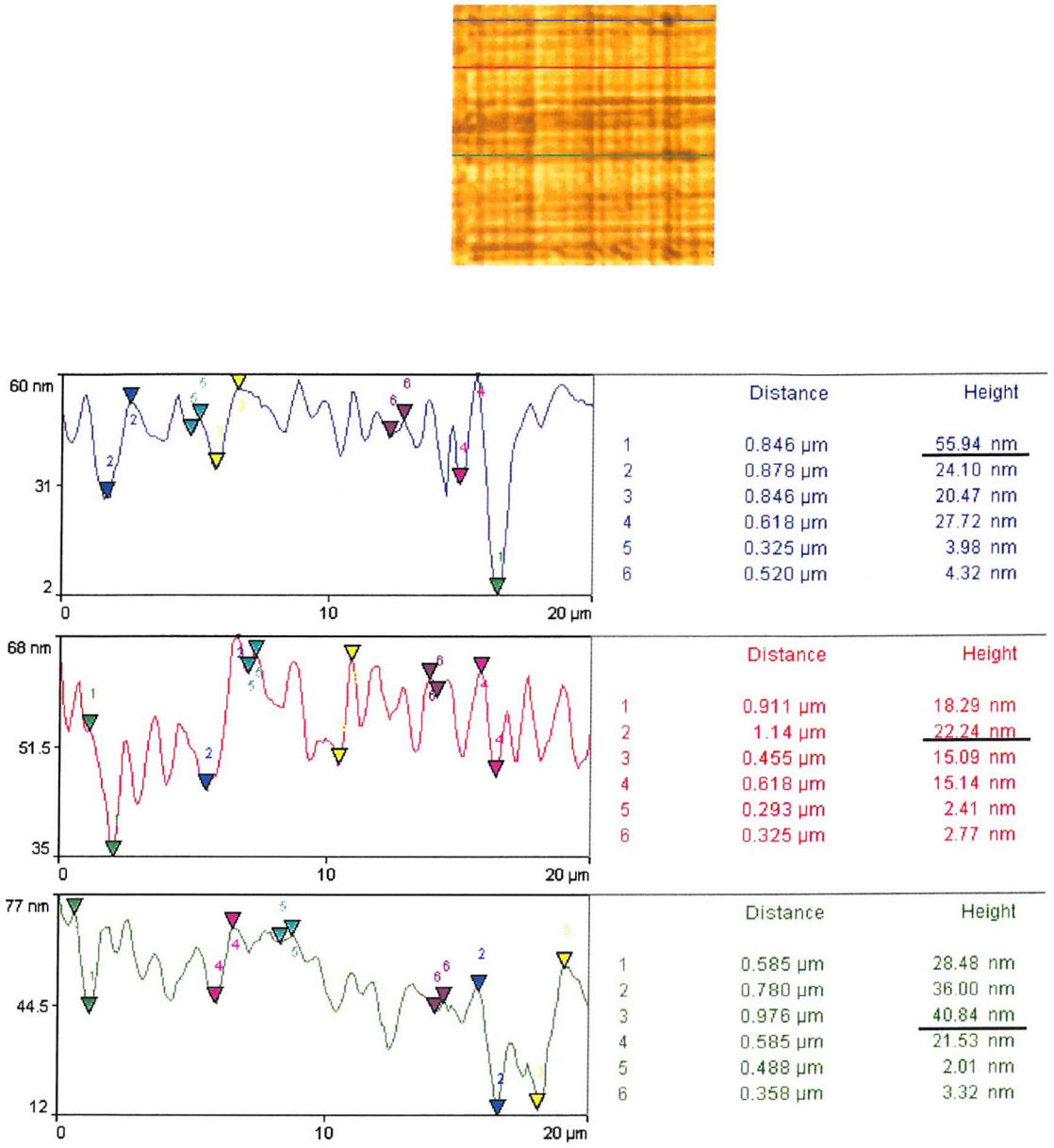

Figure 6.28. 2D AFM images of a 20 µm x 20 µm scanned area and line analysis results for the step-graded heterostructure of the first set, *774*. The underlined values correspond to the deepest pits.

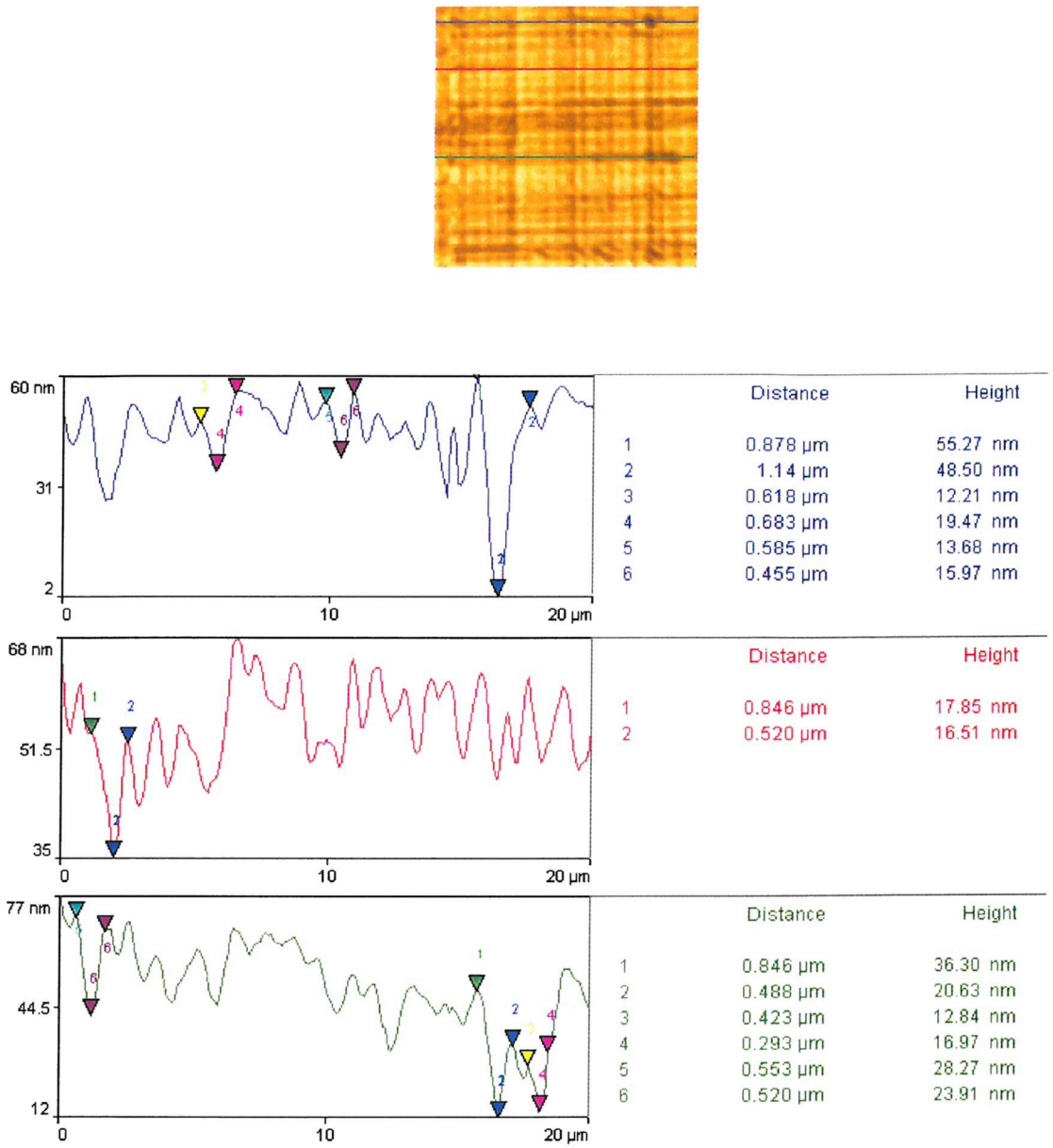

Figure 6.29. 2D AFM image of a 20 µm x 20 µm area scanned and line analysis results obtained from measuring the in-plane dimension and depth of some of the deepest pits present along the crosshatch trenches in the step-graded heterostructure of the first set, *774*.

Sample denomination	Acquisition conditions		Analysis results		
	Scan size (μm^2)	Scan rate ($\mu m/s$)	Area RMS (nm)	Area average height (nm)	Deepest pits depth (nm)
720	100 x 100	50	91.8	437.9	-
	20 x 20	10	27.3	124.9	133.5
775	100 x 100	50	35.6	473.6	-
	20 x 20	10	13.8	105.2	248.8
774	100 x 100	50	22.4	451.6	-
	20 x 20	10	9.9	56.2	55.9

Table 3. AFM analysis acquisition conditions and results obtained for the first set of heterostructures: area RMS, area average height and deepest pits depth.

6.2.3.3. First set: step-graded heterostructure Electron microscopy: TEM analysis

Once again, TEM analyses provided us with information on the internal morphology and the defect content of the step-graded heterostructure of the first set, *774*, not obtainable with any of the other characterisation techniques used, the results of which are presented in the previous two sections (§ 6.2.3.1 - 6.2.3.2). Thus, once more, TEM was used to confirm some of the results already obtained at the same time as to complement them. TEM analyses were carried out on the J.E.O.L. JEM 2000FX transmission electron microscope (Figure 5.6) using the double-tilt sample holder (Figure 5.5). A lanthanum hexaboride (LaB_6) crystal with an applied beam acceleration voltage of 200 kV and the largest spot size (for the highest brightness) was used for analysing the step-graded heterostructure of the first set.

Cross-sectional samples were analysed in bright-field, using different two-beam conditions, in order to select the best analysis settings and carry out dislocation analyses, as explained in Chapter 5, § 5.3.3 – 5.3.4. The XTEM micrographs presented in Figure 6.30 were obtained using the main beam condition.

XTEM micrographs of the step-graded heterostructure of the first set (Figure 6.31 a-f) show, once again, the presence of, what has been identified as a carbon layer, at the Si substrate-SiGe heterostructure interface (indicated by the pink arrows). Even in this case, no obvious contribution of the carbon layer to misfit strain relaxation could be observed. Furthermore, by growing the Si buffer layer, which precedes the growth of the SiGe heterostructure even in this case, the carbon layer was buried and consequently prevented from acting as a heterogeneous source for dislocation nucleation. Most defects do not appear to form at the carbon layer, some defects do not even reach the layer, while others extend beyond it, as deep as **≈ 750 nm** into the Si substrate.

There are some similarities between the interfacial defects observed in both linear-graded heterostructures of the first set (Figures 6.12 – 6.15) and in the step-graded heterostructure of the first set (Figure 6.31). Some dislocation loops running deeply into the Si substrate (**≈ 750 nm**) on **{111}** type planes as in the MFR dislocation multiplication process (described in Chapter 3, §3.2.3.5) are present even in the step-graded heterostructure of the first set. However, the topography and distribution of these deep loops as well as the lack of any of the other MFR characteristic 'traces' [12] does not support the hypothesis

on the operation of such a multiplication mechanism in the step-graded heterostructure of the first set. Other interfacial defects common to both the linear-graded and the step-graded heterostructures of the first set, consist of loops or loop segments, which intersect, forming V-shaped defects (as can be seen in Figures 6.12 – 6.15 and 6.31).

When analysed in XTEM, the step-graded heterostructure of the first set, *774*, shows a completely different internal morphology compared to the linear-graded heterostructure grown under similar conditions, *775*. The five steps of Ge concentration variation in *774* are distinctively delineated by MDs running along one of the <110> directions as imaged in the XTEM micrographs (Figure 6.30). The first step of Ge concentration appears to have the highest density of defects and their density decreases toward the surface, leaving a capping layer MD-free. The XTEM micrographs also show that, differently from the linear-graded heterostructure of the first set grown under identical conditions, the step-graded heterostructure of the first set is characterised by very fine, almost indistinguishable surface undulations (Figure 6.30). Consequently, RMS of the surface roughness measurements of the type carried out on the XTEM micrographs of the two linear-graded heterostructures of the first set (described in § 6.2.2.3) could not be performed on the XTEM micrographs of the step-graded heterostructure of the first set. Hence, the only RMS of the surface roughness results for this heterostructure remain those obtained from AFM analyses.

Similarly to the linear-graded heterostructure of the first set grown under identical conditions, the capping layer of the step-graded heterostructure of the first set, *774,* is completely free from MDs, but is characterised by dislocation segments threading to the free surface (brown and lavender arrows in Figures 6.13, 6.17, 6.18, and 6.19 c and d for *775* and brown arrows in Figures 6.30 and 6.32 for *774*). When analysed in different two-beam conditions (Figure 6.33 a–f), the TDs present in the step-graded heterostructures of the first set, similarly to those in the linear-graded heterostructures of the first set, do not satisfy the invisibility criteria (Equation 5.2 - 5.3) therefore we conclude that they are of the mixed type (Chapter 5, § 5.3.4), in good agreement with results reported in literature for the $Si_{1-x}Ge_x/Si$ (001) system (Chapter 3). TDs in the step-graded heterostructure of the first set appear very similar to the ones observed in the linear-graded heterostructures of the first set. For example, the threading segments indicated by the brown arrows in Figure 6.30 and 6.19 a-d are **60°** dislocations, lying on **{111}** type planes (as already described in § 6.2.2.3). The XTEM micrographs presented in Figure 6.32 for *774* and in Figure 6.18

for *775*, show pileups of TDs running along a **{111}** plane and threading through the whole structure (as already described in § 6.2.2.3). As previously explained, similar pileups have been observed in $Si_{1-x}Ge_x/Si$ (001) structures by other groups, who studied their formation and concluded that they are typically caused by an inhomogeneity that continuously 'punches out' dislocations, under the influence of the misfit strain introduced continuously through Ge concentration grading [4].

Differently from the linear-graded heterostructures of the first set, the type of groups of TDs terminate at faceted pits (presented in Figure 6.16 a-b for the structure *720* and in Figure 6.17 for the structure *775*) appear to be completely absent from the step-graded heterostructure of the first set.

A rough estimation of the TD density, once again, was made for the step-graded heterostructure of the first set based on XTEM results. Values obtained ($\approx$ **10^7-6x10^7 cm^{-2}**) were comparable with those for the linear graded structure grown under identical conditions, *775* ($\approx$ **2x10^7 - 4x10^7 cm^{-2}**).

PVTEM micrographs of the step-graded heterostructure of the first set (Figure 6.34) are very similar with those of the linear-graded heterostructures of the first set (Figures 6.20 – 6.21). This observation is in accordance with those made in high magnification Nomarski contrast and in the 20 μm x 20 μm AFM scans. Some MD pileups similar to the ones observed in the linear-graded heterostructures of the first set (Figures 6.20 – 6.21) can still be seen in the PVTEM micrographs of the step-graded heterostructure of the first set and they are delineated by yellow lines in Figure 6.34 a-b. Additionally, the yellow arrows on the PVTEM micrograph in Figure 6.34 b show cross-slipping dislocations. Dislocation terminations similar to those observed on the PVTEM images of the two linear-graded heterostructures of the first set (indicated by the brown arrows in Figures 6.20- 6.21) are indicated with brown arrows on the PVTEM micrographs of the step-graded structure, *774* in Figure 6.34 b-c. Figure 6.34 c shows a very thin area of the sample from which almost all the MDs have been milled away apart from two parallel ones indicated by the brown arrows. This PVTEM image also shows another type of dislocation, indicated by the red arrow, which most probably is a TD. The PVTEM micrographs presented in Figure 6.34 b-d image some very thin areas of sample from which the MDs have been completely milled away and round-shaped features are present (indicated by the pink arrows). These micrographs show no defects correlated to the round-shaped surface

features, thus indicating either that they are intrinsic to the surface morphology or they are artefacts introduced during sample preparation.

Thickness measurements were easy to perform on the XTEM micrographs of the step-graded heterostructure of the first set, due to the well-defined germanium concentration variation steps. Results obtained showed a value for the thickness of the virtual substrate of ≈ **1.32 μm**, thus in good agreement with the value interpolated from SIMS results obtained on the calibration structures (≈ **1.36 μm**, as shown in Table 1) and similar with the value obtained for the linear-graded heterostructure of the first set grown under identical conditions, *775* (≈ **1.30 μm**), thus indicating a good growth control. The capping layer thickness value for *774*, obtained from XTEM measurements, was ≈ **0.56 μm**, thus higher than the value interpolated from the SIMS results obtained on the calibration structures (≈ **0.24 μm**). This is, once again, consistent with the discrepancy obtained for *775* (≈ **0.82μm**). The discrepancies between the thickness values obtained from XTEM and SIMS seem to be consistent for the linear-graded and step-graded heterostructures of the first set grown under identical conditions. However, measurements carried out on the XTEM micrographs show a thinner capping layer for the step-graded heterostructure of the first set compared to the linear-graded one intended to have an identical thickness. A possible explanation for this concerns the references used for measuring the two thicknesses, i.e. from the upermost MD segment present in the virtual substrate to the free surface (which in the case of the linear-graded structure, *775*, is much more undulated that in the case of the step-graded one, *774*).

XTEM results reinforced the conclusion drawn from the results obtained with the other two analysis methods i.e. that under the growth conditions used for the step and corresponding linear-graded heterostructures of the first set, by grading the Ge concentration in the virtual substrate stepwise, a more efficient misfit strain relaxation mechanism is activated, which results in a superior surface morphology.

These conclusions guided the choice of the growth parameters for the second set of heterostructures. Due to the proven superiority of the relaxation mechanism operating in the step-graded virtual substrate of the first set of heterostructures, five more step-graded heterostructures and only one more linear-graded structure were grown for the second set.

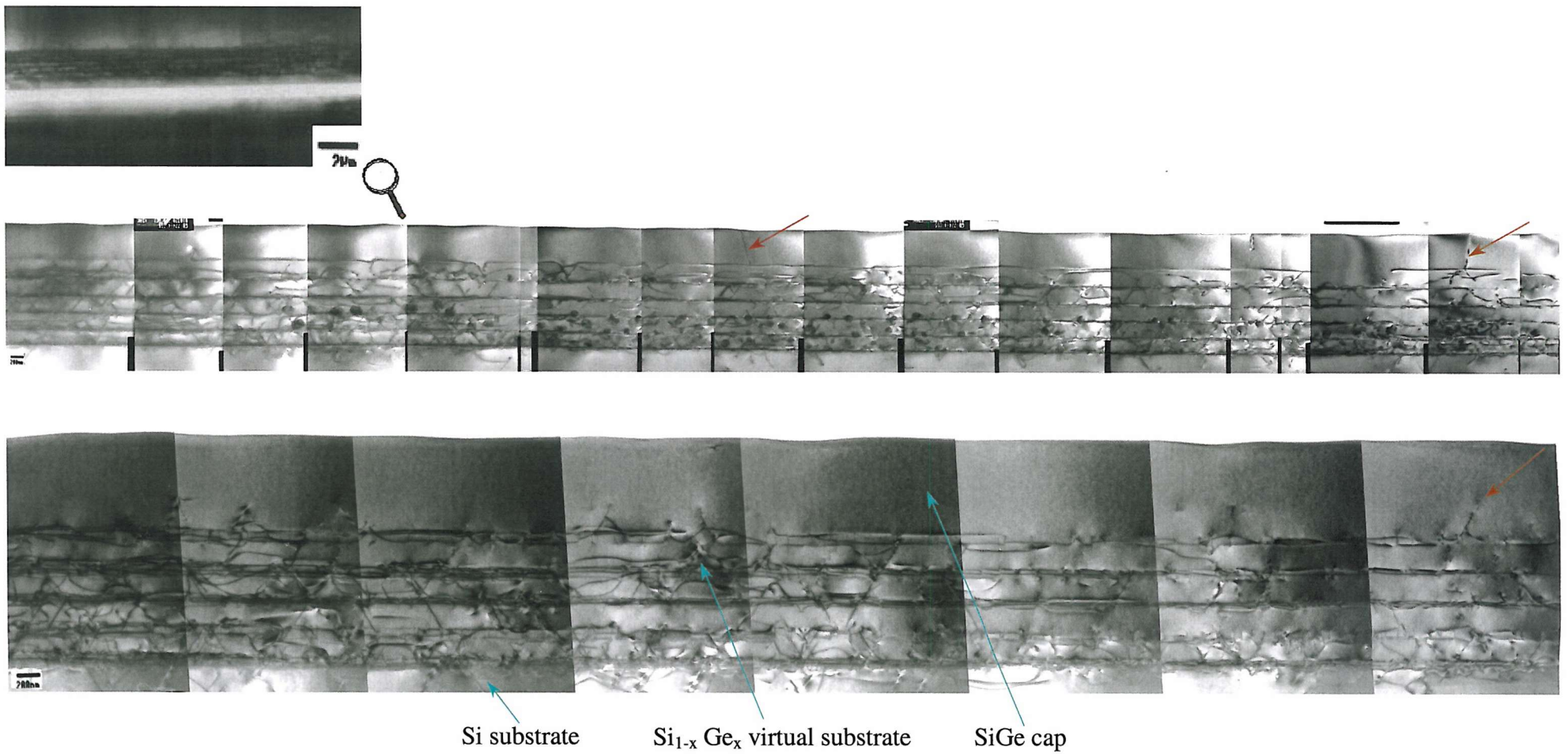

Figure 6.30. XTEM bright-field micrographs (obtained using the main beam condition) of the step-graded heterostructure of the first set, *774*, grown under identical conditions with the linear-graded heterostructure of the first set, *775*. From the top to the bottom of the page, the size of the imaged layer decreases. The brown arrows point to TDs.

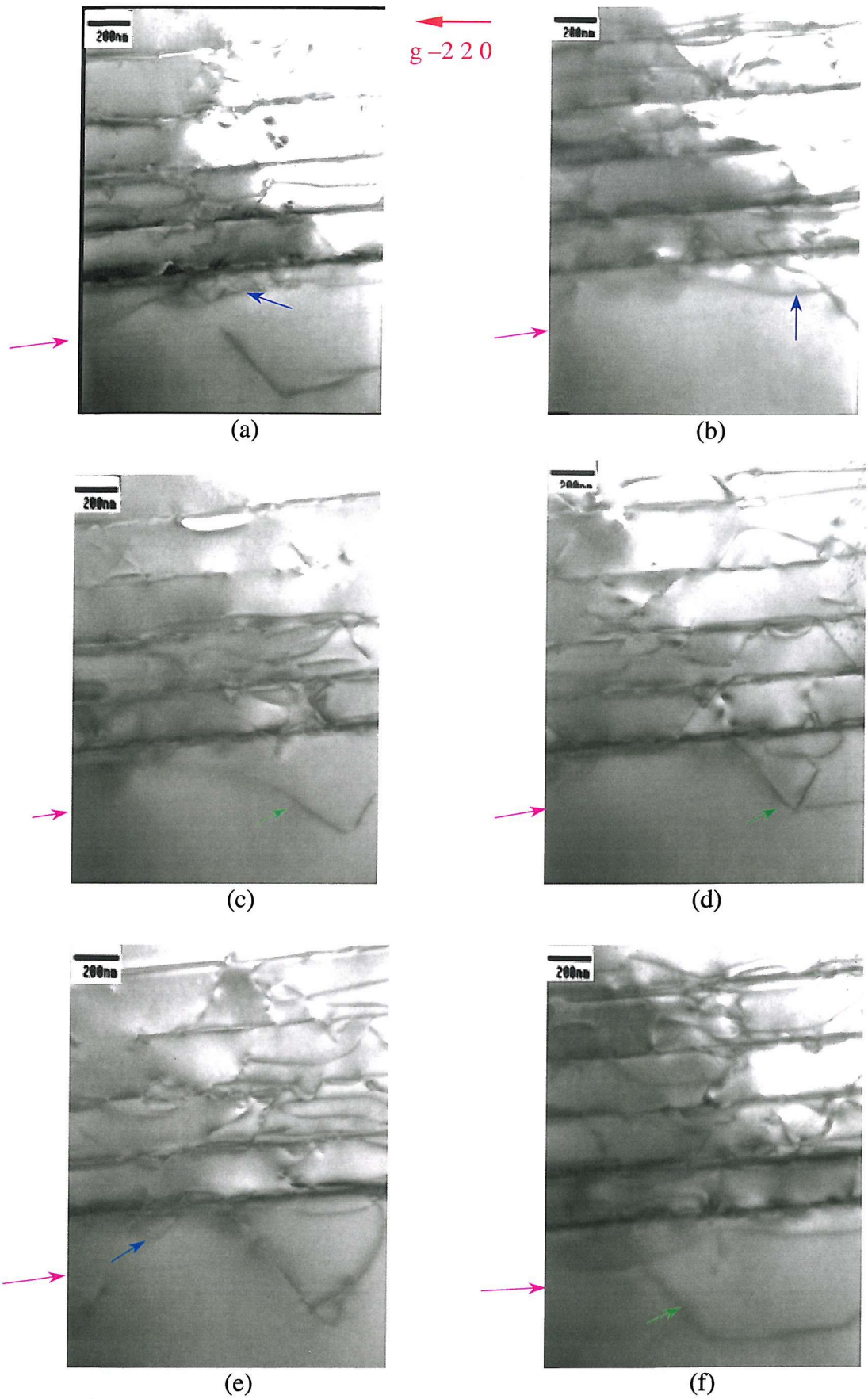

Figure 6.31. Bright-field XTEM micrographs of the step-graded heterostructure of the first set, *774*, showing the carbon layer at the epitaxy interface (pink arrows). Some defects extend into the Si substrate, well beyond the carbon layer (green arrows in c, d and f). A large number of defects do not even reach the carbon layer or stop at it (blue arrows in a, b and e).

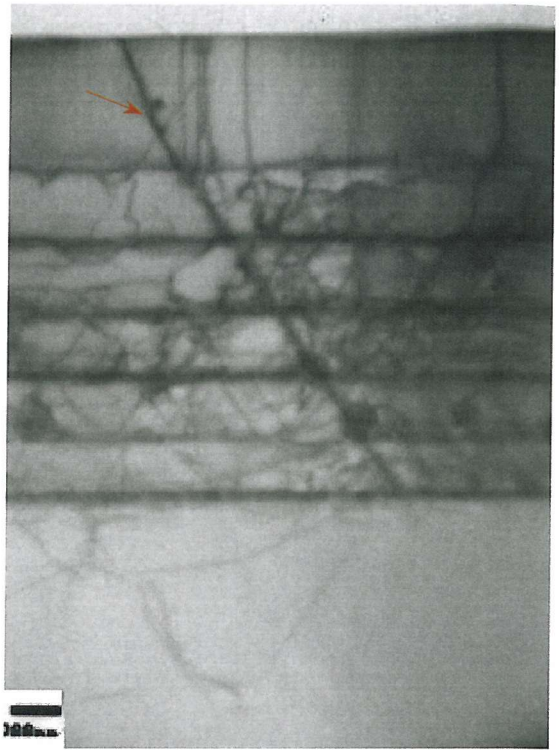

Figure 6.32. Bright-field XTEM micrograph (obtained using the main beam condition) of the step-graded heterostructure of the first set, *774*, showing a pileup of **60°** TDs running through the whole structure on a **{111}** type plane (indicated by the brown arrow), being possibly generated by a heterogeneous nucleation source of the impurity type.

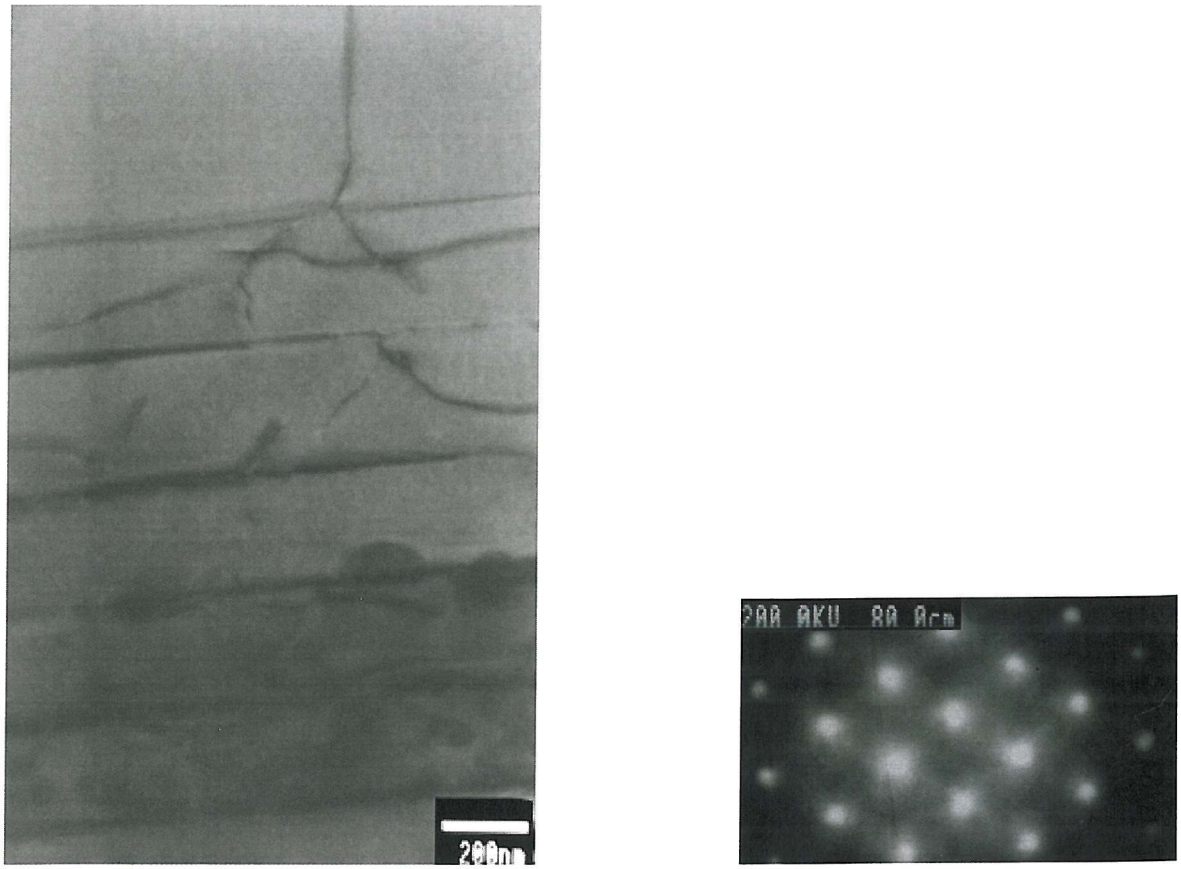

(a)

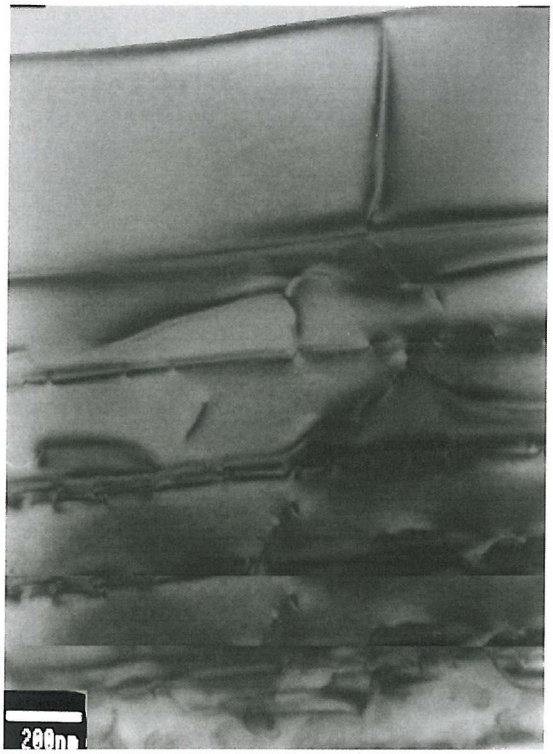

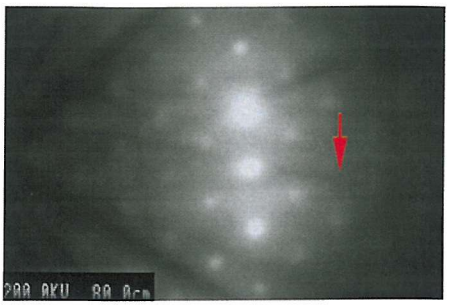

(b)

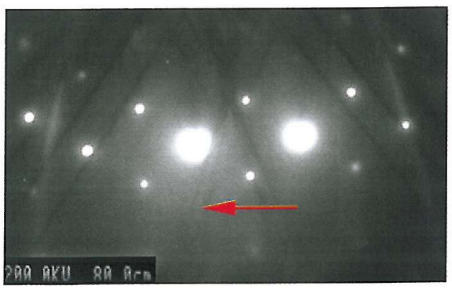

(c)

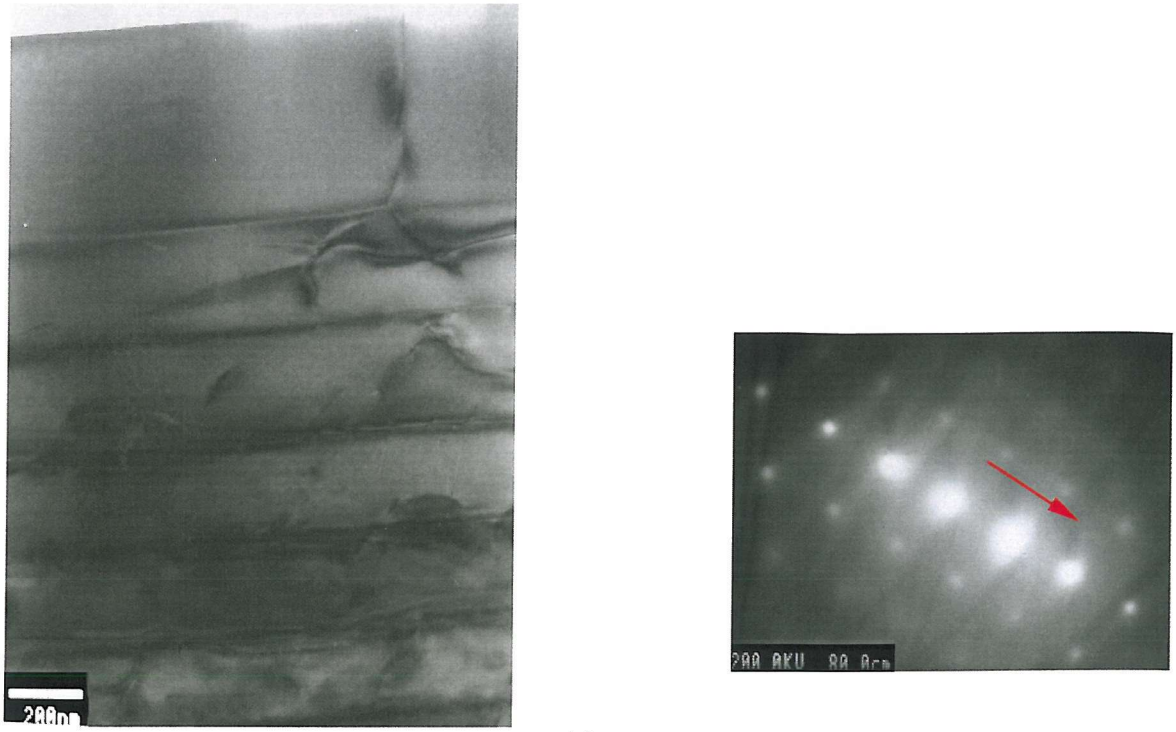

(d)

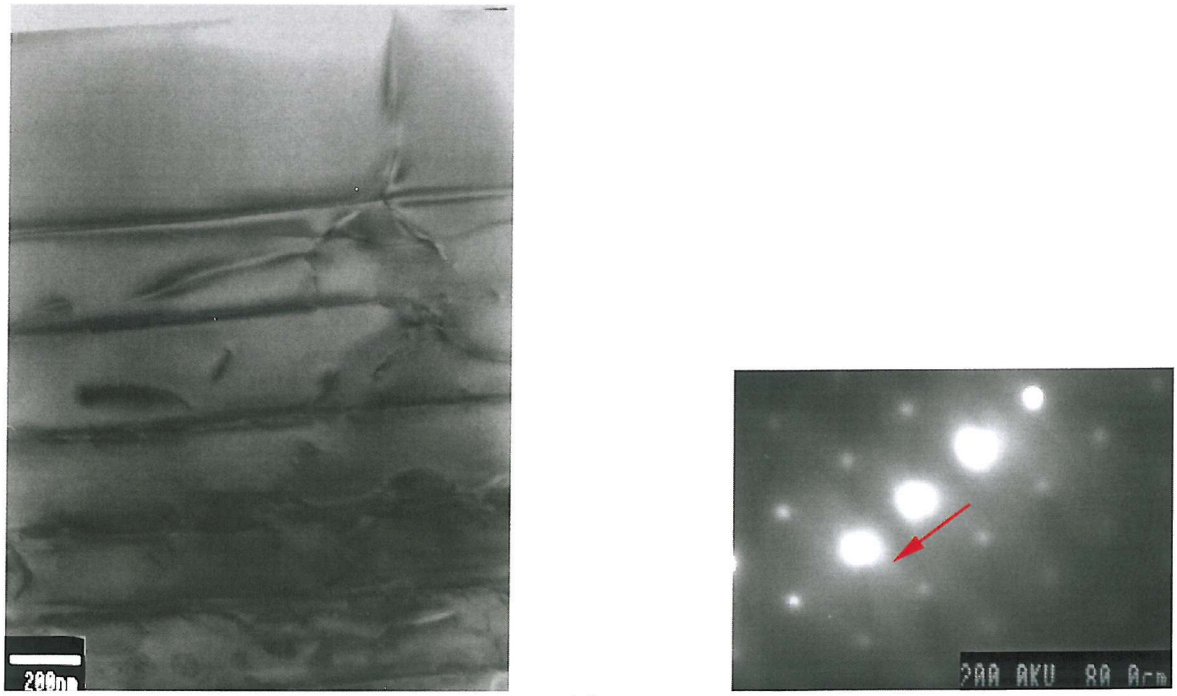

(e)

Figure 6.33. Bright-field XTEM micrographs of the step-graded heterostructure of the first set, *774*, showing the same TD imaged in different two-beam conditions and the corresponding diffraction patterns: (a) main beam condition; (b) $\mathbf{00\bar{2}}$; (c) $\mathbf{\bar{2}20}$; (d) $\mathbf{1\bar{1}\bar{1}}$; (e) $\mathbf{\bar{1}11}$. The fact that the TD is visible in all two-beam conditions indicates its mixed type.

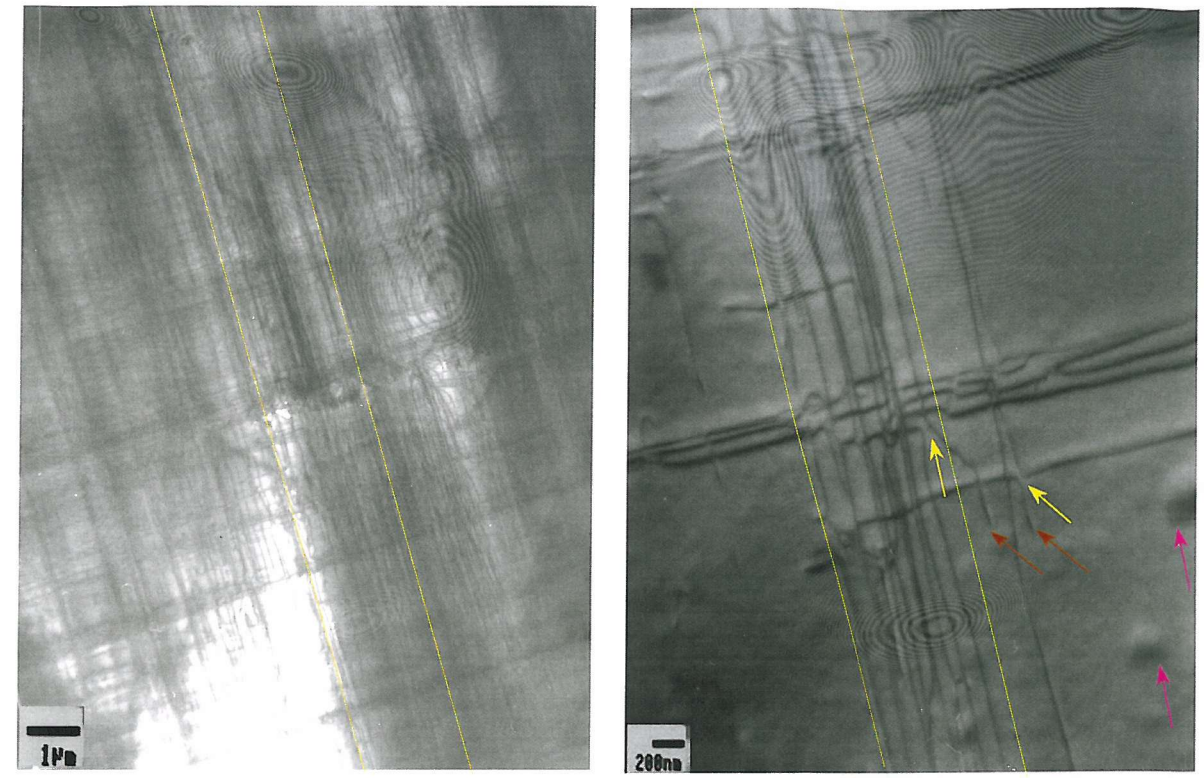

(a) (b)

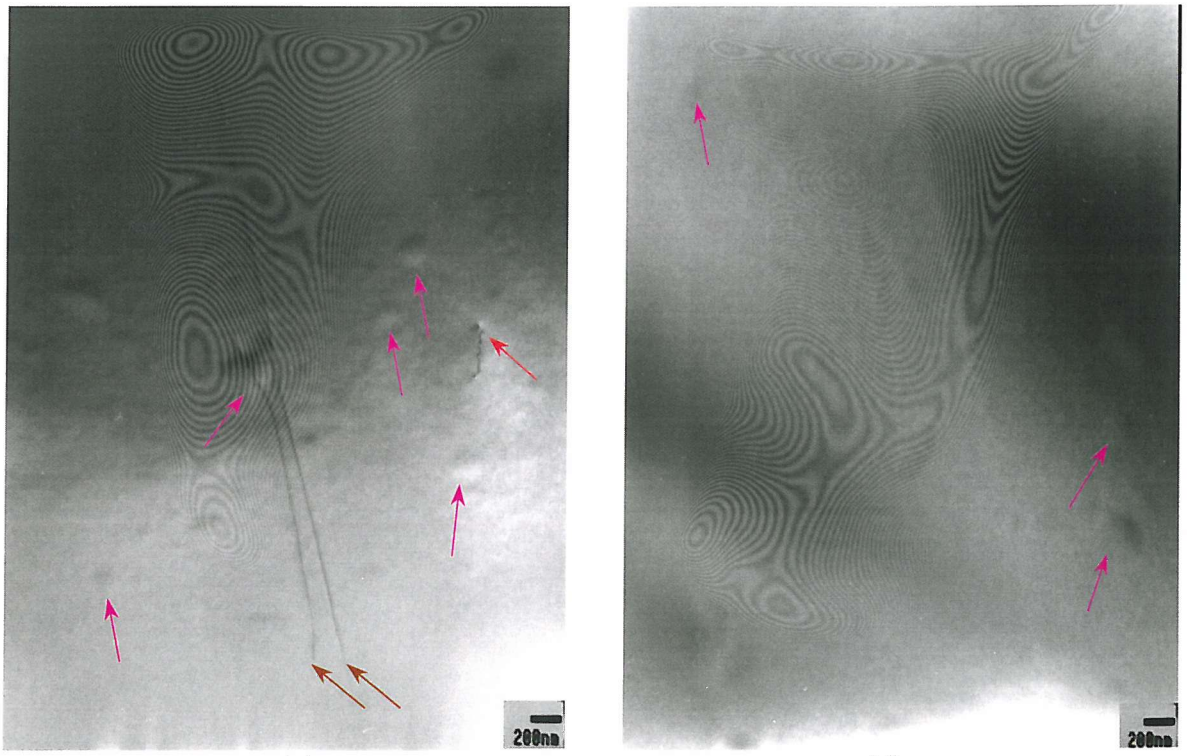

(c) (d)

Figure 6.34 a-d. Bright-field PVTEM micrographs (obtained using the main beam condition) of the step-graded heterostructure of the first set, *774*, showing: pileups of misfit dislocations lying in the **(001)** plane and running along two perpendicular **<110>** directions (delineated by the yellow lines), cross-slipping MDs (indicated by the yellow arrows), 'round'-shaped surface features possibly intrinsic to the surface morphology or introduced during sample preparation (indicated by the pink arrows), dislocations terminations, which may be either TDs or segments of MDs interrupted by the sample preparation (indicated by the brown arrows) and a TD (indicated by the red arrow).

6.2.4. FIRST SET OF HETEROSTRUCTURES DISCUSSION AND CONCLUSIONS

The results presented in § 6.2.2 - 6.2.3 illustrate the effects of the growth parameters on the surface morphology and defect content of the heterostructures grown as part of the test set. Two linear-graded heterostructures, *720* and *775*, and one step-graded heterostructure, *774*, were analysed. For the two linear-graded heterostructures the growth parameters varied were:

- temperature (**800°C** for *720* and lower, **750°C**, for *775*);
- the initial misfit (given by the initial Ge concentration in the virtual substrate): $\varepsilon \approx$ **0.0056** (for a Ge concentration of **13%**) for *720* and slightly lower, $\varepsilon \approx$ **0.0050** (for a Ge concentration of **12%**) for *775*;
- the Ge concentration gradient in the virtual substrate: ≈ **16% / μm** for *720* and higher ≈ **22% / μm**, for *775*;
- the capping layer thickness: ≈ **0.30 μm** for *720* and lower, ≈ **0.24 μm**, for *775*.

These two heterostructures are characterised by the same final Ge concentration in the virtual substrate (**42%**).

In order to compare the effects of two different types of grading profiles in the virtual substrate on the structural properties of these heterostructures, the step-graded structure of the first set, *774*, was grown under the same conditions as the linear-graded structure, *775*, but was characterised by a variation of the Ge concentration in **5 steps of 6%**.

All heterostructures of the test set were grown using the same gas sources (no change of gas bottles occurred between the three growth processes).

Surface morphology analyses showed that all three structures of the test set exhibit, to varying degrees, undulations on their surfaces along two perpendicular **<110>** directions, creating a crosshatch pattern. These undulations are aligned along the same directions as the MDs lying in the virtual substrate, thus indicating some relation with them. This correlation persists despite the fact that the virtual substrate is capped with a thicker capping layer, in the case of *720*, and a slightly thinner capping layer, in the cases of *775* and *774*.

All three analysis methods used (Nomarski, AFM and TEM) showed that for all the structures of the first set, the crosshatch pattern is made of fine, almost periodic undulations, interrupted by what appears to be randomly distributed trenches (i.e. lines of somewhat increased depth) or groups of trenches. The fine undulations form a 'small-scale' pattern, spaced by distances with values consistent for all three structures, ranging from **$\leq$ 1 μm** to **$\approx$ 2 μm**. XTEM analyses showed that the fine ripples on the surface of *720* (Figure 6.12) are characterised by steeper sides (with inclinations ranging between **$\approx$ 5° - 12°**) compared to the fine undulations on the surface of *775* (Figure 6.13), which are characterised by smaller inclination angles (**$\approx$ 2° - 5°**). Additionally, XTEM results for the step-graded heterostructure of the first set revealed a surface characterised by very fine, almost indistinguishable surface undulations (Figure 6.30).

The crosshatch trenches or groups of trenches in all three heterostructures of the first set are spaced by larger distances compared to the fine crosshatch lines. These distances are consistent for all three structures ranging from **$\leq$ 5 μm** to **$\geq$ 20 μm**. Analysed in low magnification Nomarski contrast (x50), for better statistical accuracy, the density of crosshatch trenches and groups of trenches appeared to be the highest in *720*, generating large areas of irregular, accentuated crosshatch pattern in this structure (as indicated by the red arrows in Figure 6.1 a). The other linear-graded heterostructure of the first set, *775*, is characterised by a lower density of trenches and groups of trenches, occupying reduced areas (indicated by the red arrows in Figure 6.1 b). The step-graded heterostructure of the first set, *774*, although grown under identical conditions with *775*, is characterised by the largest areas of fine uniform crosshatch pattern (indicated by the yellow arrow in Figure 6.22 a) interrupted by much reduced areas of trenches (indicated by the red arrows in Figure 6.22 a).

AFM and XTEM analyses revealed the presence of pits (i.e. undulations of somewhat increased depth) along the crosshatch trenches in all three heterostructures of the first set. AFM results showed that these pits are mainly present at the intersection of crosshatch trenches and occasionally, the crosshatch trenches appear to end at a pit. Additionally, AFM analyses showed that the pit depths are similar for the two linear-graded heterostructures of the first set (Figures 6.10 - 6.11), ranging from **$\approx$ 6 nm** to **$\approx$ 250 nm**, and that the largest pits (in-plane dimension of **$\approx$ 3 μm**) are also the deepest (up to **$\approx$250nm**) thus running all through the capping layer of the heterostructure *775*. The deepest pits found in XTEM for the heterostructure *720* (indicated by the red arrows in

Figures 6.12, 6.16 a-b) are characterised by in-plane sizes of ≈ **3 μm** (thus in good agreement with the AFM results) and depth values ranging between ≈ **300 – 600 nm** (the lower limit being in agreement with the AFM results). These pits have side facets inclined at ≈ **24° - 30°**, thus possibly corresponding to **{203}** planes. Similar faceted pits (with sides inclined at ≈ **34°**) have been observed by Cullis et al. [40] in SiGe heterostructures that relax by a surface roughening mechanism (described in Chapter 3, § 3.2.2). The deepest pits found in XTEM for the heterostructure *775* (indicated by the red arrows in Figures 6.13, 6.17) are characterised by in-plane sizes of ≈ **3 μm** (hence, again, in agreement with the AFM results) and depth values of ≈ **150 nm** (thus lower than the AFM ones). They have side facets inclined at ≈ **10° - 12°**, thus possibly corresponding to **{105}** planes. Similar facets have been previously observed in the growth of pure Ge 'huts' on Si substrates (described in [1]).

By comparison, AFM results obtained for the step-graded heterostructure of the first set, *774*, indicate a lower density of smaller and shallower pits present along its crosshatch trenches. The values obtained for the size and depth of the pits in *774* (presented in Figures 6.28 - 6.29) showed, even in this case, that the largest pits (in-plane dimension of ≈ **2 μm**) are the deepest (up to ≈ **56 nm**). Nevertheless, the deepest pits in the step-graded heterostructure, *774*, are much shallower than the pits observed in the linear-graded heterostructure grown under identical conditions, *775* (Figures 6.10 b and 6.11 b).

The fact that the largest pits are also the deepest indicates low growth rates, both at the sides and at the bottom of the pit. This observation may explain the formation of facets in the LPCVD-grown heterostructures. As already explained in Chapter 3, § 3.2.3.4, in the case of chemical vapour deposition (CVD), it was shown by Csepregi et al. [59] that the growth rate on Si surfaces is highest for **(001)**, lowest for **(111)** and intermediate for **(110)**. Consequently, during the formation of the pit, as the growth plane rotates from the **(001)** orientation above the pit, the growth rate on the local planes adjacent to it, also slows down, due to the effect of the surface orientation on the decomposition of gas species. While the growth rate above the pit is reduced, the nearby **(001)** oriented surfaces continue to increase in thickness, rotating the local planes near the pit even more and thus decreasing the growth rate even further. Eventually, facets form, as observed by Fitzgerald et al. [6] and Cullis et al. [40].

Additionally, the 3D AFM results obtained showed that the crosshatch pattern of the sample *720* (Figure 6.7 a) is characterised by a high density of small (in-plane size) crests and troughs aligned along the two perpendicular **<110>** directions, compared to the crosshatch pattern of samples *775* and *774* (Figures 6.7 b and 6.27), which display longer running ridges and channels.

The lower density of trenches and pits in the linear-graded heterostructure of the first set, *775*, results in a reduced surface roughness compared to the other linear-graded heterostructure of the first set, *720*. The structure *775* is characterised by **RMS ≈ 35.6 nm** (as shown in Figure 6.9 a for a 100 x 100 μm^2 scanned area), compared to **≈ 91.8 nm**, for *720* (as shown in Figure 6.8 a for the same size of area scanned). Furthermore, the low density of shallower trenches and pits in the step-graded heterostructure, *774*, results in the best surface quality for this structure, which is characterised by **RMS ≈ 22.4 nm** (as shown in Figure 6.26 a for a 100 x 100 μm^2 scanned area).

To summarise, the surface analysis results obtained with all three characterisation techniques (Nomarski contrast, AFM and XTEM) show a rough surface, consisting of a 'small-scale' crosshatch pattern, made of a high density of small crests and troughs, interrupted by large areas of trenches along which deep pits are present, for the linear-graded heterostructure, *720*, grown at the higher temperature, and with a virtual substrate characterised by a slightly higher initial misfit, a lower Ge concentration gradient and capped with a thicker capping layer, compared to the other linear-graded heterostructure of the first set, *775*, which is characterised by larger areas of fine uniform crosshatch pattern, that form longer running ridges on its surface, interrupted by a smaller density of crosshatch trenches. Nevertheless, there are surface features common to the linear-graded heterostructures of the first set, i.e the deep faceted pits present along the crosshatch trenches. Comparatively, the step-graded heterostructure of the first set, *774*, although grown under similar conditions with the linear-graded heterostructure, *775*, is characterised by a much smoother surface, consisting of large areas of fine uniform crosshatch lines running long distances along the surface and interrupted by a much reduced density of shallower trenches along which a low density of much shallower pits is observed. Furthermore, the deep faceted pits, that are common to the linear-graded heterostructures of the first set, are completely absent from the step-graded heterostructure of this set.

XTEM analyses enabled a better understanding of the underlying causes that generate the differences in surface morphology observed for the three different heterostructures of the first set.

XTEM analyses revealed a completely different internal morphology for the linear-graded heterostructures compared to the step-graded one. The linear-graded heterostructures are characterised by MDs running along **<110>** directions and continuously distributed through the whole virtual substrate, while in the step-graded heterostructure, the different steps of Ge concentration variation in the virtual substrate are clearly delineated by MDs pileups running along **<110>** directions at the steps and connected by **60°** TDs, that glide on **{111}** planes between the steps.

Furthermore, XTEM results revealed the differences between the defect morphologies in the two linear-graded heterostructures of the first set. Essentially, the virtual substrate of the linear-graded heterostructure, *720*, is characterised by a high density of short MD segments, which extend well into the capping layer, while the virtual substrate of the other linear-graded heterostructure of the first set, *775*, shows MD segments running longer distances along **<110>** directions and well-contained within the virtual substrate, leaving the capping layer MD-free. Nevertheless, both linear-graded heterostructures of the first set are characterised by the following common features:

- The interfacial defects in both linear-graded heterostructures of the first set (Figures 6.12 – 6.15) appear similar. Some loops run deeply into the Si substrate (**≥1 μm**) on **{111}** planes, as previously observed for the MFR dislocation multiplication process (described in Chapter 3, § 3.2.3.5). XTEM micrographs of *720* presented in Figure 6.12 show a random distribution of these deep loops, while the top XTEM micrograph of *775* presented in Figure 6.13 shows a more regular distribution of these loops (indicated by the green arrows), spaced by distances ranging between **≈ 1 – 3.5 μm**. However, the lack of any of the MFR characteristic 'traces' [12] argues against the operation of this mechanism in any of these heterostructures. Other interfacial defects common to both linear-graded heterostructures of the first set, consist of loops or loop segments, which intersect, forming V-shaped defects (as can be seen in Figures 6.12 – 6.15).
- The presence of TDs can be observed in the XTEM micrographs of the two linear-graded heterostructures of the first set (brown and lavender arrows in Figures 6.12 – 6.13, 6.16 – 6.19). When analysed in different two-beam conditions (Figure 6.18

a–f), the TDs present in the linear-graded heterostructures of the first set do not satisfy the invisibility criteria (Equation 5.2 - 5.3) therefore we concluded that they are of the mixed type (Chapter 5, § 5.3.4) in good agreement with results reported in the literature for the $Si_{1-x}Ge_x/Si$ (001) system (Chapter 3). The TD pileup shown in Figure 6.18 a-f appears to run through the whole heterostructure. Similar pileups have been observed in $Si_{1-x}Ge_x/Si$ (001) structures by other groups, who studied their formation and concluded that they are typically caused by an interfacial inhomogeneity (of the particulate type) that continuously 'punches out' dislocations, under the influence of the strain introduced continuously through Ge concentration grading [4]. The angle between this dislocation pileup and the MDs directions is **≈ 54°**, indicating that the pileup is made of **60°** dislocations (described in Chapter 3, § 3.2.1) gliding on a **{111}** plane. Figure 6.19 a-d shows other TDs, most of which are of the **60°** type, gliding on **{111}** planes.

- Most TDs appear to end at troughs rather than crests on the surface, especially in *720*. A particular case is that presented in Figure 6.16 a-b for the structure *720* and in Figure 6.17 for the structure *775*, which show groups of TDs with similar topographies terminate at faceted pits. However, the deepest pit found in XTEM for the heterostructure *720* (indicated by the red arrows in Figures 6.12) is characterised by an opening of **≈ 3 μm** and a depth of **≈ 600 nm** and has side facets inclined at **≈ 30°**, thus possibly corresponding to **{203}** planes. As previously mentioned, similar faceted pits (with sides inclined at **≈ 34°**) have been observed in SiGe heterostructures that relax by surface roughening [40]. Comparatively, the deepest pit found in XTEM for the heterostructure *775* (indicated by the red arrows in Figures 6.13) is characterised by an opening of **≈ 3 μm** (hence similar to the deepest pit found in XTEM for *720*) and a depth values of **≈ 150 nm** (thus lower than in *720*) and has side facets inclined at **≈ 10° - 12°**, hence possibly corresponding to **{105}** planes. As already mentioned, similar facets have been previously observed in the growth of pure Ge 'huts' on Si substrates (described in [1]).

From the theoretical viewpoint, three of the growth parameters, that differ between the two linear-graded heterostructures of the first set, are responsible for their different internal morphologies:

- Growth temperature, which is higher for *720*;

- Initial misfit (initial Ge concentration) in the virtual substrate, which is slightly higher for *720*;
- Ge concentration gradient in the virtual substrate, which is lower for *720*.

Both dislocation nucleation and their motion depend on all three of the above growth parameters, as already shown in Chapter 3, § 3.2. Our hypothesis is that in the case of the linear-graded heterostructure, *720*, a higher density of dislocations initially nucleate, both because of the higher growth temperature and because of the slightly higher initial misfit. Under these growth conditions, the density of dislocations initially nucleated is so high as to cause repeated interactions between them, hence the short segments observed on the XTEM micrographs. As already described in Chapter 3, § 3.2.3.5, dislocation interaction may lead to the activation of multiplication mechanisms, which result in further increase of the dislocation density. Additionally, high dislocation densities cause dislocation pinning events, as described in Chapter 3, § 3.2.3.4, which prevent dislocations from moving to relieve the excess strain introduced by the continuous composition grading. In the case of *720*, this results in the presence of MDs well into the capping layer (of constant Ge concentration).

By comparison, in the case of the other linear-graded heterostructure of the first set, *775*, as a result of the lower growth temperature and initial misfit strain, a lower initial density of dislocations nucleate. The higher Ge concentration gradient in this case, does not seem to result in a noticeable increase in the dislocation density. Additionally, XTEM micrographs showed that because of their lower density, dislocations are able to run longer distances along **<110>** directions to relieve the excess strain introduced by the continuous composition grading, despite the lower growth temperature. Furthermore, the lower dislocation density results in a decreased density of dislocation interactions making pinning events less probable. Hence, the misfit strain appears to be relieved within the virtual substrate and as a consequence, the capping layer is left MD-free. This is a typical example that proves the superior efficiency of the virtual substrate of *775*, where dislocation motion prevails over dislocation nucleation, compared to the virtual substrate of *720*, where dislocation nucleation is dominant.

During this study, the difficulty in attempting to understand morphology evolution by looking at the final result, resulted in the impossibility to identify the dislocation nucleation sources and mechanisms. The pileups of **60°** TDs running through the whole

virtual substrate indicate the possible operation of heterogeneous dislocation nucleation sources of the particulate type, as already explained. These sources account for some of the dislocations observed. However, it is most probable that there are other dislocation sources and possibly even multiplication mechanisms, which could not be identified by looking at the result.

A rough estimation of the TD densities (for the dislocations that run all the way to the surface) based on XTEM results, showed values higher by over one order of magnitude for the structure *720* ($\approx$ **$5x10^8$ - 10^9 cm^{-2}**) by comparison with 775 ($\approx$ **$2x10^7$ - $4x10^7$ cm^{-2}**). Additionally, XTEM analyses showed that most TDs appear to end at troughs rather than at crests on the surface, especially in *720*. Furthermore, XTEM analyses revealed in both linear-graded heterostructures of the first set, groups of TDs with similar morphologies, terminate at the deepest faceted pits (indicated by red arrows in Figures 6.12 and 6.13).

In relaxed graded heterostructures grown under low misfit strain conditions, it has long been known that a crosshatch surface morphology occurs when growth is carried out on **(001)** oriented substrates [1]. Although, the presence of the crosshatch has been associated with the MD lines at the mismatched interface, the exact correlation between these dislocations and the overall surface morphology has not been clarified yet.

Fitzgerald et al. demonstrated that the crosshatch pattern correlates with the MD groups present at the heterointerface [4] and argued that it is a response of the epitaxial surface to the strain fields originated from the buried MDs [5]. In the case of graded layers grown under identical conditions, the distance between the free surface and the MDs is given by the grading rate (concentration gradient), which gives the amount of misfit introduced per thickness. In support of their theory, Fitzgerald et al. demonstrated that a higher concentration gradient and hence a reduced thickness of the graded layer, which brings the free surface closer to the MDs, results in a rougher surface [5]. In order to justify a causal relation between the MD strain fields and the surface morphology, Fitzgerald et al. considered two models: a model, which determined the magnitude of the defect strain fields at the surface and a model which described the response of the surface to the strain fields [5]. The first model was derived from using continuum elastic theory and the expressions for the dislocation strain fields, and the other model was based on equilibrium calculations between the strain energy and the surface energy. Based on their model, Fitzgerald et al. explained the formation of surface trenches as a reaction of the surface to

the strain fields of groups of MDs, nucleated by heterogeneous sources. Additionally, they explained the blocking of TDs at such trenches and the formation of faceted pits as a consequence, as already described in Chapter 3, § 3.2.3.4.

Conversely, Jesson et al. [39] and Cullis et al. [40] showed that both high growth temperatures and high misfit strains (generated by high initial Ge concentrations and/or high Ge concentration gradients) can result in the formation of surface cusps and/or deep ripple troughs. The accumulation of high stresses at these types of surface features lowers the barrier to MD nucleation and, ultimately, they may act as MD sources. Cullis et al. explain surface facet formation in SiGe heterostructures as a mechanism for lowering the surface energy and stabilising the ripple arrays caused by surface roughening.

In this study, we have been faced, once again, with the difficulty of attempting to understand the evolution of the misfit strain relaxation processes that take place in the virtual substrates of the two linear-graded heterostructures of the test set, by looking at their final morphologies. For both linear-graded heterostructures of the first set, relaxation by MD nucleation at interfacial inhomogeneities, which results in groups of MDs, that create deep troughs on the surface of the sample, subsequently trapping TDs, relaxation by surface roughening, followed by half-loop dislocation nucleation at the deepest troughs, and relaxation by a combination of the previous two mechanisms, seem equally possible. The fact remains that the higher growth temperature (mainly) and the slightly higher initial misfit strain in the virtual substrate of the linear-graded heterostructure of the first set, *720*, trigger off the operation of a misfit strain relaxation mechanism, which results in an increased surface roughness and TD density compared to the other linear-graded heterostructure of the first set, *775*.

Nevertheless, the similarities in the surface morphologies of the two linear-graded heterostructures of the first set indicate similarities in their misfit strain relaxation mechanisms. By comparison the misfit strain relaxation mechanism that operates in the step-graded heterostructure of the first set, results in a completely different surface morphology, but a TD density similar to that of the linear-graded heterostructure grown under identical conditions.

XTEM analyses revealed a totally different morphology for the step-graded heterostructure of the first set, *774*, compared to the linear-graded one grown under

identical conditions, *775*. While the linear-graded heterostructure, *775*, is characterised by long MD segments running along **<110>** directions continuously through the whole virtual substrate, the step-graded heterostructure, *774*, is characterised by long MD segments running along **<110>** directions and piled-up at the Ge concentration variation steps. In both cases, the MDs are well confined within the virtual substrates, leaving capping layers, MD-free. Furthermore, comparable densities of TDs run through the capping layers of the two structures (≈ $\mathbf{10^7}$ - $\mathbf{6x10^7\ cm^{-2}}$ for *774*, compared to ≈ $\mathbf{2x10^7}$ - $\mathbf{4x10^7\ cm^{-2}}$ for *775*). When analysed in different two-beam conditions (Figure 6.33 a-f), the TDs present in the step-graded heterostructures of the first set do not satisfy the invisibility criteria, therefore we concluded that they are of the mixed type in good agreement with results previously obtained on the linear-graded heterostructures of the first set and others reported in literature for the $Si_{1-x}Ge_x/Si$ (001) system. Additionally, pileups of **60°** TDs gliding on a **{111}** plane and threading through the whole structure, typically caused by an interfacial inhomogeneity that continuously 'punches out' dislocations, under the influence of the excess strain introduced through Ge concentration grading [4], are also common to all the heterostructures of the first set (Figures 6.18 and 6.34).

However, differently from the linear-graded heterostructures of the first set, the type of groups of TDs terminating at faceted pits (presented in Figure 6.16 a-b for the structure *720* and in Figure 6.17 for the structure *775*) appear to be completely absent from the step-graded heterostructure of this set. Furthermore, very fine, almost indistinguishable ripples characterise the surface of the step-graded heterostructure. Consequently, while it looks possible for surface roughening to have occurred in the initial stages of the virtual substrate relaxation for the two linear-graded heterostructures of the first set, it appears less probable in the case of the virtual substrate of the step-graded heterostructure of the first set. If surface roughening did not occur in the early stages of misfit strain relaxation in the virtual substrate of the step-graded heterostructure of the first set, it means that its surface morphology is generated by the strain fields associated with the MDs [5] well-confined within the virtual substrate. This would justify the much smoother surface morphology that characterises this structure. The decrease in defect density observed in the upper step of Ge concentration in this structure results in a lower value of the dislocation strain fields and hence in a smoother surface.

Under the growth conditions used for the two heterostructures of the first set, *775* and *774*, it appears that step grading of the Ge concentration in the virtual substrate, results in a

distribution of misfit strain, which activates a relaxation mechanism that generates a superior surface morphology compared to linear grading.

The TD density results obtained for the heterostructures of the first set have mainly a qualitative value, due to the highly estimative approach of the technique used to determine them. As already shown, attempts to quantify the TD density by using disclosure chemical etch combined with optical microscopy for better statistical accuracy, failed because all the etchants used preferentially etched the crosshatch pattern, thus not allowing us to resolve the emergence of the TDs within the etched crosshatch lines. This suggests that both the strain fields and the local composition at the crosshatch lines locally alter the etching rate. Additionally, attempts to quantify the TD density by using PVTEM also failed. The sample preparation technique used involved thinning the samples from the substrate side. Under these conditions, when analysed in PVTEM, once again, the MDs were mainly imaged, making it difficult to resolve the emergence of the TDs.

Overall, we concluded that SUMC-LPCVD growth at 800°C with an initial misfit of 0.56%, activates an inefficient misfit strain relaxation mechanism in the linear-graded virtual substrates, whereby dislocation nucleation prevails over dislocation motion, resulting in rough surfaces, with deep trenches and deep faceted pits along the trenches, and high TD densities. Growth at 750°C, with an initial misfit of 0.50% activates a more efficient relaxation mechanism, whereby dislocation motion in order to relieve the misfit strain, dominates over dislocation nucleation, resulting in smoother surfaces and reduced TD densities. Additionally under these latter growth conditions, the step variation of the Ge concentration in the virtual substrate, results in a superior surface morphology compared to the linear variation.

The conclusions drawn from the results obtained for the test set of LPCVD-grown SiGe virtual substrate-based heterostructures, guided the choice of growth parameters for the second set.

6.3. SECOND SET OF HETEROSTRUCTURES

6.3.1. OBJECTIVES

The experimental results obtained on the first test set of heterostructures enabled conclusions regarding the effects of the growth temperature, the initial Ge composition, the Ge concentration gradient and grading profile (i.e. linear and stepwise) in the virtual substrate and of the capping layer thickness, on the surface morphology and defect content of these structures. Additionally, they prove very useful for further growth calibration. These results also showed that neither Nomarski contrast coupled with disclosure chemical etch, or PVTEM can be successfully used for TD density analysis.

Based on the conclusions drawn from the first set, the combinations of growth parameters used for the second set of heterostructures were carefully chosen, with the aim of improving their surface morphology and defect content. Consequently, all the heterostructures of the second set were grown at the same temperature (**750°C**), that characterised the heterostructures of the first set with superior structural properties, *775* and *774*. Additionally, emphasis was placed on the step grading of the Ge concentration in the virtual substrate, due to the superior properties it generated for the test samples. Consequently, five different step-graded (*VSC1-VSC3, VSC5* and *VSC6*) and only one linear-graded (*VSC4)* virtual substrates were incorporated in the heterostructures grown as part of the second set.

All structures of the second set, except that grown for reproducibility, have virtual substrates characterised by the same initial (**0%**) and final (**32%**) Ge concentration. By starting the Ge grading at **0%**, the virtual substrates of the second set, differently from those of the first set, are characterised by a very 'gentle' introduction of misfit strain, with the aim of reducing the TD density and improving the surface morphology. Additionally, the growth of the final Ge concentration step in the virtual substrate with a low gradient of only **≈ 6% / μm** (**≈ 2%** over **≈ 300 nm**) was meant to improve the results of misfit strain relaxation on the TD density by acting as a 'filter' for dislocations, as explained in Chapter 3, § 3.2.3.2 and § 3.2.4. From the representation of the critical thickness variation with the Ge content shown in Chapter 3, Figure 3.7, for a Ge concentration of **2%**, a critical thickness of **≈ 1 μm** would be required. Hence, the last step of Ge concentration in these heterostructures by being still compressively strained contributes to turning the threading segments into misfit segments, thus keeping the dislocations well confined

within the virtual substrate underneath. Moreover, should this last step relax, the growth of a tensile strained capping layer (of ≈ **30%** Ge concentration) would improve the surface morphology as tensile strain does not encourage surface roughening [1].

The final Ge concentration value in the virtual substrates of the heterostructures of the second set was chosen in order to enable their use as templates for further strained overgrowth (as described in Chapter 1).

In order to carry out Hall mobility measurements on the heterostructures of the second set, to assess their suitability for device fabrication, **p-n junctions** were incorporated in each of their capping layers.

For the step-graded heterostructures of the second set, the effects on the surface morphology and defect content of the following growth parameters were analysed:

- the presence of a microelectronic structure within the capping layer of *VSC1*, which was compared to *VSC2*, grown under identical conditions, but without the microelectronic structure;
- the thickness of the capping layer of *VSC3* (**2 μm**), grown under identical conditions with *VSC2*, with a capping layer half as thick (**1 μm**);
- the Ge concentration gradient in the virtual substrate of *VSC5* (≈ **8% / μm**), grown under identical conditions with *VSC2*, which is characterised by a Ge concentration gradient of ≈ **16% / μm**. Additionally, by using double the number of half Ge concentration steps in the virtual substrate, this structure was meant to act as an intermediary between the two types of Ge concentration grading i.e. step (*VSC2*) and linear (*VSC4*).

Additionally, a check of the growth reproducibility for these types of SiGe heterostructures was carried out, by repeating the step-graded heterostructure grown as part of the first set, *774*, in the second set, *VSC6*.

Further comparisons between the effects of step and linear grading of the Ge concentration in the virtual substrate were also carried out. One linear-graded heterostructure, *VSC4* was grown as part of the second set, under identical conditions with the step-graded heterostructure, *VSC2*.

Furthermore, only Nomarski DIC microscopy, AFM and XTEM analyses were used for the characterisation of the second set of heterostructures.

Firstly, the results obtained on the step-graded structures of the second set are presented comparatively. Secondly, the results obtained on the linear-graded heterostructure of the first set are shown and compared with the results obtained on the step-graded heterostructure grown under identical conditions. Comparisons with the test structures are carried out throughout were appropriate. Finally, the results are summarised and discussed and conclusions are drawn.

6.3.2. STEP-GRADED HETEROSTRUCTURES

6.3.2.1. Optical microscopy: Nomarski DIC analysis

Nomarski DIC microscopy analyses for the initial assessment of the surface morphology of the step-graded heterostructures of the second set were carried out using the same equipment and under the same conditions as those used for the first set of heterostructures.

Nomarski micrographs of the structure of the second set denominated *VSC6*, grown under identical conditions with the step-graded heterostructure of the first set, *774*, with the aim of checking the reproducibility of the growth process for these types of heterostructures, show similar surface morphologies for these two structures (Figure 6.35 a-b) indicating qualitatively, good reproducibility. However, quantitative results (obtained from AFM and TEM analyses), which will be presented in the following two sections, will give a more accurate appreciation of the reproducibility.

Low magnification Nomarski analyses of the other four step-graded heterostructures of the second set, *VSC1–3* and *VSC5*, show different surface morphologies compared to the step-graded heterostructure of the first set, *774* and its correspondent of the second set, *VSC6* (Figures 6.35 a-b and 6.36 a-d). These heterostructures of the second set are characterised by smooth surfaces, with a fine and regular crosshatch pattern. Some slightly more accentuated crosshatch lines can still be observed (red arrows in Figure 6.36 a-d), but the difference in contrast between them and the fine lines is much smaller than previously observed for the heterostructures of the first set, indicating that they correspond to much shallower trenches. Trenches of the type generated by the accentuated crosshatch lines observed in the first set of heterostructures are completely absent from the second set. Most crosshatch lines appear to run almost from one edge to the other of the low magnification Nomarski micrographs presented in Figure 6.36 a-d.

Nomarski micrographs of all four heterostructures of the second set grown under similar conditions, *VSC1-3* and *VSC5*, also show the presence of what was identified for the first set of heterostructures, as pits. Specific to the second set of heterostructures and completely absent from the first set, is the presence of some large surface features of both 'round' and 'square' shapes (indicated by the black arrows in Figure 6.36 a-d), the density of which is observed to decrease from *VSC1* to *VSC5*. A rough estimation of the density of these large pits shows a decrease from $\leq$ **512x10^{-6} / μm^2** for *VSC1*, to $\leq$ **213 x 10^{-6} / μm^2**

for *VSC2*, to $\leq$ **85 x 10^{-6} / μm^2** for *VSC3* and to $\leq$ **42 x 10^{-6} / μm^2** for *VSC5* (Figure 6.36 a-d). Small size, shallow pits as already encountered in the first set of heterostructures are also present along the accentuated crosshatch lines in all four step-graded heterostructures of the second set grown under similar conditions. Their density is noticeably smaller than in the step-graded heterostructure of the first set, which was grown under different conditions (Figures 6.35 b and 6.36 a-d).

High magnification Nomarski analyses (x1000) allowed the measurement of the crosshatch spacing. Values obtained are consistent for all four heterostructures of the second set grown under similar conditions and they are $\leq$ **1 μm**. Furthermore, the in-plane dimensions of the large surface features could be measured. These measurements showed that the large 'round-shaped' pits have smaller in-plane sizes, up to $\approx$ **8–10 μm** diameter (Figure 6.37 a–d), compared to the 'square-shaped' ones, which have larger linear dimensions of up to $\approx$ **20 μm** (Figure 6.38 a–d). The high magnification Nomarski micrographs also show that some of these features appear to end in a point, thus being of conical or pyramidal shapes, while others appear to end in a flat surface, thus being of truncated cone or pyramid shapes (Figure 6.39). Most of these features do not seem to influence the morphology of the crosshatch pattern around them (Figures 6.37 and 6.38), thus suggesting that they may have been incorporated during the later stages of the growth (i.e. during the growth of the capping layer). Few of them are connected to others and always align along one of the **<110>** directions (Figure 6.40 a–d) thus supporting even further the hypothesis of these features having formed after the formation of the crosshatch lines, which may have acted as nucleation sites for them.

No surface features of the type that reproduce perpendicular dislocation interaction topographies, as encountered in the step-graded heterostructure of the first set (indicated by the blue arrows in Figure 6.22 b) appear to be present in the step-graded heterostructures of the second set grown under similar conditions *VSC1-3* and *VSC5*.

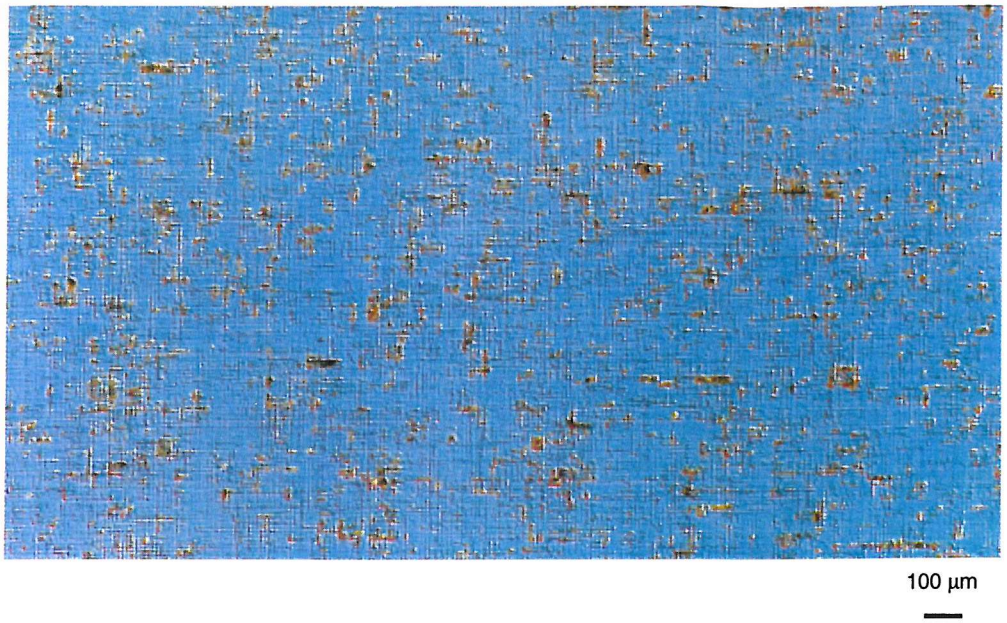

(a)

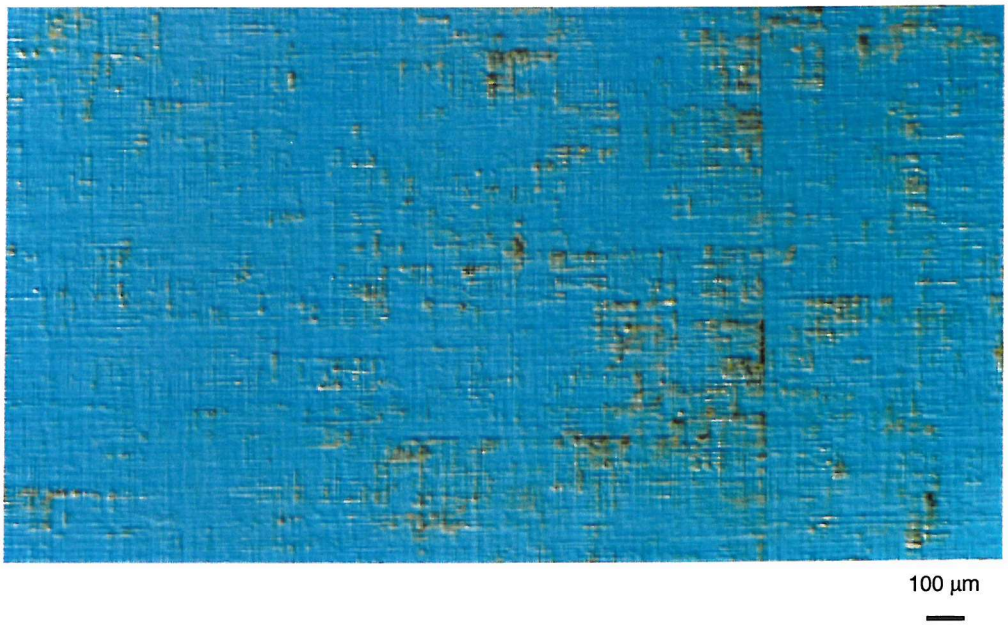

(b)

Figure 6.35. Nomarski DIC micrographs (obtained at x50 magnification) of the two step-graded heterostructures grown under identical conditions, but as part of the two different sets of samples, in order to check the reproducibility of the growth process: (a) *VSC6*, grown as part of the second set and (b) *774*, grown as part of the first test set. They show very similar surface morphologies.

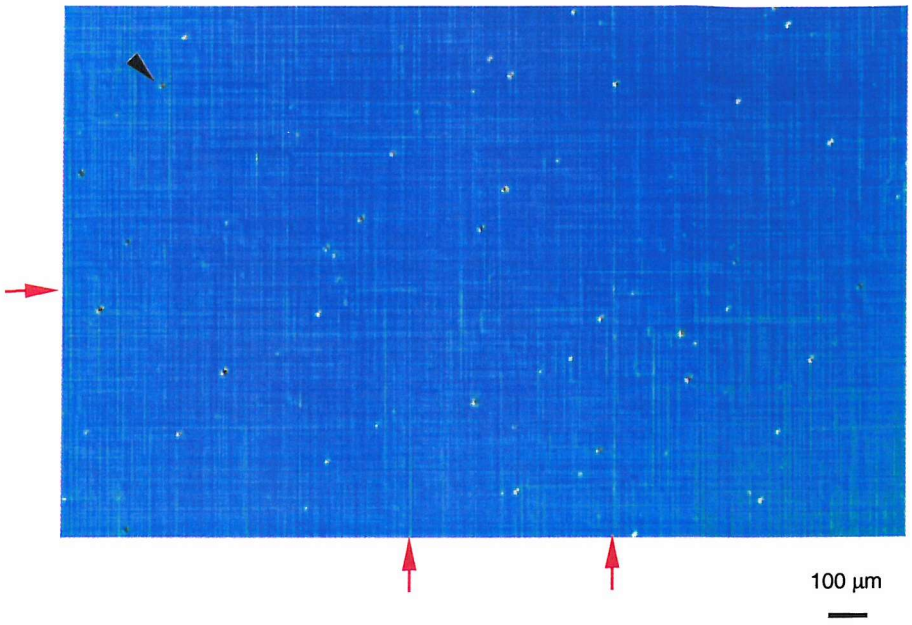

(a)

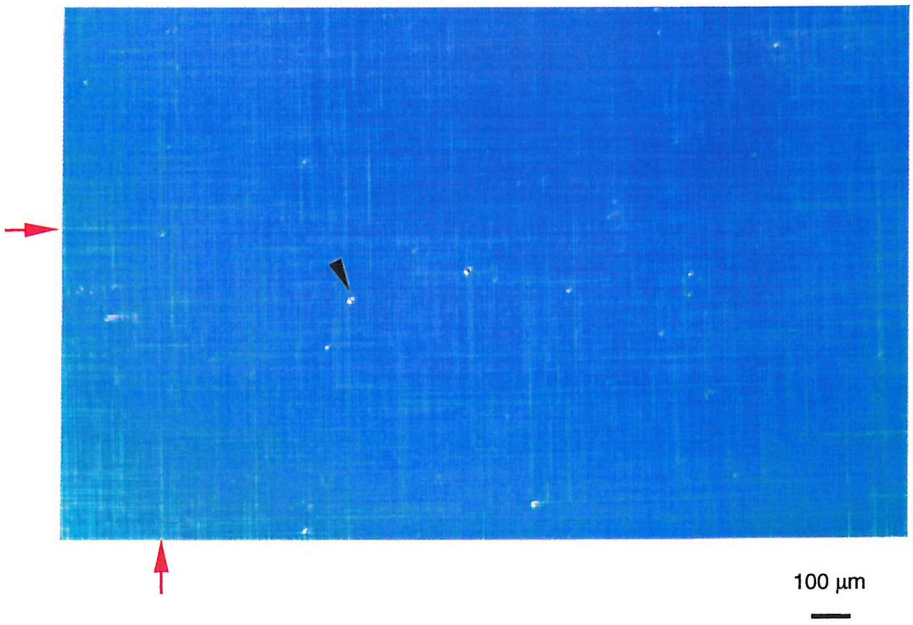

(b)

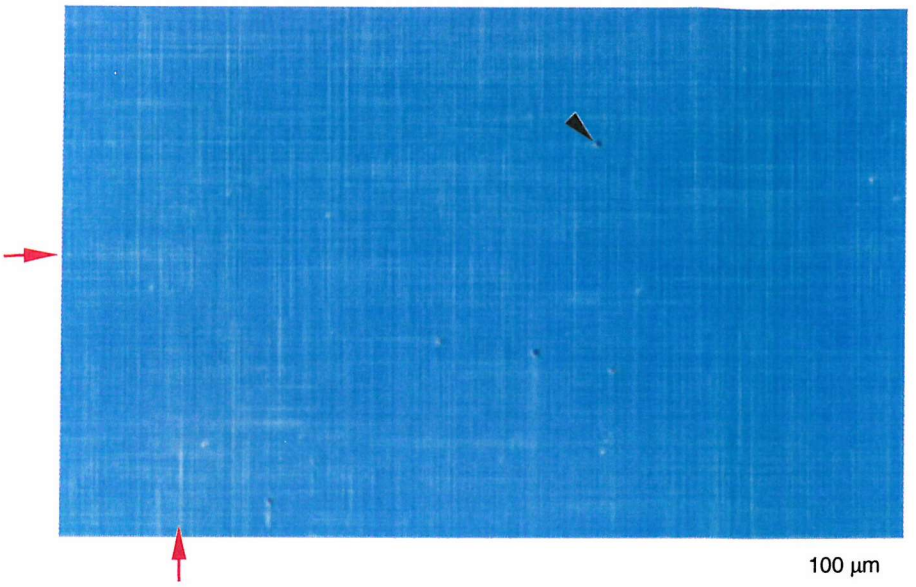

(c)

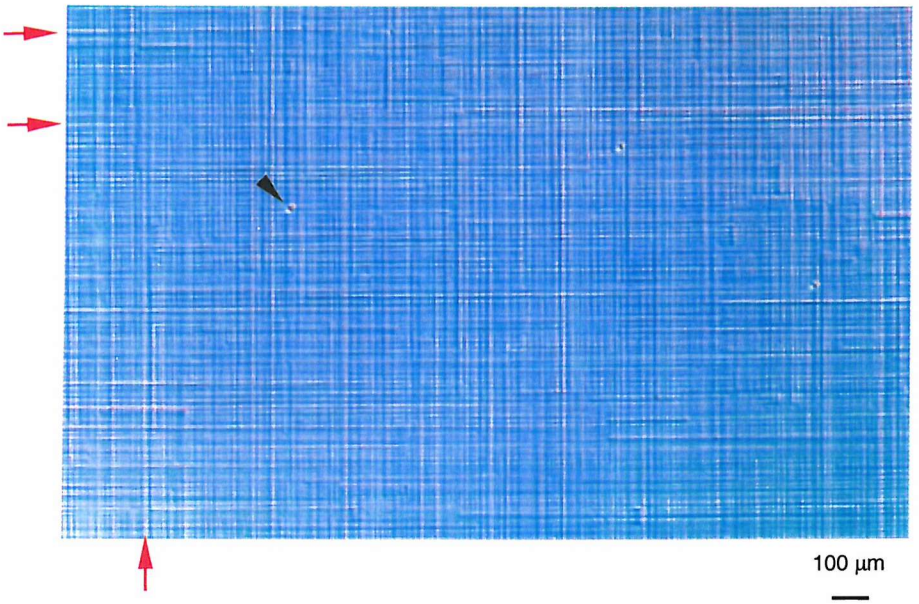

(d)

Figure 6.36. Nomarski DIC micrographs (obtained at x50 magnification) of the four step-graded heterostructures of the second set: (a) *VSC1*, grown first, which incorporates a microelectronic structure, showing a fine crosshatch pattern and the presence of large surface features; (b) *VSC2*, grown second, under identical conditions with *VSC1*, but without the microelectronic structure, showing the fine crosshatch pattern and a lower density of large-sized surface features; (c) *VSC3*, grown third, under identical conditions with *VSC2*, but with a thicker capping layer, showing the regular crosshatch pattern and an even further reduced density of large-sized surface features; (d) *VSC5*, grown fifth, under similar conditions with *VSC2*, but with a variation of the Ge concentration in the virtual substrates in double the number of half-sized Ge concentration steps, showing the fine crosshatch pattern and an even lower density of large-sized surface features. The red arrows indicate the slightly more accentuated crosshatch lines. The black arrows point to large surface features characteristic of the second set of heterostructures.

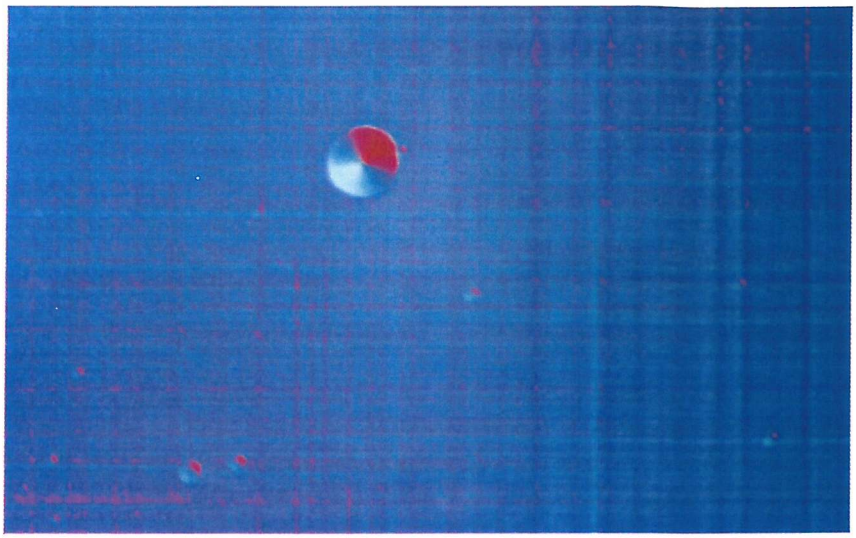

(a)

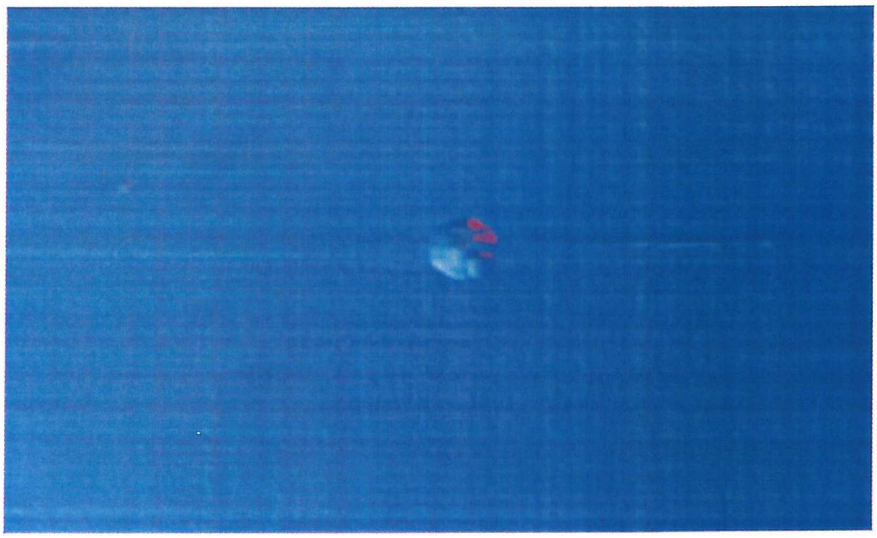

(b)

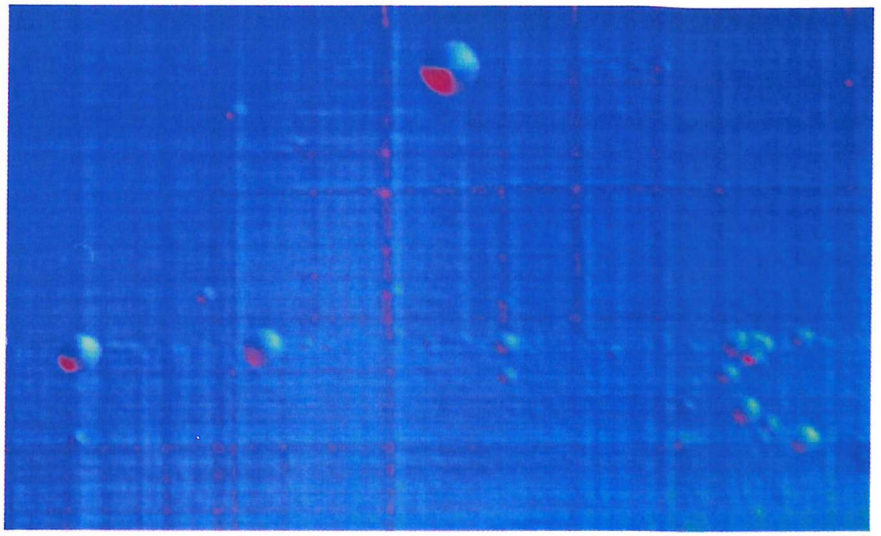

(c)

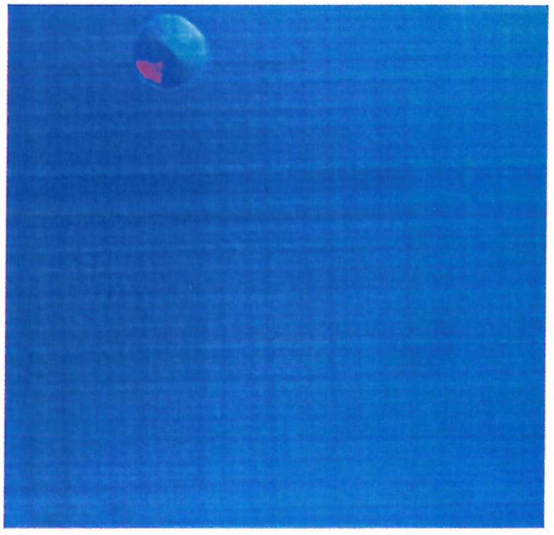

(d)

Figure 6.37. Nomarski DIC micrographs (obtained at x1000 magnification) showing large 'round-shaped' defects with diameters up to **8–10 μm** in four of the step-graded heterostructures of the second set: (a) *VSC1*; (b) *VSC2*; (c) *VSC3*;(d) *VSC5*.

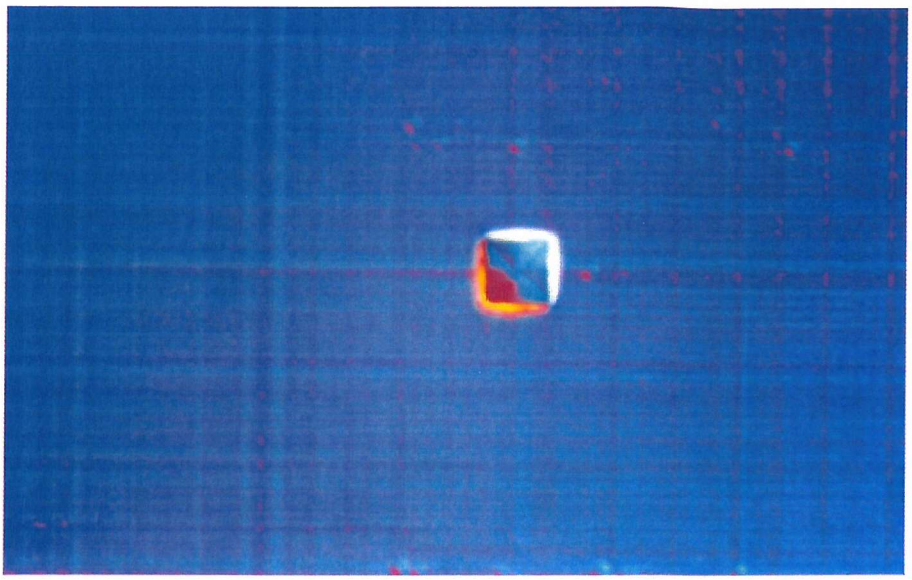

(a)

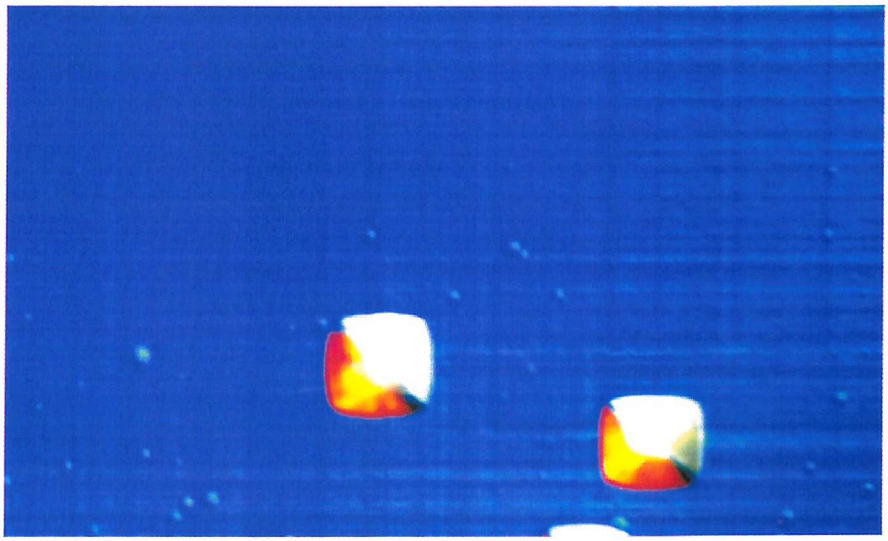

(b)

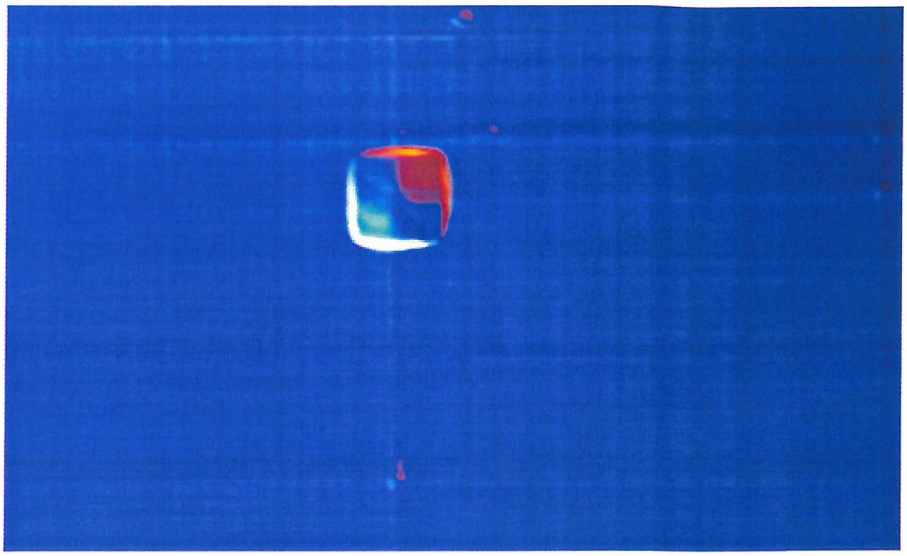

(c)

(d)

Figure 6.38. Nomarski DIC micrographs (obtained at x1000 magnification) of four of the step-graded heterostructures of the second set showing large 'square-shaped' defects with a linear dimension of up to ≈ **20 µm** in: (a) *VSC1*; (b) *VSC2*; (c) *VSC3* (d) *VSC5*.

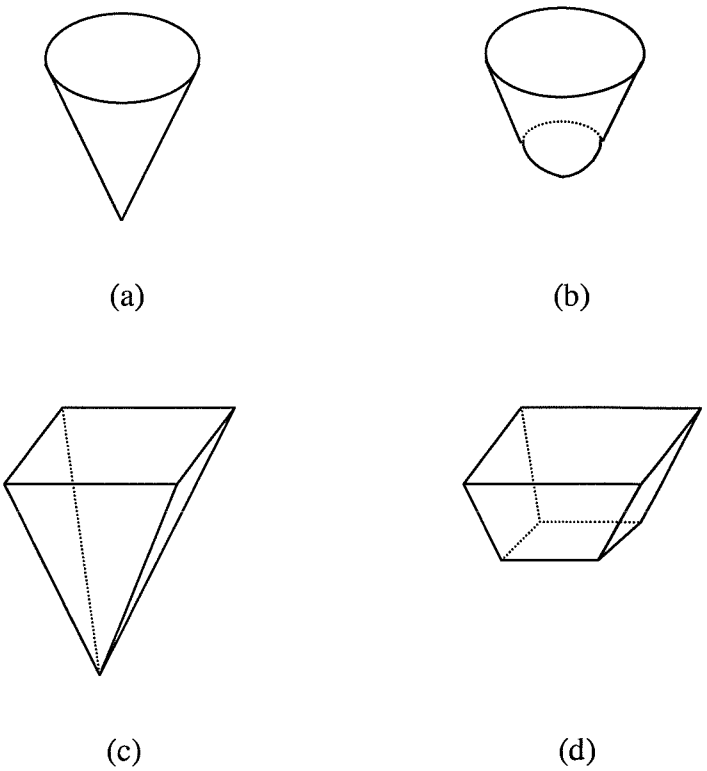

Figure 6.39. 3D schematic representation of the proposed morphology of the growth defects incorporated in the second set of heterostructures: (a) conical shape; (b) truncated-cone shape; (c) pyramidal shape and (d) truncated-pyramid shape, the latter two with a larger base dimension than the conical and truncated cone shapes.

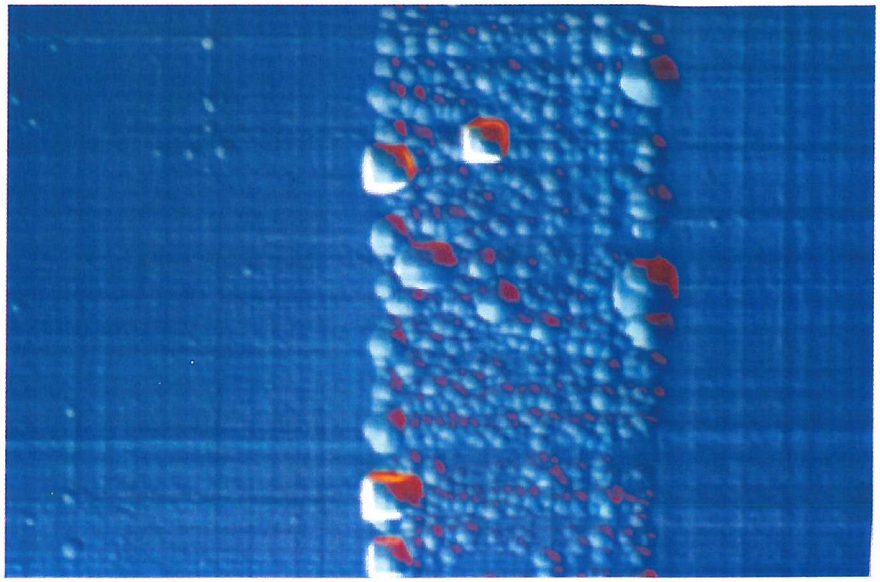

(a)

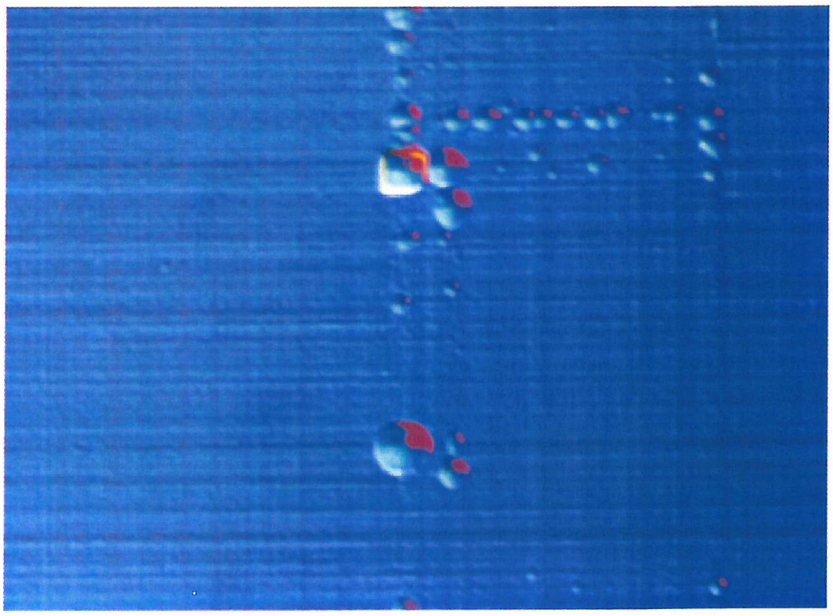

(b)

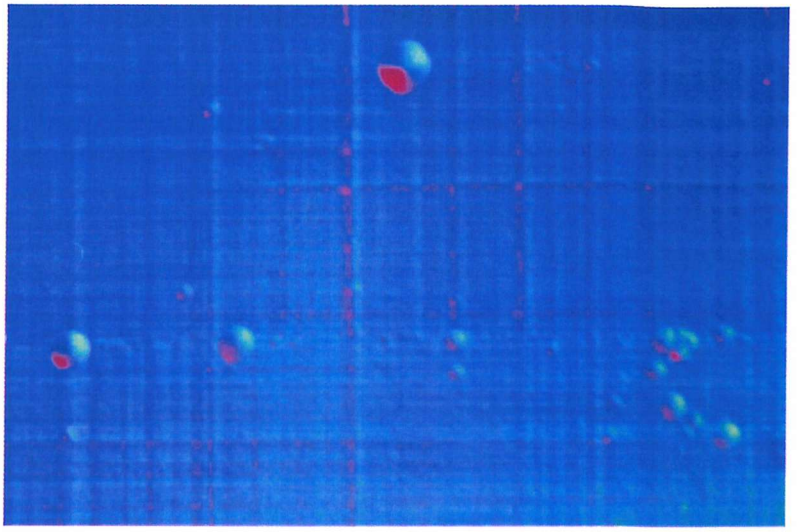

(c)

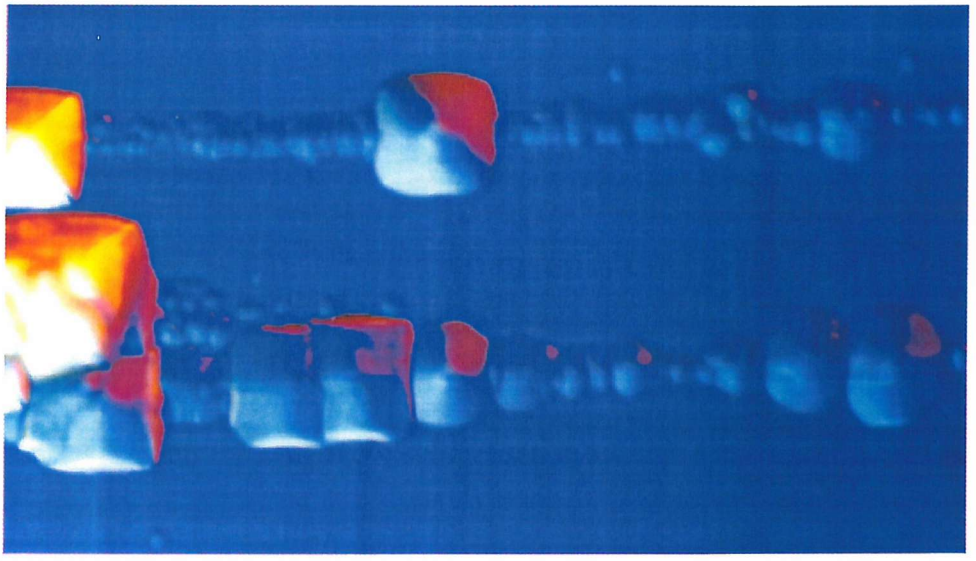

(d)

Figure 6.40. Nomarski DIC micrographs (obtained at x1000 magnification) of four of the step-graded heterostructures of the second set, showing large 'round' and 'square-shaped' connected defects aligned along the **<110>** directions in: (a) *VSC1*; (b) *VSC2*; (c) *VSC3*; (d) *VSC5*.

6.3.2.2. Second set: step-graded heterostructures Scanning probe microscopy: AFM analysis

AFM analyses were carried out on the TopoMetrix Accurex II scanning probe microscope using the 100 μm scanner and both the contact ThermoMicroscopes 1520-00 pyramidal (4μm base, 4 μm high and < 50 nm tip radius) silicon nitride probes (Figure 5.4 b) and the non-contact ThermoMicroscopes 1660-00 triangular pyramid (3-6 μm base, 10-20 μm long and < 20 nm tip radius) silicon probes (Figure 5.4 c). Image acquisition was obtained using the 'Topography Forward' method for both contact and non-contact modes. Image analyses were performed using the 'Area Analysis', 'Line Analysis' and 'Graphic' routines of the TopoMetrix SPMLab V4.0 software [65].

The AFM results confirmed some of the surface morphology information already obtained using Nomarski DIC microscopy. Additionally, AFM provided quantitative information related to the RMS of the surface roughness and depth variation along the crosshatch lines.

As already mentioned, AFM results can be dependent on the area selected to be scanned and the acquisition conditions used. This is, once again, illustrated in Figures 6.41–6.44 a-b, which show different 2D images together with their acquisition parameters and the RMS of the surface roughness values measured for the entire area of the acquired image of the step-graded heterostructures of the second set grown under similar conditions, *VSC1-3* and *VSC5*. Figure 6.45 a-b shows 2D images together with their acquisition parameters and the RMS of the surface roughness for the entire area of the acquired image and for an area without defects, for the step-graded heterostructure of the second set, *VSC6*, for comparison with the step-graded heterostructure of the first set grown under identical conditions, *774*. Figure 6.46 a-b shows 2D images together with their acquisition parameters and the RMS of the surface roughness for the entire area of the acquired image of the step-graded heterostructures of the first set, *774*, grown under identical conditions with *VSC6*.

The quantitative AFM results obtained on 100 μm x 100 μm scanned areas of the step-graded heterostructures of the second set, *VSC1-3* and *VSC5* (presented in Figures 6.41 – 6.44 a) are consistent with the qualitative Nomarski contrast results, showing very similar values for the RMS of the surface roughness (**≈ 10 nm** for *VSC1*, **≈ 11 nm** for *VSC2*,

≈11nm for *VSC3*, and ≈ **9 nm** for *VSC5*). These results indicate that under the growth conditions used for the structures *VSC1*-3 and *VSC5*, the variation of parameters applied does not result in substantial changes of the surface morphology. Nevertheless, the heterostructure with a device structure at the top, *VSC1* and that with a reduced Ge concentration gradient in the virtual substrate *VSC5* seem to be characterised by the lowest surface roughness, while the structure with the thicker capping layer, *VSC3* is characterised by the highest surface roughness. Additionally, these results support the observation previously made in Nomarski contrast concerning the fact that the large defects do not seem to have a significant effect on the surface morphology, which suggests that they may have been incorporated during the later stages of the growth (i.e. during the growth of the capping layer). This hypothesis was confirmed by non-contact AFM analyses carried out on the large defects, which enabled the measurement of their depths (Figure 6.47 a-d). The results obtained (some of which are presented in Figure 6.47 a-d) show that the large defects are grown inside the capping layer, thus, in the last stages of growth, being characterised by depth between ≈ **300 - 500 nm**. Hence, we proposed that during the growth of the capping layer, while changing the doping gas from p-type (diborane, B_2H_6) to n-type (phosphine, PH_3), in order to create the pn junctions for Hall mobility measurements, impurities may have been introduced in the system, which have further created the growth artefacts observed.

The RMS of the surface roughness results obtained for 100 μm x 100 μm scanned areas of the step-graded heterostructures of the second set grown under similar conditions (shown above) are almost half of the RMS of the surface roughness value obtained for the same size of scanned area of the step-graded heterostructure of the first set, *774* (≈ **22 nm**). This result is in good agreement with the Nomarski contrast observations. The absence of trenches from the surface of the step-graded heterostructures of the second set compared to the first set, results in lower RMS of the surface roughness values. By comparison, the RMS results obtained on both the selected sections (without defects) of 100 μm x 100 μm (**RMS ≈ 25 nm**, as shown in Figure 6.45 a) and 20 μm x 20 μm (**RMS ≈ 21 nm**, as shown in Figure 6.45 b) scanned areas of the step-graded heterostructure of the second set grown for reproducibility, *VSC6*, are similar, and very close to the RMS value obtained on a 100 μm x 100 μm scanned area of the step-graded heterostructure of the first set grown under identical conditions, *774* (≈ **22 nm**). These results indicate good growth reproducibility.

The results for the height variation measurements carried out along the crosshatch lines of the four step-graded heterostructures of the second set grown under similar conditions are presented in Figure 6.48 a–d. Line analyses showed the presence of small pits along the crosshatch lines and enabled the measurement of their in-plane dimension and their depth (Figure 6.49 a-d). Similar values for both the size of the pits and their depth, respectively, in all these four heterostructures of the second set are shown. These results show, once again, that the largest pits (with in-plane dimensions of **≈ 2 μm**) are also the deepest (up to **≈ 39 nm** depth). The pit size for the step-graded heterostructures of the second set is comparable with that of the step-graded structure of the first set, but their depth is much smaller (depths up to **≈ 39 nm** for the second set versus depths up to **≈ 56 nm** for the first set). These results also explain the lower values for the RMS of the surface roughness that characterise the four step-graded heterostructures of the second set grown under similar conditions compared to the step-graded heterostructure of the first set.

3D AFM images of 100 μm x 100 μm scanned areas provide a qualitative appreciation of the difference in surface morphology between the four step-graded heterostructures of the second set grown under similar conditions (Figure 6.50 a-d), which exhibit smooth uniform surfaces, characterised by periodic undulations, and the step-graded structure of the first set and that grown for reproducibility (Figure 6.51 a-b), characterised by rougher surfaces, with deep trenches and pits (indicated by the arrows).

Some of the AFM results obtained on the second set of heterostructures are also presented in Table 4.

Quantitatively, AFM analyses carried out on the step-graded heterostructures of the second set, show that the trend followed by the values of the RMS of the surface roughness for 100 x 100 μm^2 scanned areas (Figures 6.41-6.44 a) is not consistent with that for 20 x 20 μm^2 scanned areas (Figures 6.41-6.44 b). This observation together with the fact that the differences in the RMS of the surface roughness values between the step-graded heterostructures of the second set grown under similar conditions, are very small, allowed us to conclude that under the growth conditions used for the step-graded heterostructures of the second set, the growth parameters varied do not cause observable variations in the surface morphology. Additionally, as aimed, the step-graded heterostructures of the second set exhibit surface morphologies, superior to the step-graded structure of the first set, i.e. flatter and smoother surfaces, characterised by a fine

and regular crosshatch pattern, consisting of shallower trenches along which a lower density of small and shallow pits can be observed. This is independently of the large-sized defects, which as shown here, are not part of the virtual substrates that are of interest for this study.

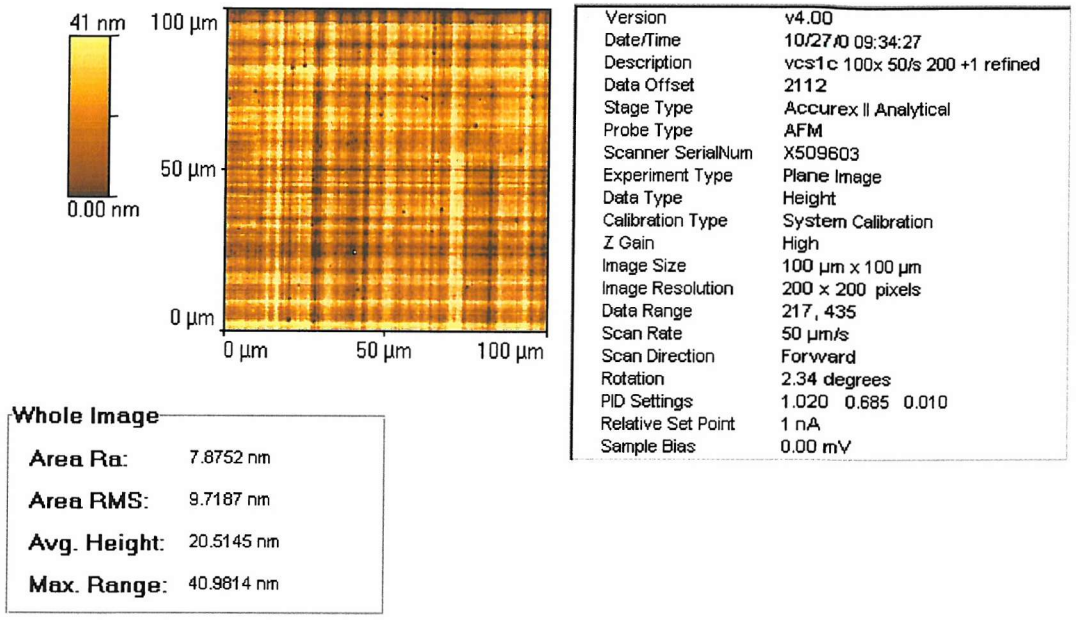

(a)

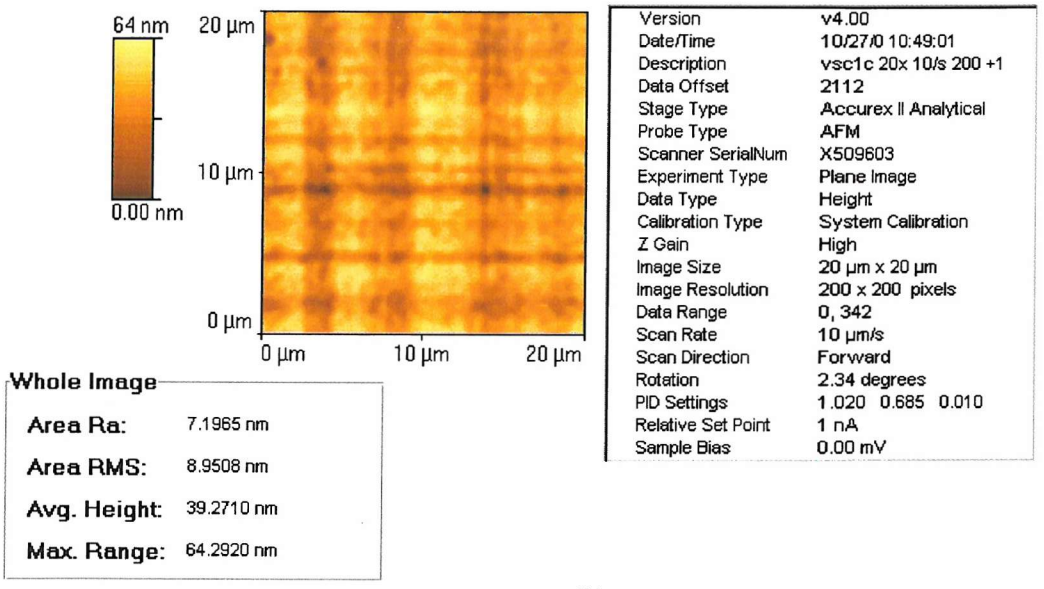

(b)

Figure 6.41. 2D AFM images, scan parameters and the RMS of the surface roughness values for the step-graded heterostructure of the second set incorporating a microelectronic structure, *VSC1*, for a: (a) 100 µm x 100 µm scanned area, with a scan rate of 50 µm/s, showing a smooth surface characterised by a more uniform crosshatch pattern than previously observed in the heterostructures of the first set; (b) 20 µm x 20 µm scanned area, with a scan rate of 10 µm/s. The presence of some accentuated crosshatch lines can still be observed, but the difference between them and the fine lines is much smaller, indicating shallower trenches. Pits are also present.

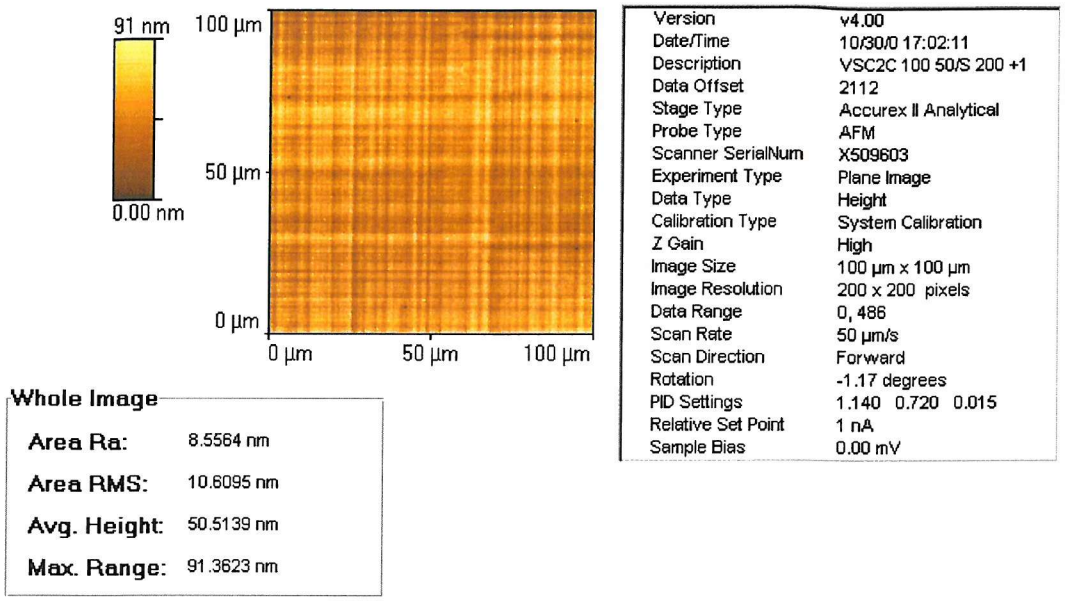

(a)

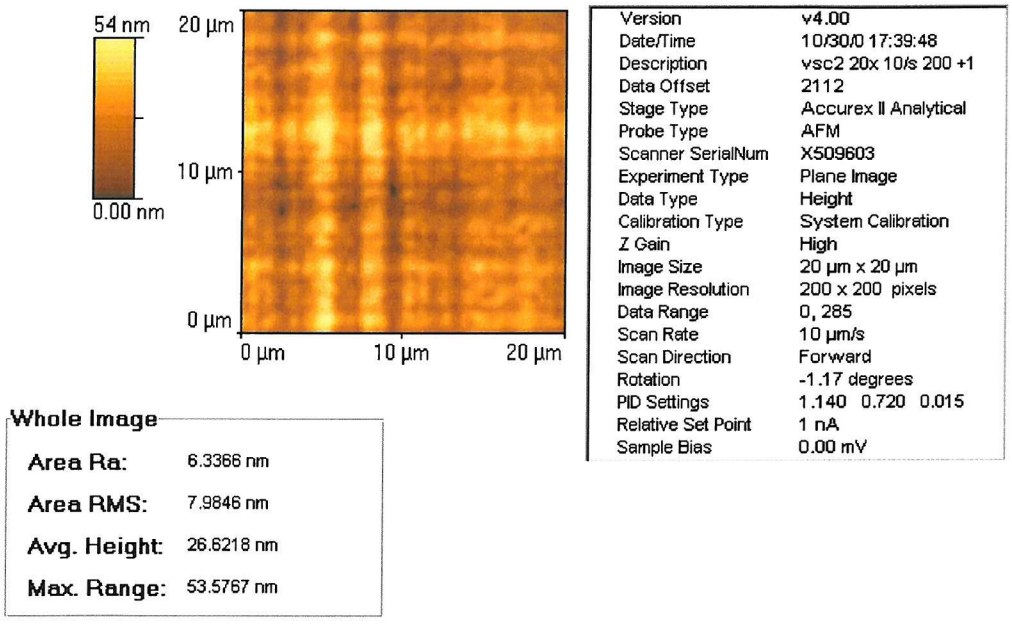

(b)

Figure 6.42. 2D AFM images, scan parameters and the RMS of the surface roughness values for the step-graded heterostructure of the second set grown under identical conditions with *VSC1*, but without the microelectronic structure, *VSC2*, for a: (a) 100 µm x 100 µm scanned area, with a scan rate of 50 µm/s, showing the fine crosshatch pattern and some pits along the crosshatch lines; (b) 20 µm x 20 µm scanned area, with a scan rate of 10 µm/s, showing a similar morphology with the 20 µm x 20 µm scanned area of *VSC1*, acquired under similar conditions.

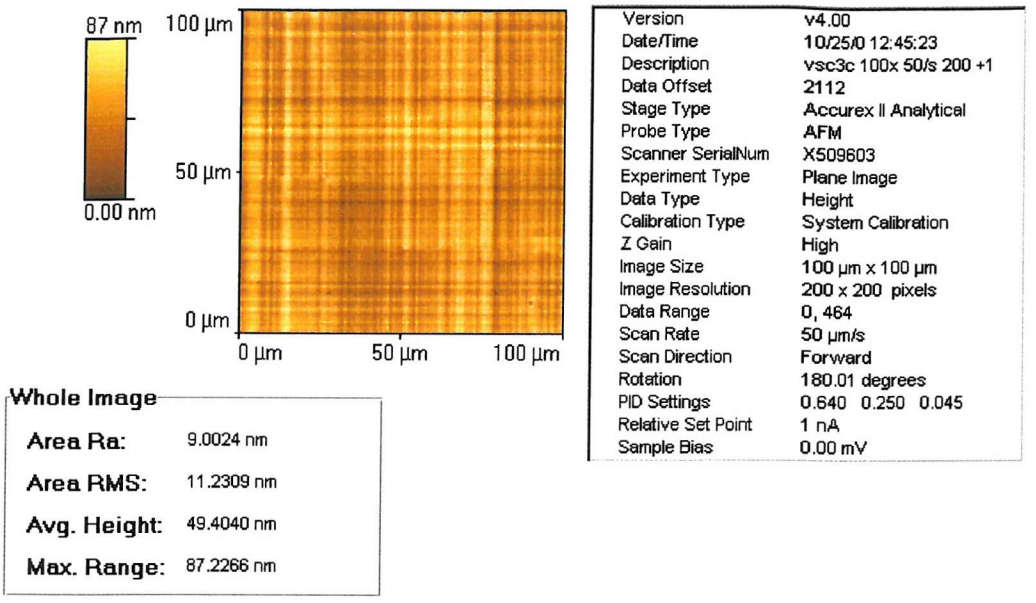

(a)

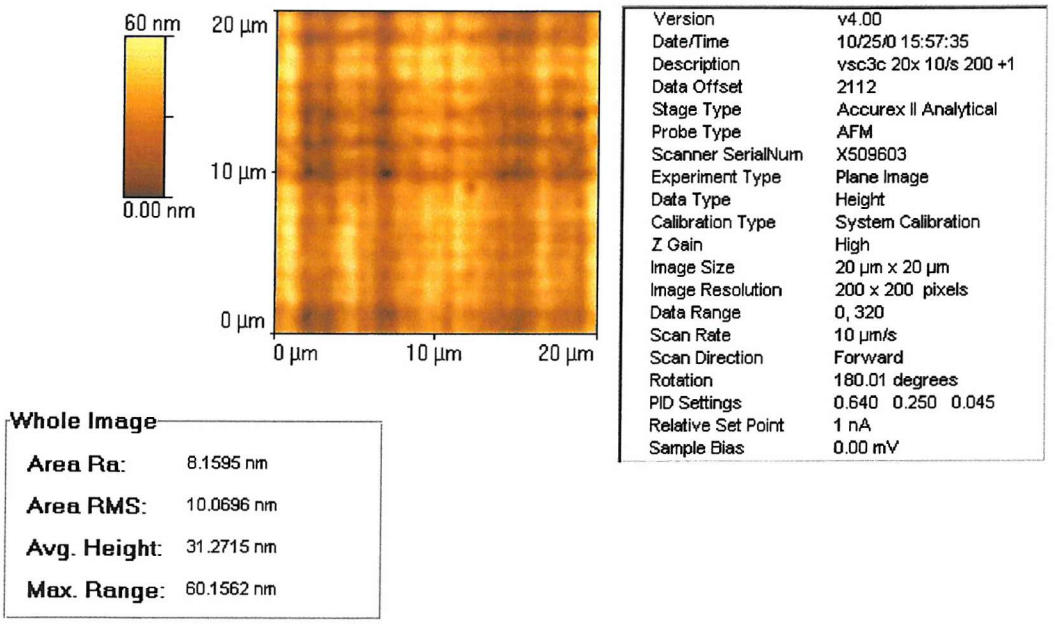

(b)

Figure 6.43. 2D AFM images, scan parameters and the RMS of the surface roughness values for the step-graded heterostructure of the second set grown under identical conditions with *VSC2*, but with a thicker capping layer, *VSC3*, for a: (a) 100 µm x 100 µm scanned area, with a scan rate of 50 µm/s, showing the fine crosshatch pattern, and also pits along the crosshatch lines; (b) 20 µm x 20µm scanned area, with a scan rate of 10µm/s, showing a similar morphology with the 20µm x 20µm scanned areas, acquired under similar conditions, of *VSC1* and *VSC2*.

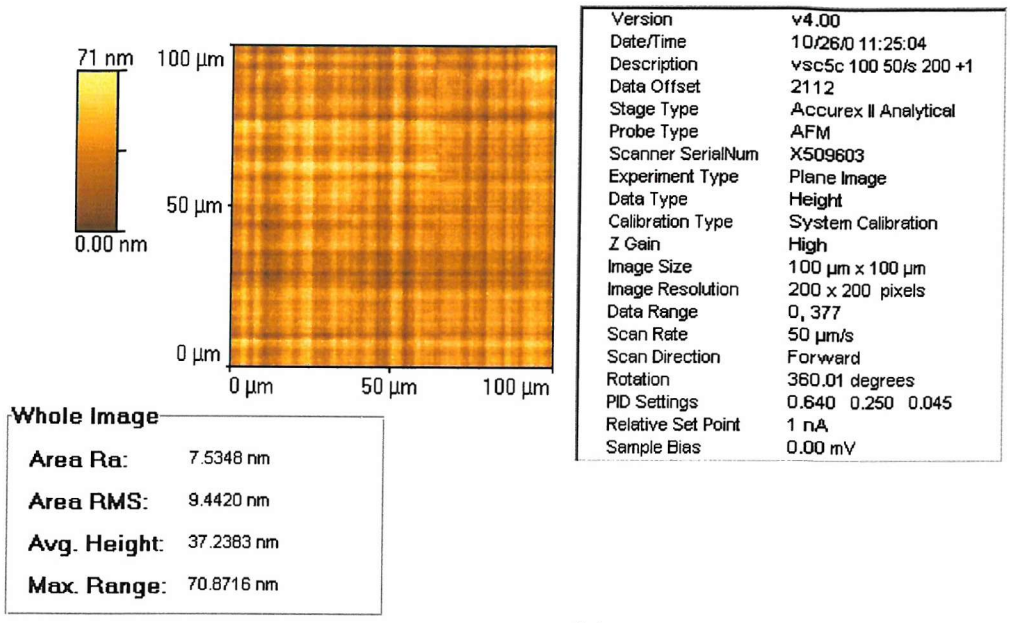

(a)

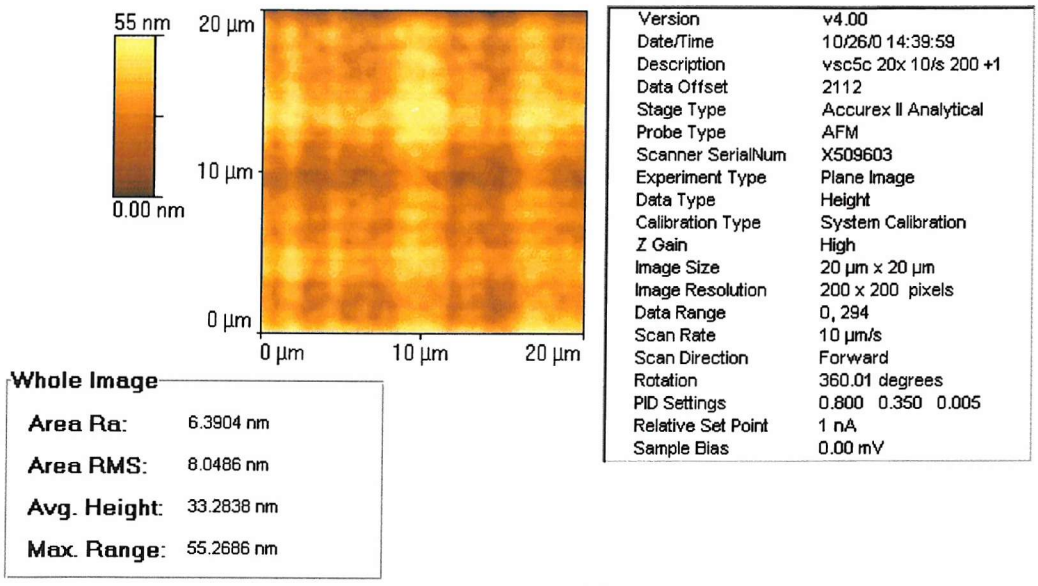

(b)

Figure 6.44. 2D AFM images, scan parameters and the RMS of the surface roughness values for the step-graded heterostructure of the second set grown under similar conditions with *VSC2*, but with a variation of the Ge concentration in the virtual substrate in double the number of half-sized (in Ge concentration) steps, *VSC5*, for a: (a) 100 µm x 100 µm scanned area, with a scan rate of 50 µm/s, showing the fine crosshatch pattern and no obvious pits; (b) 20 µm x 20 µm scanned area, with a scan rate of 10 µm/s, showing a similar morphology with the 20 µm x 20 µm scanned areas, acquired under similar conditions, of the other step-graded heterostructures of the second set grown under similar conditions, *VSC1-3*.

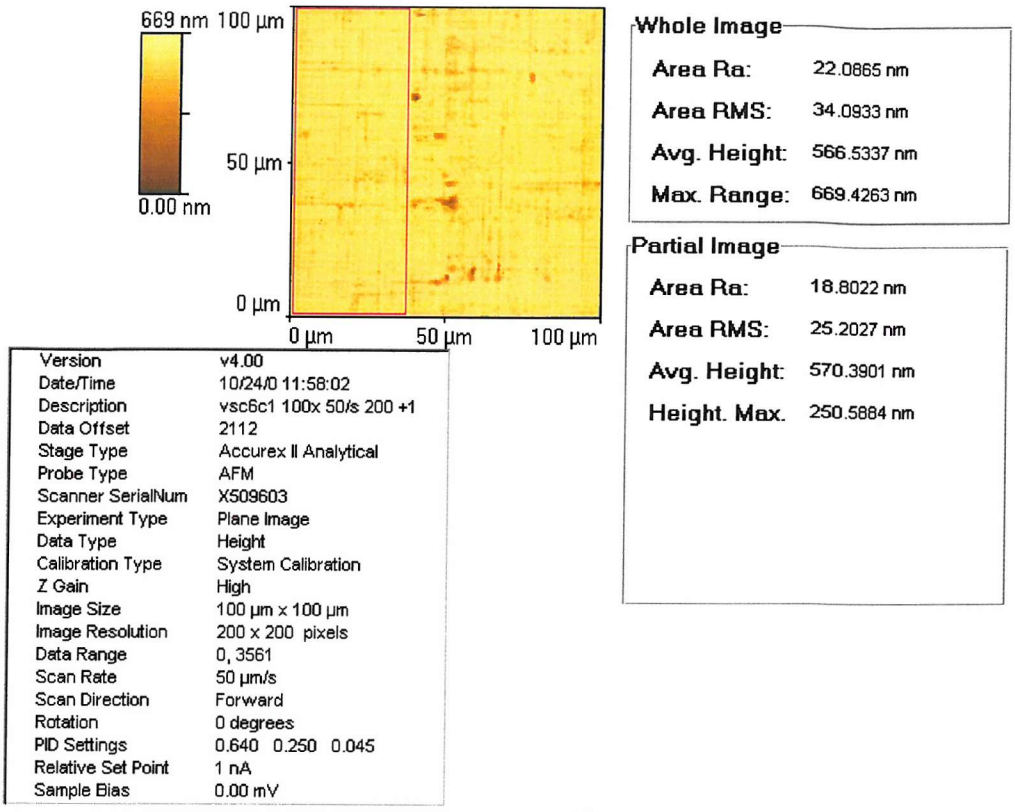

(a)

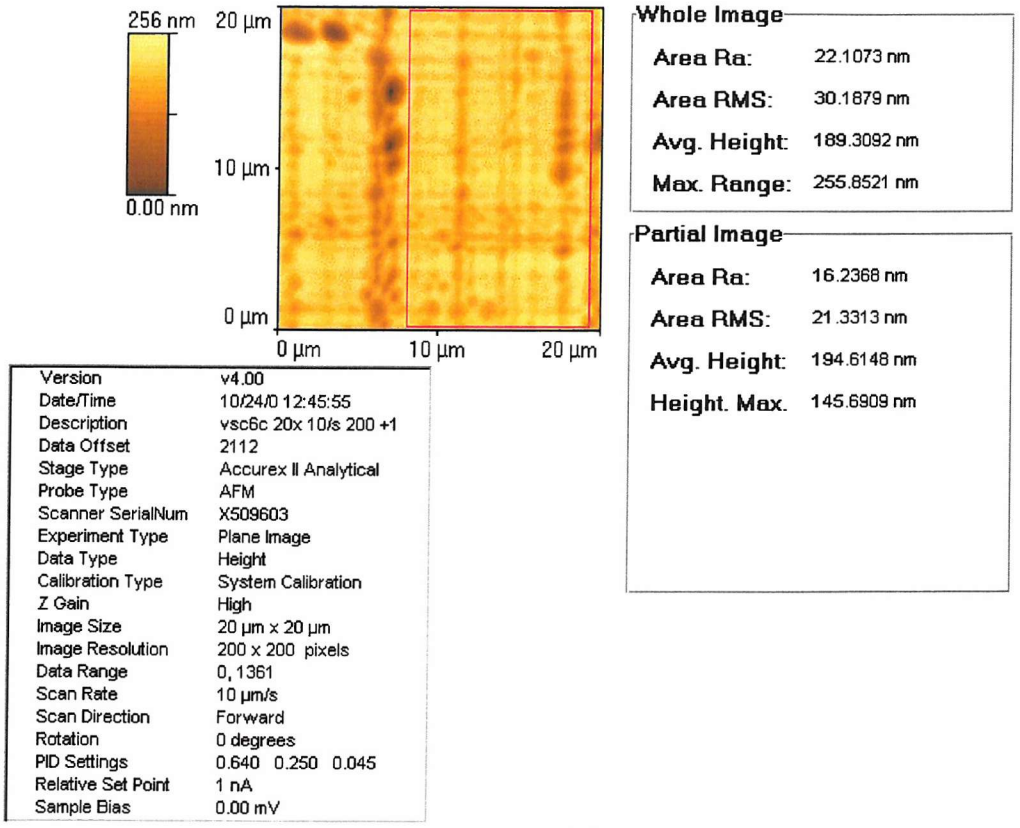

(b)

Figure 6.45. 2D AFM images, scan parameters and the RMS of the surface roughness values for the entire area of the acquired image and for an area without defects of the step-graded heterostructure *VSC6*, grown as part of the second set of heterostructures, in order to check the reproducibility of the growth process for a: (a) 100 µm x 100 µm scanned

area, with a scan rate of 50 μm/s; (b) 20 μm x 20 μm scanned area, with a scan rate of 10 μm/s. Both images show a less regular crosshatch pattern compared to the other step-graded heterostructures of the second set.

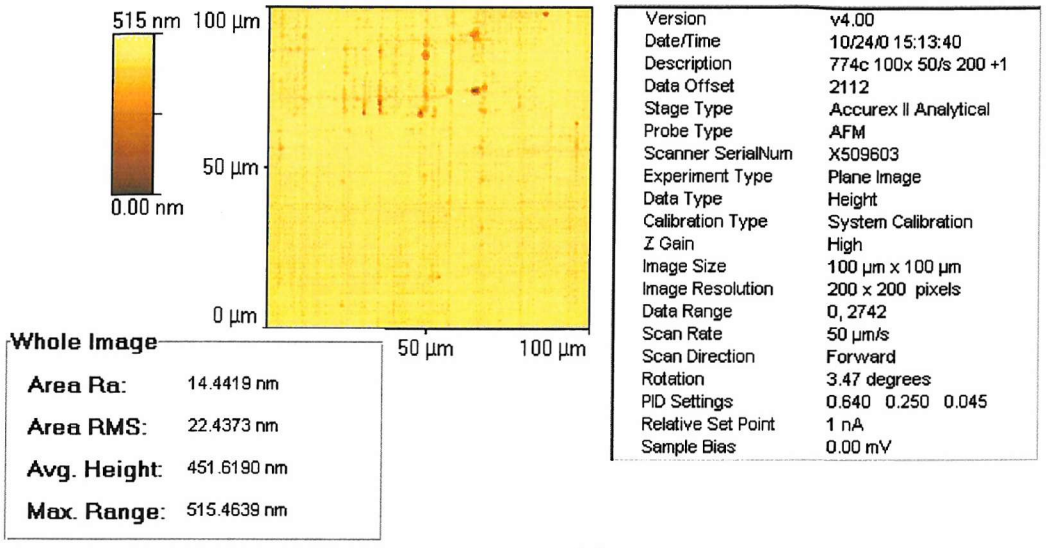

(a)

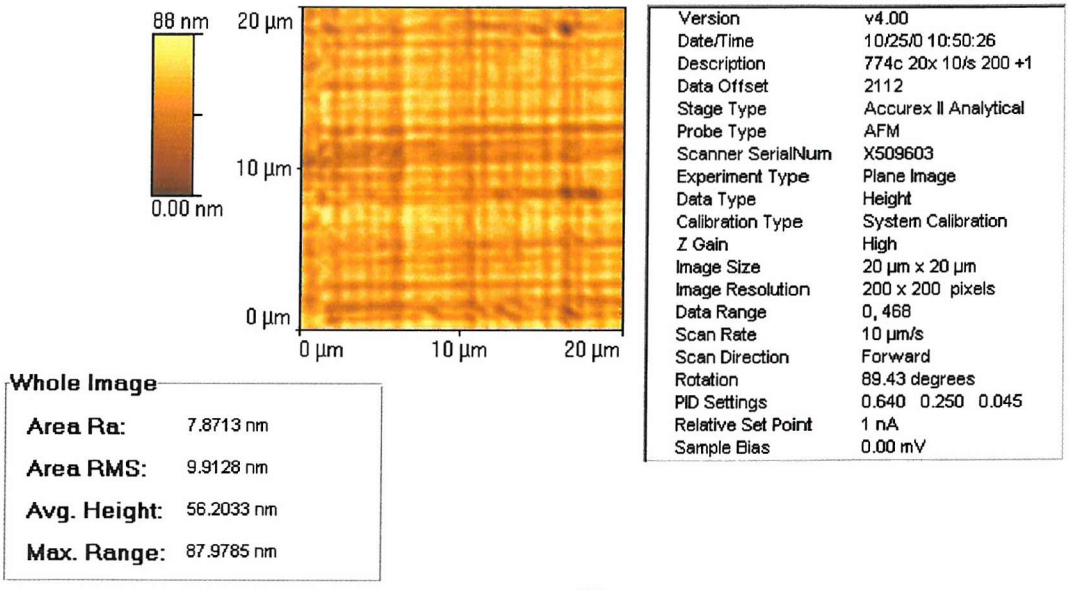

(b)

Figure 6.46. 2D AFM images, scan parameters and the RMS of the surface roughness values for the entire area of the step-graded heterostructure *774*, grown under identical conditions with *VSC6*, but as part of the first set for a: (a) 100 μm x 100 μm scanned area, with a scan rate of 50 μm/s; (b) 20 μm x 20 μm scanned area, with a scan rate of 10 μm/s. Both images show similar surface morphologies with the corresponding delineated areas of the step-graded heterostructure of the second set, *VSC6* (Figure 6.45 a-b).

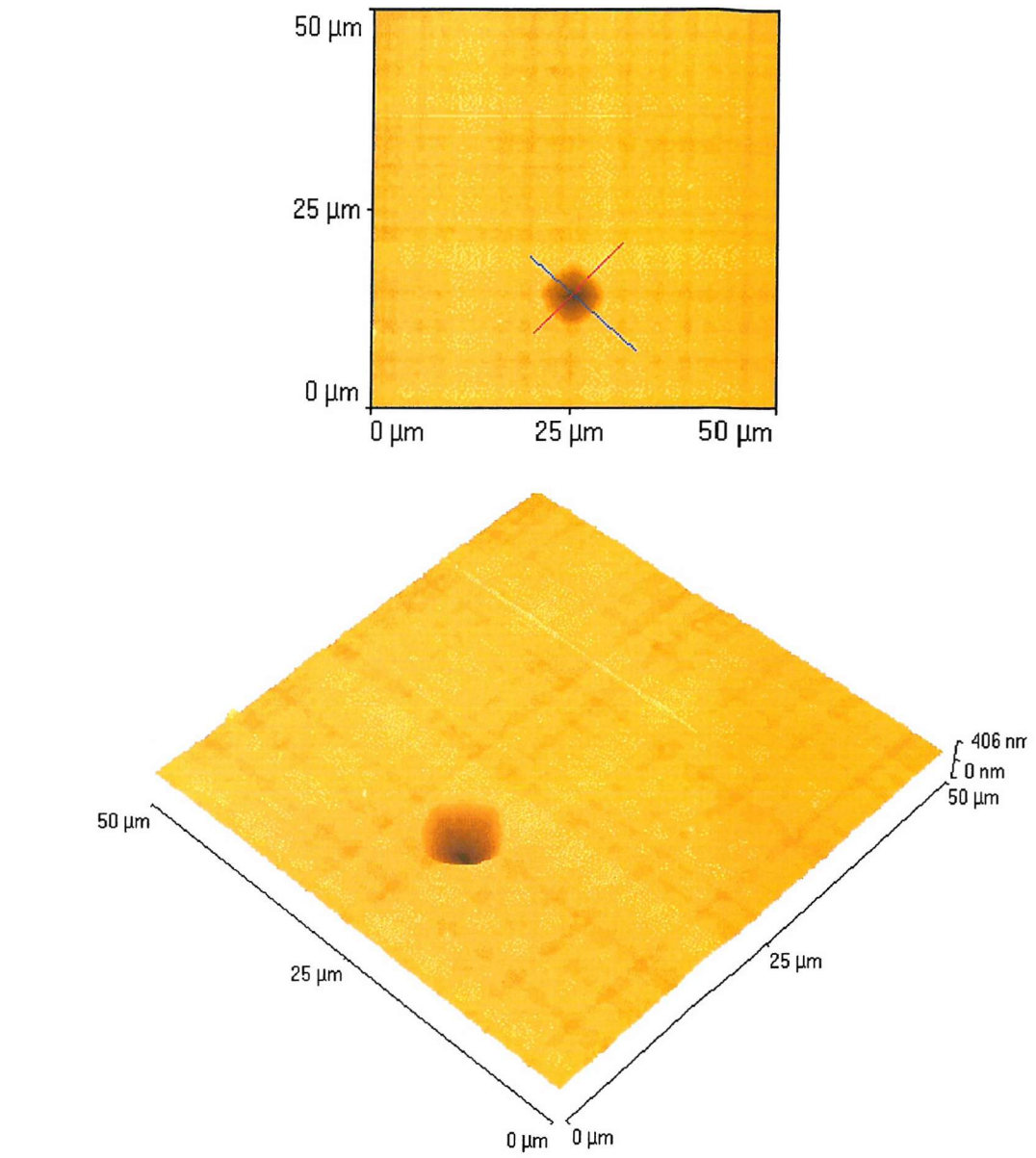
50 µm
25 µm
0 µm
0 µm
25 µm
50 µm
406 nm
0 nm
50 µm
50 µm
25 µm
25 µm
0 µm
0 µm
406 nm
203
0
0
25
50 µm
Distance
Height
1 4.19 µm 305.6 nm
2 3.94 µm 320.1 nm
406 nm
203
0
0
25
50 µm
Distance
Height
1 4.19 µm 291.6 nm
2 3.61 µm 297.1 nm

(a)

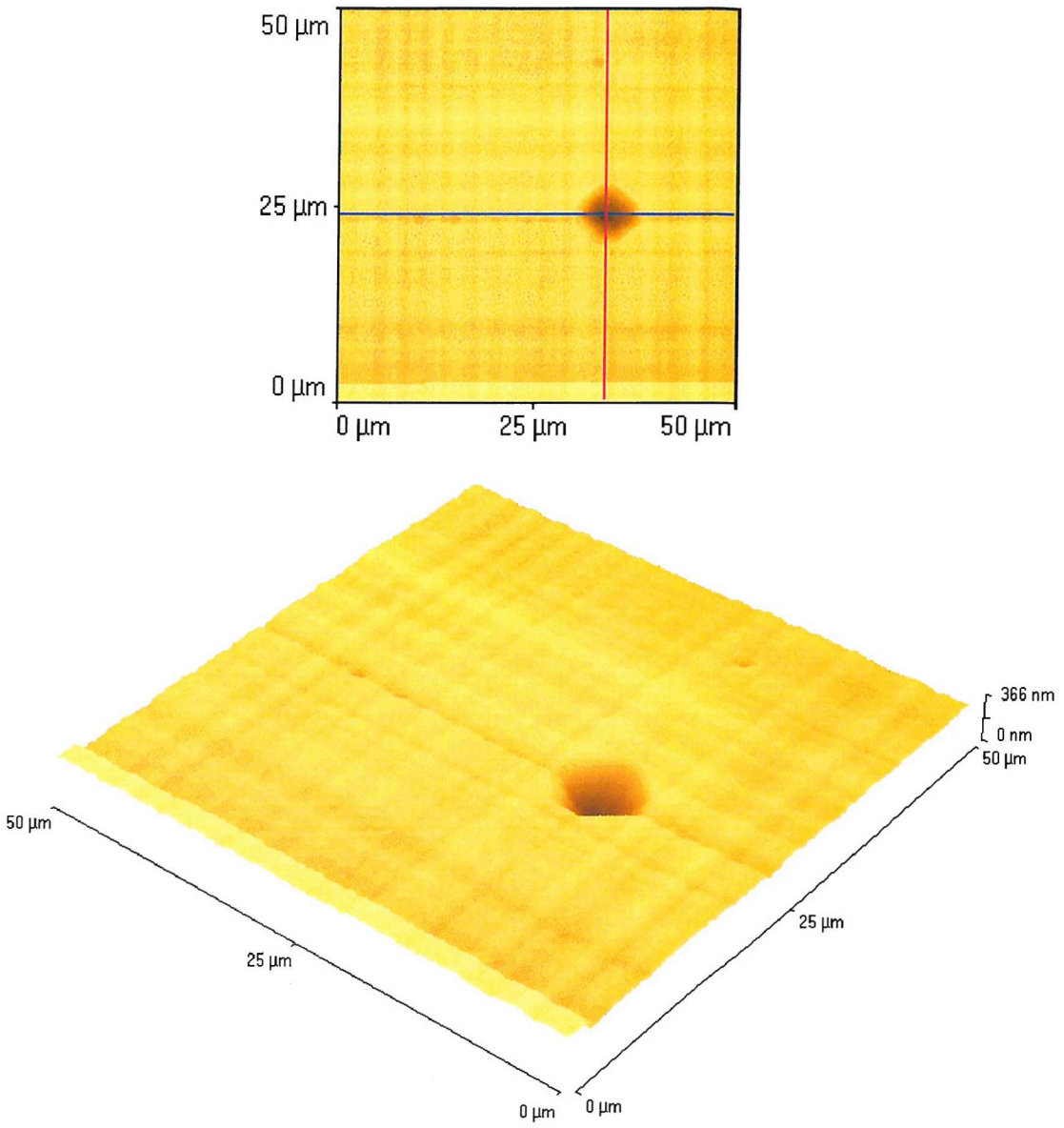
50 µm
25 µm
0 µm
0 µm
25 µm
50 µm
366 nm
0 nm
50 µm
50 µm
25 µm
25 µm
0 µm
0 µm
367 nm
183.5
0
0
25
50 µm
Distance
Height
1
3.61 µm
300.0 nm
2
5.25 µm
300.0 nm
367 nm
183.5
0
0
25
50 µm
Distance
Height
1
4.27 µm
298.3 nm
2
3.61 µm
280.3 nm

(b)

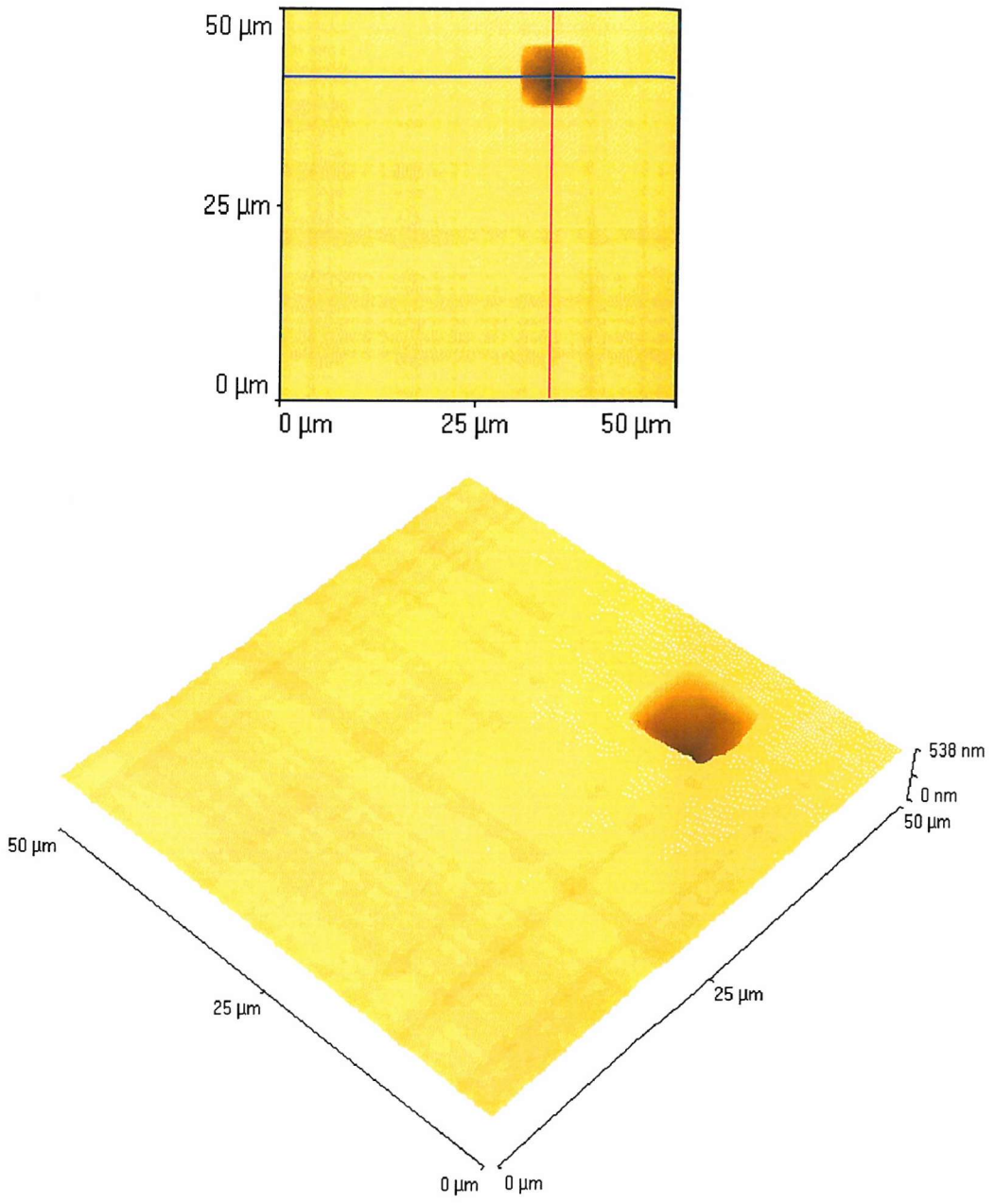
50 µm
25 µm
0 µm
0 µm
25 µm
50 µm
538 nm
0 nm
50 µm
50 µm
25 µm
25 µm
0 µm
0 µm
539 nm
269.5
0
0
25
50 µm
Distance
Height
1 4.27 µm 489.7 nm
2 5.09 µm 472.4 nm
539 nm
269.5
0
0
25
50 µm
Distance
Height
1 5.50 µm 505.7 nm
2 3.37 µm 474.0 nm

(c)

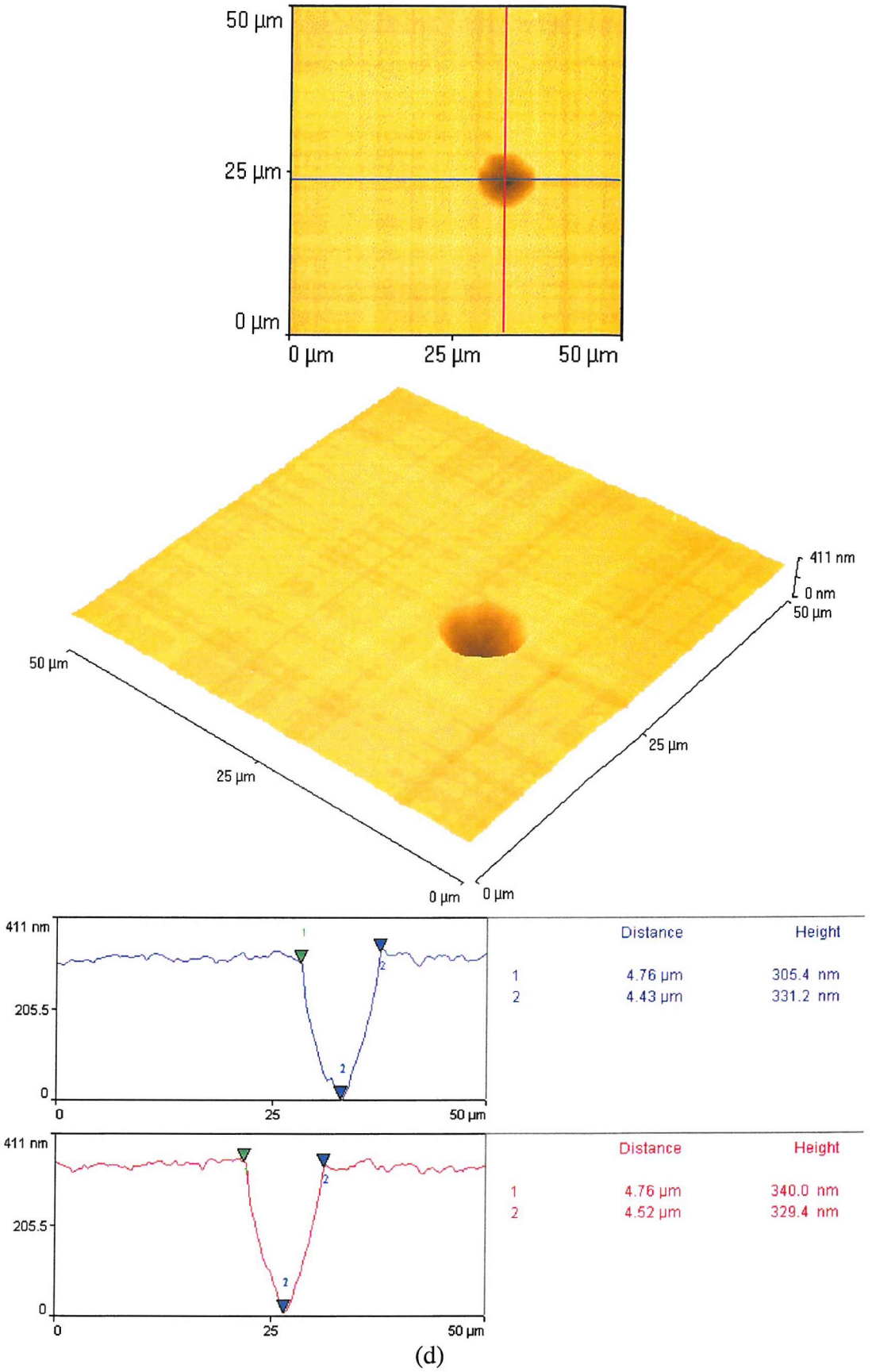

(d)

Figure 6.47. 2D and 3D images of 50 µm x 50 µm scanned areas and line analysis results obtained for the growth defects observed in: (a) *VSC1*, showing a pyramidal-shaped large pit, with in-plane sides aligned along two perpendicular **<100>** directions in the growth plane; (b) *VSC2*, showing a pyramidal-shaped large pit, with in-plane sides aligned along two perpendicular **<100>** directions in the growth plane; (c) *VSC3*, showing a pyramidal-

shaped large pit with in-plane sides aligned along two perpendicular **<110>** directions in the growth plane; (d) *VSC5*, showing a conical-shaped large pit.

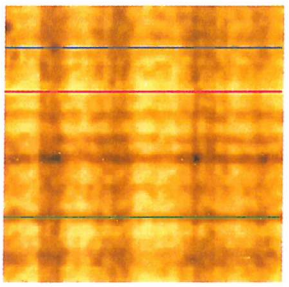

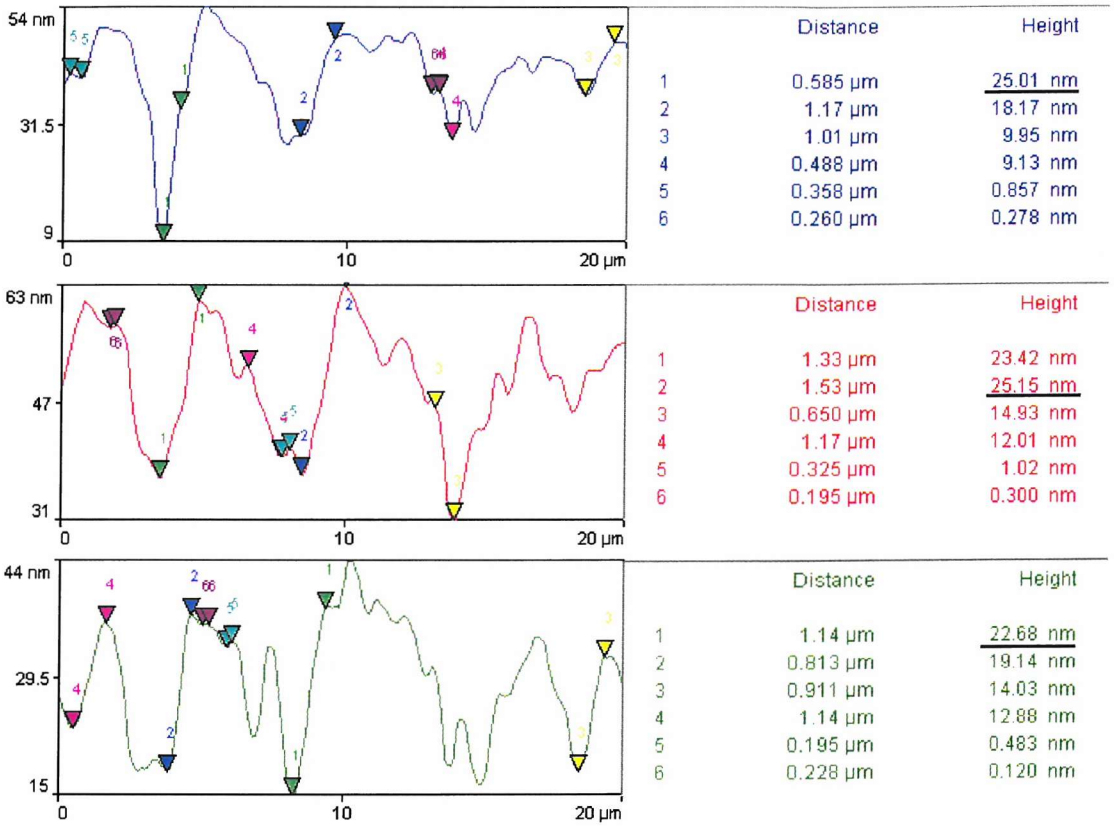

(a)

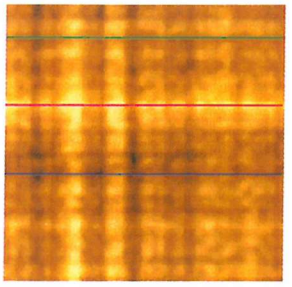

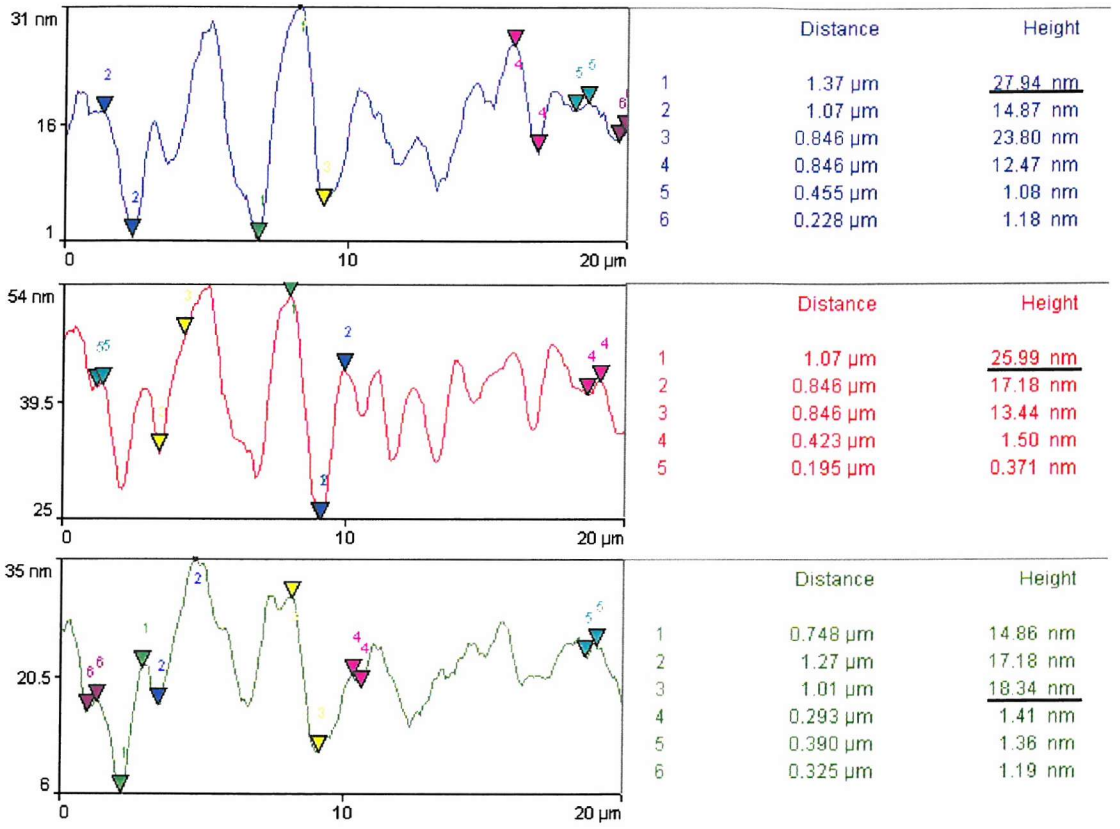
31 nm
16
1
0
10
20 µm
Distance
Height
1 1.37 µm 27.94 nm
2 1.07 µm 14.87 nm
3 0.846 µm 23.80 nm
4 0.846 µm 12.47 nm
5 0.455 µm 1.08 nm
6 0.228 µm 1.18 nm
54 nm
39.5
25
0
10
20 µm
Distance
Height
1 1.07 µm 25.99 nm
2 0.846 µm 17.18 nm
3 0.846 µm 13.44 nm
4 0.423 µm 1.50 nm
5 0.195 µm 0.371 nm
35 nm
20.5
6
0
10
20 µm
Distance
Height
1 0.748 µm 14.86 nm
2 1.27 µm 17.18 nm
3 1.01 µm 18.34 nm
4 0.293 µm 1.41 nm
5 0.390 µm 1.36 nm
6 0.325 µm 1.19 nm

(b)

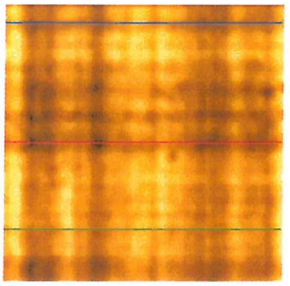

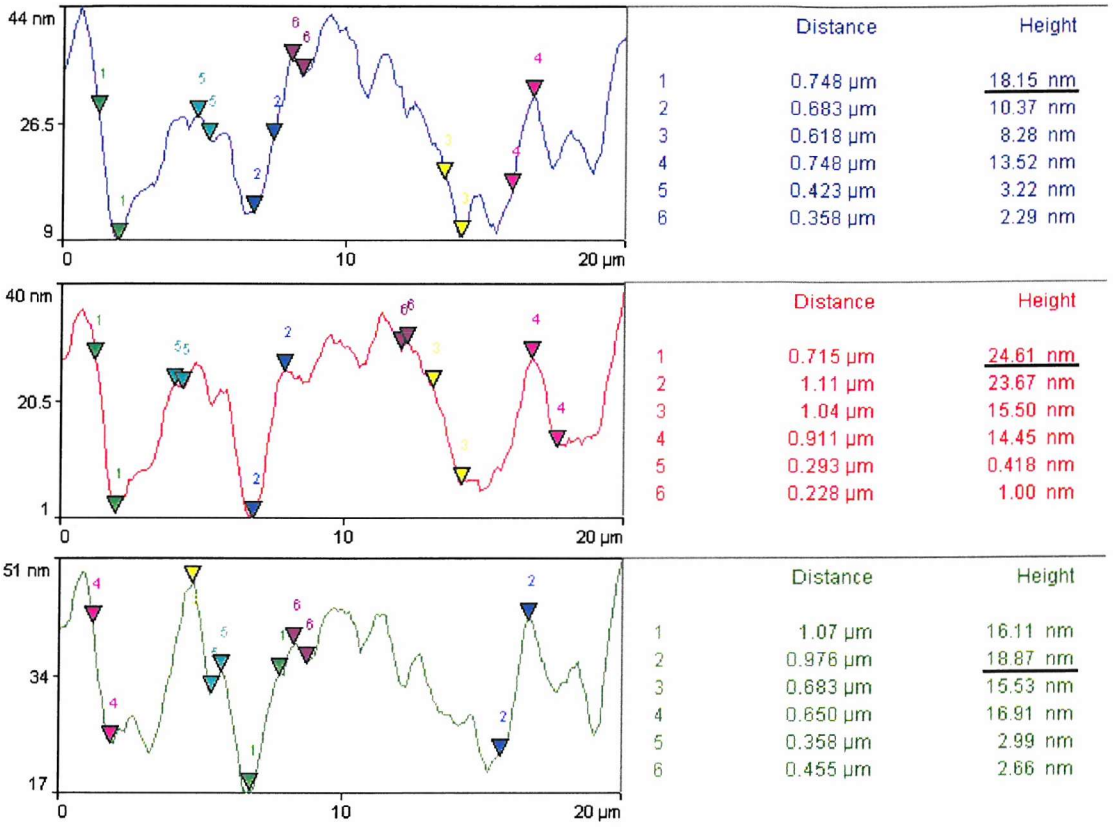
44 nm
26.5
9
0
10
20 µm
Distance
Height
1 0.748 µm 18.15 nm
2 0.683 µm 10.37 nm
3 0.618 µm 8.28 nm
4 0.748 µm 13.52 nm
5 0.423 µm 3.22 nm
6 0.358 µm 2.29 nm
40 nm
20.5
1
0
10
20 µm
Distance
Height
1 0.715 µm 24.61 nm
2 1.11 µm 23.67 nm
3 1.04 µm 15.50 nm
4 0.911 µm 14.45 nm
5 0.293 µm 0.418 nm
6 0.228 µm 1.00 nm
51 nm
34
17
0
10
20 µm
Distance
Height
1 1.07 µm 16.11 nm
2 0.976 µm 18.87 nm
3 0.683 µm 15.53 nm
4 0.650 µm 16.91 nm
5 0.358 µm 2.99 nm
6 0.455 µm 2.66 nm

(c)

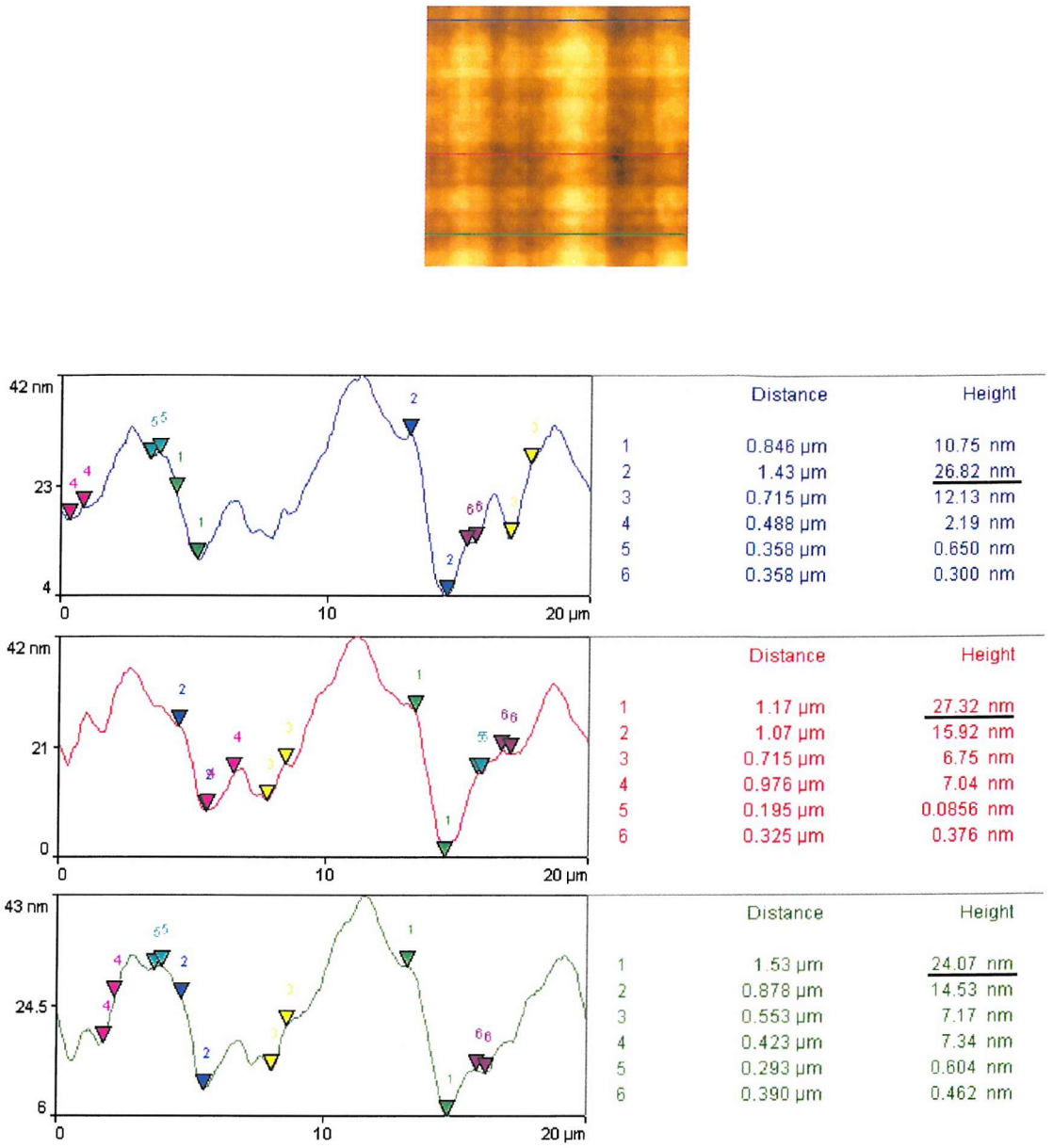

(d)

Figure 6.48. 2D AFM image of a 20 µm x 20 µm scanned area and line analysis results for the step-graded heterostructure of the second set: (a) *VSC1*; (b) *VSC2*; (c) *VSC3*; (d) *VSC5*. The underlined values correspond to the deepest pits.

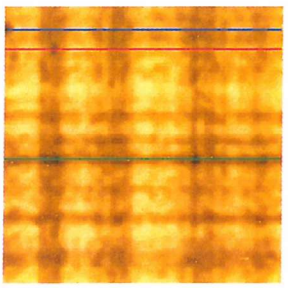

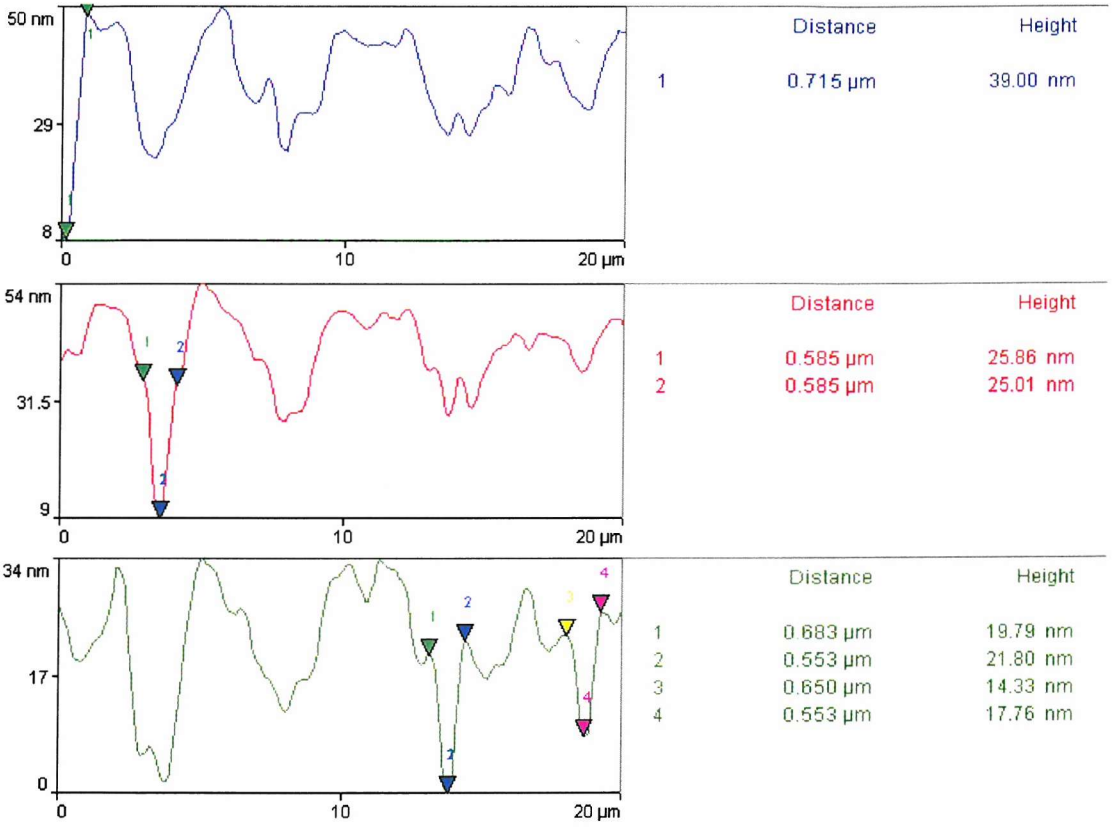
50 nm
29
8
0
10
20 µm
Distance
Height
1
0.715 µm
39.00 nm
54 nm
31.5
9
0
10
20 µm
Distance
Height
1
0.585 µm
25.86 nm
2
0.585 µm
25.01 nm
34 nm
17
0
0
10
20 µm
Distance
Height
1
0.683 µm
19.79 nm
2
0.553 µm
21.80 nm
3
0.650 µm
14.33 nm
4
0.553 µm
17.76 nm

(a)

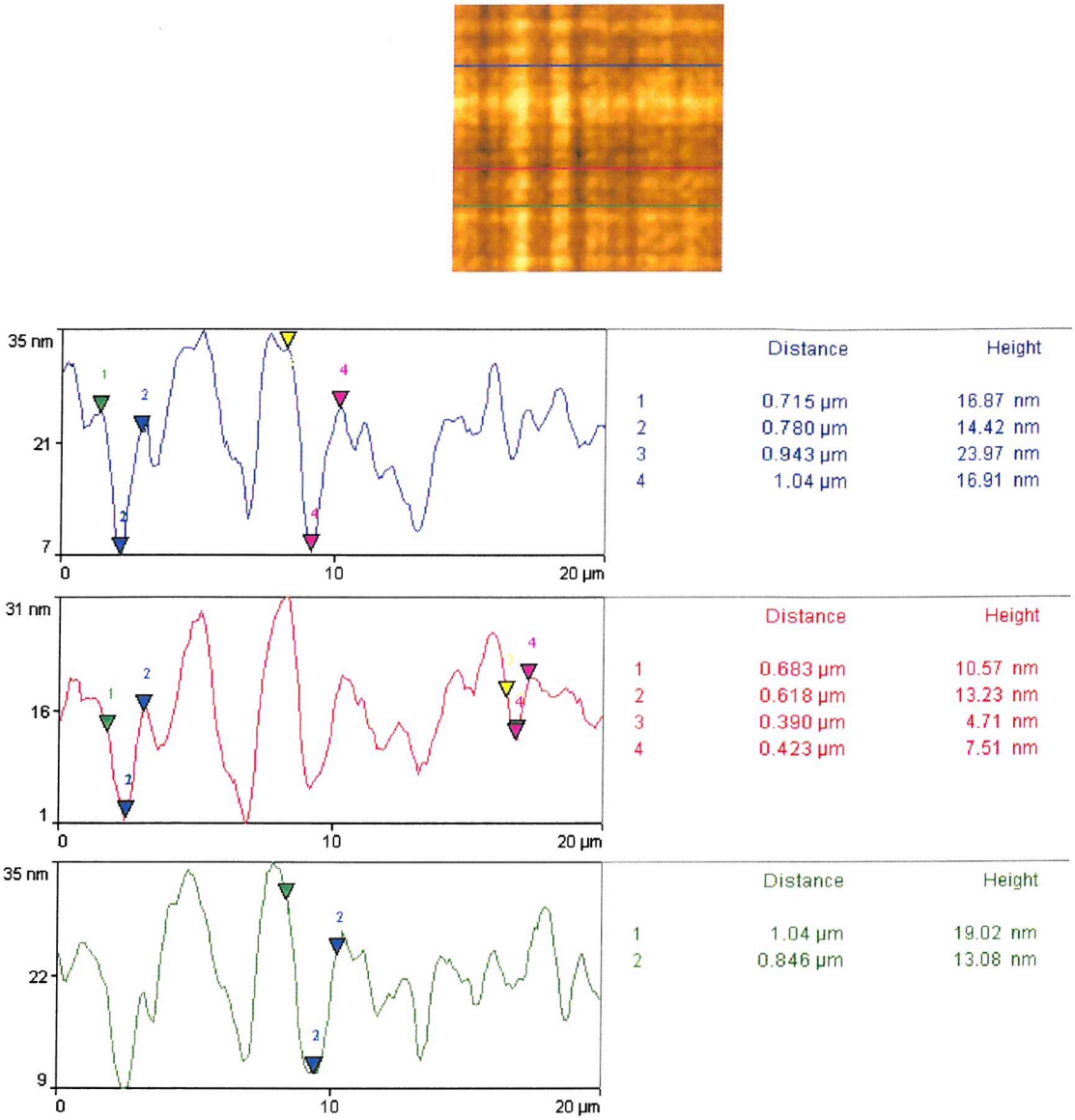
35 nm
21
7
0
10
20 µm
Distance
Height
1 0.715 µm 16.87 nm
2 0.780 µm 14.42 nm
3 0.943 µm 23.97 nm
4 1.04 µm 16.91 nm
31 nm
16
1
0
10
20 µm
Distance
Height
1 0.683 µm 10.57 nm
2 0.618 µm 13.23 nm
3 0.390 µm 4.71 nm
4 0.423 µm 7.51 nm
35 nm
22
9
0
10
20 µm
Distance
Height
1 1.04 µm 19.02 nm
2 0.846 µm 13.08 nm

(b)

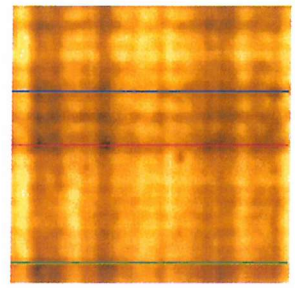

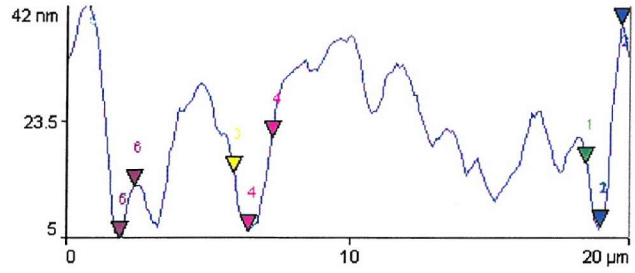

	Distance	Height
1	0.488 µm	9.64 nm
2	0.780 µm	31.04 nm
3	0.520 µm	8.92 nm
4	0.846 µm	14.41 nm
5	1.14 µm	35.53 nm
6	0.520 µm	7.93 nm

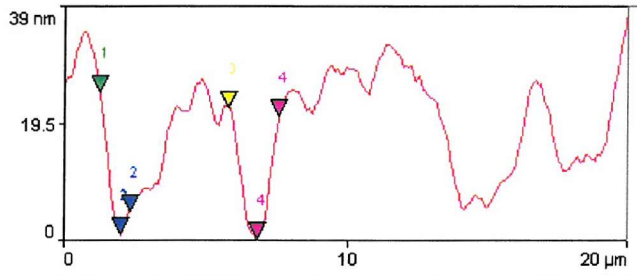

	Distance	Height
1	0.748 µm	23.42 nm
2	0.325 µm	3.73 nm
3	1.01 µm	21.87 nm
4	0.780 µm	20.43 nm

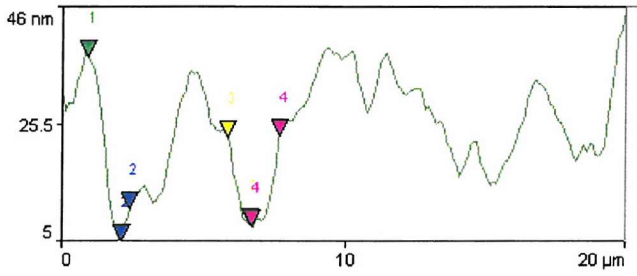

	Distance	Height
1	1.20 µm	31.27 nm
2	0.325 µm	5.41 nm
3	0.813 µm	14.62 nm
4	0.976 µm	15.29 nm

(c)

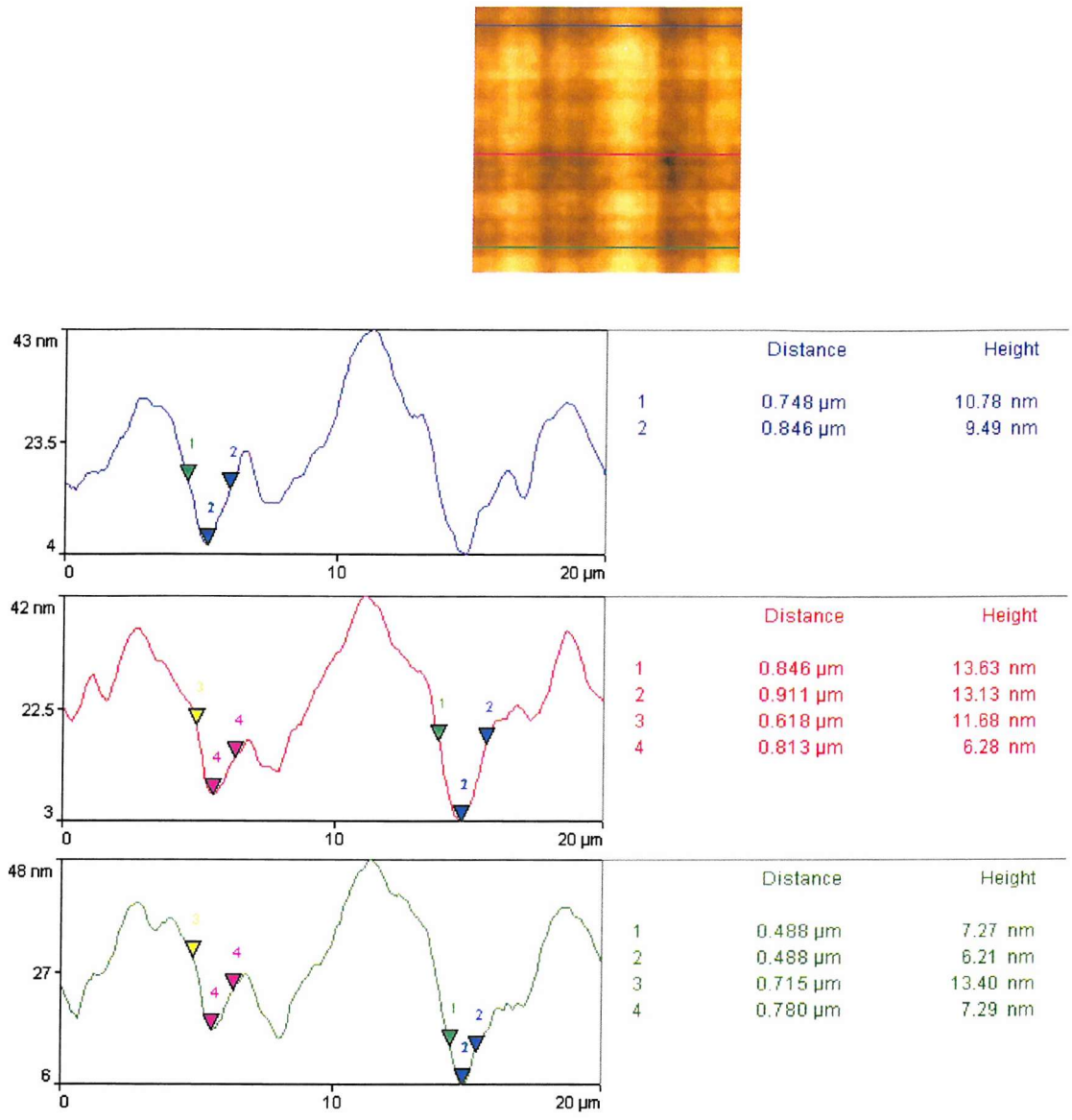

(d)

Figure 6.48. 2D AFM images of 20 µm x 20 µm scanned areas and line analysis results obtained from measuring the lateral spacing and depth of the small pits present along the crosshatch lines in the four step-graded heterostructures of the second set grown under similar conditions: (a) *VSC1*; (b) *VSC2*; (c) *VSC3*; (d) *VSC5*.

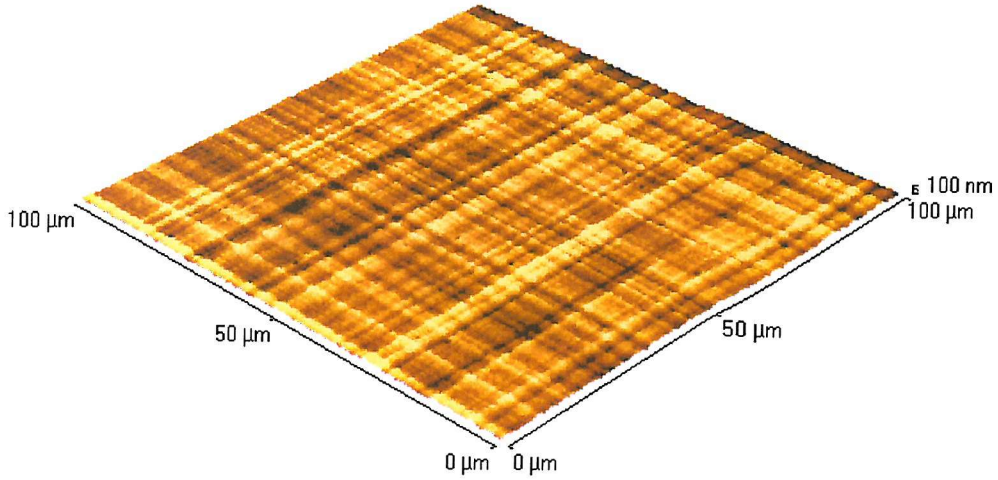
100 µm
50 µm
0 µm
0 µm
50 µm
100 µm
100 nm

(a)

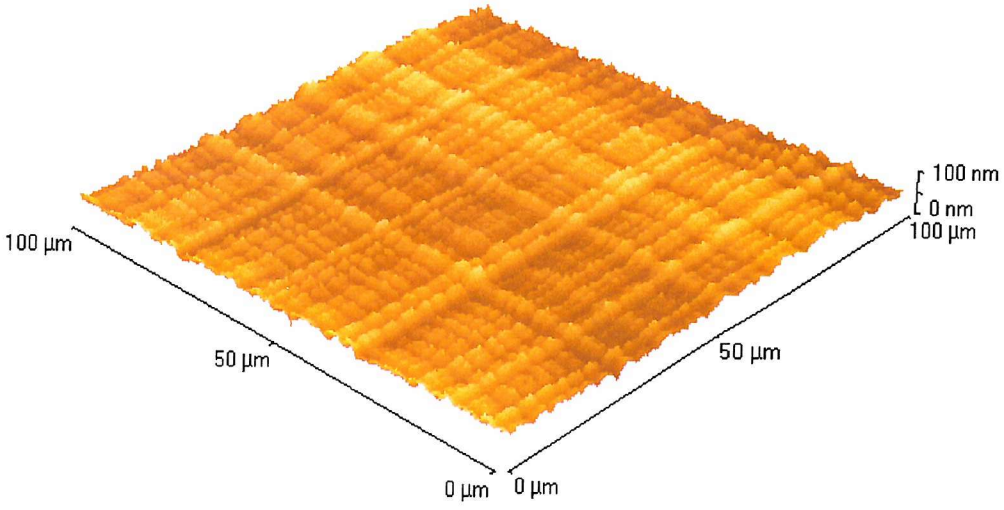
100 µm
50 µm
0 µm
0 µm
50 µm
100 µm
100 nm
0 nm

(b)

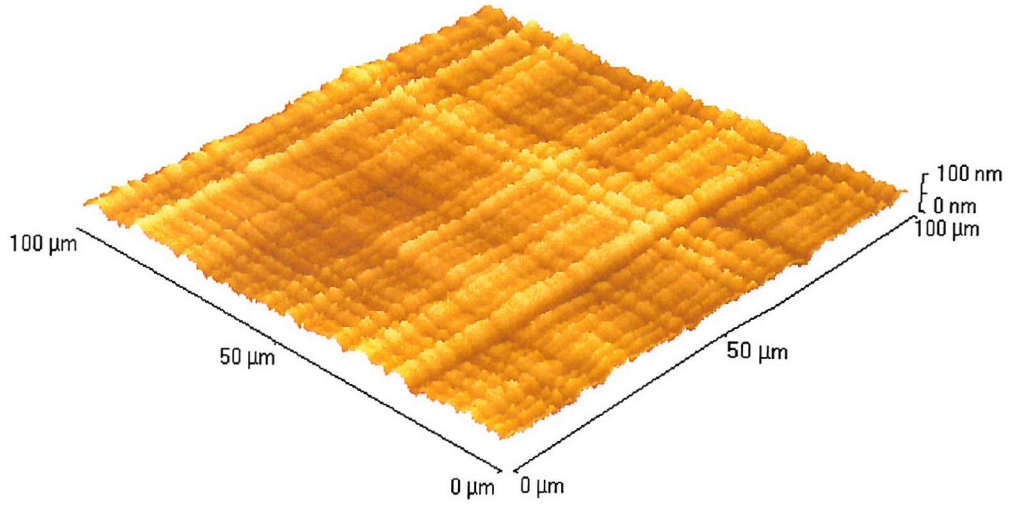

(c)

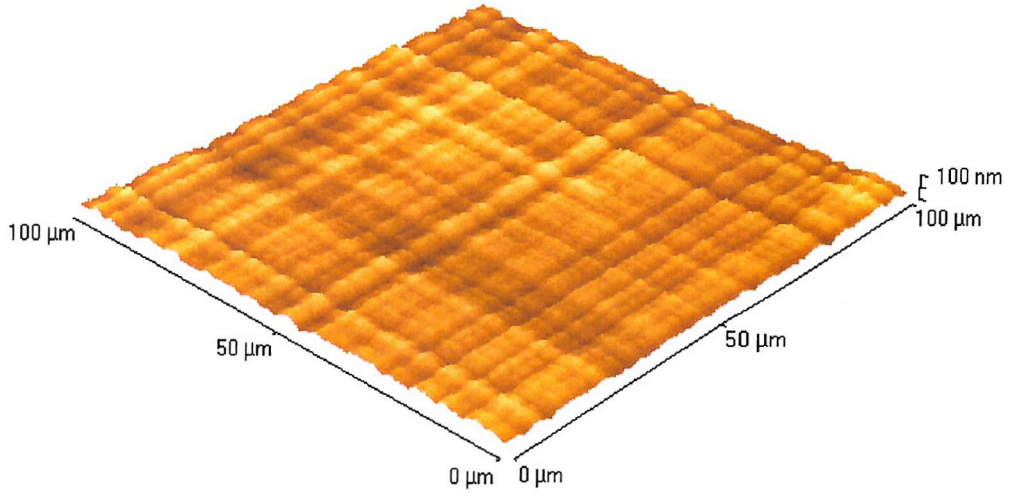

(d)

Figure 6.48. 3D AFM images of 100 µm x 100 µm scanned areas of the four step-graded heterostructures of the second set grown under similar conditions: (a) *VSC1*; (b) *VSC2*; (c) *VSC3*; (d) *VSC5*. These images show very similar surface morphologies, characterised by a fine uniform crosshatch pattern.

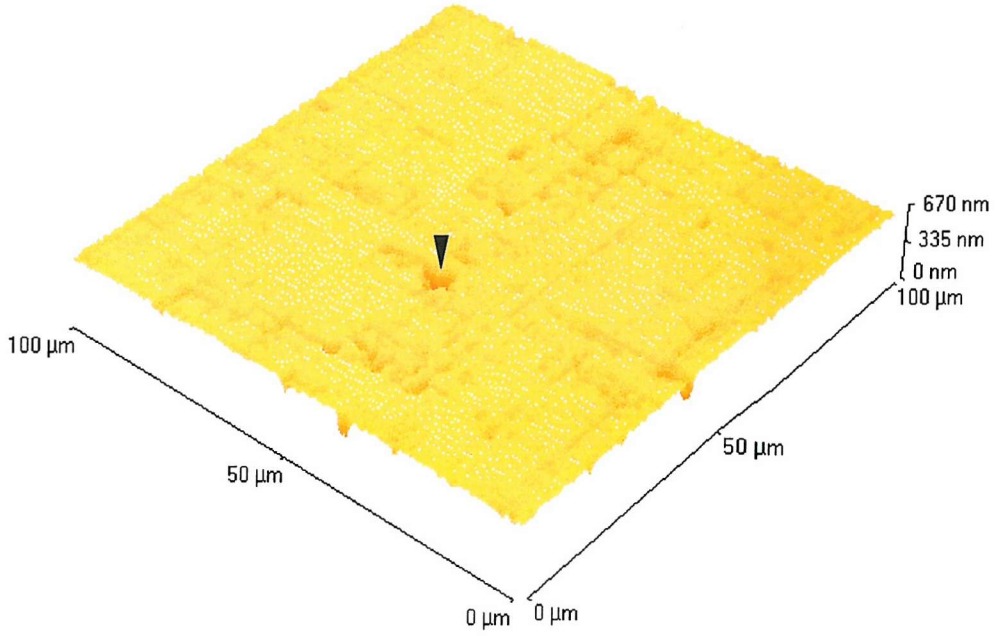

(a)

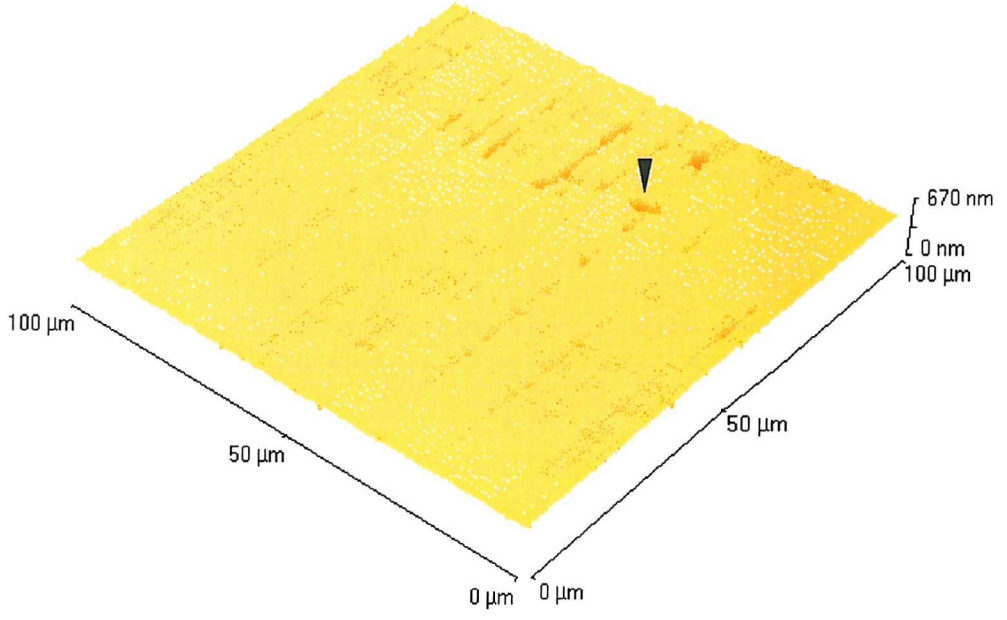

(b)

Figure 6.51. 3D AFM images of 100 µm x 100 µm scanned areas of the two step-graded heterostructures grown under identical conditions in order to check for reproducibility: (a) *VSC6*, grown as part of the second set; (b) *774*, grown as part of the first set, showing a similar surface morphology with *VSC6*, characterised by trenches with deep pits indicated by the arrows.

6.3.2.3. Second set: step-graded heterostructures Electron microscopy: XTEM analysis

Once again, XTEM analyses provided us with information concerning the internal morphology and the defect content of the step-graded heterostructures of the second set, which was not obtainable by using the Nomarski contrast or AFM techniques. XTEM results confirmed as well as complemented the results already presented in § 6.3.2.1 – 6.3.2.2, which were obtained using the other two analysis methods mentioned above. XTEM analyses of the step-graded heterostructures of the second set were carried out on the J.E.O.L. JEM 2000FX transmission electron microscope (Figure 5.6) using the double-tilt sample holder (Figure 5.5). The lanthanum hexaboride (LaB_6) crystal with an applied voltage of 200 kV and the largest spot size (for highest brightness) was used.

Samples were analysed in bright field, using different two-beam conditions, in order to select the best analysis settings and carry out dislocation analyses, as explained in Chapter 5, § 5.3.3 – 5.3.4. The XTEM micrographs of the step-graded heterostructures of the second set *VSC1*-3, *VSC5* and *VSC6*, presented in Figures 6.52 – 6.56 were obtained using the main beam condition.

XTEM collages of the five step-graded heterostructures of the second set show very clearly the Ge concentration steps delineated by MDs. The four structures grown under similar conditions i.e. at the same temperature of **750°C**, with the same Ge concentration variation in the virtual substrate **0 - 32%** and with capping layers characterised by a constant Ge composition of **30%** (*VSC1–VSC3* and *VSC5)*, show almost flat surfaces (Figures 6.52 – 6.55). The step-graded heterostructure of the second set grown for reproducibility purposes, *VSC6*, shows very fine surface ripples (Figure 6.56), similarly to the structure of the first set, that was intended to be reproduced, *774* (Figure 6.30).

The presence of the carbon layer at the onset of the LPCVD growth is, once again, noticeable on the XTEM micrographs of the step-graded heterostructures of the second set (Figure 6.57 a-p). As observed in the previously analysed structures, this layer shows no evident contribution to misfit strain relaxation. Most defects do not form at the carbon layer, hence it does not act as a heterogeneous nucleation source. Furthermore, the Si layer, which precedes the SiGe heterostructure, even in this case, acts as a buffer burying the effects of the presence of the carbon layer. It was observed that most defects do not even reach the carbon layer, while others extend beyond it, deep into the Si substrate, as

indicated by the green arrows especially in Figures 6.57 a-d and f-o. The depths at which the interfacial defects extend into the Si substrates of the step-graded heterostructures of the second set are: ≈ **600 nm** for *VSC1*, much higher for *VSC2* (≈ **1.6 μm**), similar for *VSC3* (≈ **1 μm**) and similar again for *VSC5*, (≈ **1.4 μm**). The step-graded heterostructure of the second set grown for reproducibility, *VSC6* is also characterised by deep defects extending into the Si substrate at depths as great as ≈ **1 μm** (Figure 6.57 o), similarly to *VSC2*, *VSC3* and *VSC5*, but extending slightly deeper than in the step-graded heterostructure of the first set, which it was meant to reproduce, *774* (characterised by defects extending into the Si substrate to depths of ≈ **750 nm**). These depth values are rough estimations, because they are highly dependant on the quality of the XTEM sample. However, the topography of these deep dislocations indicates that the misfit strain introduced by increasing the Ge concentration in the virtual substrate is relieved through a mechanism that involves the participation of the Si substrate.

The interfacial defects observed in all step-graded heterostructures of the second set (Figure 6.57 a-p) are very similar to those observed in both the step-graded and the linear-graded heterostructures of the first set. Some of the commonly encountered interfacial defects consist of loops or loop segments, which intersect, forming V-shaped defects (as can be seen in Figures 6.52 – 6.57, 6.12 – 6.15 and 6.31).

The virtual substrates of the step-graded heterostructures of the second set grown under similar conditions, *VSC1-VSC3*, show similar internal morphologies (Figures 6.52 – 6.54 and 6.58 b, 6.59 b and 6.60 a). The six steps of 5% Ge concentration variation, which characterise these three heterostructures are very clearly delineated by MD. All six steps seem to have approximately the same thickness of **280 nm** and the same thickness as the step of 2% Ge concentration variation (evidenced by the different contrast in the XTEM micrographs) thus indicating good growth control. In all three step-graded heterostructures, the defect density decreases toward the upper steps of Ge concentration and the step of 2% Ge concentration variation is completely free from MDs, hence, possibly, still elastically strained. The capping layer of constant Ge composition, is also completely MD-free, thus proving the efficiency of the relaxation mechanism operating in the virtual substrate.

The XTEM micrographs of the step-graded heterostructures grown as an intermediary, *VSC5*, between the step-graded heterostructure of the second set, *VSC2* and the linear-

graded heterostructure of the second set, *VSC4*, both grown under the same conditions, and which is characterised by double the number of half-sized Ge concentration steps compared to *VSC2* (i.e. 12 steps of 2.5% Ge concentration for *VSC5*, compared to 6 steps of 5% Ge concentration for *VSC2*), show, once again very distinctively the 12 steps of Ge concentration delineated by MDs (Figures 6.55, 6.60 b). All 12 steps seem to have approximately the same thickness of **≈ 280 nm** and the same thickness as the step of 2% Ge concentration variation. These thickness values correspond to those obtained for the Ge concentration steps in the other three step-graded heterostructures of the second set, *VSC1*-3, thus indicating, once again, good growth control. In *VSC5*, similarly to *VSC1-3*, the defect density decreases toward the upper steps of Ge concentration and the step of 2% Ge concentration variation is completely free from MDs, hence still elastically strained, even in this case. Additionally, the capping layer is completely MD-free, thus proving once again, the efficiency of the relaxation mechanism operating in the virtual substrate.

The step-graded heterostructure of the second set, *VSC6* (Figure 6.56) and the step-graded heterostructure of the first set, *774* (Figure 6.30), grown for reproducibility under identical conditions, show very similar internal morphologies. The five steps of Ge concentration variation are, once again, clearly delineated by MDs. They have similar thicknesses for both structures (**≈ 260 nm**), thus indicating good growth reproducibility. The defect density in the step-graded heterostructure of the second set, *VCS6* also decreases toward the upper steps, leaving a capping layer MD-free. Also on the XTEM micrographs of *VSC6*, the absence of the step of different contrast can be observed, hence reinforcing our assumption that it corresponds to the strained step of 2% Ge concentration variation, which is present in the other four step-graded heterostructures of the second set, *VSC1-3* and *VSC5*.

The layer of constant composition in the step-graded heterostructures of the second set *VSC1-3*, *VSC5* and *VSC6* is free from MD segments (Figures 6.52 – 6.56, 6.58 b and 6.59 b and 6.60 a-b). However, there are dislocation segments threading to the free surface. When analysed in different two-beam conditions (Figure 6.61 – 6.64), the TDs present in the step-graded heterostructures of the second set, similarly to the other heterostructures previously analysed, do not satisfy the invisibility criteria (Equation 5.2 - 5.3) therefore we conclude that they are of the mixed type (Chapter 5, § 5.3.4) in good agreement with results reported in literature for the $Si_{1-x}Ge_x$/Si (001) system (Chapter 3). TDs in the step-

graded heterostructure of the second set appear very similar to those observed in both the linear-graded and the step-graded heterostructures of the first set. For example, the TD pileup shown in the left column of Figure 6.61 present in the step-graded heterostructure of the second set, *VSC1*, is very similar that shown in the left corner of Figure 6.62 corresponding to the step-graded heterostructure of the second set, *VSC2*, in the left hand column of Figure 6.63, characteristic of the step-graded heterostructure of the second set, *VSC3* and to that presented in Figure 6.18 (for the linear-graded heterostructure of the first set, *775*), Figure 6.19 a-b (for the linear-graded heterostructure of the first set, *720*) and Figure 6.32 (for the step-graded heterostructure of the first set, *774*). These dislocation pileups are running on **{111}** planes and are threading through part or the whole structure (as already described in § 6.2.2.3). As previously explained, similar pileups have been observed in $Si_{1-x}Ge_x$/Si (001) structures by other groups, who studied their formation and concluded that they are typically caused by an inhomogeneity that continuously 'punches out' dislocations, under the influence of the misfit strain introduced continuously through Ge concentration grading [4]. Similarly, the threader shown in the right hand column of Figure 6.61, corresponding to the step-graded heterostructure of the second set, *VSC1*, is matching the one in Figure 6.64 (the step-graded heterostructure of the second set, *VSC5*), the one in Figure 6.65 f (the step-graded heterostructure of the second set, *VSC6*) and also the one in Figure 6.19 c (the linear-graded heterostructure of the first set, *775*) and the one in Figure 6.33 (step-graded heterostructure of the second set, 774). These similarities indicate the possibility of similar nucleation sources.

Differently from the linear-graded heterostructures of the first set, but similarly to the step-graded structure of the first set, the type of groups of TDs terminated at faceted pits (presented in Figure 6.16 a-b for the structure *720* and in Figure 6.17 for the structure *775*) appear to be completely absent from the step-graded heterostructures of the second set. Furthermore, differently from the linear-graded heterostructures of the first set, but similarly to the step-graded one, the step-graded heterostructures of the second set show almost flat surfaces in XTEM. Extremely fine (almost undistinguishable) surface undulations can be observed on the surface of the step-graded heterostructures grown for reproducibility (*VSC6* in Figure 6.56, and *774* in Figure 6.30).

A rough estimation of the TD density was made, once again, based on the XTEM results for the step-graded heterostructures of the second set. Values obtained ($\approx$ **10^7 – 3x10^7 cm^{-2}** for *VSC1*, $\approx$ **3x10^6 – 3x10^7 cm^{-2}** for *VSC2*, $\approx$ **3 – 5x10^7 cm^{-2}** for *VSC3* and $\approx$ **6x10^6-4x10^7**

cm^{-2} for *VSC5*) are comparable with those for the step-graded heterostructure of the first set, *774* (**≈10^7 - 6x10^7 cm^{-2}**) and for the linear graded structure of the first set, grown under similar conditions, *775* (**≈ 2x10^7 - 4x10^7 cm^{-2}**). Slightly lower values for the TD densities of the step-graded heterostructures *VSC2* and *VSC5* have been obtained.

An estimation of the TD density in the step-graded heterostructure of the second set grown for reproducibility, *VSC6* was also made. The values obtained ranged between **≈2 - 8x10^7 cm^{-2}**, thus similar to the range of values obtained for *774* (**≈10^7 – 6x10^7 cm^{-2}**). Overall, we conclude that the test for growth reproducibility was successful.

To summarise, from the XTEM results obtained for the step-graded heterostructures of the second set grown under similar conditions (*VSC1-3* and *VSC5*), we conclude that under the growth conditions used, structures with very similar morphologies are obtained, regardless of the growth parameters varied. Furthermore, as aimed, these heterostructures exhibit superior surface quality (also observed in Nomarski contrast and AFM). However, their defect content is not changed much from the test structures of the first set (similar ranges of values for the TD densities), but the results obtained on the TD densities have mostly a qualitative value, due to the highly estimative approach of the technique used to determine them.

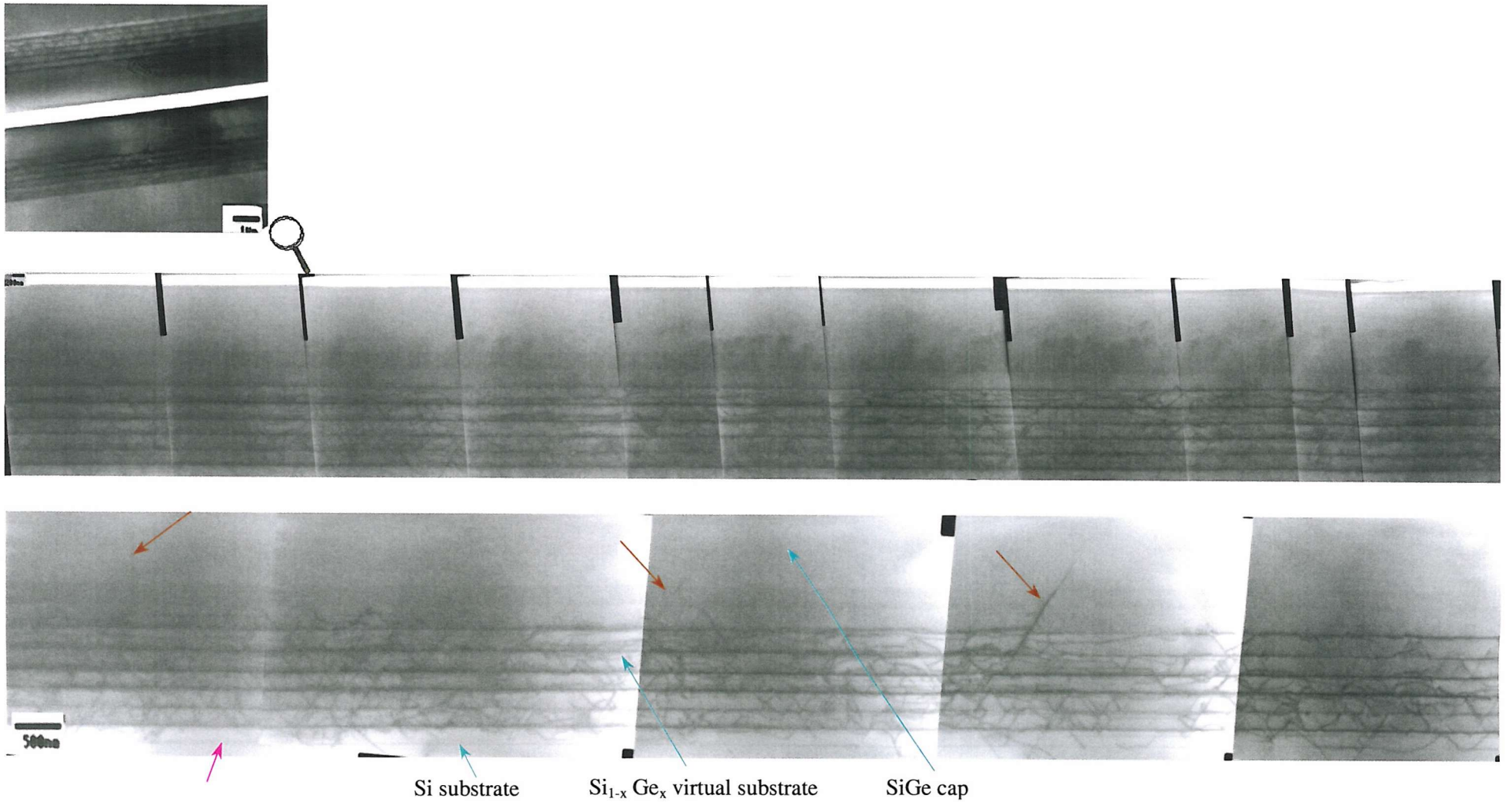

Figure 6.52. XTEM bright-field micrographs (obtained using the main beam condition) of the step-graded heterostructure of the second set, which incorporates a microelectronic structure at the top, *VSC1*. From the top to the bottom of the page, the size of the imaged layer decreases. The pink arrow points to the interfacial carbon layer. The brown arrows indicate TDs.

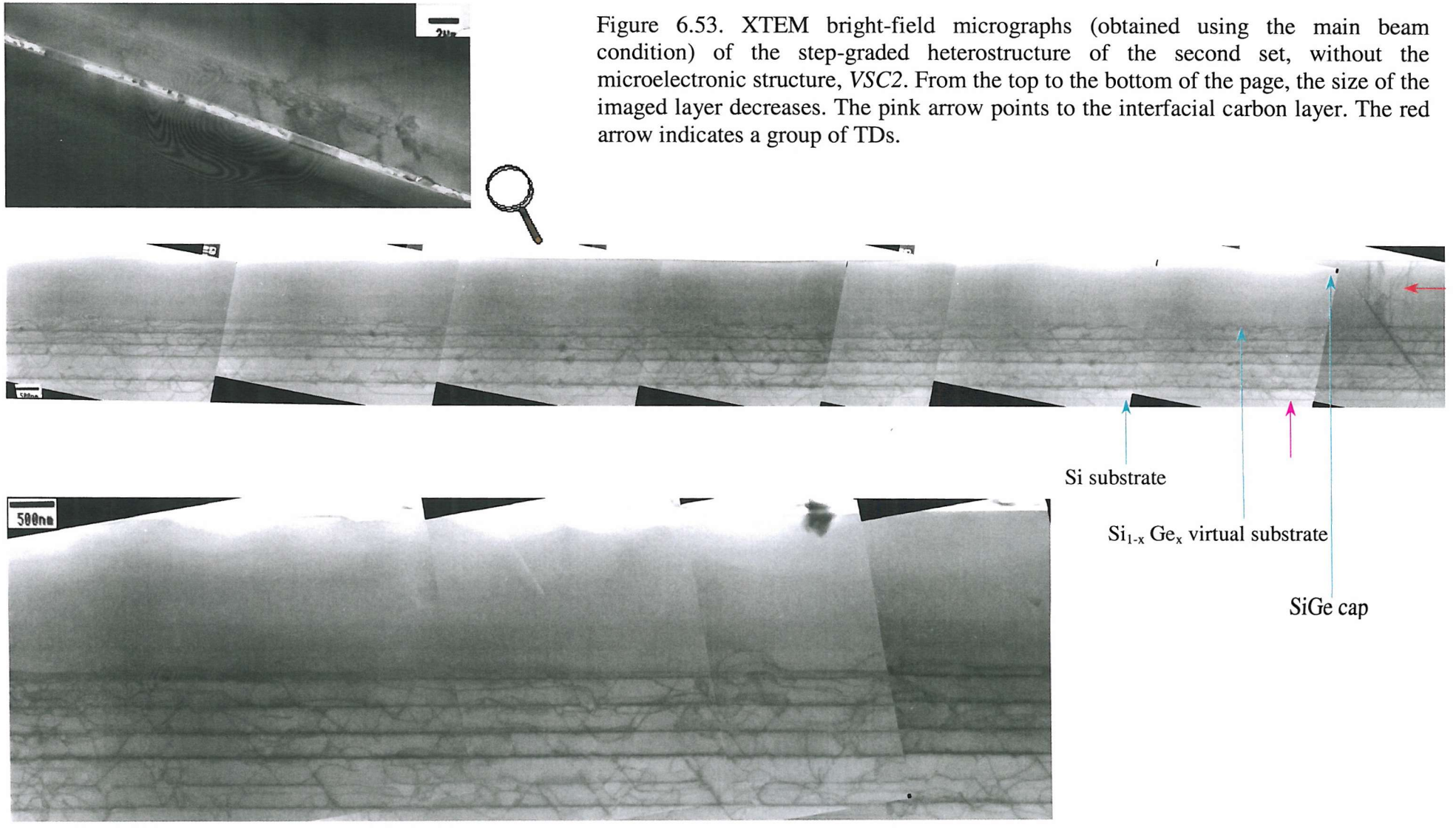

Figure 6.53. XTEM bright-field micrographs (obtained using the main beam condition) of the step-graded heterostructure of the second set, without the microelectronic structure, *VSC2*. From the top to the bottom of the page, the size of the imaged layer decreases. The pink arrow points to the interfacial carbon layer. The red arrow indicates a group of TDs.

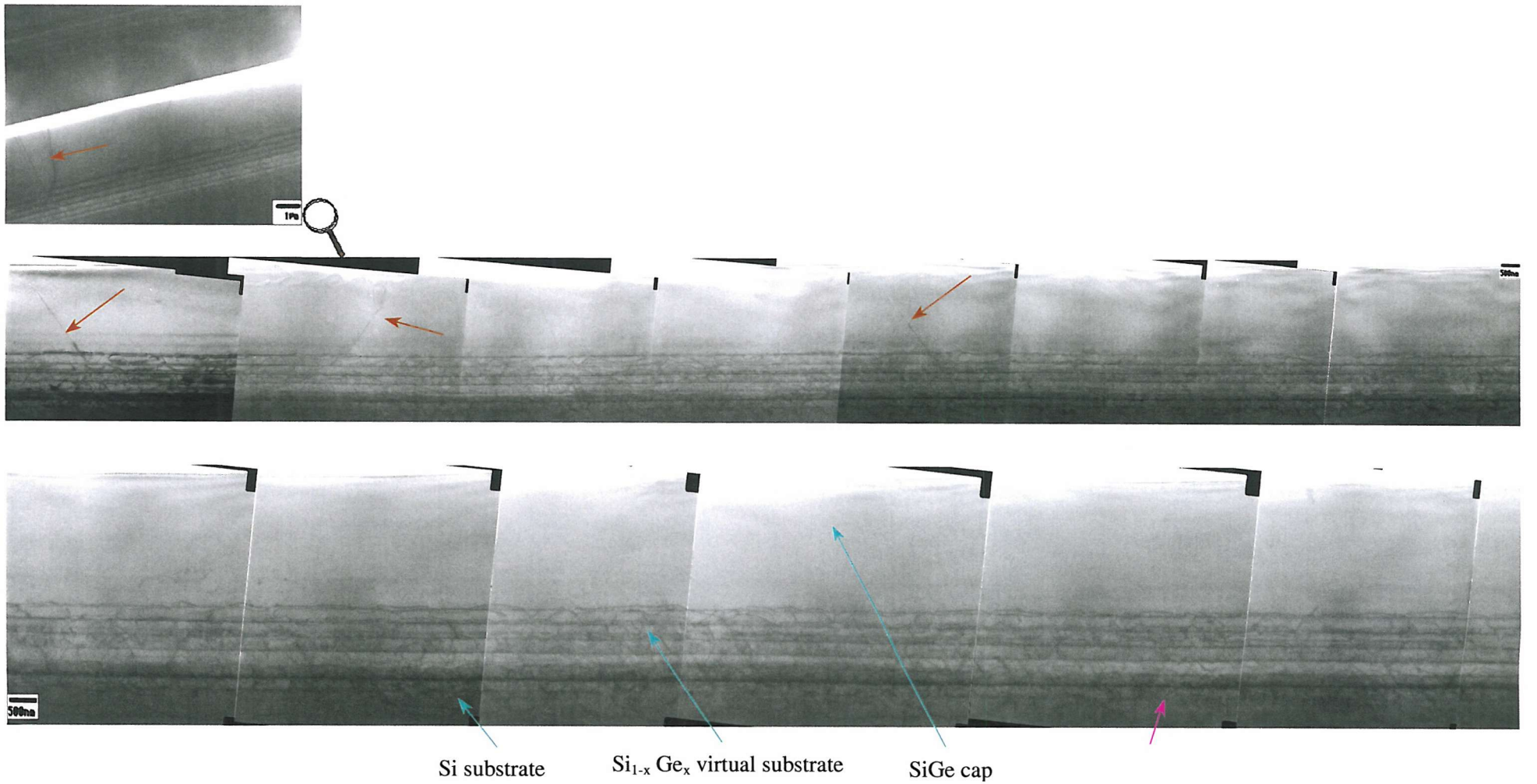

Figure 6.54. XTEM bright-field micrographs (obtained using the main beam condition) of the step-graded heterostructure of the second set, with the thick capping layer, *VSC3*. From the top to the bottom of the page, the size of the imaged layer decreases. The pink arrow points to the interfacial carbon layer. The brown arrows indicate TDs.

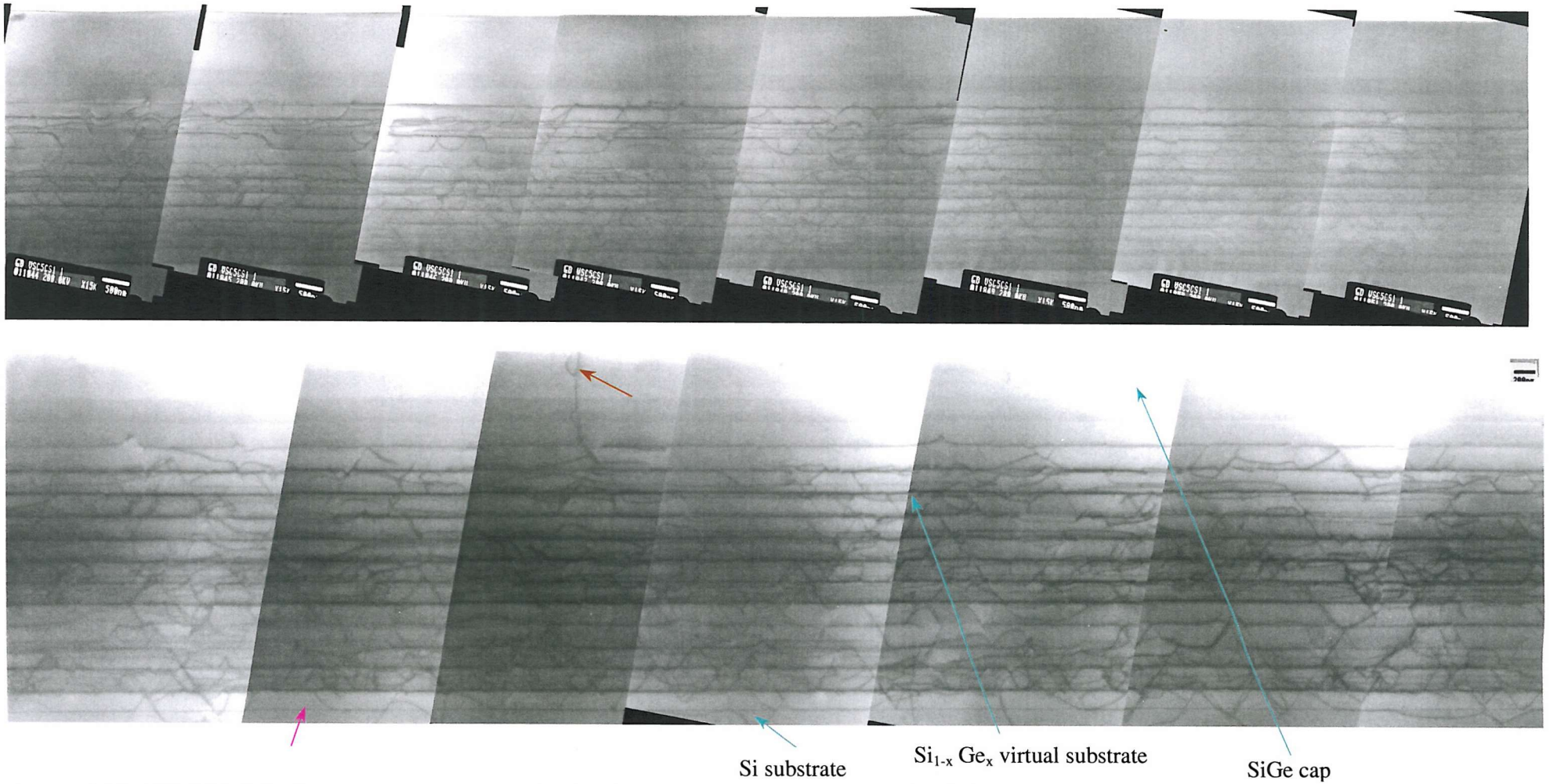

Figure 6.58. XTEM bright-field micrographs (obtained using the main beam condition) of the step-graded heterostructure of the second set grown under identical conditions with *VSC2*, but with a variation of the Ge concentration in the virtual substrates in double the number of half-sized steps, *VSC5*. From the top to the bottom of the page, the size of the imaged layer decreases. The pink arrow points to the interfacial carbon layer. The brown arrow indicates a TD.

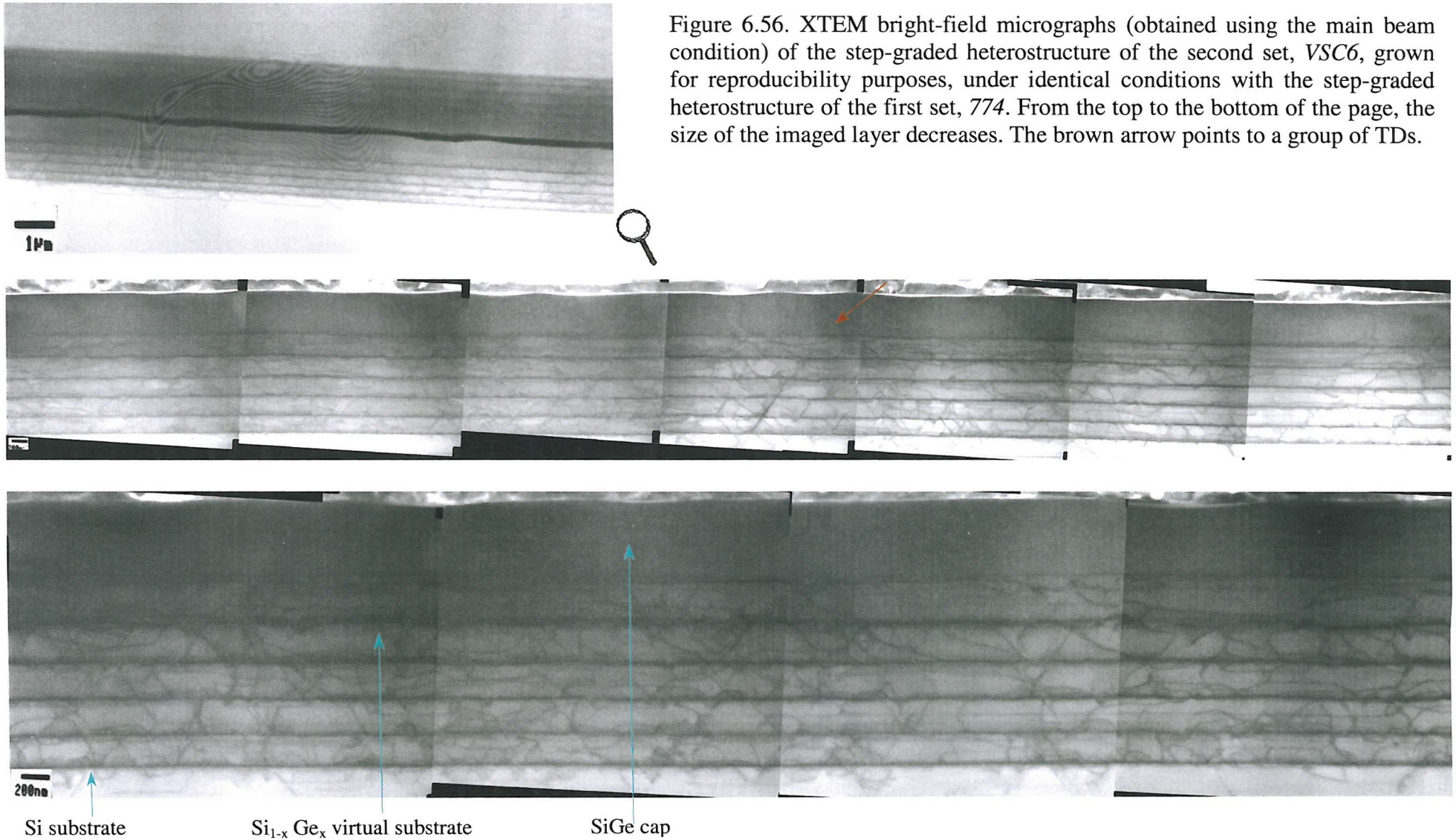

Figure 6.56. XTEM bright-field micrographs (obtained using the main beam condition) of the step-graded heterostructure of the second set, *VSC6*, grown for reproducibility purposes, under identical conditions with the step-graded heterostructure of the first set, *774*. From the top to the bottom of the page, the size of the imaged layer decreases. The brown arrow points to a group of TDs.

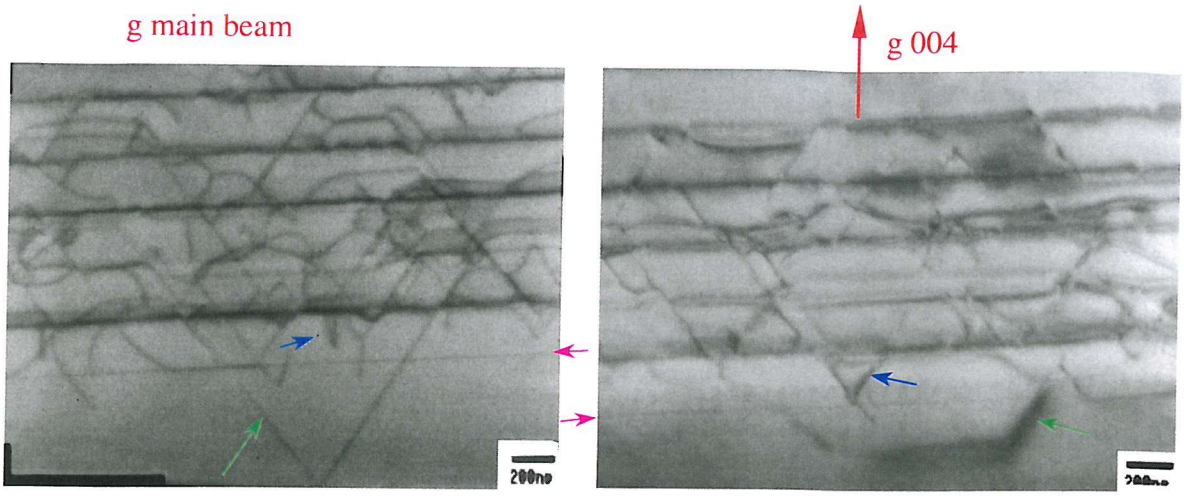

(a) (b)

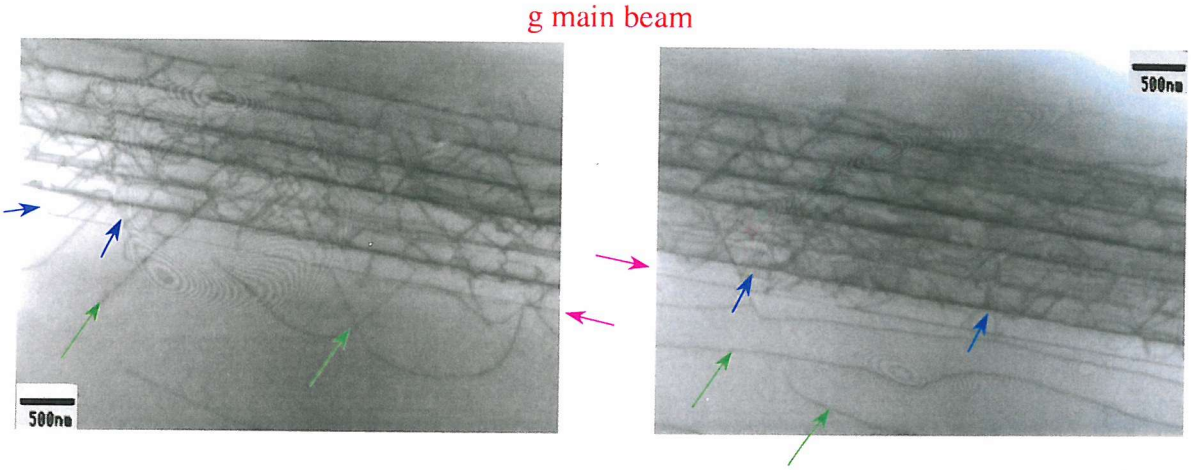

(c) (d)

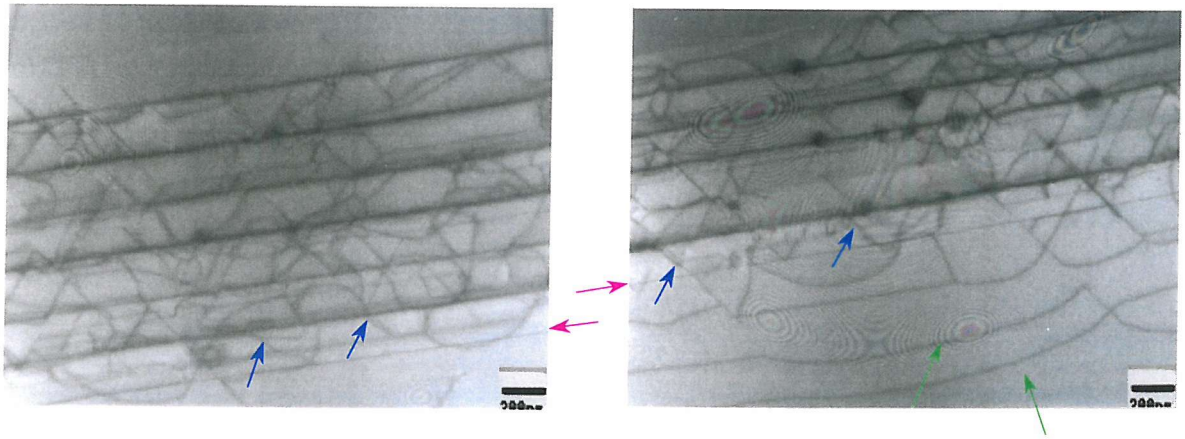

(e) (f)

g main beam

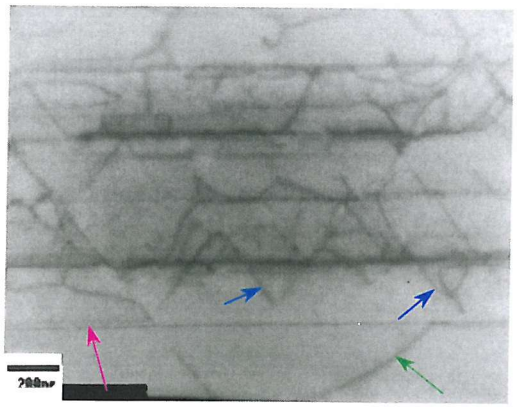

(g)

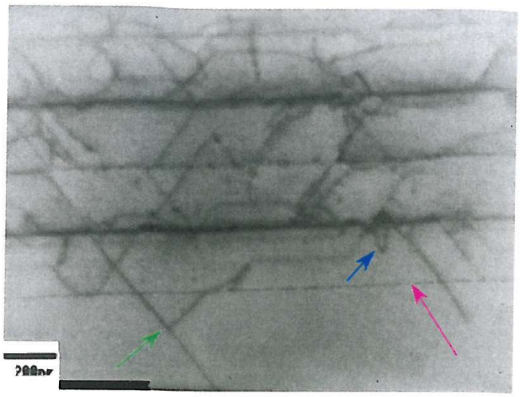

(h)

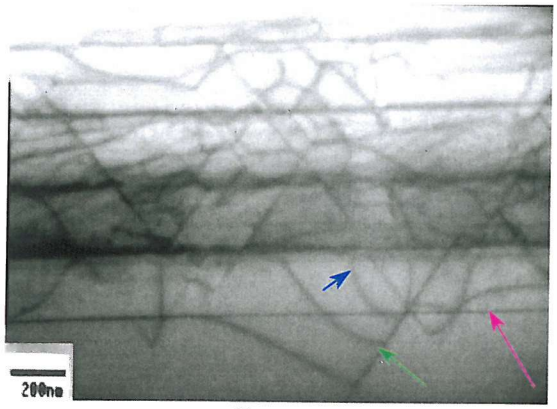

(i)

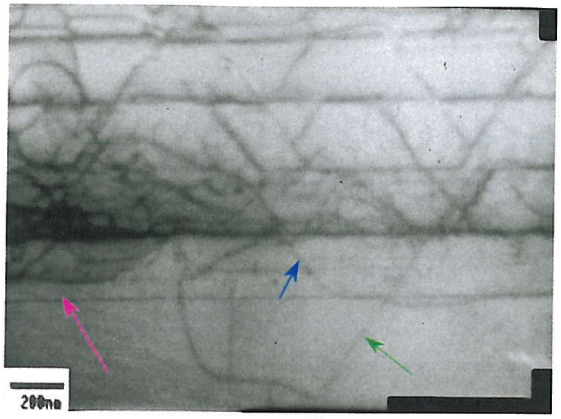

(j)

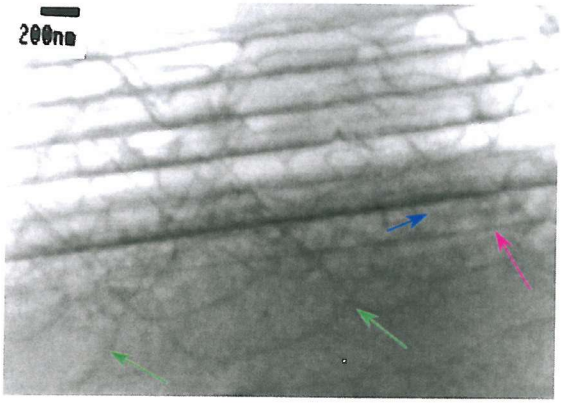

(k)

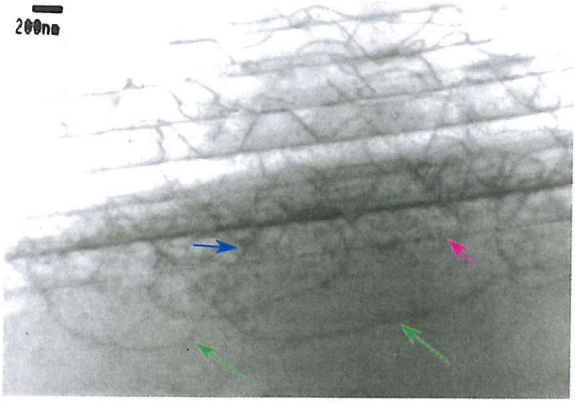

(l)

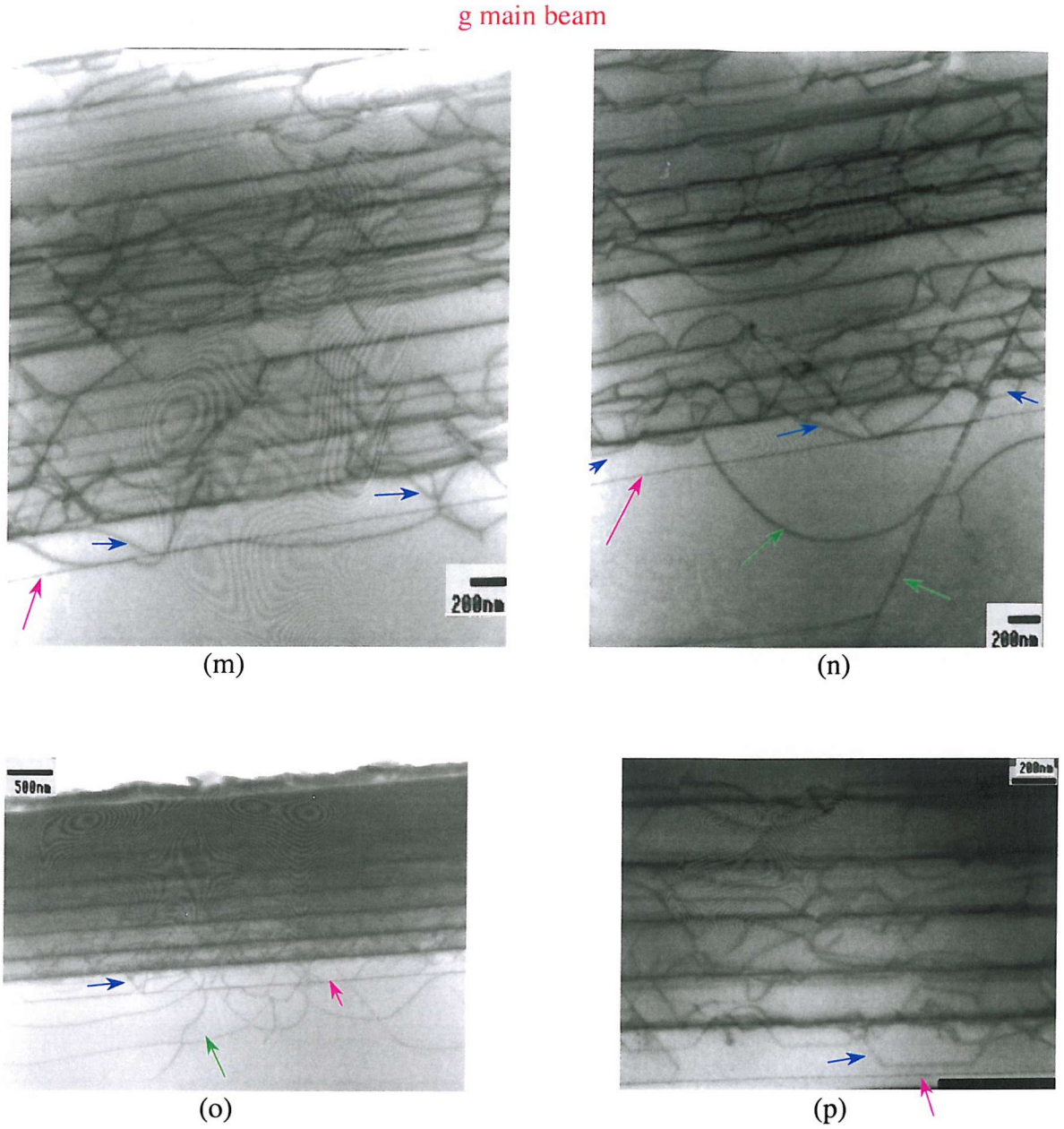

(m) (n)

(o) (p)

Figure 6.57. Bright-field XTEM micrographs of the step-graded heterostructures of the second set showing the carbon layer present at the onset of the LPCVD growth (indicated by the pink arrows). This layer shows no contribution to misfit strain relaxation. Some defects extend well beyond the carbon layer, into the Si substrate (green arrows). A number of defects stop at or do not even reach the carbon layer, as indicated by the blue arrows: (a-b) *VSC1*; (c-f) *VSC2*, showing a large number of defects extending deeper into the Si substrate than observed in any of the heterostructures previously analysed (indicated by the green arrows especially in c, d and f; (g-l) *VSC3*, showing defects extending deep into the Si substrate similarly to *VSC2*; (m-n) *VSC5*, showing, once again, the deep defects similar to those in *VSC2* and *VSC3*; (o-p) *VSC6*, grown for reproducibility, showing the presence of the deep defects, similarly to the other step-graded heterostructure of the second set, but also with the step-graded heterostructure of the first set, *774*, grown under identical conditions (Figure 6.31 a-f).

(a)

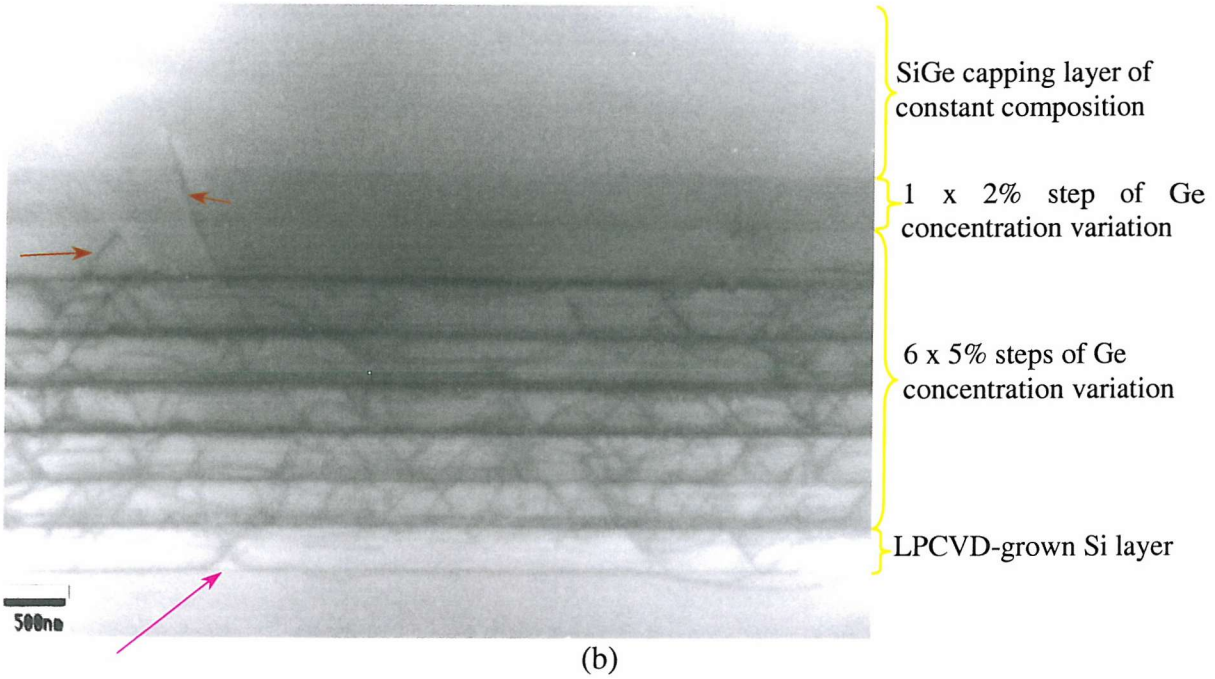

(b)

Figure 6.58. Bright-field XTEM micrographs of the step-graded heterostructure of the second set, which incorporates a microelectronic structure at the top, *VSC1*, showing: (a) the microelectronic structure indicated by the red arrows; (b) the whole heterostructure in which the pink arrow points to the carbon layer present at the Si substrate-LPCVD grown heterostructure interface. From the bottom to the top of the image, the heterostructure consists of: the LPCVD-grown Si layer, incorporating some of the relaxation-induced defects followed by 6 steps of 5% Ge concentration variation, with a decrease in defect concentration toward the upper steps, leaving the last step almost MD-free, one step of 2% Ge concentration variation, which looks elastically strained (has no MDs) and the SiGe capping layer of constant composition at the top, MD-free, but with some dislocation segments threading to the free surface (indicated by the brown arrows).

(a)

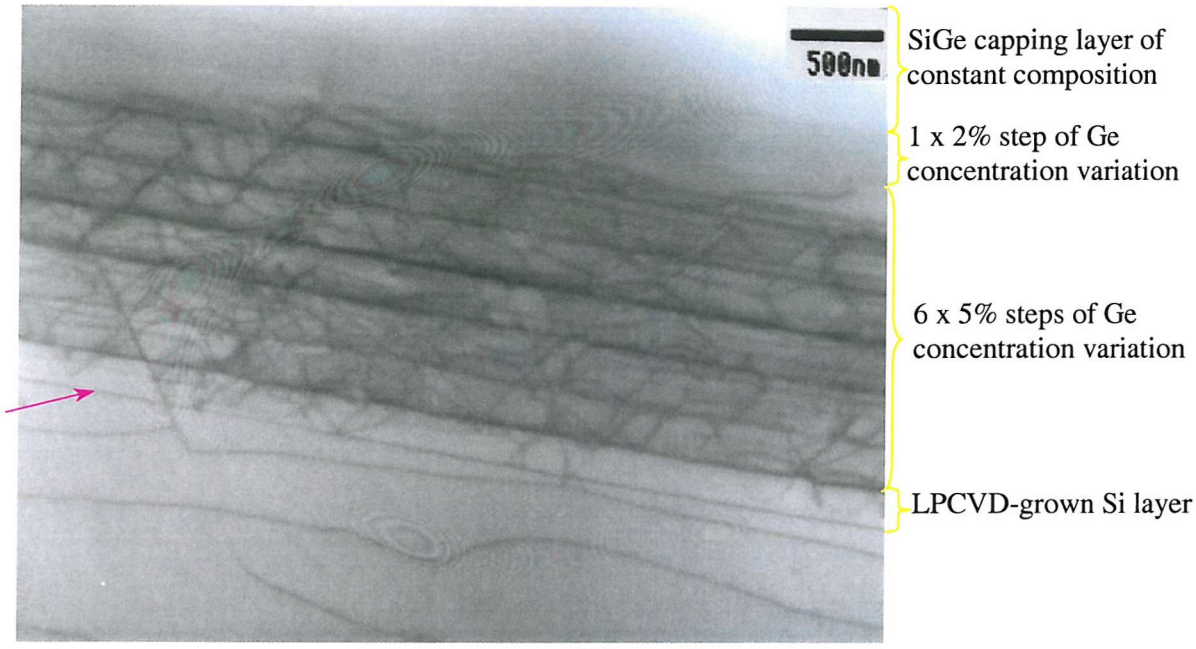

(b)

Figure 6.59. Bright-field XTEM micrographs of the step-graded heterostructure of the second set, without the microelectronic structure, *VSC2*, showing: (a) the surface of the heterostructure from which the microelectronic structure is absent (by comparison with Figure 6.58 a); (b) the whole heterostructure in which the pink arrow points to the carbon layer present at the Si substrate-LPCVD-grown heterostructure. From the bottom to the top of the image, the heterostructure consists of: the LPCVD-grown Si layer, incorporating some of the relaxation-induced defects followed by 6 steps of 5% Ge concentration variation, one step of 2% Ge concentration variation, which looks elastically strained (has no MDs) and the SiGe capping layer of constant composition at the top, MD-free.

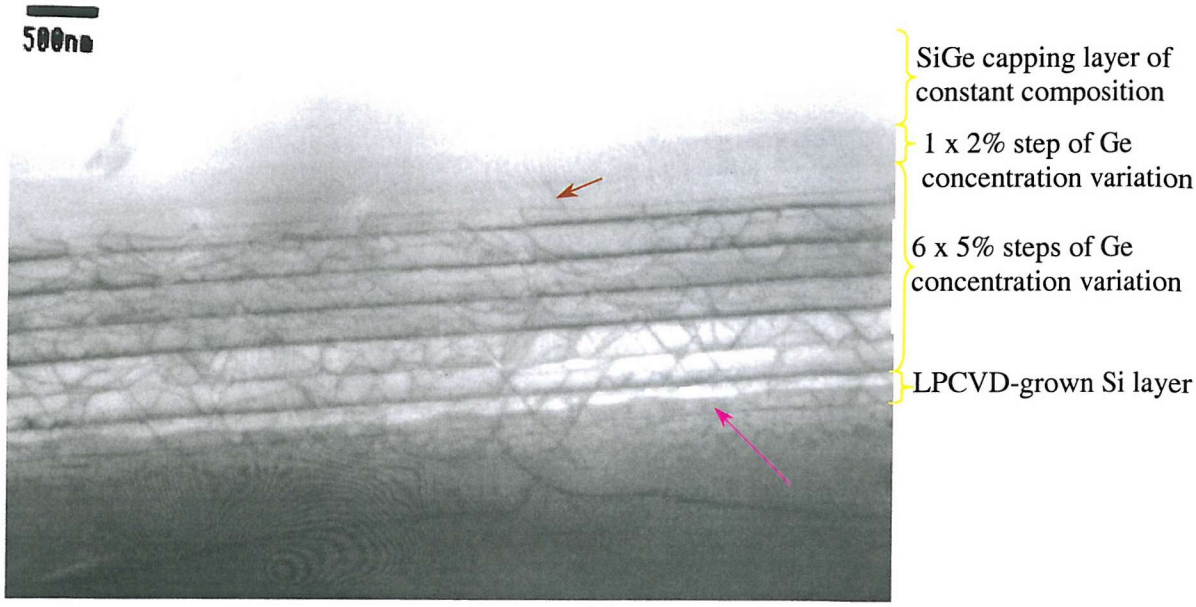

(a)

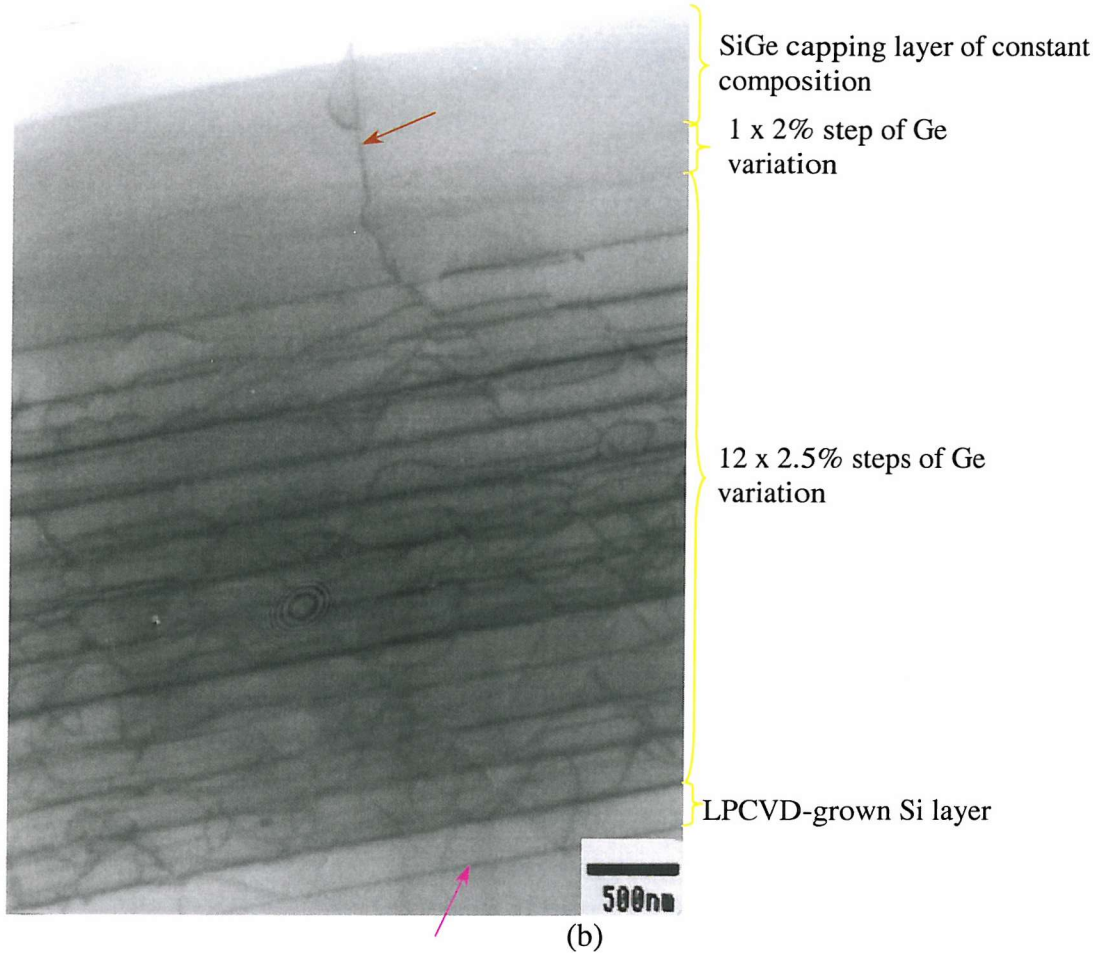

(b)

Figure 6.60. Bright-field XTEM micrographs showing: (a) the step-graded heterostructure of the second set, with the thicker capping layer, *VSC3*, which from the bottom to the top of the image consists of: the LPCVD-grown Si layer, incorporating some of the relaxation-induced defects followed by 6 steps of 5% Ge concentration variation, with a decrease in defect concentration toward the upper steps, one step of 2% Ge concentration

variation, which looks elastically strained (has no MDs) and the SiGe capping layer of constant composition at the top, MD-free, but with some dislocation segments threading to the free surface (indicated by the brown arrow) and: (b) the step-graded heterostructure of the second set, with double the number of half-sized Ge concentration steps, *VSC5*, which from the bottom to the top of the image consists of: the LPCVD-grown Si layer, incorporating some of the relaxation-induced defects followed by 12 steps of 2.5% Ge concentration variation, with a decrease in defect concentration toward the upper steps, leaving the last step almost MD-free, one step of 2% Ge concentration variation, which looks elastically strained (has no MDs) and the SiGe capping layer of constant composition at the top, MD-free, but with some dislocation segments threading to the free surface (indicated by the brown arrow).

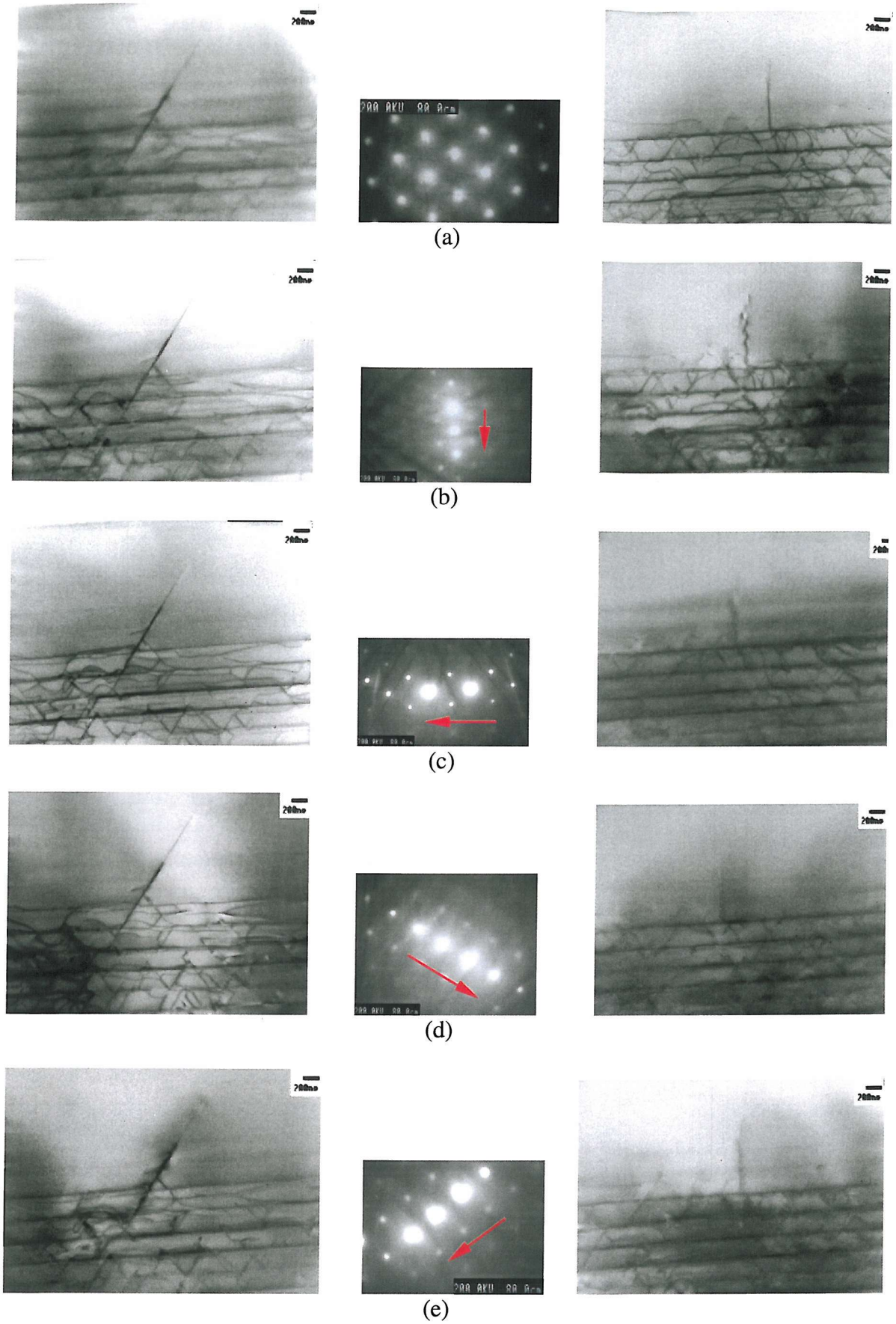

Figure 6.61. Bright-field XTEM micrographs of the step-graded heterostructure of the second set, *VSC1*, showing TDs (one pileup, in the left column, and one single threader, in the right column) imaged in different two-beam conditions and the corresponding

diffraction patterns: (a) main beam condition; (b) $00\bar{2}$; (c) $\bar{2}20$; (d) $1\bar{1}\bar{1}$; (e) $\bar{1}11$. The fact that the threaders are visible in all two-beam conditions indicates their mixed type.

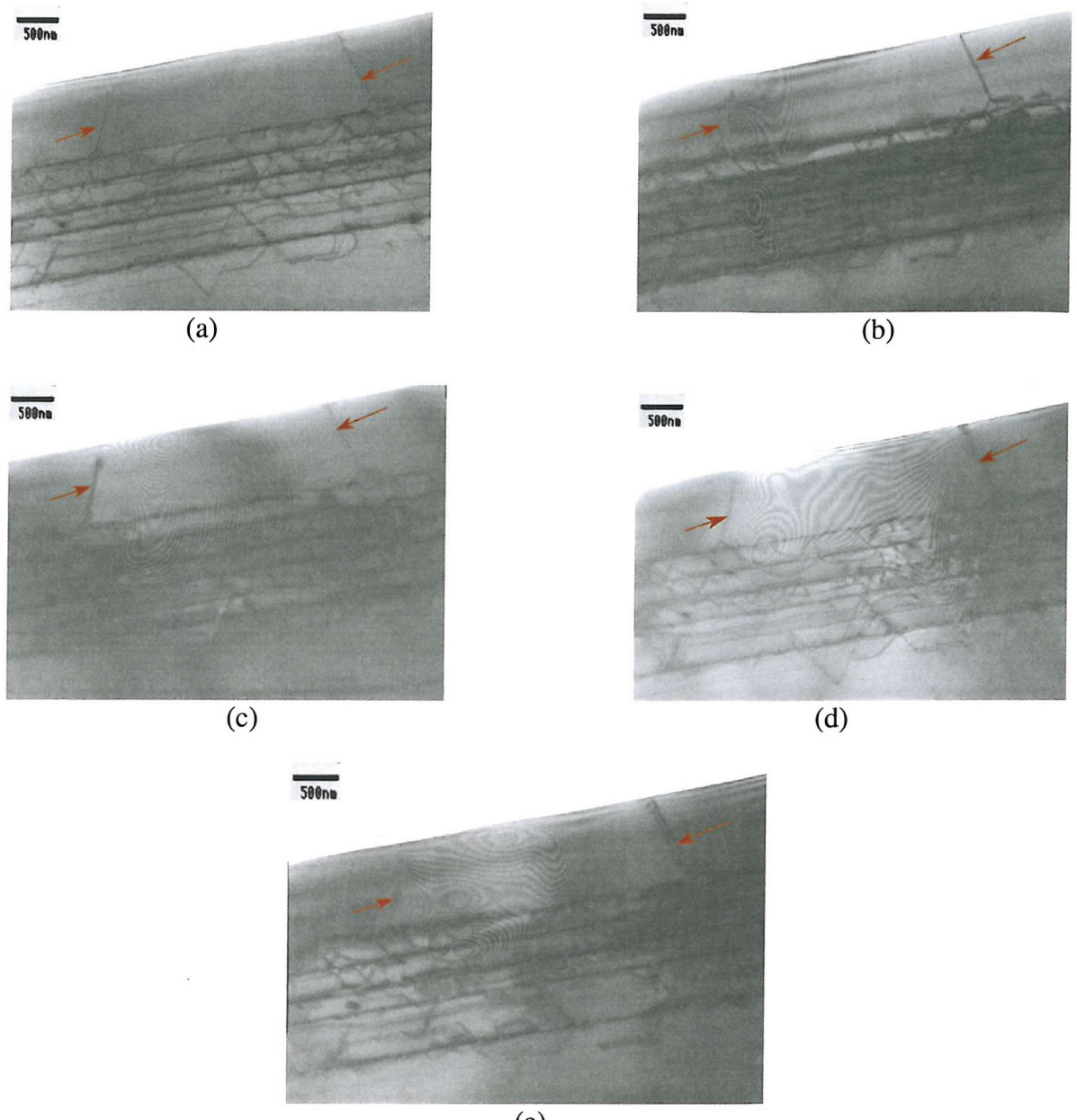

Figure 6.62. Bright-field XTEM micrographs of the step-graded heterostructure of the second set, *VSC2*, showing two TDs (indicated by the brown arrows) imaged in different two-beam conditions: (a) main beam condition; (b) $00\bar{2}$; (c) $\bar{2}20$; (d) $1\bar{1}\bar{1}$; (e) $\bar{1}11$. The diffraction patterns corresponding to each of the two-beam conditions are shown in Figure 6.61. The fact that the threaders are visible in all two-beam conditions indicates their mixed type.

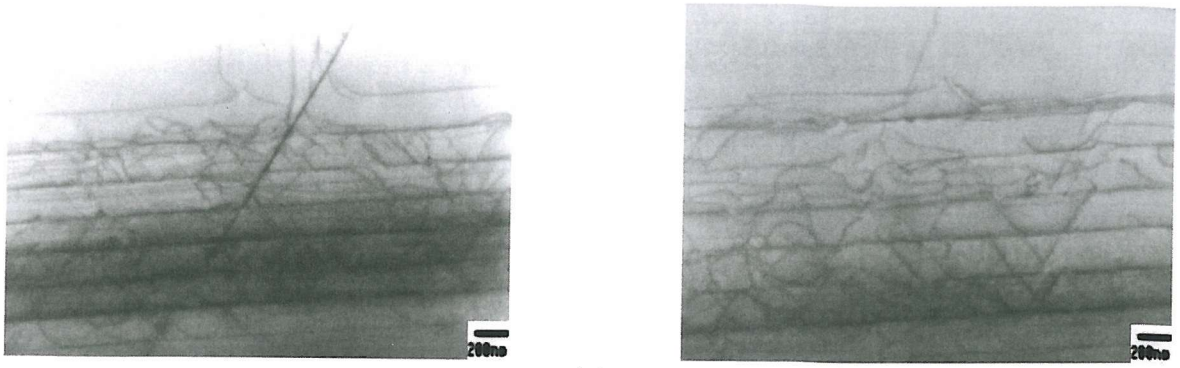

(a)

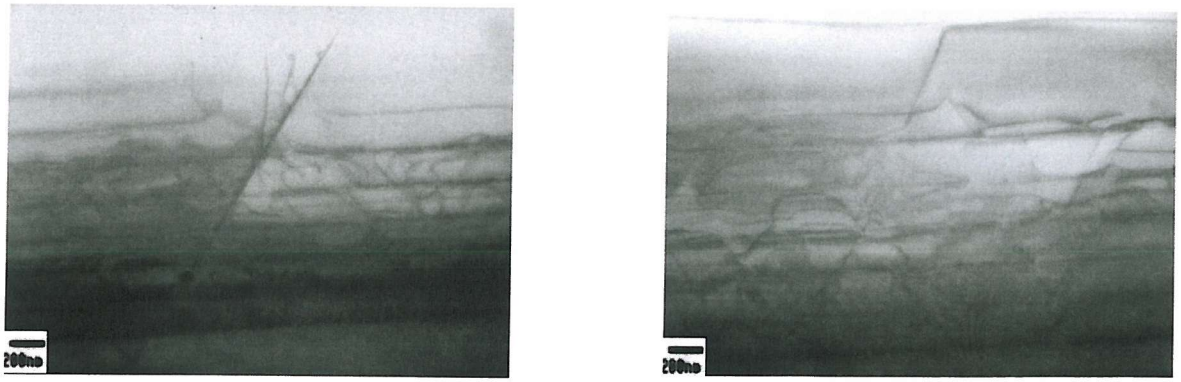

(b)

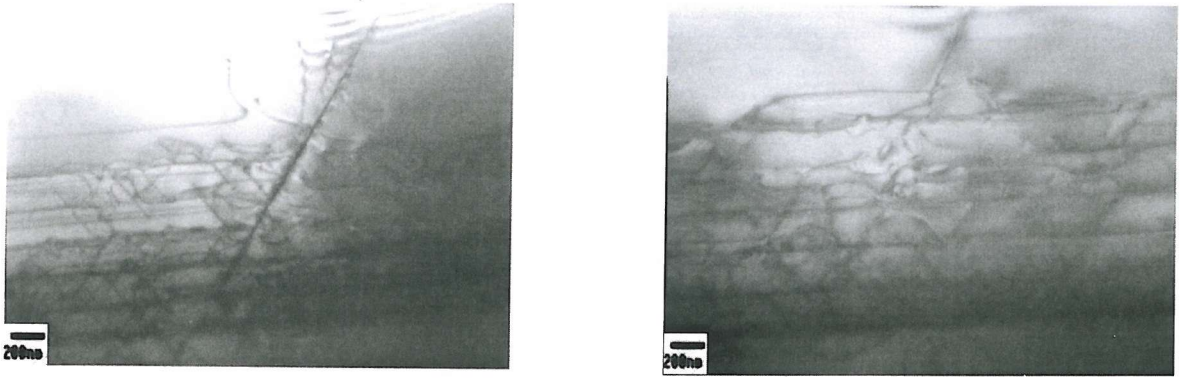

(c)

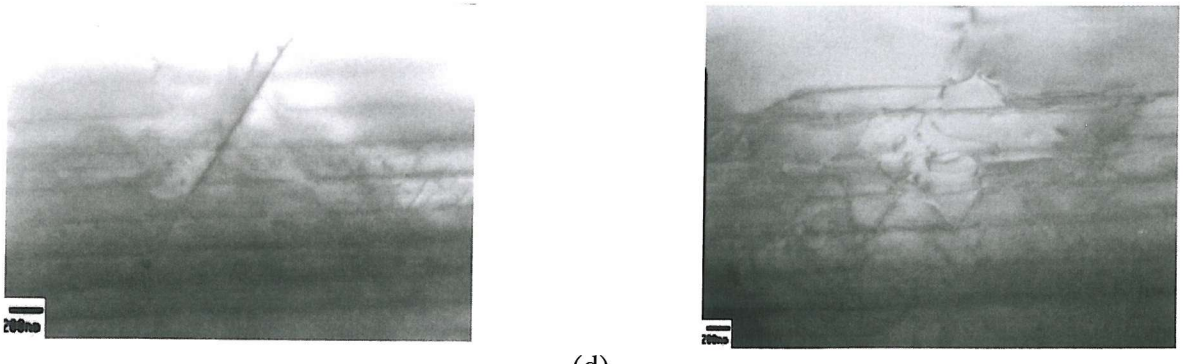

(d)

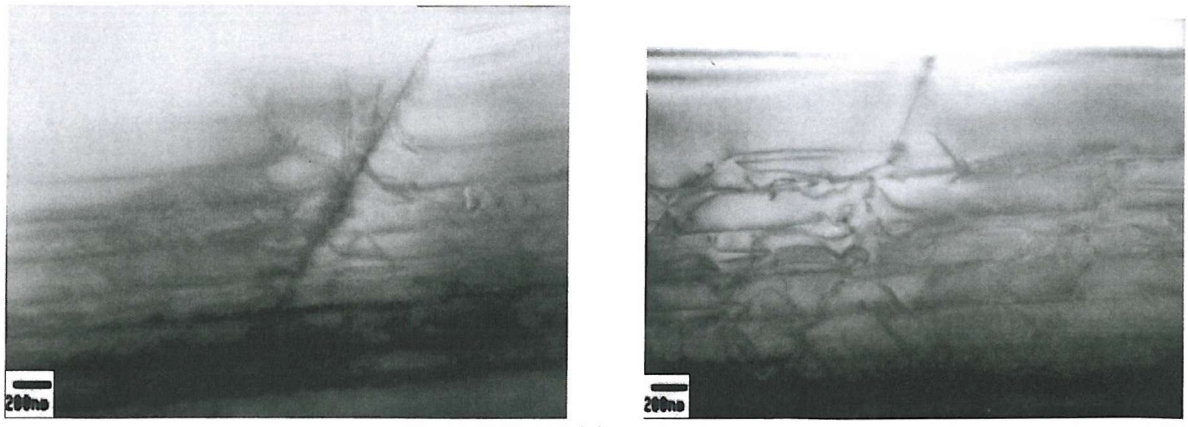

(e)

Figure 6.63. Bright-field XTEM micrographs of the step-graded heterostructure of the second set, *VSC3*, showing a pileup of TDs, in the left column, and a single threader, in the right column, imaged in different two-beam conditions: (a) main beam condition; (b) $\mathbf{00\bar{2}}$; (c) $\mathbf{\bar{2}20}$; (d) $\mathbf{1\bar{1}\bar{1}}$; (e) $\mathbf{\bar{1}11}$. The diffraction patterns corresponding to each of the two-beam conditions are shown in Figure 6.61. The fact that the threaders are visible in all two-beam conditions indicates their mixed type.

(a)

(b)

(c)

(d)

(e)

Figure 6.64. Bright-field XTEM micrographs of the step-graded heterostructure of the second set, VSC5, showing a TD imaged in different two-beam conditions: (a) main beam condition; (b) $\mathbf{00\bar{2}}$; (c) $\mathbf{\bar{2}20}$; (d) $\mathbf{1\bar{1}\bar{1}}$; (e) $\mathbf{\bar{1}11}$. The diffraction patterns corresponding to

each of the two-beam conditions are shown in Figure 6.61. The fact that the threader is visible in all two-beam conditions, indicates its mixed type.

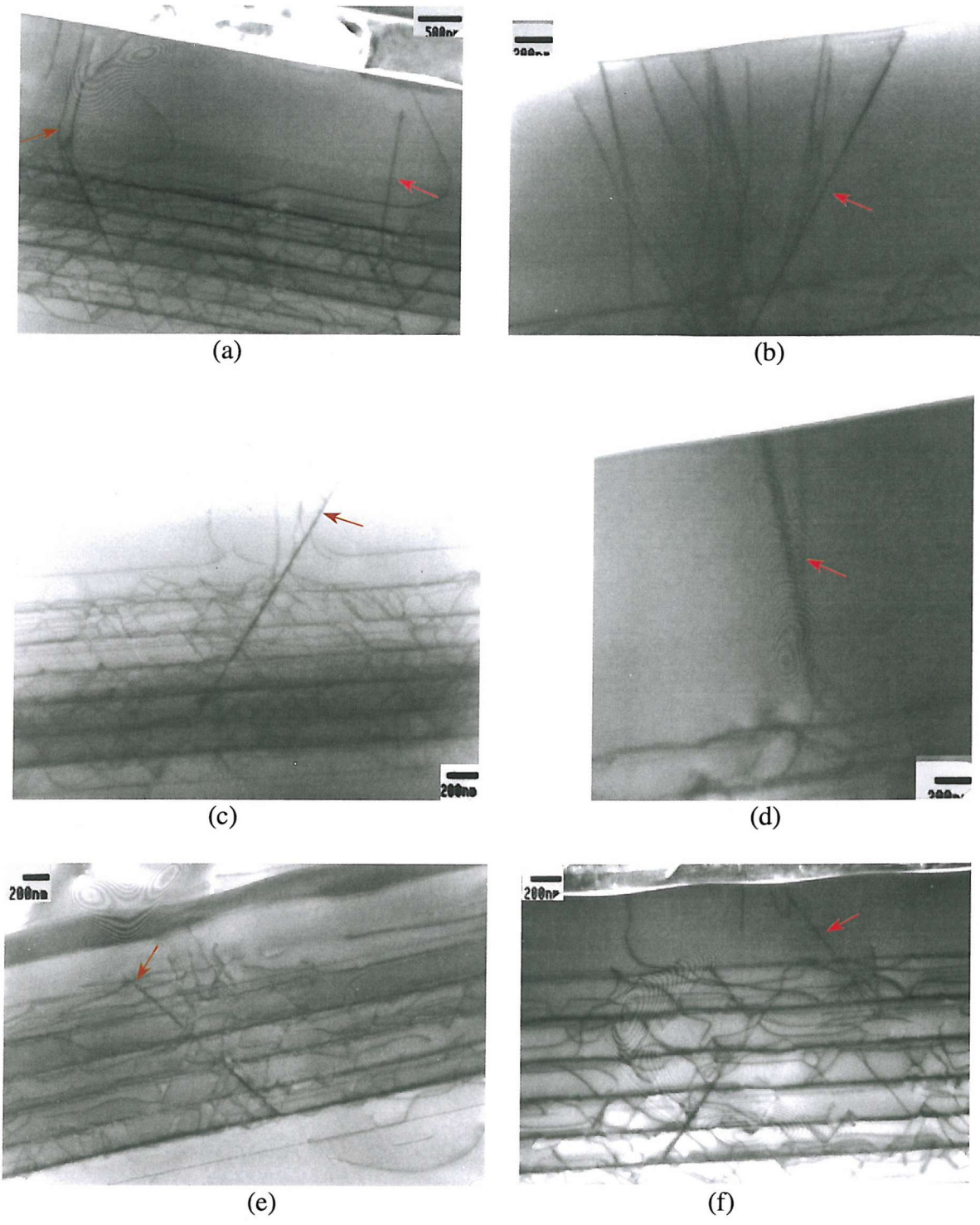

Figure 6.65. Bright-field XTEM micrographs (obtained using the main beam condition) of the step-graded heterostructures of the second set showing different TDs in: (a) *VSC2*, the brown arrow points to a pileup of 60° TDs, running through the whole structure, the red arrow indicates a single threader; (b) *VSC2*, the red arrow points to a group of TDs; (c) *VSC3*, the brown arrow points to a pileup of 60° TDs, running through the whole structure; (d) *VSC5*, the red arrow indicates a group of TDs; (e-f) *VSC6*, the brown arrow points to a pileup of 60° TDs, running through the whole structure, the red arrow indicates a single TD.

6.3.3. SECOND SET: LINEAR-GRADED HETEROSTRUCTURE

6.3.3.1. Optical microscopy: Nomarski DIC analysis

Nomarski DIC microscopy analyses were carried for an initial assessment of the surface morphology of the linear-graded heterostructure of the second set, using the same equipment under the same conditions as for all the previously studied structures.

Nomarski DIC analyses of the linear-graded heterostructure of the second set, *VSC4*, grown at **750°C**, with a **zero** initial Ge content in the virtual substrate, a Ge concentration gradient in the virtual substrate of **16%/μm** and a **1 μm** thick capping layer, show a completely different surface morphology by comparison with the linear-graded heterostructures of the first set, *720*, grown at a higher temperature (**800°C**), with a higher initial Ge content in the virtual substrate (**13%**), a slightly higher Ge concentration gradient in the virtual substrate (**16%/μm**) and a thinner capping layer (**0.30 μm**) and *775*, grown at the same temperature (**750°C**), with an initial Ge concentration in the virtual substrate of **12%**, a higher Ge concentration gradient in the virtual substrate (**≈ 22 %/μm**) and a much thinner capping layer (**0.24 μm**), as can be seen in Figure 6.66 a-c. The linear-graded heterostructure of the second set exhibits a very similar surface morphology with the step-graded heterostructures of the second set grown under similar conditions, *VSC1–3* and *VSC5* (Figure 6.36 a-d), being characterised by a smooth surface with a fine and uniform crosshatch pattern. Some accentuated crosshatch lines can still be observed, even in this case (indicated by the red arrows in Figure 6.66 c), but similarly with the step-graded heterostructures of the second set, grown under similar conditions, these lines look very shallow and their density is very low. Deep trenches of the type corresponding to the accentuated crosshatch lines in the first set of linear-graded heterostructures (red arrows in Figure 6.66 a and b) are completely absent from the linear-graded structure of the second set (Figure 6.66 c). Additionally, Nomarski micrographs show, in this case also, the presence of what was identified as pits of various shapes and sizes. Furthermore, the presence of the large pits, identified as being growth defects of both 'round' and 'square' shapes can be observed (Figure 6.67 a-b). A rough estimation of their density (calculated in the same way as for the step-graded heterostructures of the second set) shows: **≤ 128 x 10^{-6} / μm^2**. The upper limit of this density is somewhere in between the upper limit of the density displayed by *VSC2* (**≈ 213 x 10^{-6} / μm^2**) and the upper limit of the density for *VCS3* (**≈ 85 x 10^{-6} / μm^2**), thus slightly higher than expected. Based on the growth

sequence for the heterostructures of the second set, we expected this value to be somewhere between the value for *VSC3* and that for *VSC5*. This result may have been caused by the area chosen for the counting, which may not have been the most representative of the structure.

High magnifications (x1000) Nomarski studies allowed measurements of the crosshatch spacing. Values obtained are consistent with those for the step-graded heterostructures of the first set *VSC1–3* and *VSC5* and are **≤ 1 μm**. Furthermore, the in-plane dimensions of the large growth defects could be measured. Once again, these measurements showed that the large 'round-shaped' pits have smaller in-plane sizes, diameter **≤ 8–10 μm** (Figure 6.67 a), compared to the 'square-shaped' ones, which have larger linear dimensions of **≤ 20μm** (Figure 6.67 b). High magnification Nomarski contrast micrographs of the linear-graded heterostructure of the second set also show the shapes for these surface features, which are similar to those already observed for the step-graded heterostructures of the second set and schematically represented in Figure 6.39 a-d, being of conical/truncated cone or pyramidal/truncated pyramid shapes. Furthermore, even in this case, most of these surface features seem to be isolated and do not appear to influence the crosshatch pattern around them (Figure 6.67 a-b) thus, indicating, once again, that they have been incorporated in the later stages of growth as already shown for the step-graded heterostructures of the second set in § 6.3.2.1 – 6.3.2.2. Very few of them are connected to others and they are always aligned along one of the **<110>** directions (Figure 6.68) similarly to the step-graded heterostructures of the second set grown under similar conditions (Figure 6.40 a-d).

Once again, as aimed, in the case of the linear-graded heterostructure of the second set, the growth conditions used result in a better surface morphology compared to the linear-graded structures of the first set.

The effects of the different types of grading of the Ge composition in the virtual substrate on the surface morphology of the heterostructures of the second set were studied by comparing step-graded *VSC2* and linear-graded *VSC4*, which were grown under identical conditions. Nomarski studies of these two heterostructures show very similar surface morphologies (Figure 6.69 a-b). This result is very different from the one obtained by comparing the two heterostructures of the first set grown under identical conditions, but characterised by a different type of variation of the Ge composition in the virtual substrate

(step-graded *774* versus linear-graded *775*). From this observation, we conclude that under the growth conditions used for the second set of heterostructures, the different types of Ge concentration grading in the virtual substrate (stepwise or linear) do not result in large differences in the surface morphology, whereas under the growth conditions used for the first set of heterostructures, they do.

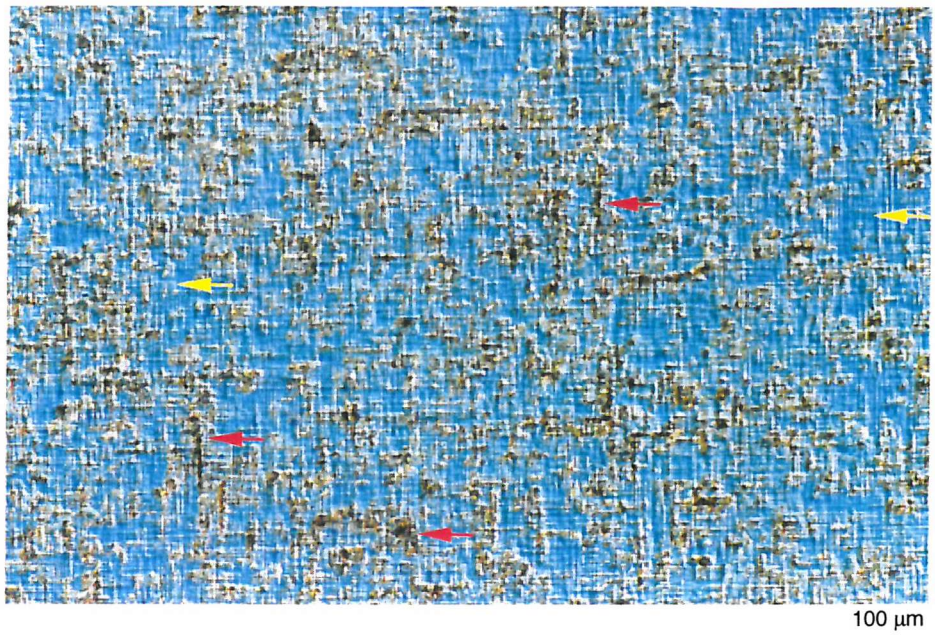

(a)

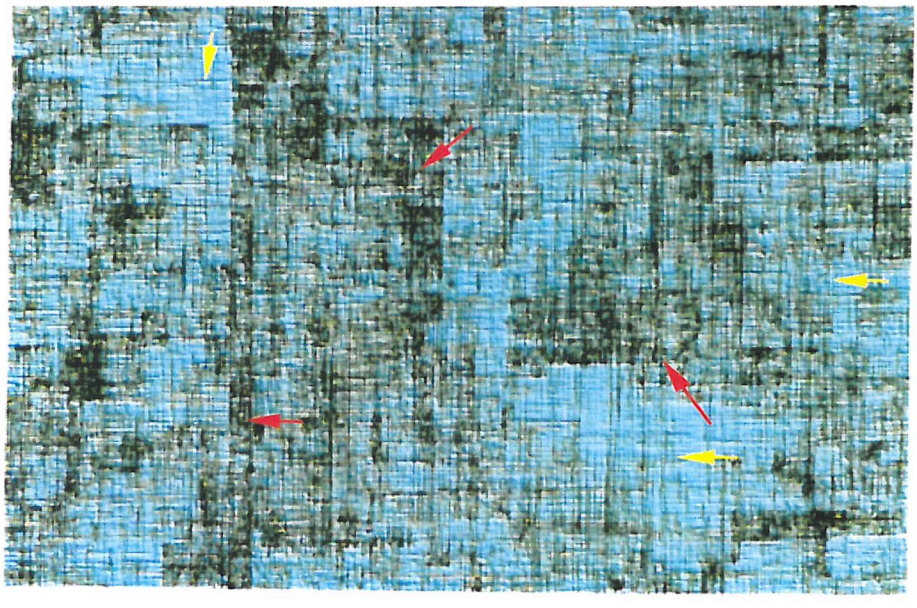

(b)

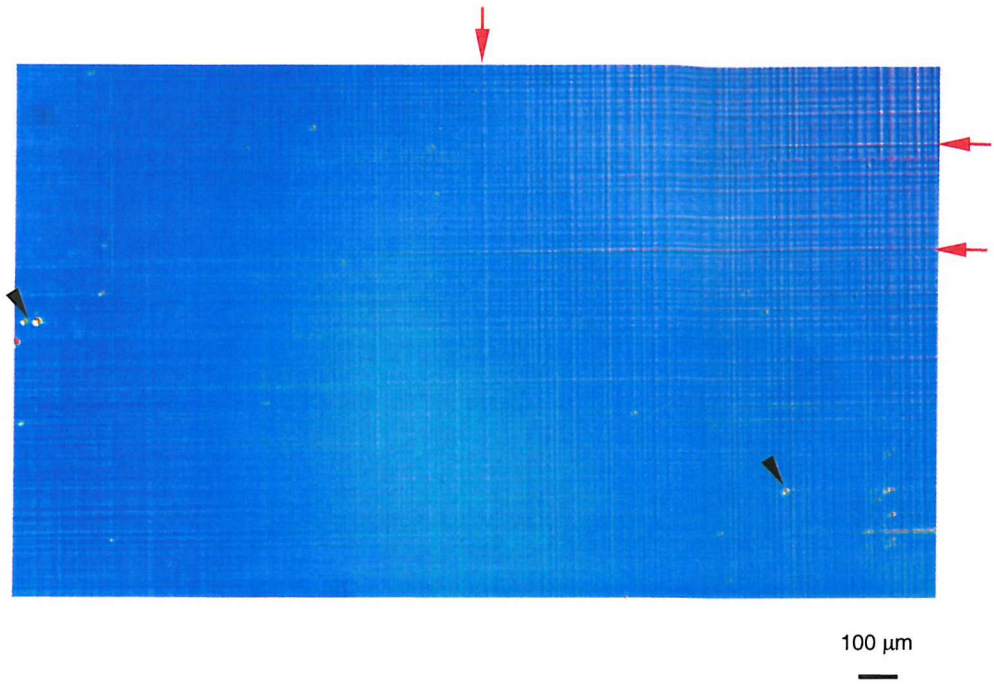

(c)

Figure 6.66. Nomarski contrast micrographs (obtained at x50 magnification) of the three linear-graded heterostructures studied: (a) *720*, of the first set, grown at **800°C**, with a high initial Ge content in the virtual substrate (**13.5%**), a Ge concentration gradient in the virtual substrate of **16.76%/µm** and a capping layer **0.30 µm** thick, showing a high density of accentuated crosshatch lines (indicated by the red arrows) and reduced areas of fine pattern (indicated by the yellow arrows); (b) *775*, of the first set, grown at the lower temperature of **750°C**, with a lower initial Ge content in the virtual substrate (**12%**), a higher Ge concentration gradient in the virtual substrate (≈ **22.06%/µm**) and a thinner capping layer (**0.24 µm**), showing larger areas of fine crosshatch pattern (indicated by the yellow arrows); (c) *VSC4*, of the second set, grown at the same temperature as *775*, but with a **zero** initial Ge content in the virtual substrate, a lower Ge concentration gradient in the virtual substrate (**16.67%/µm**) and a much thicker capping layer (**1 µm**) than both *720* and *775*, showing a much smoother surface, characterised by a fine crosshatch pattern. Some accentuated crosshatch lines are still present (indicated by the red arrows), but they are much shallower than in *720* and *775*. The large-size pits characteristic of the heterostructures of the second set are indicated by the black arrows.

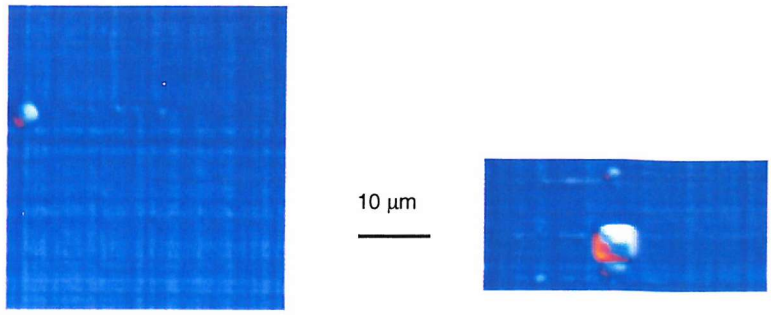

Figure 6.67. Nomarski contrast micrographs (obtained at x1000 magnification) of the linear-graded heterostructure of the second set, *VSC4*, showing the large growth defects: (a) 'round-shaped' with diameters **≤ 8–10 μm**; (b) larger 'square-shaped' with a linear dimension of **≤ 20 μm**.

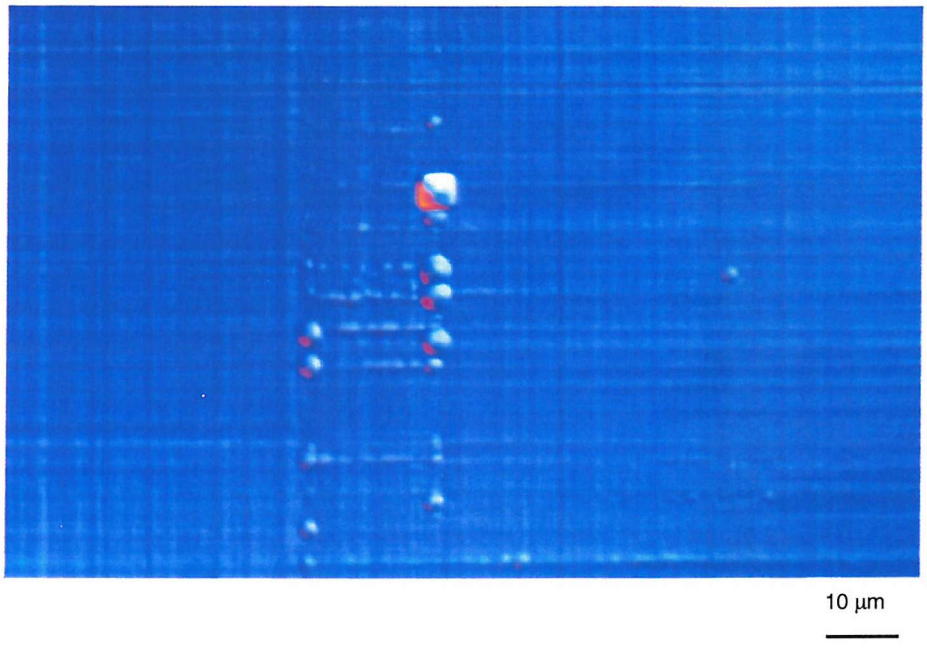

Figure 6.68. Nomarski micrographs (obtained at x1000 magnification) showing large round and square-shaped defects connected and aligned along the **<110>** directions in the linear-graded heterostructure of the second set, *VSC4*.

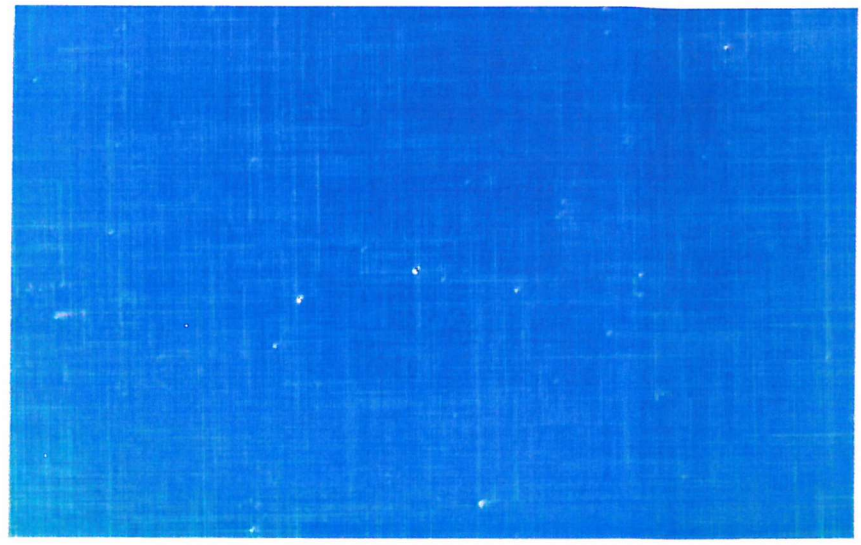

(a)

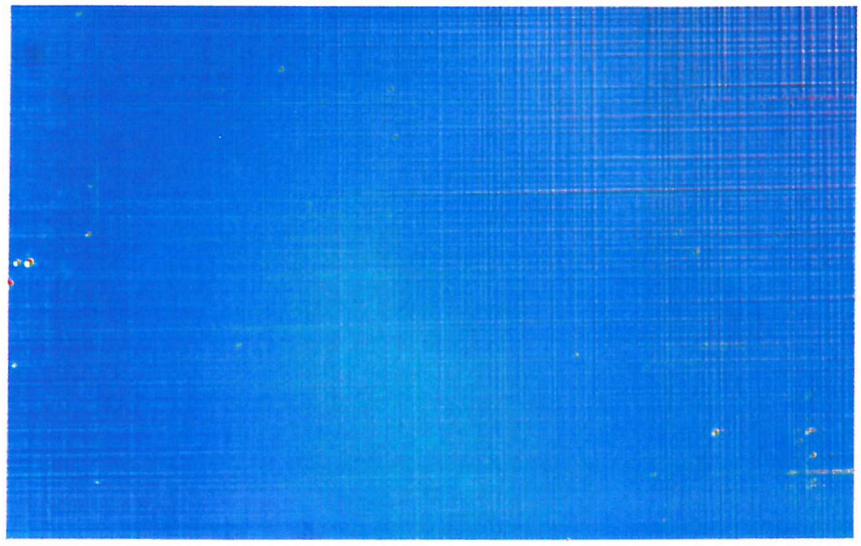

(b)

Figure 6.69. Nomarski DIC micrographs (obtained at x50 magnification) for comparison between two heterostructures of the second set grown under identical conditions, but with different types of grading of the Ge concentration in the virtual substrate: (a) stepwise, *VSC2* and (b) linearly, *VSC4*.

6.3.3.2. Second set: linear-graded heterostructure Scanning probe microscopy: AFM analysis

AFM analyses were carried out using the same equipment and under the same conditions as reported previously for all the heterostructures studied.

Once again, the AFM results confirmed some of the surface morphology information already obtained using Nomarski DIC microscopy, but also provided quantitative information related to the surface topography (e.g. values for the RMS of the surface roughness and for depth variation along the crosshatch lines).

The AFM results, concerning the RMS of the surface roughness, obtained on 100 μm x 100 μm scanned areas of the linear-graded heterostructure of the second set, *VSC4* (≈**9.8nm**, as shown in Figure 6.70 a), of the step-graded heterostructure of the second set, *VSC2*, grown under identical conditions (≈ **10.6 nm**, as presented in Figure 6.71 a), and of the step-graded heterostructure of the second set *VSC5*, grown as an intermediate option between the previous two, being characterised by the same overall variation of the Ge concentration as the previous two, the variation occurring in double the number of half Ge concentration steps (≈ **9.4 nm**, as shown in Figure 6.72 b), indicate that the highest value corresponds to *VSC2* and the lowest to *VSC5*, while *VSC4*, shows an intermediate value. However, the RMS of the surface roughness values for 20 μm x 20 μm scanned areas of the linear-graded heterostructure of the second set, *VSC4* (≈ **9.1 nm**, as shown in Figure 6.70 b), of the step-graded heterostructure of the second set, *VSC2* (≈ **8 nm**, as presented in Figure 6.42 b) and of the step-graded heterostructure of the second set *VSC5*, grown as an intermediate option between the previous two (≈ **8.1 nm**, as shown in Figure 6.44 b) do not follow the same trend as for 100 μm x 100 μm scanned areas, as also previously observed for the step-graded heterostructures of the second set (§ 6.3.2.2). Hence, we could not conclude whether the surface roughness of *VSC5* is intermediary between *VSC2* and *VSC4*, as initially proposed. Nevertheless, the differences in the RMS values between the three heterostructures are so small that we concluded that all three are characterised by a similar surface quality.

Qualitatively, both the 2D and 3D AFM images of the 100 μm x 100 μm area of the linear-graded heterostructure of the second set, *VSC4* (Figures 6.70 a and 6.74 b) show similar surface morphologies with the images of corresponding areas of the step-graded

heterostructures of the second set grown under similar conditions *VSC1-3* and *VSC5* (Figures 6.41 - 6.44 a, 6.50 a-d), being characterised by a fine, uniform crosshatch pattern. The density of the large defects characteristic to the heterostructures of the second set is reasonably low for the linear-graded heterostructure of the second set, *VSC4* (as already seen in Nomarski contrast) and no such defect can be observed in both the 2D and the 3D AFM images presented.

The results obtained from comparing the better quality linear-graded heterostructure of the first set, *775* and the linear-graded heterostructure of the second set grown at the same temperature, *VSC4*, showed a value for the RMS of the surface roughness almost four times lower for the heterostructure of the second set (i.e. for a 100 μm x 100 μm scanned area, RMS of the surface roughness for *VSC4* is ≈ **9.8 nm**, as shown in Figure 6.70 a compared to ≈ **35.6 nm** for *775*, as shown in Figure 6.9 a). Qualitatively, the large difference in surface roughness between the two linear-graded heterostructures belonging to the two different sets of structures analysed, can also be observed in the 3D AFM images presented in Figures 6.75 a-b.

Results of the height variation measurements along the crosshatch lines for the linear-graded heterostructure of the second set, *VSC4*, presented in Figures 6.72, show the presence of small pits along the crosshatch lines, similar to those observed in the step-graded heterostructures of the second set grown under similar conditions. Results of the measurement of their in-plane dimension and depth are shown in Figure 6.73. These results show similar values for both the size and the depth, with those obtained for the four step-graded heterostructures of the same set, grown under similar conditions. These results show, once again, that the largest pits, with a size of ≈ **2 nm** are also the deepest (up to ≈ **26 nm** depth). The in-plane sizes of the pits present in the linear-graded heterostructure of the second set are comparable with those of the linear-graded structures of the first set, but their depths are much smaller (depths up to ≈ **26 nm** for the second set versus depths up to ≈ **250 nm** for the first set). These results justify further the RMS of the surface roughness results. The much shallower pits present in the linear-graded heterostructure of the second set account for the much reduced value of the RMS of the surface roughness for this structure compared to the linear-graded heterostructures of the first set.

Qualitatively, the linear-graded heterostructure of the second set exhibits similar surface properties compared to the step-graded heterostructure of the second set grown under identical condition. Quantitatively, the differences in the RMS of the surface roughness values obtained for 100 x 100 μm^2 scanned areas and 20 x 20 μm^2 scanned areas respectively, for the two different structures with the different Ge concentration grading profiles in the virtual substrate (step-wise, *VSC2*, and linearly, *VSC4*) are, once again, inconsistent. However, the differences between the RMS of the surface roughness values for theses two types of heterostructures are very small.

Consequently, we conclude, once more, that under the growth conditions used for the second set of heterostructures, the different types of Ge concentration grading in the virtual substrate (stepwise or linear) do not produce considerable changes in the surface morphology, differently from the first set of test structures, where step grading of the Ge concentration in the virtual substrate resulted in a much improved surface morphology (lower RMS of the surface roughness) compared to linear grading.

As aimed, the linear-graded heterostructure of the second set exhibits superior surface properties compared to the linear-graded heterostructures of the first set (i.e. flatter and smoother surface, characterised by a fine and uniform crosshatch pattern, generated by shallower trenches along which a lower density of small and shallow pits can be observed).

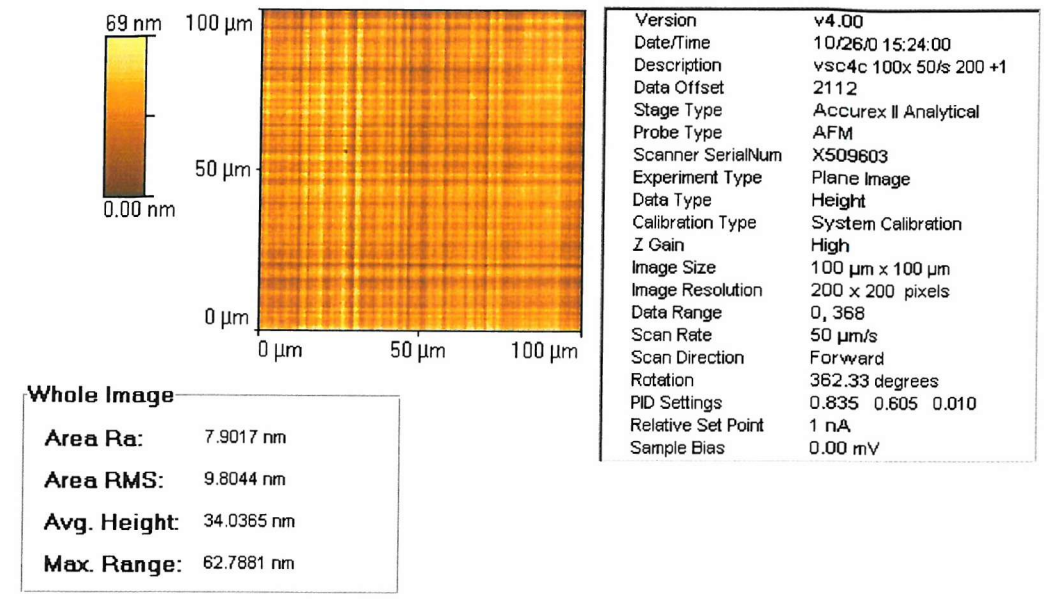

(a)

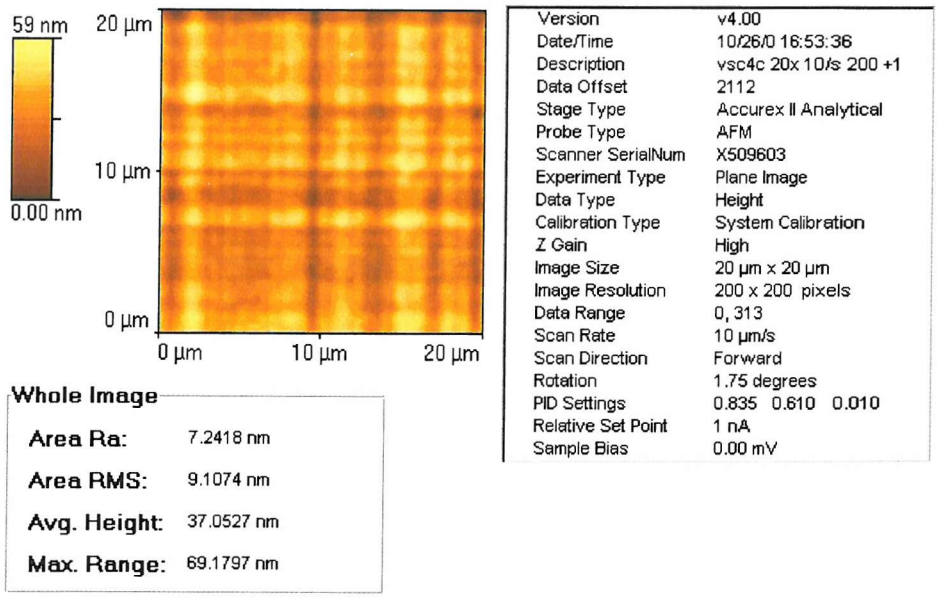

(b)

Figure 6.70. 2D AFM images, scan parameters and the RMS of the surface roughness values for the linear-graded heterostructure of the second set of heterostructures, *VSC4*, for a: (a) 100 µm x 100 µm scanned area, with a scan rate of 50 µm/s, showing a smooth surface, characterised by a much more uniform and fine crosshatch pattern than previously observed in the linear-graded heterostructures of the first set. Some accentuated crosshatch lines can be observed, but the difference between them and the rest of the pattern is much smaller, indicating shallower trenches. Pits are also observed along the trenches; (b) 20 µm x 20 µm scanned area, with a scan rate of 10 µm/s.

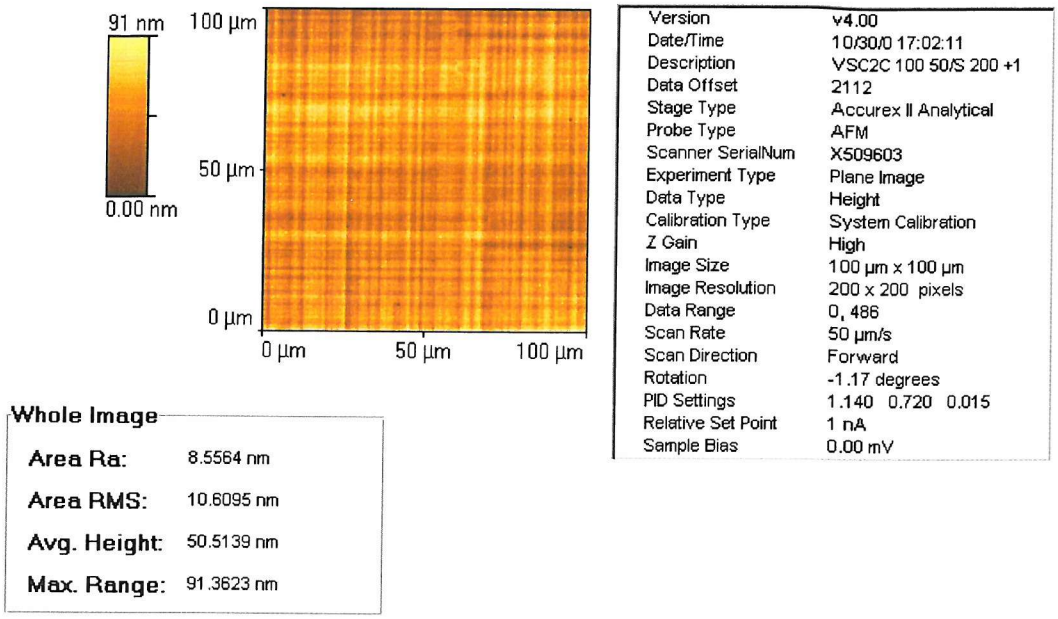

(a)

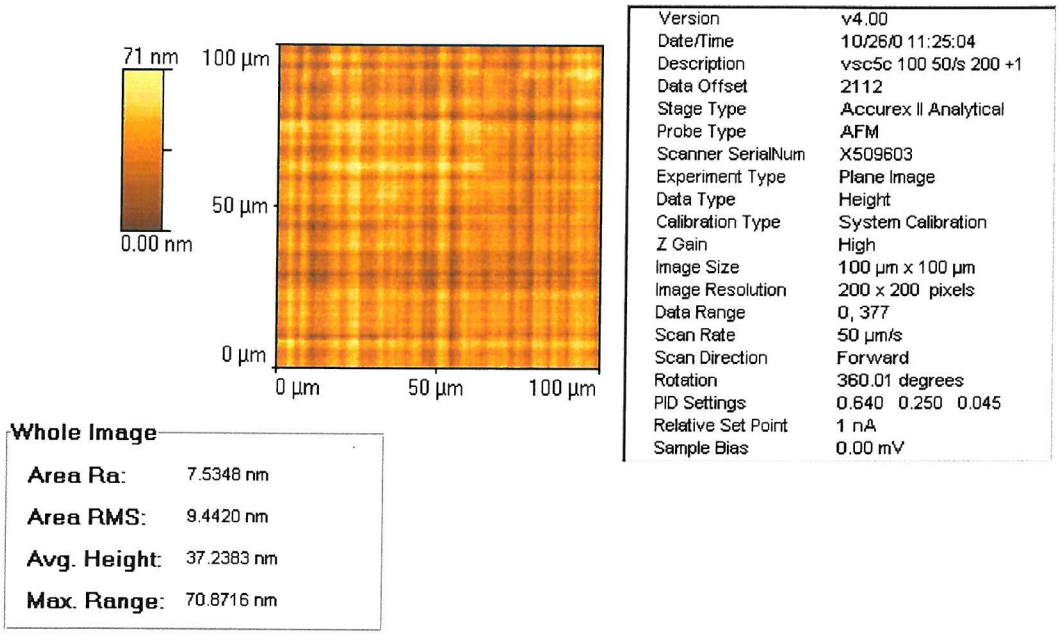

(b)

Figure 6.71. 2D AFM images, scan parameters and the RMS of the surface roughness values for 100 µm x 100 µm scanned areas, with a scan rate of 50 µm/s of: (a) the heterostructure *VSC2*, grown under identical conditions with *VSC4*, but with a step variation of the Ge concentration in the virtual substrate, showing a similar surface morphology, but a higher value for the RMS of the surface roughness; (b) the heterostructure *VSC5*, grown under the same conditions as *VSC2* and *VSC4*, but characterised by a type of variation of the Ge concentration in the virtual substrate, which was meant to be an intermediate option between step grading (*VSC2*) and linear grading (*VSC4*), showing a similar surface morphology with *VSC2* and *VSC4*, but the smallest value for the RMS of the surface roughness.

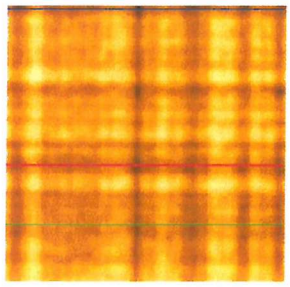

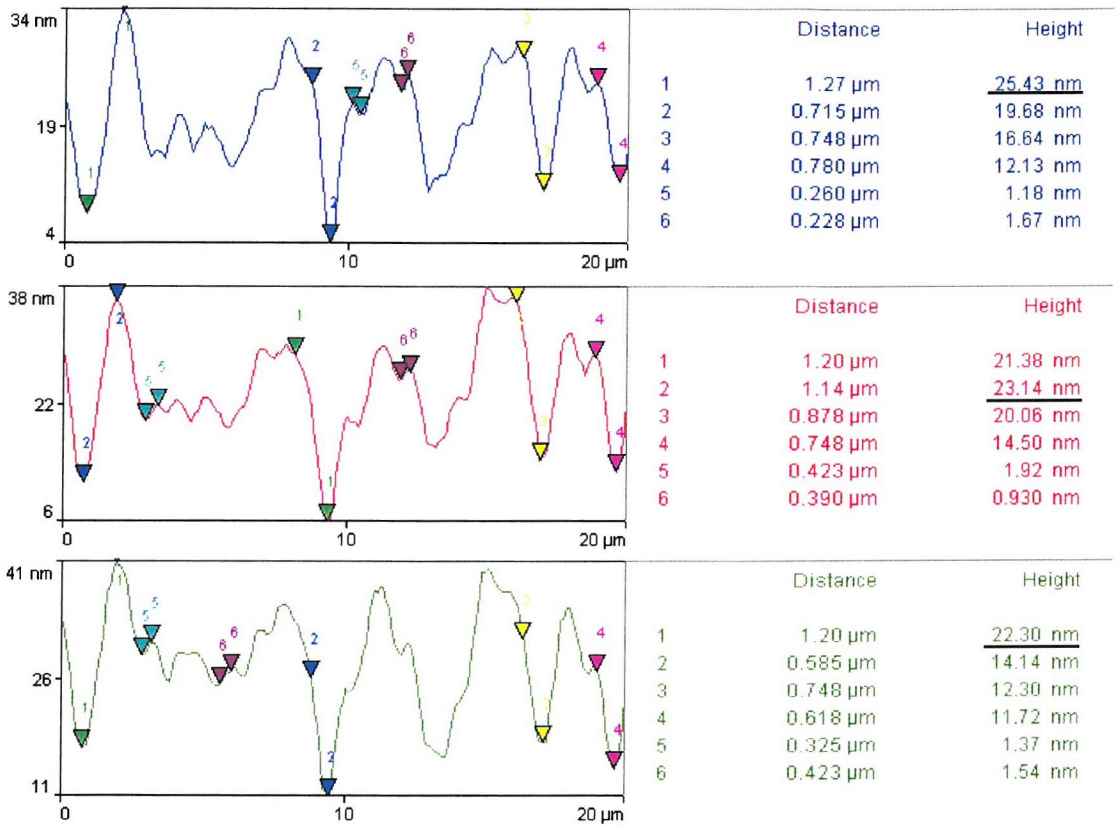

(a)

Figure 6.72. 2D AFM image of a 20 µm x 20 µm scanned area and line analysis results for the linear-graded heterostructure of the second set, *VSC4*. The underlined values correspond to the deepest pits.

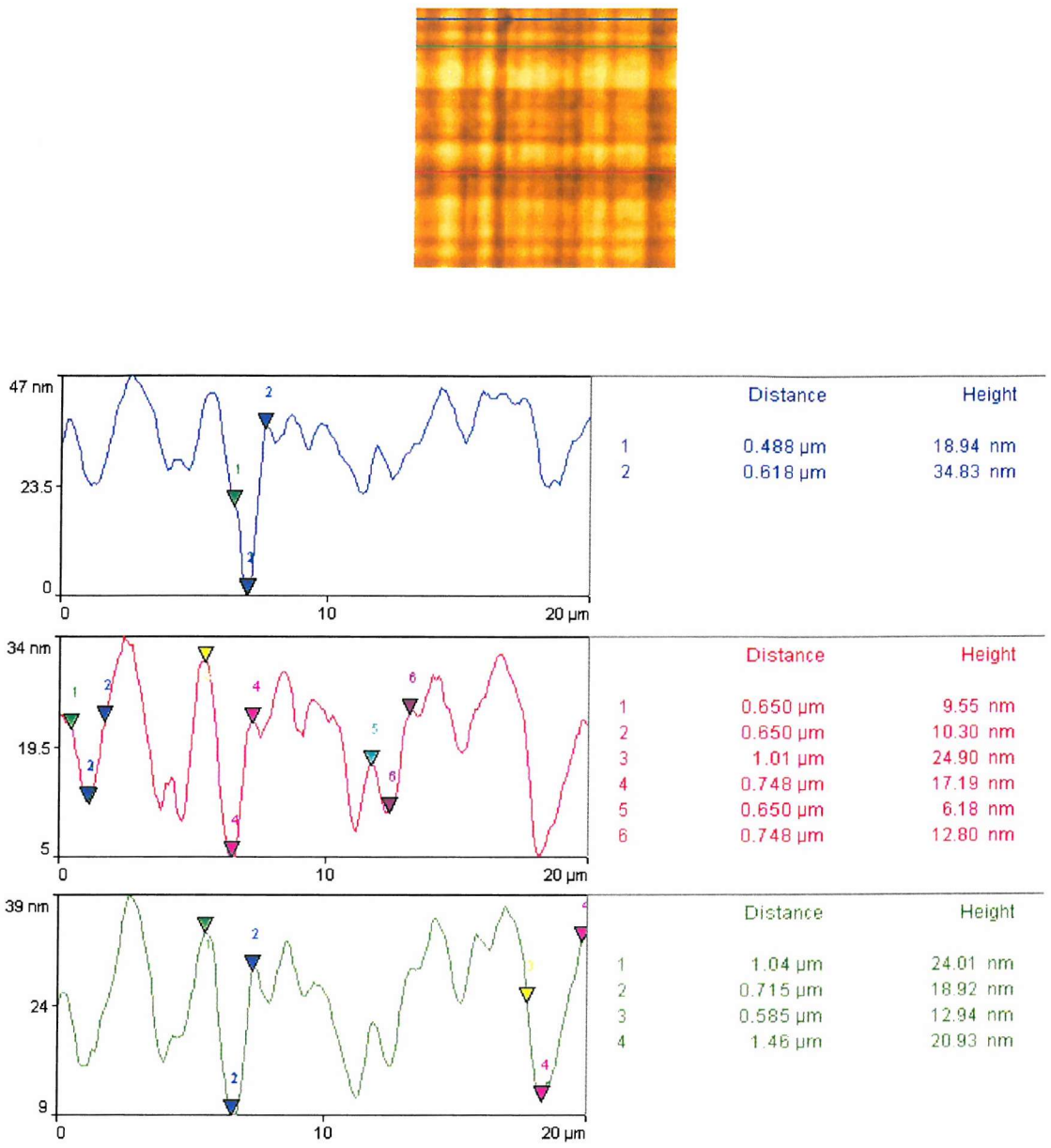

Figure 6.73. 2D AFM image of a 20 µm x 20 µm scanned area and line analysis results obtained from measuring the lateral spacing and depth of the pits present along the crosshatch lines in the linear-graded heterostructure of the second set, *VSC4*.

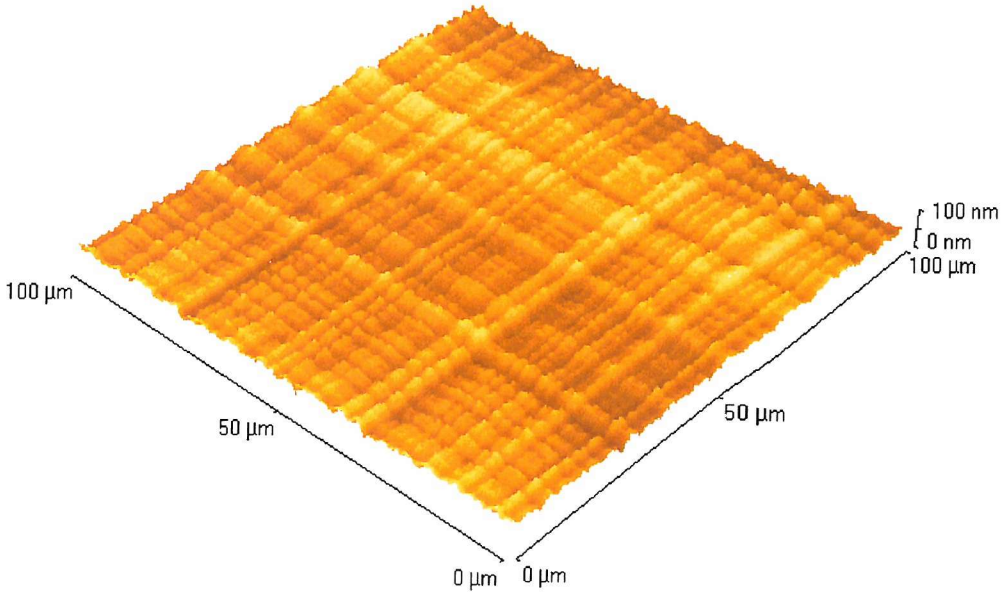
100 nm
0 nm
100 µm
100 µm
50 µm
50 µm
0 µm
0 µm

(a)

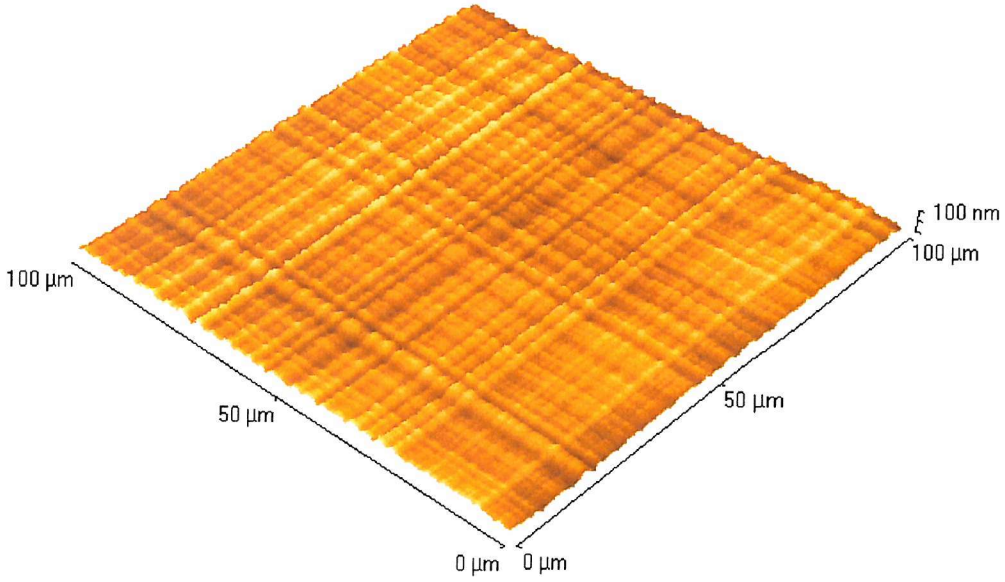
100 nm
100 µm
100 µm
50 µm
50 µm
0 µm
0 µm

(b)

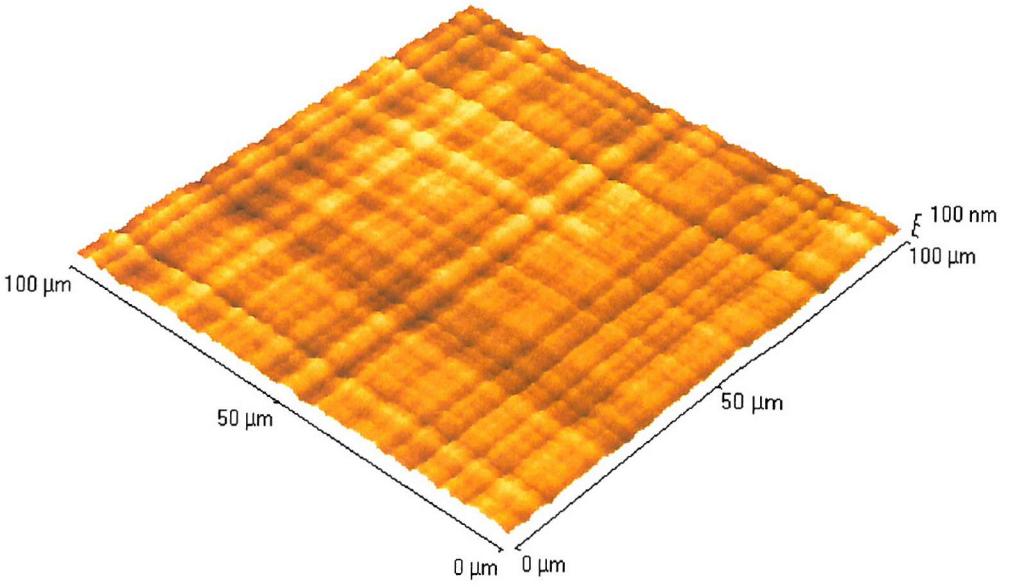

(c)

Figure 6.74. 3D AFM images of 100 µm x 100 µm scanned areas of: (a) the step-graded heterostructure of the second set, *VSC2*; (b) the linear-graded heterostructure of the second set, *VSC4*, grown under identical conditions with *VSC2*, showing a more uniform surface morphology; (c) the step-graded heterostructure of the second set, *VSC5*, grown under the same conditions as *VSC2* and *VSC4*, but characterised by a type of variation of the Ge concentration in the virtual substrate, which was meant to be an intermediate option between the step grading (*VSC2*) and the linear grading (*VSC4*) showing a very similar surface morphology with *VSC4*.

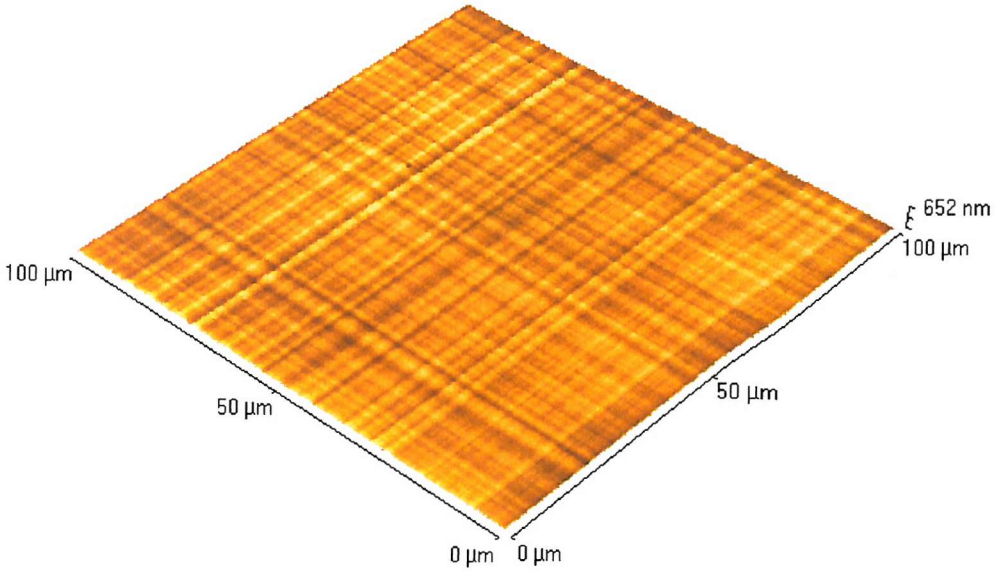

(a)

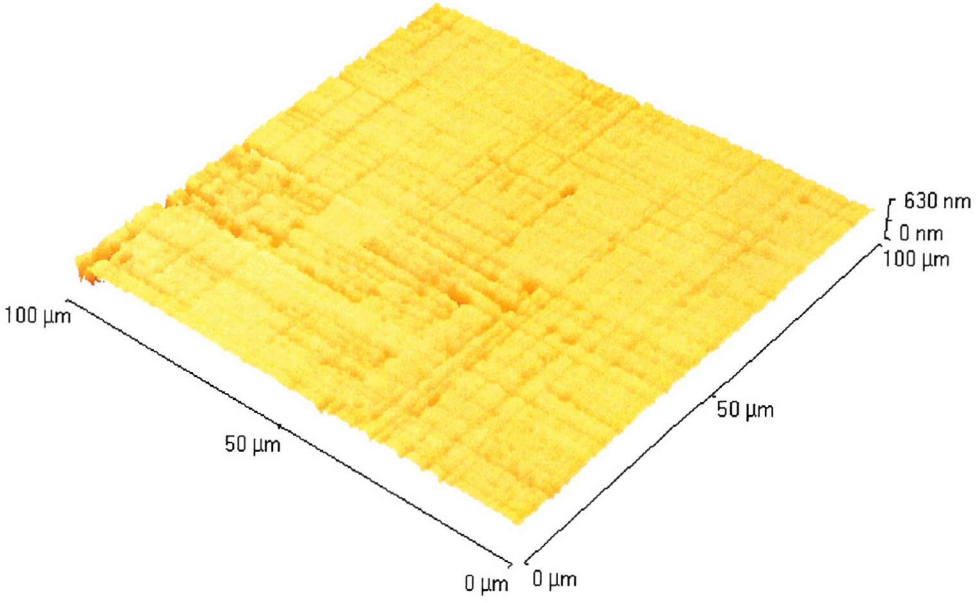

(b)

Figure 6.75. 3D AFM images of 100 µm x 100 µm scanned areas of: (a) the linear-graded heterostructure of the second set, *VSC4*, showing a smooth surface, with a fine, uniform crosshatch pattern; (b) the linear-graded heterostructure of the first set grown at the same temperature, *775*, showing a much rougher surface, with trenches and pits.

Sample denomination	Acquisition conditions		Analysis results		
	Image size (μm^2)	Scan rate ($\mu m/s$)	Area RMS (nm)	Area average height (nm)	Deepest pits depth (nm)
VSC1	100 x 100	50	9.7	20.5	-
	20 x 20	10	9.0	39.3	25.0
VSC2	100 x 100	50	10.6	50.5	-
	20 x 20	10	8.0	26.6	27.9
VSC3	100 x 100	50	11.2	49.4	-
	20 x 20	10	10.1	31.2	24.6
VSC5	100 x 100	50	9.4	37.2	-
	20 x 20	10	8.1	33.3	27.3
VSC6	100 x 100	50	25.2	570.4	-
	20 x 20	10	21.3	194.6	-
VSC4	100 x 100	50	9.8	37.1	-
	20 x 20	10	9.1	34.0	25.4

Table 4. AFM analysis acquisition conditions and results obtained for the second set of heterostructures: area RMS, area average height and deepest pits depth.

6.3.3.3. Second set: linear-graded heterostructure Electron microscopy: TEM analysis

XTEM analyses were, once again, used in order to provide information on the internal morphology and defect content of the linear-graded heterostructure of the second set, *VSC4*, not obtainable by using any of the other techniques, the results of which are presented in the previous two sections (§ 6.3.3.1 - 6.3.3.2). Even in this case, XTEM complemented Nomarski DIC and AFM techniques, at the same time as confirming some of their results. XTEM analyses of the linear-graded heterostructure of the second set were carried out on the J.E.O.L. JEM 2000FX transmission electron microscopy (Figure 5.6) using the double-tilt sample holder (Figure 5.5). The lanthanum hexaboride (LaB_6) crystal with an applied voltage of 200 kV and the largest spot size (for obtaining the highest brightness) was used. XTEM samples were analysed in bright-field, using different two-beam conditions, in order to select the best analysis settings and carry out dislocation analyses, as explained in Chapter 5, § 5.3.3 - 5.3.4. The XTEM micrographs presented in Figure 6.76 were obtained using the main beam condition.

The presence of the carbon layer at the onset of the LPCVD-grown heterostructure can, once again, be observed on the XTEM micrographs of the linear-graded heterostructure of the second set (Figures 6.76 - 6.78 a-b). As already observed in the previously analysed structures, even in this case, the carbon layer does not show any evident contribution to misfit strain relaxation. Most defects do not form at the carbon layer hence it does not act as a heterogeneous nucleation source. This observation proves, once again, the positive effect of growing a Si buffer to bury the carbon layer together with all the interfacial impurities and defects. Even in this case, some of the defects do not even reach the carbon layer (blue arrow in Figure 6.78 b) while others extend beyond it, deep into the Si substrate, as can be seen especially in Figures 6.78 a (the green arrows). The depths at which these defects extend into the Si substrate of *VSC4* are $\approx$ **1 μm**, thus similar to most of the step-graded heterostructures of the second set, *VSC2-3* and *VSC6*, indicating that the misfit strain introduced by increasing the Ge concentration in the virtual substrate is relieved through a mechanism that involves the participation of the Si substrate.

Furthermore, some of the interfacial defects observed in all heterostructures of the second set (Figures 6.52 – 6.55, 6.57, 6.76 - 6.78 a-b) are very similar and correspond to those previously observed in the heterostructures of the test set, consisting of intersecting loops or loop segments, which often form V-shaped defects.

As expected, the linear-graded heterostructure of the second set, *VSC4*, shows a different internal morphology by comparison with the step-graded heterostructure of the second set grown under identical conditions, *VSC2*, thus reflecting the different type of variation of the Ge concentration in the virtual substrate (linear versus stepwise). While in the XTEM micrographs of *VSC2* (Figures 6.53, 6.57 c-f, 6.59 b) the different steps of Ge concentration variation in the virtual substrate are very clearly delineated by the **<110>** running MDs, in the XTEM micrographs of *VSC4* (Figures 6.76 - 6.77) there is no such delineation and the MDs are distributed continuously through the whole thickness of the virtual substrate. Nevertheless, in both cases, the MDs are well contained within the virtual substrate, thus leaving the capping layer, completely MD-free. From the viewpoint of the internal morphology, the virtual substrate of the linear-graded heterostructure of the second set, *VSC4*, appears similar with the virtual substrate of the linear-graded heterostructure of the first set, *775* (Figure 6.13), grown at the same temperature (**750°C**), being characterised by long segments of MDs distributed over the whole thickness of the virtual substrate and well contained within it. However, the morphologies of the capping layers of these two linear-graded heterostructures are different reflecting the influence of the different growth parameters, which characterise them:

- The initial Ge concentration in the virtual substrate (**zero** for *VSC4* and **12%** for *775*);
- The different Ge concentration gradient in the virtual substrate (**≈ 16% / μm** for *VSC4* compared to **≈ 22% / μm** for *775*);
- The different capping layer thickness (**≈ 1 μm** for *VSC4* and **≈ 0.24 μm** for *775*).

Differently from the linear-graded heterostructures of the first set, *720* and *775* (Figures 6.12 - 6.13), the linear-graded heterostructure of the second set, *VSC4* (Figure 6.76), shows a rather flat surface, similar to the step-graded heterostructures of the second set grown under comparable conditions, *VSC1-3* and *VSC5* (Figures 6.52 - 6.55).

The last step of Ge concentration variation (**30%-32%**) in the virtual substrate of the linear-graded heterostructure of the second set, *VSC4* (Figures 6.76 - 6.77) appears similar to the corresponding step in all the step-graded heterostructures of the second set grown under similar conditions, *VSC1-3* and *VSC5* (Figures 6.52 - 6.55). It is free from MDs, thus suggesting that it is still elastically strained. The capping layer of constant composition in the linear-graded heterostructure of the second set, *VSC4*, is also free from MD segments (Figures 6.76 - 6.77) similarly to the linear-graded heterostructure of the first set grown at the same temperature, *775* and the step-graded heterostructures of the

first and second sets. However, there are dislocation segments threading to the free surface. When analysed in different two-beam conditions (Figure 6.79 a-e), the TDs present in the linear-graded heterostructure of the second set, similarly to the other heterostructures previously analysed, do not satisfy the invisibility criteria (Equation 5.2 - 5.3) therefore we conclude that they are of the mixed type (Chapter 5, § 5.3.4) in good agreement with results reported in literature for the $Si_{1-x}Ge_x/Si$ (001) system (Chapter 3). TDs in the linear-graded heterostructure of the second set appear very similar to those observed in all the previously analysed heterostructures. For example, the TD pileup shown in Figures 6.77 and 6.79 present in the linear-graded heterostructure of the second set, *VSC4*, matches that shown in the left column of Figure 6.61 present in the step-graded heterostructure of the second set, *VSC1*, that shown in the left corner of Figure 6.62 corresponding to the step-graded heterostructure of the second set, *VSC2*, in the left hand column of Figure 6.63, characteristic of the step-graded heterostructure of the second set, *VSC3* and to that presented in Figure 6.18 (for the linear-graded heterostructure of the first set, *775*), Figure 6.19 a-b (for the linear-graded heterostructure of the first set, *720*) and Figure 6.32 (for the step-graded heterostructure of the first set, *774*). These dislocation pileups are running along **{111}** planes and are threading through part or the whole structure (as already described in § 6.2.2.3). As previously explained, similar pileups have been observed in $Si_{1-x}Ge_x/Si$ (001) structures by other groups, who studied their formation and concluded that they are typically caused by an inhomogeneity that continuously 'punches out' dislocations, under the influence of the misfit strain introduced continuously through Ge concentration grading [4]. Other TDs, like that indicated by the brown arrow in Figure 6.76, are typical **60°** dislocations gliding on **{111}** planes to the free surface.

Differently from the linear-graded heterostructures of the first set, but similarly to the step-graded ones of the first and second sets, the type of groups of TDs terminated at faceted pits (presented in Figure 6.16 a-b for the structure *720* and in Figure 6.17 for the structure *775*) appear to be completely absent from the linear-graded heterostructure of the second set.

A rough estimation of the TD density in the linear-graded heterostructure of the second set was made based on the XTEM results. The values obtained range between $\approx$ **$6x10^6$ – $5x10^7$ cm^{-2}**, thus similar to the step-graded heterostructure of the second set grown under similar conditions, *VSC2* ($\approx$ **$3x10^6$ – $3x10^7$ cm^{-2}**), and also similar to the value obtained

for the linear-graded heterostructure of the first set grown at the same temperature, *775*, ($\approx$**2x10^7 - 4x10^7 cm^{-2}**).

Overall, from the XTEM results obtained we conclude, once more, that under the growth conditions used for the second set of heterostructures, the different types of Ge concentration grading in the virtual substrate (stepwise or linear) do not produce considerable changes to the TD density. Previously, we have drawn the same conclusion for the heterostructures of the first set. Consequently, we emphasize, once again, the highly qualitative value of the results obtained on the TD densities. However, while for the heterostructures of the first set, the different types of grading resulted in completely different surface morphologies, for the heterostructures of the second set, they result in very similar surface morphologies.

As aimed, the linear-graded heterostructure of the second set exhibits superior structural properties compared to the linear-graded heterostructures of the first set (i.e. flatter surface and no faceted pits). Consequently, we conclude that the choice of growth parameters used for the second set of heterostructures, aimed at improving their surface morphology and defect content, was successful.

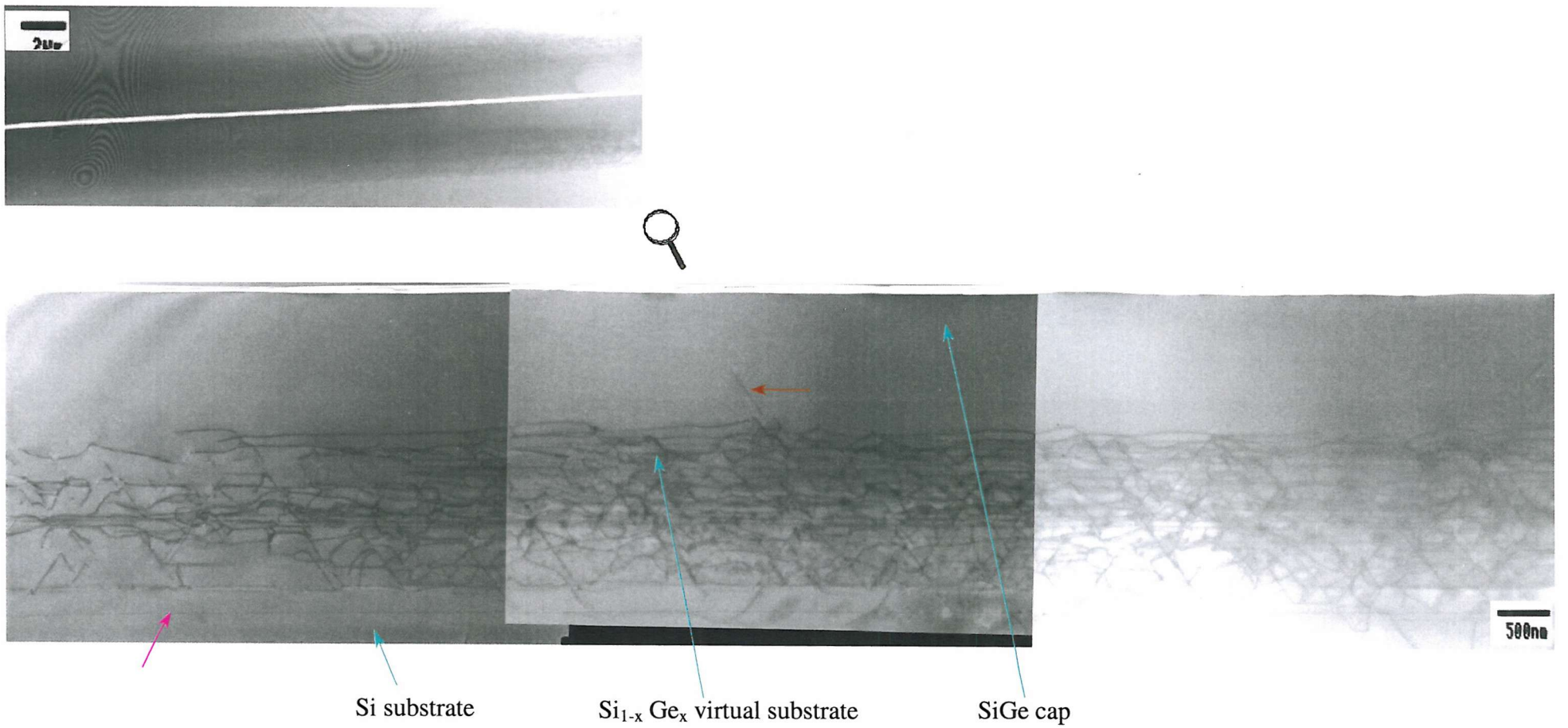

Figure 6.76. XTEM bright-field micrographs (obtained using the main beam condition) of the linear-graded heterostructure of the second set, *VSC4*, grown under the same conditions as the step-graded heterostructure of the second set, *VSC2*. From the top to the bottom of the page, the size of the imaged layer decreases. The pink arrow points to the carbon layer present at the Si substrate-LPCVD heterostructure interface. The brown arrow points to a TD.

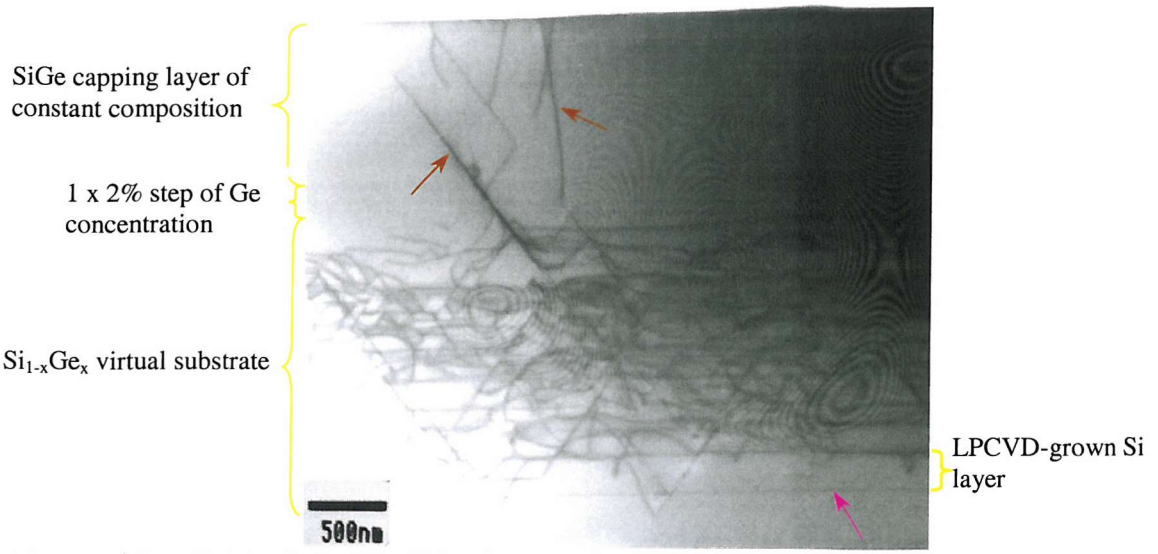

Figure 6.77. Bright-field XTEM micrograph of the linear-graded heterostructure of the second set, *VSC4*, grown under identical conditions with the step-graded heterostructure of the second set, *VSC2*. The presence of the interfacial carbon layer is indicated by the pink arrow. From the bottom to the top of the image, the heterostructure consists of: the LPCVD-grown Si layer, incorporating some of the relaxation-induced defects followed by the virtual substrate, with a linear Ge concentration variation between **0-32%**, the upper part of which looks elastically strained (has a different contrast and no MDs) and the SiGe capping layer of constant composition at the top, MD-free, but with some dislocation segments threading to the free surface (indicated by the brown arrows).

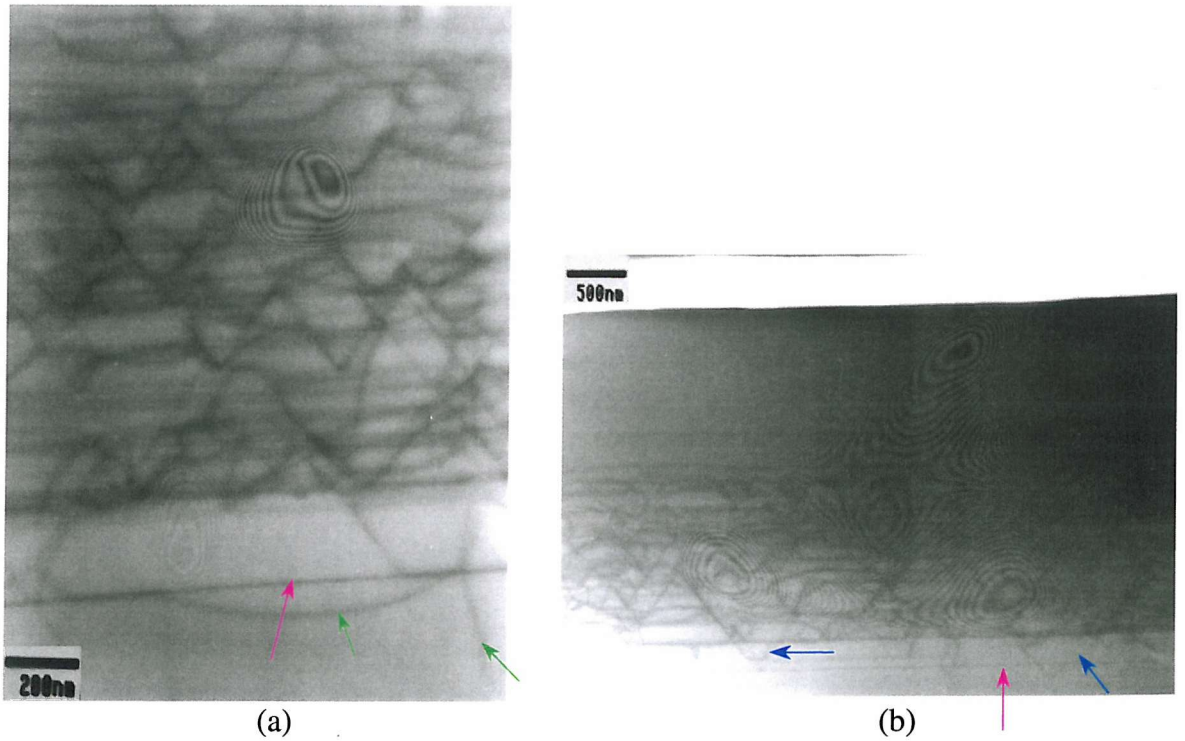

(a) (b)

Figure 6.78 a-b. Bright-field XTEM micrographs of the linear-graded heterostructure of the second set, *VSC4*, showing the carbon layer present at the onset of the LPCVD growth (pink arrows). The interfacial layer shows no contribution to misfit strain relaxation. Some defects extend well beyond it, into the Si substrate (green arrows in a). A number of defects stop at or do not even reach the carbon layer, as indicated by the blue arrows in (b).

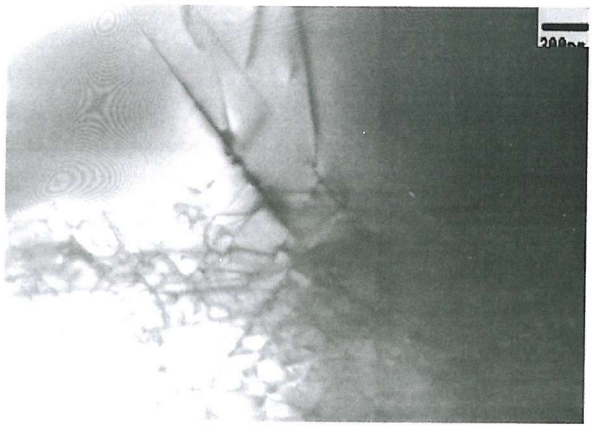

(a)

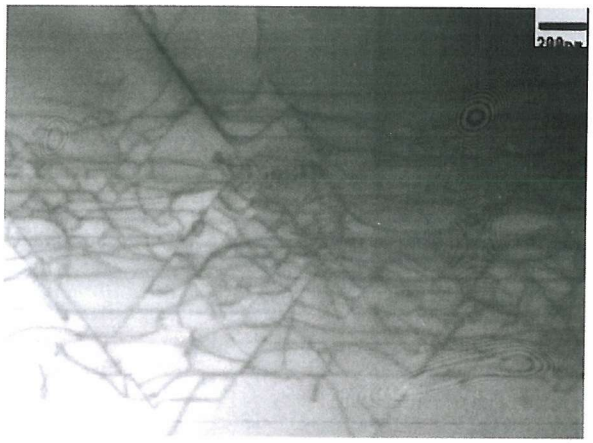

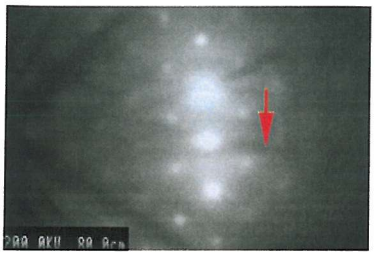

(b)

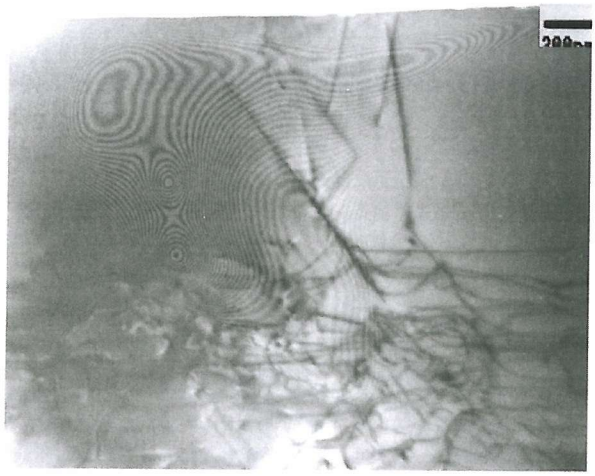

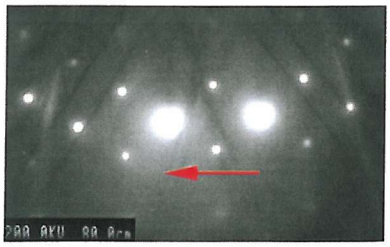

(c)

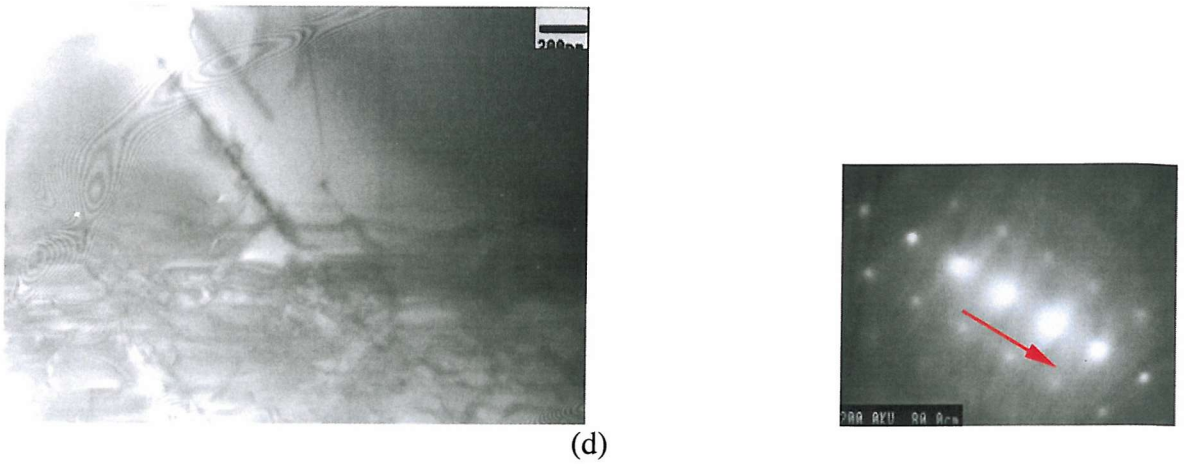

(d)

(e)

Figure 6.79. Bright-field XTEM micrographs of the linear-graded heterostructure of the second set, *VSC4*, showing TDs imaged in different two-beam conditions and the corresponding diffraction patterns: (a) main beam condition; (b) $\mathbf{00\bar{2}}$; (c) $\mathbf{\bar{2}20}$; (d) $\mathbf{1\bar{1}\bar{1}}$; (e) $\mathbf{\bar{1}11}$. The fact that the threaders are visible in all two-beam conditions indicates their mixed type.

6.3.4. SECOND SET OF HETEROSTRUCTURES DISCUSSION AND CONCLUSIONS

The experimental results obtained on the first (test) set of heterostructures enabled conclusions regarding the effects of the growth temperature, initial Ge content, Ge concentration gradient and grading profile (i.e. linear and stepwise) in the virtual substrate, and of the capping layer thickness, on the surface morphology and defect content of these structures.

Based on the conclusions drawn from the first set, the combinations of growth parameters used for the second set of heterostructures were carefully chosen, with the aim of improving their surface morphology and defect content. Consequently, all the heterostructures of the second set were grown at the same temperature (**750°C**), that characterised the heterostructures of the first set with superior structural properties, *775* and *774*. Additionally, emphasis was placed on the step grading of the Ge concentration in the virtual substrate, due to the superior properties it generated for the test samples. Consequently, five different step-graded (*VSC1-VSC3, VSC5* and *VSC6*) and only one linear-graded (*VSC4*) virtual substrates were incorporated in the heterostructures grown as part of the second set.

All structures of the second set, except that grown for reproducibility, have virtual substrates, characterised by the same initial (**0%**) and final (**32%**) Ge concentration, respectively. By starting the Ge concentration grading at **0%**, the virtual substrates of the second set, differently from those of the first set, are characterised by a very 'gentle' introduction of misfit strain, with the aim of reducing the TD density, by nucleating a reduced density of MDs and thus allowing them to run longer distances, and improving the surface morphology, by suppressing surface roughening. Additionally, the growth of the final step of the virtual substrate with a low Ge concentration gradient of only **≈ 6% / μm** (**≈ 2%** over **≈ 300 nm**) was meant to improve the results of misfit strain relaxation on the TD density by acting as a 'filter' for dislocations, as explained in Chapter 3, § 3.2.3.2 and § 3.2.4. Essentially, by ensuring that the last step of Ge concentration in these heterostructures is still compressively strained, dislocations are meant to be kept confined within the virtual substrate underneath. Moreover, should this last step relax, the growth of a tensile strained capping layer (of **≈ 30%** Ge concentration) would improve the surface morphology as tensile strain does not encourage surface roughening [1].

The final Ge concentration value in the virtual substrates of the second set was chosen in order to enable their use as templates for further strained overgrowth (as described in Chapter 1).

Additionally, the second set of heterostructures was grown after a long period of contamination problems with the LPCVD equipment. The growth time sequence for the heterostructures of the second set is reflected in their denomination: from *VSC1*, grown first to *VSC6*, grown last. However, all heterostructures of the second set were grown using the same gas sources (no change of gas bottles occurred between the growth processes).

The results presented in § 6.3.2 - 6.3.3 illustrate the effects of the growth parameters on the surface morphology and defect content of the heterostructures grown as part of the second set. For the step-graded heterostructures of the second set, the effects of the following growth parameters were analysed:

- the presence of a microelectronic structure within the capping layer of *VSC1*, which was compared to *VSC2*, grown under identical conditions, but without the microelectronic structure;
- the thickness of the capping layer of *VSC3* (**2 μm**), grown under identical conditions with *VSC2*, with a capping layer half as thick (**1 μm**);
- the Ge concentration gradient in the virtual substrate of *VSC5* (**≈ 8% / μm**), grown under identical conditions with *VSC2*, characterised by a Ge concentration gradient of **≈ 16% / μm**. Furthermore, by using double the number of half Ge concentration steps in the virtual substrate, this structure was meant to act as an intermediary between the two types of Ge concentration grading i.e. stepwise (*VSC2*) and linear (*VSC4*).

Additionally, a check of the growth reproducibility for these types of SiGe heterostructures was carried out, by repeating the step-graded heterostructure grown as part of the first set, *774*, in the second set, *VSC6*.

Further comparisons between the effects of step and linear grading of the Ge concentration in the virtual substrate were also carried out. One linear-graded heterostructure, *VSC4* was grown as part of the second set, under identical conditions with the step-graded heterostructure, *VSC2*.

The results obtained from the analysis of the test set showed that neither Nomarski contrast coupled with disclosure chemical etch, nor PVTEM can be successfully used for TD density analysis. Consequently, only Nomarski DIC microscopy, AFM and XTEM analysis methods were used for the characterisation of the second set of heterostructures.

Surface morphology analyses showed that all heterostructures of the second set (except for that grown for reproducibility purposes, *VSC6*) exhibit similar surface morphologies, independently of the growth parameters varied. All heterostructures of the second set, *VSC1-5* show a fine, uniform crosshatch pattern on their surface, characterised by fine regular undulations aligned along two perpendicular **<110>** directions. Some crosshatch lines showing slightly different contrast in Nomarski microscopy and corresponding to very shallow trenches, as revealed in AFM, are randomly distributed on the surfaces of all the heterostructures of the second set, grown under similar conditions, as indicated by the red arrows in Figures 6.36 a-d, 6.66 c. Nevertheless, the deep trenches observed along the surfaces of the heterostructures of the first set, are completely absent from all the heterostructures of the second set grown under similar conditions, as shown by both Nomarski contrast micrographs (Figure 6.35 compared to 6.36, and 6.66 a-b compared to 6.66 c) and 3D AFM images (Figure 6.50 a-d compared to 6.51 a-b, and 6.78 a-b).

Surface analyses for the two heterostructures grown for reproducibility, *774* of the first set and *VSC6* of the second set, show very similar surface morphologies (Figure 6.35 a-b and 6.51 a-b). The surfaces of these two heterostructures, differently from those of the other heterostructures of the first set (characterise by large areas of deep trenches and high densities of deep pits along the trenches) and from those of the other heterostructures of the second set (characterised by smooth regular surfaces, with fine crosshatch pattern), show reduced areas of deep trenches and the presence of some deep pits along these trenches (as indicated by the arrows in Figure 6.54 a-b).

AFM line analyses carried out on the heterostructures of the second set, grown under similar conditions, *VSC1-5*, revealed the presence of shallow pits on their surfaces, mainly at the intersection of crosshatch lines. The deepest pits in these structures (in-plane dimension $\approx$ **2 μm**), although similar in size to those observed in the step-graded heterostructure of the first set and hence smaller than those observed in the linear-graded heterostructures of the first set are much shallower (depths $\approx$ **39 nm**). We could not identify these pits on the XTEM micrographs of the heterostructures of the second set, all

of which show rather flat surfaces. Faceted pits, of the type observed in the linear-graded heterostructures of the first set (Figures 6.12-6.13) are completely absent from the structures of the second set, *VSC1-5*.

The flatter, regular surfaces that characterise the second set of heterostructures, grown under similar conditions, by comparison with the rough surfaces that characterise the first set of heterostructures are also reflected by their values for the RMS of the surface roughness. These values are similar for the second set of heterostructures, *VSC1-5*, and range **RMS ≈ 9 – 11 nm** (for a 100 x 100 μm^2 scanned area), and show large differences for the heterostructures of the first set, ranging **RMS ≈ 29 – 91 nm**, for the same size of scanned area.

The two heterostructures grown for reproducibility show comparable values for the RMS of 100 x 100 μm^2 scanned areas (**≈ 25 nm** for *VSC6* and **≈ 22 nm** for *774*).

Qualitatively, all the analysis techniques used show very similar surface morphologies for the heterostructures of the second set, grown under similar conditions. Quantitatively, the trend followed by the values of the RMS of the surface roughness for 100 x 100 μm^2 scanned areas compared is not consistent with that for 20 x 20 μm^2 scanned areas compared (as can be seen in Table 4). Because of the very small differences between the RMS values obtained, we concluded that the heterostructures of the second set are characterised by similar surface quality. Furthermore, under the growth conditions used for the heterostructures of the second set, *VCS1-5*, the growth parameters varied do not result in observable changes of the surface morphology. Nevertheless, as aimed, the combinations of growth parameters used for the heterostructures of the second set result in superior surface morphologies compared to the heterostructures of the first set.

Surface analysis results for the heterostructures of the second set also revealed the presence of some large growth defects, which were identified as being introduced during the growth of the capping layer, possibly by the dopant gases. Their density decreased with time (from the first structure to the last), thus reinforcing our assumption. The analyses of these defects showed that they do not affect the surface topography directly related to the incorporation of a virtual substrate in these heterostructures, hence they do not influence the conclusions of this study.

When analysed in XTEM, the defect content of the heterostructures of the second set grown under similar conditions appeared very similar for the same profile of grading of the Ge concentration in the virtual substrate. XTEM micrographs of all the step-graded heterostructures of the second set grown under similar conditions, *VSC1-3* and *VSC5*, (Figures 6.52-6.55 and 6.58-6.60) show very clearly the different Ge concentration variation steps, which are delineated by groups of parallel **<110>** running MDs. The steps of Ge concentration are characterised by the same thickness (**≈ 280 nm**) in all the step-graded heterostructures of the second set grown under similar conditions, thus indicating good growth control. Furthermore, the steps of Ge concentration in the two heterostructures grown for reproducibility are also characterised by similar thicknesses (**≈260 nm**), thus indicating not only good growth control, but also good reproducibility of the growth process.

When analysed in XTEM, the linear-graded heterostructure of the second set showed parallel **<110>** MD segments distributed continuously throughout the thickness of the virtual substrate (Figures 6.76-6.77), similarly to the linear-graded heterostructures of the first set (Figures 6.12-6.13).

Consequently, we concluded that from the viewpoint of the internal morphology, for similar profiles of the Ge concentration grading, the virtual substrates of the second set of heterostructures are similar to those of the first set. However, their surface morphologies are different and the differences are more accentuated in the case of the linear grading of the Ge concentration.

By comparing the two linear-graded heterostructures grown at the same temperature, *775*, of the first set, and *VSC4*, of the second set, we observed that in both cases, the virtual substrate is characterised by long segments of MDs distributed over the whole thickness of the virtual substrate and well contained within it. However, the capping layer morphologies for these two structures are very different. As already described, the capping layer of the linear-graded heterostructure of the second set, *VSC4*, is characterised by fine, almost indistinguishable undulations, while the capping layer of the linear-graded heterostructure of the first set, *775*, is characterised by periodic undulations interrupted by faceted pits, where groups of TDs terminate. The different surface morphologies reflect the influence of the different growth parameters, which characterise these two heterostructures:

- The initial Ge concentration in the virtual substrate (**zero** for *VSC4* and **12%** for *775*);
- The different Ge concentration gradient in the virtual substrate (**≈ 16% / μm** for *VSC4* compared to **≈ 22% / μm** for *775*);
- The different capping layer thickness (**≈ 1 μm** for *VSC4* and **≈ 0.24 μm** for *775*).

In this study, we have been faced, once again, with the difficulty of attempting to understand the evolution of the misfit strain relaxation processes that takes place in the virtual substrates of these two linear-graded heterostructures, by looking at their final morphologies. In § 6.2.4, it is explained why we could not conclude whether the virtual substrate of the linear-graded heterostructure of the first set, *775*, relaxes through a surface roughening mechanism, followed by MD nucleation, or the MDs are nucleated first and the strain fields associated with them generate the surface morphology observed or whether both mechanisms are operating simultaneously. Nevertheless, in the case of the linear-graded heterostructure of the second set, *VSC4*, it seems unlikely that surface roughening occurred, because of the very 'gentle' introduction of misfit strain in the virtual substrate, by starting the Ge concentration grading at zero. This may explain the much reduced surface roughness that characterises this heterostructure. Additionally, the lower Ge concentration gradient in *VSC4* results in a better distribution of misfit strain throughout the virtual substrate, which may also explain the improved surface morphology. Furthermore, the thicker capping layer of *VSC4* allows surface reshaping to take place, which may also contribute to its superior surface quality.

The same arguments can be brought to explain the improved surface morphologies of the step-graded heterostructures of the second set, grown under similar conditions, *VSC1-3* and *VSC5*, by comparison with the step-graded heterostructure of the first set, *774*. In the case of the step-graded heterostructures of the second set, similarly to that of the first set, it is unlikely that misfit strain relaxation occurred through a surface roughening mechanism, as already explained in § 6.2.4.

XTEM analyses also revealed the presence of TDs in all heterostructures of the second set. When analysed in different two-beam conditions (Figures 6.61-6.64 and 6.79), these TDs do not satisfy the invisibility criteria, therefore we concluded that they are of the mixed type in good agreement with results obtained for the heterostructures of the first set and other results reported in literature for the $Si_{1-x}Ge_x$/Si (001) system (as shown in Chapter 3).

A rough estimation of the TD (that end at the free surface) densities based on XTEM results, showed very similar values for all heterostructures of the second set. Values obtained ($\approx 10^7 - 3x10^7$ **cm**$^{-2}$ for *VSC1*, $\approx 3x10^6 - 3x10^7$ **cm**$^{-2}$ for *VSC2*, $\approx 3 - 5x10^7$ **cm**$^{-2}$ for *VSC3*, $\approx 6x10^6 - 5x10^7$ **cm**$^{-2}$ for *VSC4*, $\approx 6x10^6$-$4x10^7$ **cm**$^{-2}$ for *VSC5*, $\approx 2 - 8x10^7$ **cm**$^{-2}$ for *VSC6*) are comparable with those for the step-graded heterostructure of the first set, *774* ($\approx 10^7 - 6x10^7$ **cm**$^{-2}$) and for the linear graded heterostructure of the first set grown at the same temperature, *775* ($\approx 2x10^7 - 4x10^7$ **cm**$^{-2}$). These values show, once again that from the viewpoint of TD densities, the two different types of grading of the Ge concentration in the virtual substrate, give similar results. Furthermore, the TD densities of the two heterostructures grown for reproducibility have similar values indicating, once again good reproducibility.

Additionally, the fact that the TD densities, estimated from XTEM analyses, appear similar for the heterostructures of the first set, *775* and *774* and for all the heterostructures of the second set, while the surface morphologies of their capping layers are different, suggests that the strained SiGe step of 2% Ge concentration that characterises the heterostructures of the second set, may have a contribution to improving the surface morphology rather than the defect density.

Nevertheless, as already suggested, the TD density results obtained for all heterostructures studied have mainly a qualitative value, due to the highly estimative approach of the technique used to determine them.

Similarly to the heterostructures of the first set, all the structures of the second set are characterised by defects running deep into the Si substrate ($\geq$ **1 μm**), thus suggesting that the misfit strain introduced by increasing the Ge concentration in the virtual substrate is relieved through a mechanism that involves the participation of the Si substrate (of the MFR type, described in Chapter 3, § 3.2.3.5). However, the lack of other MFR characteristic 'traces' [12], does not support the hypothesis on the operation of such a multiplication mechanism in any of the studied heterostructures.

Additionally, all the heterostructures studied display dislocation pileups gliding on **{111}** planes and threading through the whole structure. As previously explained, similar pileups have been observed in $Si_{1-x}Ge_x$/Si (001) structures by other groups, who studied their formation and concluded that they are typically caused by an interfacial inhomogeneity, of

the particulate type, that continuously 'punches out' dislocations, under the influence of the misfit strain introduced continuously through Ge concentration grading [4]. Consequently, heterogeneous dislocation nucleation at interfacial impurities represents one of the dislocation sources common for all the heterostructures analysed. Obviously, there are other sources, which we could not identify by looking at the final morphology.

The results obtained from the characterisation of the heterostructures of the second set show that under the similar growth conditions used for the structures, *VSC1-5*, the different growth parameters varied result in similar surface morphologies and defect contents. Additionally, as aimed, the heterostructures of the second set exhibit superior surface morphologies compared to the structures of the test set (i.e. much flatter and smoother surfaces). The TD densities for the structures of the first set grown under similar conditions, *774* and *775*, and the heterostructures of the second set are comparable. However, the TD density results obtained from XTEM analysis have mainly a qualitative value.

Overall, we conclude that the choice of growth parameters used for the second set of heterostructures, aimed at improving their structural properties, has been successful. Furthermore, good growth reproducibility for these types of heterostructures has also been demonstrated.

7. OVERVIEW AND FURTHER WORK

Extensive analysis of the effects of growth parameters on the structural properties of SiGe heterostructures incorporating compositionally graded virtual substrates have been carried out and reported for structures grown by methods, in which different growth regimes operate, i.e. UHVCVD and MBE (very low growth rates), APCVD (higher growth rates), LEPECVD (very high growth rates), as summarised in Chapter 1. Furthermore, results obtained from growth by LPCVD, at growth rates lower than those used in the SUMC equipment have also been reported (Chapter 1, [22-24]).

This work presents a comprehensive systematic study of the effects of growth parameters on the surface morphology and defect content of two sets of SiGe virtual substrate-based heterostructures grown in a LPCVD reactor designed and fabricated at SUMC, which is characterised by a different growth regime than previously reported in literature. Growth rates used in the SUMC-LPCVD machine are intermediate between those in high vacuum techniques, UHVCVD and MBE, and those in low vacuum techniques, APCVD and LEPECVD, and higher than in other LPCVD machines reported [22-24]. Furthermore, for both growth temperatures analysed, the growth rates are similar (slightly higher at the lower temperature, as described in Chapter 4, § 4.1) and have similar variation with the Ge concentration (Chapter 4, Figure 4.1). Additionally, growth in the SUMC-LPCVD reactor is characterised by thermal budget limitations, as already explained in Chapter 4, §4.1.

The first set of heterostructures was a test set and consisted of two structures, *720* and *775*, characterised by a linear variation of the Ge concentration in the virtual substrate, and one structure, denominated *774*, grown under identical conditions with *775* and characterised by a step variation of the Ge concentration in the virtual substrate. The growth parameters varied for the first set of heterostructures were:

- For the virtual substrate: the growth temperature (750°C for *774* and *775*, and 800°C for *720*), initial Ge content (12% for *774* and *775*, and 13% for *720*) and hence the initial lattice misfit, Ge concentration gradient (16% / μm for *720* and 22% / μm for *775*) and type of Ge concentration grading (linear for *775* and stepwise for *774*);
- For the capping layer: thickness (0.24 μm for *774* and *775*, and 0.30 μm for *720*).

All structures of the first set were characterised by the same final Ge concentration value in the virtual substrate (42%) and were grown using the same gas sources (no change of gas bottles occurred between the three growth processes).

For the heterostructures of the first set, starting the Ge concentration grading at values different from zero (the value, which is commonly reported) was motivated by the thermal budget limitations of the epitaxy machine. In order to obtain the final Ge concentration intended which is in the medium-high range, by starting the grading at zero, either higher gradients or thicker virtual substrates would have been required, both of which present disadvantages for the structural properties.

Based on the results obtained from the analysis of the test set, a second set was grown with emphasis on the step grading of the Ge concentration, due to the superior properties of this type of grading displayed in the first set. Furthermore, step grading of the Ge composition is less reported in literature by comparison with linear grading. The second set of heterostructures consisted of three step-graded heterostructures, *VSC1-3*, grown under similar conditions, each differing by one growth parameter; one step-graded structure, *VSC6*, grown under identical conditions with the step-graded structure of the first set, *774*, in order to check the growth reproducibility for these types of structures; one linear-graded heterostructure, *VSC4*, grown under identical conditions with *VSC2*, in order to characterise the effects of the two types of grading of the Ge concentration in the virtual substrate; and one heterostructure grown as an intermediate option between step grading of the Ge concentration, as in *VSC2* and linear grading of the Ge concentration, as in *VSC4*. This last structure denominated *VSC5* has a virtual substrate characterised by double the number of steps of *VSC2* of half the Ge concentration over double the thickness and a capping layer of the same thickness with the capping layers of *VSC2* and *VSC4*. The growth parameters varied for the second set of structures were:

- For the virtual substrate: the Ge concentration gradient (8% / μm for *VSC5* and 16%/μm for *VSC1-4*) and the type of the Ge concentration grading (linear for *VSC4*, stepwise for *VSC2*, grown under the same conditions as *VSC4* and intermediate between linear grading and step grading, *VSC5*);
- For the capping layer: thickness (1 μm for *VSC1-2, 4 and 5*, and 2 μm for *VSC3*) and the presence of a device structure at the top of *VSC1*.

All the structures of the second set were grown at the same temperature, **750°C,** corresponding to the growth temperature for the heterostructures of the first set, that exhibited superior structural properties. Additionally, all the structures of the second set, with the exception of that grown for reproducibility, are characterised by the same Ge concentration variation in the virtual substrate between **0 - 32%**, of which the last step of **2%** variation is grown over the same thickness of ≈ **300 nm**, in all cases, and remained elastically strained, thus contributing to turning the threaders into misfit segments. Due to the lower final Ge concentration aimed for in this second set of heterostructures, grading in their virtual substrates started at zero.

All heterostructures studied have been grown at intermediate-high temperatures for this technique as well as by comparison with others. The growth temperatures have been chosen to be high enough to thermally activate MD nucleation and elongation, but not too high, so as to cause thermal roughening (Chapter 3, § 3.2.2 [41]).

The Ge concentration gradients in the virtual substrates of the heterostructures studied, with the exception of *VSC5*, have been kept in the intermediate range, higher than those reported by E. A. Fitzerald et al. as 'ideal' in UHVCVD (10% / μm) [3-5], comparable with those used by A. J. Pidduck et al. in LPCVD growth (4-50% / μm) [22-24] and lower than those used by P. Mooney et al. in UHVCVD (50% / μm) [8 –18]. Nevertheless, the Ge concentration gradients used in this study have been well below the limit for generating high TD densities reported by D. Dutartre as applicable to all growth techniques (137% / μm) [28]. These gradients together with the growth rates used resulted in relatively thin virtual substrates (Tables 1 and 2). The lower Ge concentration gradient used for *VSC5* resulted in a thick virtual substrate.

Preliminary quantitative high resolution micro-Raman spectroscopy results obtained for the second set of heterostructures (Chapter 6, § 6.1) as well as qualitative XTEM results for both sets showed that all the heterostructures studied have been relaxed from misfit strain during growth, as originally intended. However, further analysis using micro-Raman spectroscopy and/or high resolution X-ray diffraction (HRXRD) would need to be carried out in order to provide values for the degree of relaxation.

Surface analysis results showed that all the heterostructures studied exhibit, to varying degrees, undulations on their surfaces along two perpendicular **<110>** directions, creating

a crosshatch pattern. This surface morphology is typical of SiGe heterostructures incorporating virtual substrates and has been widely reported in literature for all the growth methods and conditions used. The crosshatch undulations are aligned along the same directions as the MDs lying in the virtual substrate, thus indicating a correlation with them, which persists despite the fact that the virtual substrates are capped with thicker capping layers in the case of the heterostructures of the second set *VSC1-5* (**1-2 μm**) compared to those of the first set, *720*, *775* and *774* (**0.24-0.30 μm**).

However, there are variations within the crosshatch morphology for the two sets of heterostructures studied, due to the different growth conditions used. Results obtained showed that for all structures of the first set, the crosshatch pattern is made of fine, almost periodic undulations, which form a 'small-scale pattern', spaced by distances ranging from **≤ 1 μm** to **≈ 2 μm, and** interrupted by what appear to be, randomly distributed trenches or groups of trenches, spaced by larger distances, ranging from **≤ 5 μm** to **≥20μm.** By comparison, all the heterostructures of the second set (with the exception of that grown for reproducibility) exhibit only the fine, regular undulations. XTEM analyses showed that the fine ripples on the surface of the linear-graded heterostructure *720* grown at the higher temperature and with the higher initial misit, are characterised by steeper sides (with inclinations ranging between **≈ 5° - 12°**) compared to the fine surface undulations of the other linear-graded heterostructure of the first set, *775*, which are characterised by smaller inclination angles (**≈ 2° - 5°**). Furthermore, for the step-graded heterostructure of the first set, XTEM results showed a rather surface.

When analysed in low magnification Nomarski contrast (x50), for better statistical accuracy, the density of crosshatch trenches and groups of trenches appears to be the highest in *720*, generating large areas of irregular, accentuated crosshatch pattern in this structure. The other linear-graded heterostructure of the first set, *775*, is characterised by a lower density of trenches and groups of trenches, occupying more reduced areas. The step-graded heterostructure of the first set, *774*, although grown under identical conditions with *775*, is characterised by the largest areas of fine uniform crosshatch pattern interrupted by much reduced areas of trenches. The heterostructures of the second set grown under similar conditions, display only a fine small-scale pattern which is similar for all the structures of the second set and characterised by consistent values of its lateral spacing (**≤ 1 μm**).

AFM and XTEM analyses carried out on the heterostructures of the first set revealed the presence of pits along the crosshatch trenches in all three structures. AFM results showed that these pits are mainly present at the intersection of crosshatch trenches and occasionally, the trenches appear to end at a pit. The deepest pits found in XTEM for the heterostructure *720* are characterised by in-plane sizes of ≈ **3 μm** and depth values ranging between ≈ **300 – 600 nm** and have side facets inclined at ≈ **24° - 30°**, thus possibly corresponding to **{203}** planes. Similar faceted pits (with sides inclined at ≈ **34°**) have been observed by Cullis et al. [41] in SiGe heterostructures grown by a lower growth rate LPCVD, that have been found to relax by a surface roughening mechanism. The deepest pits found in XTEM for the other linear-graded heterostructure of the first set, *775*, are characterised by in-plane sizes of ≈ **3 μm** and depth values of ≈**150 nm** and have side facets inclined at ≈ **10° - 12°**, thus possibly corresponding to **{105}** planes. Similar facets have been previously observed in the growth of pure Ge 'huts' on Si substrates (described in [1]) and have been found to be caused by the high lattice mismatch between the two materials (≈ 4.2%).

The AFM results obtained for the step-graded heterostructure of the first set, *774*, and that of the second set grown for reproducibility, *VSC6*, indicate a lower density of smaller and shallower pits present along their crosshatch trenches. The values obtained for the size and depth of the pits in *774* show, even in this case, that the largest pits (in-plane dimension of ≈ **2 μm**) are the deepest (up to ≈ **56 nm**). Nevertheless, the deepest pits in the step-graded heterostructures, *774* and *VSC6*, are much shallower than those observed in the linear-graded heterostructure grown under identical conditions, *775*. Furthermore, no faceted pits, of the types encountered in the two linear-graded heterostructures of the first set, *720* and *775*, could be observed in the step-graded heterostructures *774* and *VSC6*.

AFM line analyses carried out on the heterostructures of the second set, grown under similar conditions, *VSC1-5*, revealed the presence of extremely shallow (compared to those found in the first set of heterostructures) pits on their surfaces, mainly at the intersection of crosshatch lines. The deepest pits in these structures, although similar in size to those observed in the heterostructures of the first set (in-plane dimension ≈ **2 μm**) are much shallower (depths ≈ **39 nm**). No pits were observed in the XTEM micrographs of the heterostructures of the second set, all of which show flat surfaces. Faceted pits, of

the type observed in the linear-graded heterostructures of the first set are completely absent from the structures of the second set, *VSC1-5*.

The 3D AFM results showed best the qualitative differences in the surface morphologies of all the heterostructures analysed. The crosshatch pattern of the linear-graded heterostructure of the first set grown at 800°C and with a higher initial misfit, *720,* is characterised by a high density of small (in-plane size) crests and troughs aligned along two perpendicular **<110>** directions. This surface morphology is characterised by a RMS of the surface roughness value of ≈ 27.3 nm (for a 20 x 20 μm^2 scanned area). This value is similar to that obtained by A. J. Pidduck et al. for LPCVD growth with lower growth rates in what they characterise as the 'high temperature-high grading rate regime' (800°C and 45% / μm) [22]. In their study, Pidduck and co-workers concluded that the temperature was the main factor responsible for the surface roughening observed. In our case, the crosshatch patterns of the other two heterostructures of the first set, linear-graded *775* and step-graded *774*, grown at a lower temperature, 750°C, display longer running ridges and channels, which result in lower values of the RMS of the surface roughness, ≈13.8 nm for *775* and ≈ 9.9 nm for *774* (for a 20 x 20 μm^2 scanned areas). Consequently, Pidduck's conclusion appears to be applicable even in our case; growth at a lower temperature results in reduced surface roughness. Furthermore, it also appears that for growth at the same lower temperature, under the growth conditions used for *774* and *775* the two different types of Ge concentration grading result in different surface morphologies, with step grading showing superiority.

The surfaces of the heterostructures of the second set, grown at 750°C, are very similar, despite the variations in growth parameters, and are characterised by regular long running ridges and channels. The flatter, surfaces that characterised the second set of heterotructures grown under similar conditions, by comparison with the rough surfaces that characterise the first set of heterostructures are also reflected by their values for the RMS of the surface roughness. These values are similar for the heterostructures of the second set, independent of the growth parameters that were varied, and range **≈ 8 – 10 nm** (for 20 x 20 μm^2 scanned areas). The RMS of the surface values obtained for the second set of heterostructures are much improved by comparison with the first set and are comparable with others obtained for much thicker virtual substrates by A. J. Pidduck et al. for LPCVD growth with lower growth rates in what is characterised as the 'low

temperature-low grading rate regime' (610°C and 5% / μm) [22]. These values are also comparable with others obtained for compositionally graded structures by different growth methods and for different growth regimes, i.e. modified UHCVD at high temperatures (900°C) by E. A. Fitzerald et al. [8] and UHVCVD at low temperatures (500°C) by LeGoues et al. [12].

RMS of the surface roughness values as low as 2 nm have been reported. Such values have been obtained for example by LPCVD growth with lower growth rates in what was characterised as the 'high temperature-low grading rate regime' (800°C and 5% / μm) [22]. The disadvantage in this case, was the thickness of the virtual substrate obtained (≈6μm). Such low values for the RMS of the surface roughness have also been obtained by using surfactants in SS-MBE growth at low temperatures (510°C), through pushing the surface further from the strain fields of the interfacial MDs [21]. The use of surfactants in CVD or gas source MBE has not yet been reported, but may represent a direction for further research.

To date, compositional grading alone does not appear to result in the low RMS of the surface roughness values required for further device processing. However, compositional grading coupled with CMP for planarising the surface, as used by Fitzgerald et al. [7] appears to be successful in obtaining low RMS of the surface roughness values without the need for thick virtual substrates or high thermal budgets, hence easily achievable even with the SUMC-LPCVD technique. Hence this techniques needs to be explored further.

The different surface morphologies observed for the different heterostructures analysed in this study are correlated with the misfit strain relaxation mechanisms that operate in their virtual substrates. XTEM analyses enabled a better understanding of the characteristics of these relaxation mechanisms.

XTEM analyses showed that the two different Ge concentration grading profiles (linear and stepwise) used in the virtual substrates of both sets of heterostructures studied generate two distinctive internal morphologies. While linear grading of the Ge concentration results in MD segments running along **<110>** directions and distributed continuously through the thickness of the virtual substrate, step grading, even with very small steps (*VSC5*), is reflected by MD segments running along **<110>** directions and grouped only at the different steps of Ge concentration. The different growth parameters

used for the first set of heterostructures activate different misfit strain relaxation mechanisms in their virtual substrates, which result in different structural properties, while the different growth parameters used for the second set of heterostructures activate relaxation mechanisms that result in comparable structural properties.

All the heterostructures analysed appear to be characterised by relaxation mechanisms, which involve the Si substrate. Dislocations loops and loop segments run long distances ($\geq$ 1 μm) into the Si substrate. To date, the only relaxation mechanism reported to involve the Si substrate has been the MFR dislocation multiplication mechanism, observed in compositionally graded SiGe heterostructures grown by UHVCVD at low temperatures (≈500-560°C) and explained by LeGoues et al. [9, 10, 12, 13]. This mechanism has been found to operate only in heterostructures grown under 'very clean' conditions, because it requires the MD nucleation sources to be spaced by at least 1300 Å, consequently it has not been widely reported. As mentioned above, the relaxation mechanisms observed in the different heterostructures of this study are different, but they all involve a substrate contribution. XTEM analyses clearly show that the linear-graded heterostructures of the first set are characterised by high densities of MD nucleation sources, thus making it improbable that a MFR mechanism is operating. The step-graded heterostructure of the first set and all heterostructures of the second set are characterised by lower densities of MD nucleation sources. Nevertheless, all the heterostructures analysed show the same type of contribution of the Si substrate to misfit strain relaxation. Hence, the author of this study concludes that it is improbable that a MFR dislocation multiplication mechanism is operating in the heterostructures analysed. The contribution of the Si substrate to misfit strain relaxation observed in the SiGe–virtual substrate based heterostructures studied here does not appear to have been reported yet, hence it would require further investigation.

XTEM results also revealed the differences between the defect morphologies in the three linear-graded heterostructures grown under different conditions, *720*, *775* and *VSC4*. Essentially, the virtual substrate of the linear-graded heterostructure grown at the higher temperature and with the higher initial misfit, *720*, is characterised by a high density of short MD segments, which extend well into the capping layer, while the other two linear-graded heterostructures *775* and *VSC4*, show MD segments running longer distances along **<110>** directions and well-contained within their virtual substrates, leaving their capping layers MD-free. Additionally, the two linear-graded heterostructures of the first,

720 and *775* set are characterised by groups of TDs with similar topographies, terminating at faceted pits. This type of groups of TDs terminated at faceted pits is totally absent from the linear-graded heterostructure of the second set, *VSC4*, which exhibits a flat surface when analysed in XTEM.

By comparison, all the step-graded heterostructures analysed are characterised by similar virtual substrate morphologies i.e. long MD segments running along **<110>** directions, concentrated at the different steps of Ge concentration and well-contained within the virtual substrates, and flat capping layers, MD-free.

During this study, the author has been faced with the difficulty of attempting to understand the evolution of the misfit strain relaxation processes that take place in the virtual substrates of the heterostructures analysed, by looking at their final morphologies. Considering the morphologies observed, we could not conclude whether the virtual substrates of the linear-graded heterostructures of the first set, *720* and *775*, relax through a surface roughening mechanism, followed by MD nucleation, or the MDs are nucleated first and the strain fields associated with them generate the surface morphologies observed or both these mechanisms operate together. Nevertheless, by comparison with literature [22, 41], it appears more probable that the heterostructure grown at the higher temperature, with a higher initial Ge concentration in the virtual substrate, *720* relaxed through a surface roughening mechanism, resulting in the deep pits with side facets inclined at $\approx$ **24° - 30°**, thus possibly corresponding to **{203}** planes, at which a high density of TD are nucleated ($\approx$ **5×10^{8} - 10^{9} cm^{-2}**). However, the other linear-graded heterostructure of the first set, *775*, grown at a lower temperature and with a lower initial Ge concentration appears to be characterised by MD nucleation at randomly distributed non-homogeneities, as also found by E. A Fitzgerald et al. in heterostructures grown at 900°C by modified UHVCVD [5]. The strain fields of these dislocations create deep trenches along the surface, where TD segments are blocked, impeding growth even further and finally resulting in the faceted pits observed in XTEM, through a mechanism also explained by Fitzgerald and co-workers [6].

In the case of the linear-graded heterostructure of the second set, *VSC4*, it seems highly unlikely that surface roughening occurred, because of the very 'gentle' introduction of misfit strain in the virtual substrate, by starting the Ge concentration grading at zero. This also explains the much reduced surface roughness that characterises this heterostructure.

Additionally, the lower Ge concentration gradient in this heterostructure by comparison with *775*, results in a better distribution of misfit strain throughout the virtual substrate, which again contributes to the improved surface morphology and reduced TD density, as the blocking of threading segments does not occur. Furthermore, the thicker capping layer of this heterostructure allows surface reshaping to take place, which also contributes to its superior surface quality.

The morphologies observed for all the step-graded heterostructures analysed, indicate that it is highly unlikely that misfit strain relaxation through surface roughening takes place in these structures. In all step-graded heterostructures, MD densities decrease toward the steps of higher Ge concentration and their capping layers exhibit flat surfaces. For the heterostructures of the first set, grown under similar conditions, it appears that step grading of the Ge concentration in the virtual substrate, results in a distribution of misfit strain, which activates a relaxation mechanism that generates superior surface morphologies. For the heterostructures of the second set, grown under similar conditions, the different types of Ge concentration grading result in similar surface properties.

XTEM analyses showed the presence of TDs in all the heterostructures analysed. When analysed in different two-beam conditions, these TDs do not satisfy the invisibility criteria, therefore we concluded that they are of the mixed type (60° dislocations gliding on {111} planes) in good agreement with results reported in literature for the $Si_{1-x}Ge_x$/Si (001) system (as shown in Chapter 3). All the heterostructures analysed appear to be characterised by TD running along the whole structure. Similar morphologies have been observed in $Si_{1-x}Ge_x$/Si (001) structures by other groups, who studied their formation and concluded that they are typically caused by an interfacial inhomogeneity, of the particulate type, that continuously 'punches out' dislocations under the influence of the misfit strain introduced continuously through Ge concentration grading [4]. Consequently, heterogeneous dislocation nucleation at interfacial impurities occurs, despite the growth of the Si buffer, and it represents one of the dislocation sources common to all the heterostructures analysed for this study. Most certainly, there are other sources, which we could not identify by looking at the final morphology. In-situ TEM can provide more information on such sources, but the SUMC-LPCVD machine is not equipped with such a facility.

A rough estimation of the TD densities based on XTEM results, showed very similar values for all heterostructures grown at the same temperature, *774*, *775*, *VSC1-6* (in the range (≈ **$3x10^6$ - $8x10^7$ cm^{-2}**) and higher values for the linear-graded heterostructure of the first set grown at the higher temperature and with the higher initial misfit, *720* (≈ **$5x10^8$ - 10^9 cm^{-2}**). The TD density values obtained from XTEM have mainly a qualitative value, due to the highly estimative approach of the technique used to determine them. The use of more (statistically) accurate TD density quantification methods, such as CMP for removing the crosshatch contours coupled with optical microscopy, that can image large areas, or electron beam induced current (EBIC), would need to be explored.

The TD density values obtained make all the heterostructures studied, with the exception of that grown at the higher temperature, suitable for integration in majority carrier devices, according to [1]. Nevertheless, other methods for reducing the TD densities in SUMC-LPCVD grown SiGe heterostructures would need to be studied. One of these is the introduction of a CMP step, both for surface planarisation and for turning the threaders into misfit segments.

TD densities as low as 10^2 cm^{-2} have been obtained through step-grading of the Ge concentration in the virtual substrate coupled with an in situ equilibration anneal after each step, in atmospheric pressure CVD (APCVD) [19]. By annealing each Ge concentration step at temperatures of 1050-1095°C for ≈ 1h, G. Kissinger et al. ensured that total relaxation of each step occurred prior to the growth of the following step, thus resulting in heterostructures with low TD densities. Furthermore, due to the high temperature-long duration induced relaxation, the Ge concentration steps were much thinner than in usual compositionally graded layers. However, the thermal budget required by this method is not suitable for all growth techniques, hence it cannot been widely used.

TD densities of 10^4 cm^{-2} are commonly reported in the literature and have been obtained with most growth methods available and with different reduction techniques, summarised in Chapter 1. However, in order for comparisons with results shown in the literature to be accurate, it would be extremely useful to have consistency in the technique used for the TD density quantification, which does not seem to be the case at present.

Overall the results obtained showed that the linear-graded heterostructure of the first set grown at the higher temperature with a slightly higher initial misfit in the virtual substrate

is characterised by the most inefficient misfit strain relaxation mechanism, in which dislocation nucleation prevails over dislocation motion resulting in unacceptably high dislocation densities and rough surfaces. Under the growth conditions used for this structure, temperature appears to be the determining factor for these structural properties. The growth parameters used for the other two heterostructures of the first set activate different relaxation mechanisms for the two different profiles of Ge concentration grading, with step grading triggering off a more efficient relaxation mechanism, which results in a flatter surface. The growth parameters used for the second set of heterostructures activated relaxation mechanisms that result in similar morphologies, independent of the growth parameters that were varied. Additionally, as intended, the growth conditions used for the second set of heterostructures resulted in further improved structural properties.

To summarise, in this study, we have characterised the effects of some growth parameters used in SUMC-LPCVD on the surface morphology and defect content of SiGe heterostructures incorporating compositionally graded virtual substrates, and identified suitable growth conditions for device-grade heterostructures. The effects on the properties of SiGe virtual substrate-based heterostructures of some of the growth parameters already considered, such as lower growth temperatures, smaller Ge concentration gradients in the virtual substrate, as well as of other parameters not yet considered in this study, such as growth rate, which fundamentally differentiate the SUMC-LPCVD techniques from others, need to be further studied. Furthermore, the use of methods other than compositional grading in the virtual substrate for improving the structural properties of these heterostructures need to be explored in the future.

8. CONCLUSIONS

The aim of the research carried out, the results of which are presented in this study, was to study the effects of growth parameters on the morphology and defect content of SiGe virtual substrate-based heterostructures, SiGe/$Si_{1-x}Ge_x$/Si (001), grown in a low pressure chemical vapour deposition (LPCVD) reactor characterised by growth rates which have not been explored previously, in order to reproducibly fabricate heterostructures with structural properties suitable for device fabrication.

The growth parameters varied were:

- For the virtual substrate: growth temperature, initial and final Ge content, thickness, Ge concentration gradient, type of variation of the Ge concentration (linear and stepwise);
- For the capping layer: thickness and the presence of a device structure.

The conclusions reached are:

- All the heterostructures studied exhibit, to varying degrees, undulations on their surfaces, along two perpendicular <110> direction generating a crosshatch pattern;
- The topography of the crosshatch pattern is determined by the growth conditions used and ultimately reflects the efficiency of the misfit strain relaxation mechanism operating in the virtual substrates of these heterostructures;
- All the heterostructures analysed showed the presence of threading dislocations, the distribution and density of which also reflect the efficiency of the misfit strain relaxation mechanism operating in their virtual substrates;
- Growth at 800°C, with a high initial misfit (0.56%) and a linear grading of the Ge concentration in the virtual substrate, triggered off an inefficient relaxation mechanism, whereby dislocation nucleation prevailed over dislocation motion. This mechanism resulted in high threading dislocation densities and rough irregular surfaces, characterised by a high density of trenches, along which a high density of deep faceted pits are present, thus making the heterostructures unsuitable for device fabrication;
- Growth at the lower temperature of 750°C and with a lower initial misfit (0.50%) resulted in different types of relaxation mechanisms for structures grown with different types of grading of the Ge concentration in the virtual substrate (i.e. linear and stepwise). Under these growth conditions, the step grading of the Ge concentration in the virtual substrate activated a more efficient misfit strain relaxation

mechanism, generating much smoother surfaces, with very few shallower trenches and pits, thus resulting in a structurally superior heterostructure;

- Growth at 750°C, with a Ge concentration grading from zero, resulted in misfit strain relaxation mechanisms that generated similar structural properties independently of the other growth parameters varied (presence of a microelectronic structure in the capping layer, thickness of the capping layer, Ge concentration gradient, type of Ge concentration grading in the virtual substrate, linear or stepwise). The misfit strain relaxation mechanism activated under these conditions resulted in the best structural properties, thus making these heterostructures suitable for device fabrication;
- SiGe virtual substrate-based heterostructures with structural properties suitable for device fabrication can be successfully grown by SUMC-LPCVD;
- The growth of SiGe virtual substrate-based heterostructures by the SUMC-LPCVD technique is reproducible.

9. BIBLIOGRAPHY

[1] "Germanium Silicon: Physics and Materials", *Semiconductors and semimetals* **vol. 56** ed. R. Hull, J. C. Bean, Academic Press (1999).

[2] E. A. Fitzgerald, G. P. Watson, R. E. Proano, D. G. Ast, P. D. Kirchner, G. D. Pettit and J. M. Woodall "Nucleation mechanisms and the elimination of misfit dislocations at mismatched interfaces by reduction in growth area" *J. Appl. Phys.* **65** (1989) p. 2220-2237.

[3] E. A. Fitzgerald, Y. –H. Xie, M. L. Green, D. Brasen, A. R. Kortan, J. Michel, Y. -J Mii and B. E. Weir "Totally relaxed Ge_xSi_{1-x} layers with low threading dislocation densities grown on Si substrates" *Appl. Phys. Lett.* **59** (1991) p. 811-813.

[4] E. A. Fitzgerald, Y. -H. Xie, D. Monroe, P. J. Silverman J. M. Kuo, A. R. Kortan, F. A. Thiel, B. E. Weir "Relaxed Ge_xSi_{1-x} structures for III-V integration with Si and high mobility two-dimensional electron gases" *J. Vac. Sci. Technol. B* **10** (1992) p. 1807-1819.

[5] J. W. P. Hsu, E. A. Fitzgerald, Y. H. Xie, P. J. Silverman, M. J. Cardillo "Surface morphology of related Ge_xSi_{1-x} films" *Appl. Phys. Lett.* **61** (1992) p. 1293–1295.

[6] S. B. Samavedam, E. A. Fitzgerald "Novel dislocation structure and surface morphology effects in relaxed Ge/Si-Ge(graded)/Si structures" *J. Appl. Phys.* **81** (1997) p. 3108–3116.

[7] M. T. Currie, S. B. Samavedam, T. A. Langdo, C. W. Leitz, E. A. Fitzgerald "Controlling Threading Dislocation Densities in Ge on Si Using Graded SiGe Layers and Chemical-Mechanical Polishing" *Appl. Phys. Lett.* **72** (1998) p. 1718–1720.

[8] B. S. Meyerson, K. J. Uram, F. K. LeGoues "Cooperative growth phenomena in silicon/germanium low-temperature epitaxy" *Appl. Phys. Lett.* **53** (1988) p. 2555-2557.

[9] F. K. LeGoues, B. S. Meyerson, J. F. Morar "Anomalous Strain Relaxation in SiGe Thin Films and Superlattices" *Phys. Rev. Lett.* **66** (1991) p. 2903-2906.

[10] F. K. LeGoues, B. S. Meyerson, J. F. Morar, P. D. Kirchner "Mechanism and conditions for anomalous strain relaxation in graded thin films and superlattices" *J. Appl. Phys.* **71** (1992) p. 4230-4243.

[11] F. K. LeGoues, P. M. Mooney, J. Chu "Crystallographic tilting resulting from nucleation limited relaxation" *Appl. Phys. Lett.* **62** (1993) p. 140-142.

[12] F. K. LeGoues "Self-Aligned Sources for Dislocation Nucleation: The Key to Low Threading Dislocation Densities in Compositionally Graded Thin Films Grown at Low Temperature" *Phys. Rev. Lett.* **72** (1994) p. 876-879.

[13] P. M. Mooney, F. K. LeGoues, J. Tersoff, J. O. Chu "Nucleation of dislocations in SiGe layers grown on (001)Si" *J. Appl. Phys.* **75** (1994) p. 3968-3977.

[14] P. M. Mooney, F. K. LeGoues, J. L. Jordan-Sweet "Dislocation nucleation barrier in SiGe/Si structures graded to pure Ge" *Appl. Phys. Lett.* **65** (1994) p. 2845-2847.

[15] P. M. Mooney "Strain relaxation and dislocations in SiGe/Si structures" *Mat. Sci. Eng.* **R17** (1996) p. 105-146.

[16] K. Ismail, F. K. LeGoues, K. L. Saenger, J. O. Chu, P. M. Mooney, B. S. Meyerson "Identification of a mobility scattering mechanism in Si/SiGe modulation-doped heterostructures" *Phys. Rev. Lett.* **73** (1994) p. 3447-3450.

[17] K. Ismail, M. Arafa, F. Stern, J. O. Chu, B. S. Meyerson "Gated Hall effect measurements in high-mobility n-type Si/SiGe modulation-doped heterostructures" *Appl. Phys. Lett.* **66** (1995) p. 842-844.

[18] K. Ismail, M. Arafa, K. L. Saenger, J. O. Chu, B. S. Meyerson "Extremely high electron mobility in SiGe/Si modulation-doped heterostructures" *Appl. Phys. Lett.* **66** (1995) p. 1077-1079.

[19] G. Kissinger, T. Morgenstern, G. Morgenstern, H. Richter "Stepwise equilibrated graded Ge_xSi_{1-x} buffer with very low threading dislocation density on Si(001)" *Appl. Phys. Lett.* **66** (1995) p. 2083-2085.

[20] K. Lyutovich, E. Kasper, F. Ernst, M. Bauer, M. Oehme "Relaxed SiGe buffer layer growth with point defect injection" *Mat. Sci. Eng. B* **71** (2000) p. 14-19.

[21] J. L. Liu, C. D. Moore, G. D. U'Ren, Y. H. Luo, Y. Lu, G. Jin, S. G. Thomas, M. S. Goorsky, K. L. Wang "A surfactant-mediated relaxed $Si_{0.5}Ge_{0.5}$ graded layer with a very low threading dislocation density and smooth surface" *Appl. Phys. Lett.* **75** (1999) p. 1586-1588.

[22] A. J. Pidduck, D. J. Robbins, D. Wallis, G. M. Williams, A. C. Churchill, J. P. Newey, C. Crumpton, P. W. Smith "On the growth of high quality relaxed $Si_{1-x}Ge_x$ layers on Si by vapour phase epitaxy" *Microscopy of Semiconductor Materials* **164** (1997) p. 135-144.

[23] D. J. Paul, A. Ahmed, M. Pepper, A. C. Churchill, D. J. Robbins, D. J. Wallis, A. J. Pidduck "Electrical properties and uniformity of two dimensional electron gases grown on cleaned SiGe virtual substrates" *J. Vac. Sci. Technol. B* **16** (1998) p. 1644-1647.

[24] W. Y. Leong, A. C. Churchill, D. J. Robbins, J. L. Glasper, G. M. Williams "A self-aligned epitaxially grown channel MOSFET device architecture for strained Si/SiGe systems" *Thin Solid Films* **369** (2000) p. 375-378.

[25] C. Rosenblad, T. Graf, J. Stangl, Y. Zhuang, G. Bauer, J. Schulze, H. von Känel "Epitaxial growth at high rates with LEPECVD" *Thin Solid Films* **336** (1998) p. 89-91.

[26] C. Rosenblad, M. Kummer, A. Dommann, E. Müller, M. Gusso, L. Tapfer, H. von Känel "Virtual substrates for n- and p-type Si-MODFET grown at very high rates" *Mat. Sci. Eng. B* **74** (2000) p. 113-117.

[27] R. Hull, J. C. Bean, D. J. Werder, R. E. Leibenguth "Role of strained layer superlattices in misfit dislocation reduction in growth of epitaxial $Ge_{0.5}Si_{0.5}$ alloys on Si (100) substrates" *J. Appl. Phys.* **65** (1989) p. 4723-4729.

[28] D. Dutartre, P. Warren, F. Provenier, F. Chollet, A. Pério "Fabrication of relaxed $Si_{1-x}Ge_x$ layers on Si substrates by rapid thermal chemical vapour deposition" *J. Vac. Sci. Technol. A* **12** (1994) p. 1009-1014.

[29] "Properties of Silicon Germanium and SiGe: Carbon", *emis Datareviews Series* **24**, INSPEC publication, ed. E. Kasper and K. Lyutovich (2000).

[30] D. J. Dunstan "Strain and strain relaxation in semiconductors" *J. Mat. Sci.: Mat. El.* **8** (1997) p. 337-376.

[31] C. Frank, J. H. van der Merwe "One-dimensional dislocations" *Proc. R. Soc. A* **198** (1949) p. 205-225.

[32] J. H. van der Merwe "Strains in Crystalline Overgrowths" *Phil. Mag.* **7** (1962) p. 1433-1434.

[33] J. H. van der Merwe "Crystal Interfaces. Part I. Semi-Infinite Crystals", "Crystal Interfaces. Part II. Finite Overgrowths", *J. Appl. Phys.* **34** (1963) p. 117-127.

[34] J. H. van der Merwe "Strain Relaxation in Epitaxial Overlayers" *J. El. Mat.* **20** (1991) p. 793-803.

[35] J. W. Matthews, "Accommodation of Misfit across the Interface between Single-crystal Films of Various Face-centered Cubic Metals" *Phil. Mag.* **13** (1966) p. 1207-1221.

[36] J. W. Matthews, S. Mader, T. B. Light "Accommodation of Misfit Across the Interface Between Crystals of Semiconducting Elements or Compounds" *J. Appl. Phys.* **41** (1970) p. 3800-3804.

[37] J. W. Matthews, A. E. Blakeslee "DEFECTS IN EPITAXIAL MULTILAYERS" *J. Cryst. Growth* **27** (1974) p. 118-125.

[38] J. W. Matthews "Defects associated with the accommodation of misfit between crystals" *J. Vac. Sci. Technol.* **12** (1975) p. 126-133.

[39] J. W. Matthews, A. E. Blakeslee "Almost perfect epitaxial multilayers" *J. Vac. Sci. Technol.* **14** (1977) p. 989-991.

[40] D. E. Jesson, S. J. Pennycook, J. -M. Baribeau, D. C. Houghton "Direct Imaging of Surface Cusp Evolution During Strained-Layer Epitaxy and Implications for Strain Relaxation" *Phys. Rev. Lett.* **71** (1993) p. 1744–1747.

[41] A. G. Cullis, D. J. Robbins, S. J. Barnett, A. J. Pidduck "Growth ripples upon strained SiGe epitaxial layers on Si and misfit dislocation interactions" *J. Vac. Sci. Technol. A* **12** (1994) p. 1924–1931.

[42] T. Walther, C. J. Humphreys, A. G. Cullis "Observation of vertical and lateral Ge segregation in the thin undulating SiGe layers on Si by electron energy-loss spectroscopy" *Appl. Phys. Lett.* **71** (1997) p. 809–811.

[43] J. Tersoff, F. K. LeGoues "Competing Relaxation Mechanisms in Strained Layers" *Phys. Rev. Lett.* **72** (1994) p. 3570–3573.

[44] D. J. Eaglesham, E. P. Kvam, D. M. Maher, C. J. Humphreys and J. C. Bean, "Dislocation nucleation near the critical thickness in GeSi/Si strained layers" *Phil. Mag. A* **59** (1989) p. 1059-1073.

[45] W. Hagen, H. Strunk "A New type of Source Generating Misfit Dislocations" *Appl. Phys. Lett.* **17** (1978) p. 85-87.

[46] H. Strunk, W. Hagen, E. Bauser "Low-Density Dislocation Arrays at Heteroepitaxial Ge/GaAs-Interfaces Investigated by High Voltage Electron Microscopy" *Appl. Phys. Lett.* **18** (1978) p. 67-75.

[47] F. R. N. Nabarro "Theory of Crystal Dislocations" Clarendon, Oxford (1967).

[48] J. C. Bean, L. C. Feldman, A. T. Fiory, S. Nakahara, I. K. Robinson "Ge_xSi_{1-x}/Si strained-layer superlattice grown by molecular beam epitaxy" *J. Vac. Sci. Technol. A* **2** (1984) p. 436-440.

[49] E. Kasper, H. - J. Herzog, H. Kibbel "A one-dimensional SiGe superlattice grown by UHV epitaxy" *Appl. Phys.* **8** (1975) p. 199-205.

[50] M. L. Green, B. E. Weir, D. Brasen, Y. F. Hsieh, G. Higashi, A. Feygenson, L. C. Feldman, R. L. Headrick "Mechanically and thermally stable Si-Ge films and heterojunction bipolar transistors grown by rapid thermal chemical vapor deposition at 900°C" *J. Appl. Phys.* **69** (1991) p. 745-751.

[51] D. C. Houghton, C. J. Gibbings, C. G. Tuppen, M. H. Lyons, M. A. G. Halliwell "Equilibrium critical thickness for $Si_{1-x}Ge_x$ strained layers on (100) Si " *Appl. Phys. Lett.* **56** (1990) p. 460-462.

[52] R. Hull, J. C. Bean "Nucleation of misfit dislocations in strained-layer epitaxy in the Ge_xSi_{1-x}/Si system"*J. Vac. Sci. Technol. A* **7** (1989) p. 2580-2585.

[53] D. D. Perovic, D. C. Houghton " 'Barrierless' misfit dislocation nucleation in SiGe/Si strained layer epitaxy" *Mat. Res. Soc. Proc.* **514** (1992) p. 391-402.

[54] C. G. Tuppen, C. J. Gibbings "A quantitative analysis of strain relaxation by misfit dislocation glide in $Si_{1-x}Ge_x$/Si heterostructures" *J. Appl. Phys.* **68** (1990) p. 1526-1534.

[55] D. C. Houghton "Nucleation rate and glide velocity of misfit dislocations in $Si_{1-x}Ge_x$/ (100) Si heterostructures" *Appl. Phys. Lett.* **57** (1990) p. 2124-2126.

[56] R. Hull, J. C. Bean "New insights into the microscopic motion of dislocations in covalently bonded semiconductors by in-situ electron microscope observations of misfit dislocations in thin strained epitaxial layers" *phys. stat. sol. (a)* **138** (1993) p. 533-546.

[57] W. Dodson and J. Y. Tsao "Relaxation of strained-layer semiconductor structures via plastic flow" *Appl. Phys. Lett.* **51** (1987) p. 1325-1327.

[58] K. Rajan, M. Denhoff "Misfit dislocation structure at a Si/Si_xGe_{1-x} strained-layer interface" *J. Appl. Phys.* **62** (1987) p. 1710-1712.

[59] M. A. Capano "Multiplication of dislocations in $Si_{1-x}Ge_x$ layers on Si(001)" *Phys. Rev. B* **45** (1992) p. 11768-11773.

[60] L. Csepregi, E. F. Kennedy, J. W. Mayer "Substrate-orientation dependence of the epitaxial re-growth rate of Si-implanted amorphous Si" *J. Appl. Phys.* **49** (1978) p. 3906-3911.

[61] J. Bonar "Thesis for the Degree of Doctor of Philosophy" Department of Electronics and Computer Science, University of Southampton (1996).

[62] Olympus BHSM-313L microscope Manual.

[63] F. Secco d'Aragona "Dislocation etch for (100) planes in silicon" *J. Electrochem. Soc.* **119** (1972) p. 948-951.

[64] K. H. Yang "An etch for delineation of defects in silicon" *J. Electrochem. Soc.* **131** (1984) p. 1140-1145.

[65] TopoMetrix Accurex II^{TM} Manual.

[66] M. H. Loretto "Electron Beam Analysis of Materials" Chapman & Hall (1994).

[67] Gatan precision ion beam polishing PIPS Model 691 Manual.